Modeling of blood flow in aorta

MRI-based computational fluid dynamics of aortic hemodynamics

Perinajová, R.

DOI
10.4233/uuid:1cc9228c-514c-42ee-9edb-6d7596d66f11

Publication date
2023

Document Version
Final published version

Citation (APA)
Perinajová, R. (2023). *Modeling of blood flow in aorta: MRI-based computational fluid dynamics of aortic hemodynamics*. [Dissertation (TU Delft), Delft University of Technology]. https://doi.org/10.4233/uuid:1cc9228c-514c-42ee-9edb-6d7596d66f11

MODELING OF BLOOD FLOW IN AORTA

MRI-BASED COMPUTATIONAL FLUID DYNAMICS OF AORTIC HEMODYNAMICS

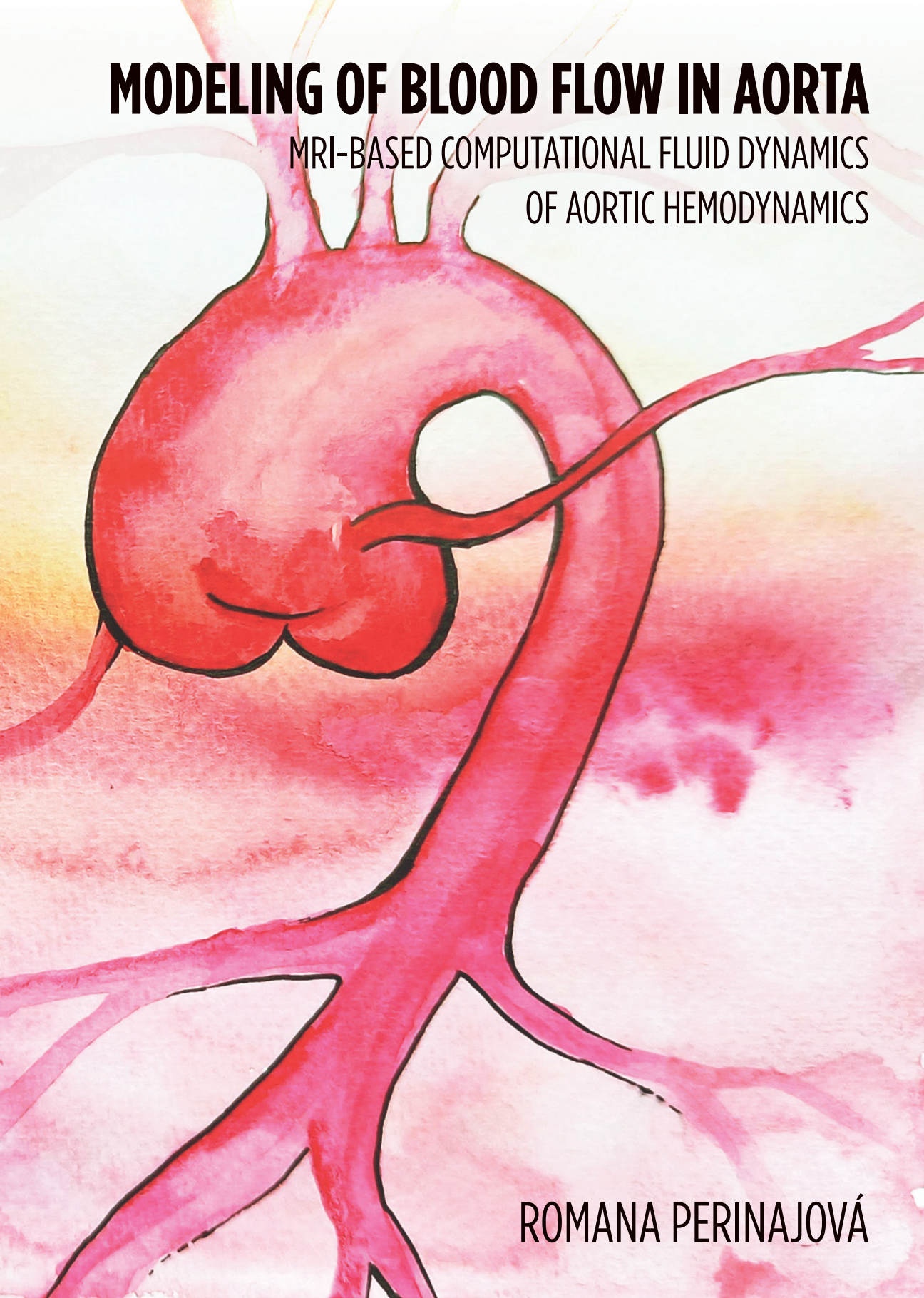

ROMANA PERINAJOVÁ

Modeling of blood flow in aorta

MRI-based computational fluid dynamics of aortic hemodynamics

Modeling of blood flow in aorta
MRI-based computational fluid dynamics of aortic hemodynamics

Dissertation

for the purpose of obtaining the degree of doctor
at Delft University of Technology,
by the authority of the Rector Magnificus Prof. dr. ir. T. H. J. J. van der Hagen,
chair of the Board of Doctorates,
to be defended publicly
on Tuesday 13 June, 2023 at 15.00 hours

by

Romana PERINAJOVÁ

Master of Science in Chemical Engineering,
Delft University of Technology,
born in Martin, Slovakia.

This dissertation has been approved by the promotors.

promotors: Prof. dr. Dipl.-Ing. S. Kenjereš en Prof. dr. H. J. Lamb, MD

Composition of the doctoral committee:

Rector Magnificus,	chairperson
Prof. dr. Dipl.-Ing. S. Kenjereš,	Delft University of Technology
Prof. dr. H. J. Lamb, MD,	Leiden University Medical Center
Independent members:	
Dr. S. Celi,	FTGM / University of Pisa, Italy
Dr. C. A. Bertoglio,	University of Groningen
Prof. dr. ir. P. Segers,	Ghent University, Belgium
Prof. dr. ir. C. Vuik,	Delft University of Technology
Prof. dr. ir. C. R. Kleijn,	Delft University of Technology

Dr. ir. J. J. M. Westenberg, Leiden University Medical Center, has, as co-supervisor, contributed significantly to the preparation of this dissertation.

Keywords: Computational Fluid Dynamics, 4D-flow MRI, Aorta, Simulations

Printed by: Ridderprint

Cover: Visualization of Thoracic Aortic Aneurysm painted utilizing the principles of fluid dynamics, watercolor on paper.

The research described in this thesis was supported by a grant of the Dutch Heart Foundation (CVON2018-08-RADAR). Financial support by the Dutch Heart Foundation for the publication of this thesis is gratefully acknowledged.

ISBN 978-94-6483-167-2

An electronic version of this dissertation is available at
`http://repository.tudelft.nl/`.

I was always at my best when I was learning, when I was curious. When I had yet to see past the next horizon...

Reinhold Messner

Contents

Summary

Aortic aneurysm, a balloon-like enlargement of the healthy artery, is a cardiovascular disease with one of the highest mortality rates. These numbers are due to the usual late diagnosis of the aneurysm, which is often asymptomatic until a fatal event occurs. Such an event can progress to aortic dissection or rupture. Due to the urgent nature of a rupture, we require early detection of asymptomatic aneurysms and proper evaluation of the rupture risk. The clinical guidelines suggest a close follow-up of the luminal size evolution, with advice for surgery based on threshold values. The thresholds are based on the annual maximum arterial diameter or growth rate. However, these guidelines are lacking in many cases.

Therefore, we need to define new biomarkers that consider factors other than the luminal diameter, for example, hemodynamics. The presence of an aneurysm causes an abnormal flow that might affect its pathogenesis. Currently, we use imaging techniques to assess the aortic flow, such as 4D-flow magnetic resonance imaging (4D-flow MRI). 4D-flow MRI can provide hemodynamic information of the whole aorta in 3D space and time. However, the scan time currently limits its resolution. Since high spatiotemporal resolution is necessary to capture hemodynamic effects on aneurysm pathogenesis adequately, we need to implement a new method to assess the aortic flow.

We could base the new diagnostic method on computational fluid dynamics (CFD). Progress in computational power allows for solving complex flows, geometries, and species transport using CFD. However, the anatomy of the aorta, its mechanobiological properties, and the flow are complex and vary from patient to patient. The system's patient-specific nature should always be reflected as close as possible. To do this, CFD can be coupled with 4D-flow MRI to obtain the necessary information, such as aortic morphology and initial flow properties. Nevertheless, the intricate nature of the flow within the aorta and its mechanobiological properties bring an additional layer of complexity to the CFD simulations. We must define appropriate models for many of these physiological features must be modeled appropriately, to represent the flow in the aorta and aneurysm adequately. In this thesis, we attempt to unravel some modeling approaches to simulate the flow and movement of the aortic wall and species transport in arteries.

First, in chapter 2, we try to understand the level of uncertainty in simulations, in terms of wall shear stress (WSS), due to minor morphological variations originating from the segmentation of a 4D-flow MRI scan. To perform statistical analysis, we evaluated four different segmentations (scan, rescan, intraobserver, and interobserver) for ten volunteers. We introduced three different ways of analysis: (1) 0D analysis - average of examined data in a specific section of the aorta (a common approach in a clinical setting); (2) 1D analysis - average alongside the centerline; (3) 2D analysis - direct comparison of surface data (voxel-to-voxel). We found that the agreement between the different segmentations highly depends on the chosen analysis method. While the segmentations agreed well (correlation between 0.78 to 1.00) for the 0D analysis, the correlation between different segmentations

was much lower for the 1D and 2D analysis. This relationship was evident in the exact locality of WSS minima/maxima. Hence, the interpretation of 4D-flow MRI-based CFD results should be taken with caution, especially when the detailed distribution of WSS is the point of interest.

In chapter 3, we assessed the most suitable method to model the turbulent nature of the aortic flow, focusing on local disturbances. For this study, we have considered three different turbulence models ($k-\epsilon$, shear stress transport - SST, and Reynolds stress model - RSM). We analyzed the turbulent flow in two different geometries, representing an aortic coarctation (CoA), a 180° tube with obstruction (phantom), and a patient-specific morphology with narrowing in the descending thoracic aorta. Based on a direct comparison of the simulated flow and WSS to 4D-flow MRI data in the phantom, we have concluded that RSM represents the flow, turbulent kinetic energy, and WSS best. Because of this, we have proceeded to perform the patient-specific simulations with RSM. The direct comparison of in-vivo 4D-flow MRI and CFD with RSM showed that 4D-flow MRI is a good technique for analyzing the global distribution of relative WSS. However, if the exact values of WSS and more detailed analysis are required, CFD using RSM is the preferred method.

In chapter 4, we investigated a novel, robust approach to simulate the motion of the aorta throughout a cardiac cycle. We based the model for the aortic motion on Radial Basis Function (RBF) interpolation of segmentations from 4D-flow MRI. The simulations and subsequent validation utilizing 4D-flow MRI were performed for two cases: a healthy control and a patient with a big root thoracic aortic aneurysm (TAA). For both, our simulations revealed that the movement was most pronounced in the ascending aorta and that it agreed well with the measurements. Additionally, we observed that the variation in flow and related parameters was highest in this region as well when compared to the simulations based on a rigid wall assumption. Given the significant differences between static and dynamic simulations, we advocate for this robust method to simulate aortic wall motion in further research.

Chapter 5 explored a model for joined transport of species (oxygen - O_2 and nitric oxide - NO) in the aorta and aortic wall. Both of these species have been hypothesized to play a role in the pathogenesis of aneurysms. Therefore, elucidating their distribution and effects in the presence of thoracic aortic aneurysms is of critical significance. Therefore, we have compared the flow and mass transfer of O_2 and NO in two morphologies: a healthy control and a patient with TAA. Both O_2 and NO showed a non-uniform distribution in the lumen and the wall. For NO, this behavior was especially dominant in the wall within TAA. Here, the concentration highly varied between the aortic in- and outseam. This variation can have a significant effect on the progression of TAA. On the other hand, we found several locations with lumen-side resistance in the mass transfer of O_2 due to aberrant flow. This limitation in mass transport could lead to hypoxia in the aortic wall, which can potentially cause the genesis of an aneurysm. Hence, we proposed NO to be a predictive biomarker for the diagnosis of TAA and O_2 as a potential biomarker for predicting the genesis of TAA.

Since aneurysms are not limited to the aorta, we showed an application of the developed methods in a different part of the circulatory system - the brain, in chapter 6. Here, the circle of Willis (CoW) distributes the blood from the main vessels to the entire brain. Finally, as previously shown for the aorta, we outlined a similar approach for modeling O_2 mass transfer and identified several locations with a severe lack of O_2 mass transfer toward the

wall, resulting in hypoxia. As prolonged hypoxia can cause the onset of an aneurysm and other diseases, we emphasized the importance of studying the distribution of O_2 in the cerebrovascular system and hypoxia as a potential trigger for various arterial pathologies.

Finally, in the concluding chapter of this thesis, we presented recommendations for essential future advancements in modeling and simulations of diseased arteries, particularly concerning applying these methods in clinical settings. With this thesis, we demonstrated how blood flow in various aortic pathologies can be modeled for both research and clinical purposes. We emphasized the critical importance of the patient-specific nature of the simulations, underscoring the necessity for the seamless integration of imaging, specifically 4D-flow MRI, with CFD. Through the synergistic use of these two techniques, we can enhance our understanding of the pathogenesis of aneurysms.

Samenvatting

Aorta-aneurysma, een ballonachtige vergroting van de gezonde arterie, is een hart- en vaatziekte met een van de hoogste sterftecijfers. Deze aantallen zijn te wijten aan de vaak late diagnose van het aneurysma, dat vaak asymptomatisch is totdat zich een fatale gebeurtenis voordoet. Een dergelijke gebeurtenis kan zich ontwikkelen tot aortadissectie of ruptuur. Vanwege de urgente aard van een ruptuur hebben we een vroege detectie van asymptomatische aneurysma's en een goede evaluatie van het ruptuurrisico nodig. De klinische richtlijnen suggereren een nauwgezette opvolging van de luminale grootte ontwikkeling, met advies voor chirurgie op basis van drempelwaarden. Deze drempelwaarden zijn gebaseerd op de jaarlijkse maximale arteriële diameter of groeisnelheid. Deze richtlijnen zijn echter voor veel gevallen ontoereikend.

Daarom moeten we nieuwe biomarkers definiëren die rekening houden met andere factoren dan de luminale diameter, bijvoorbeeld hemodynamica. De aanwezigheid van een aneurysma veroorzaakt een abnormale stroom die de pathogenese kan beïnvloeden. Momenteel gebruiken we beeldvormende technieken om de aortastroom te beoordelen, zoals 4D-flow magnetische resonantie beeldvorming (4D-flow MRI). 4D-flow MRI kan hemodynamische informatie verschaffen van de gehele aorta in 3D-ruimte en tijd. De scantijd beperkt momenteel echter de resolutie. Aangezien een hoge spatiotemporele resolutie nodig is om hemodynamische effecten op de pathogenese van aneurysma's adequaat vast te leggen, moeten we een nieuwe methode ontwikkelen om de aortastroom te beoordelen.

We zouden de nieuwe diagnostische methode kunnen baseren op computational fluid dynamics (CFD). Vooruitgang in rekenkracht maakt het mogelijk om complexe stromen, geometrieën en soortentransport op te lossen met behulp van CFD. De anatomie van de aorta, de mechanobiologische eigenschappen en de stroming zijn echter complex en variëren van patiënt tot patiënt. Het patiëntspecifieke karakter van het systeem moet altijd zo goed mogelijk worden weergegeven. Om dit te doen, kan CFD worden gekoppeld aan 4D-flow MRI om de nodige informatie te verkrijgen, zoals aortamorfologie en initiële stroomeigenschappen. Desalniettemin zorgen de ingewikkelde aard van de stroming in de aorta en de mechanobiologische eigenschappen ervan voor een extra laag complexiteit in de CFD-simulaties. We moeten geschikte modellen definiëren, want veel van deze fysiologische kenmerken moeten op de juiste manier worden gemodelleerd om de stroom in de aorta en het aneurysma adequaat weer te geven. In dit proefschrift proberen we enkele modelleringsbenaderingen te ontrafelen om de stroming en beweging van de aortawand en soortentransport in slagaders te simuleren.

Ten eerste proberen we in hoofdstuk 2 het niveau van onzekerheid in simulaties te begrijpen, in termen van wandschuifspanning (WSS), als gevolg van kleine morfologische variaties die voortkomen uit de segmentatie van een 4D-flow MRI-scan. Om statistische analyses uit te voeren, evalueerden we vier verschillende segmentaties (scan, rescan, intra-observer en interobserver) voor tien vrijwilligers. We introduceerden drie verschillende

manieren van analyse: (1) 0D-analyse - gemiddelde van onderzochte gegevens in een specifiek deel van de aorta (een gebruikelijke benadering in een klinische setting); (2) 1D-analyse - gemiddelde langs de hartlijn; (3) 2D-analyse - directe vergelijking van oppervlaktegegevens (voxel-naar-voxel). We ontdekten dat de overeenkomst tussen de verschillende segmentaties sterk afhangt van de gekozen analysemethode. Terwijl de segmentaties goed overeenkwamen (correlatie tussen 0,78 en 1,00) voor de 0D-analyse, was de correlatie tussen de verschillende segmentaties veel lager voor de 1D- en 2D-analyse. Deze relatie was duidelijk in de exacte plaats van WSS minima/maxima. Daarom moet de interpretatie van 4D-flow MRI-gebaseerde CFD-resultaten met de nodige voorzichtigheid worden genomen, vooral wanneer de gedetailleerde distributie van WSS van belang is.

In hoofdstuk 3 hebben we onderzocht wat de de meest geschikte methode is om de turbulente aard van de aortastroom te modelleren, met de nadruk op lokale verstoringen. Voor deze studie hebben we drie verschillende turbulentiemodellen overwogen ($k-\epsilon$, shear stress transport - SST, en Reynolds stress model - RSM). We analyseerden de turbulente stroming in twee verschillende geometrieën, die een aorta coarctatie (CoA), een 180° buis met obstructie (fantoom) en een patiëntspecifieke morfologie met vernauwing in de dalende thoracale aorta. Op basis van een directe vergelijking van de gesimuleerde stroming en WSS met 4D-flow MRI-gegevens in het fantoom, hebben we geconcludeerd dat RSM de stroming, turbulente kinetische energie en WSS het beste vertegenwoordigt. Daarom zijn we overgegaan tot het uitvoeren van de patiëntspecifieke simulaties met RSM. De directe vergelijking van in-vivo 4D-flow MRI en CFD met RSM toonde aan dat 4D-flow MRI een goede techniek is voor het analyseren van de globale distributie van relatieve WSS. Als echter de exacte waarden van WSS en een gedetailleerde analyse vereist zijn, heeft CFD met RSM de voorkeur.

In hoofdstuk 4 hebben we een nieuwe, robuuste benadering onderzocht om de beweging van de aorta gedurende een hartcyclus te simuleren. We baseerden het model voor de aortabeweging op Radial Basis Function (RBF)-interpolatie van segmentaties van 4D-flow MRI. De simulaties en de daaropvolgende validatie met behulp van 4D-flow MRI werden uitgevoerd voor twee gevallen: een gezonde vrijwilliger en een patiënt met een grote aneurysma van de thoracale aorta (TAA). Voor beiden toonden onze simulaties aan dat de beweging het meest uitgesproken was in de aorta ascendens en dat deze goed overeenkwam met de metingen. Bovendien hebben we vastgesteld dat de variatie in stroming en gerelateerde parameters ook in deze regio het hoogst was in vergelijking met de simulaties op basis van een rigide wandaanname. Gezien de significante verschillen tussen statische en dynamische simulaties, pleiten we voor deze robuuste methode om aortawandbewegingen te simuleren in verder onderzoek.

Hoofdstuk 5 verkende een model voor gecombineerd transport van stoffen (zuurstof - O_2 en stikstofmonoxide - NO) in de aorta en de aortawand. Van beide soorten wordt verondersteld dat ze een rol spelen bij de pathogenese van aneurysma's. Daarom is het ophelderen van hun verspreiding en effecten in de aanwezigheid van thoracale aorta-aneurysma's van cruciaal belang. Hierom hebben we de stroom en massaoverdracht van O_2 en NO in twee morfologieën vergeleken: een gezonde vrijwilliger en een patiënt met TAA. Zowel O_2 als NO vertoonden een niet-uniforme verdeling in het lumen en de wand. Voor NO was dit gedrag vooral dominant in de wand binnen TAA. Hier varieerde de concentratie sterk tussen de binnen- en buitennaad van de aorta. Deze variatie kan een significant

effect hebben op de progressie van TAA. Aan de andere kant hebben we verschillende locaties gevonden met weerstand aan de lumenzijde in de massaoverdracht van O_2 als gevolg van afwijkende stroming. Deze beperking in massatransport kan leiden tot hypoxie in de aortawand, wat mogelijk het ontstaan van een aneurysma kan veroorzaken. Daarom stellen we NO voor als voorspellende biomarker voor de diagnose van TAA en O_2 als potentiële biomarker voor het voorspellen van het ontstaan van TAA.

Aangezien aneurysma's niet beperkt zijn tot de aorta, hebben we in hoofdstuk 6 een toepassing van de ontwikkelde methoden in een ander deel van de bloedsomloop, de hersenen, laten zien. Hier verdeelt de cirkel van Willis (CoW) het bloed van de hoofdvaten naar de hele hersenen. Ten slotte schetsten we, zoals eerder getoond voor de aorta, een vergelijkbare benadering voor het modelleren van O_2-massaoverdracht en identificeerden we verschillende locaties met een ernstig gebrek aan O_2-massaoverdracht naar de wand, resulterend in hypoxie. Aangezien langdurige hypoxie het ontstaan van een aneurysma en andere ziekten kan veroorzaken, benadrukten we het belang van het bestuderen van de verdeling van O_2 in het cerebrovasculaire systeem en hypoxie als een mogelijke trigger voor verschillende arteriële pathologieën.

Ten slotte hebben we in het afsluitende hoofdstuk van dit proefschrift aanbevelingen gepresenteerd voor essentiële toekomstige vorderingen in het modelleren en simuleren van zieke slagaders, in het bijzonder met betrekking tot de toepassing van deze methoden in klinische settings. Met dit proefschrift hebben we laten zien hoe de bloedstroom in verschillende aortapathologieën kan worden gemodelleerd voor zowel onderzoeks- als klinische doeleinden. We benadrukten het cruciale belang van de patiëntspecifieke aard van de simulaties, en onderstreepten de noodzaak van de naadloze integratie van beeldvorming, met name 4D-flow MRI, met CFD. Door het synergetische gebruik van deze twee technieken kunnen we ons begrip van de pathogenese van aneurysma's vergroten.

1 Introduction

1.1 Motivation and Background

According to the World Health Organization, cardiovascular diseases (CVD) are the leading cause of death in the world, accounting for 32% of the deaths worldwide in 2019 [1]. Among other CVD, the aortic aneurysm has one of the highest mortality rates. An aortic aneurysm (AA) is a balloon-like enlargement of the aorta. It is a life-threatening condition since it can lead to dissection or rupture. Additionally, they are often asymptomatic, until one of these fatal events occurs, causing the high mortality rates of this pathology. The incidence of an aneurysm is 5.3 per 100,000 patients/year [2] (for thoracic aortic aneurysm (TAA)), and between 55-112 per 100,000 patients/year, [3] (for abdominal aortic aneurysm (AAA), that is strongly dependent on age and sex). Almost 70% of patients do not survive a rupture [4, 5]. In total, ruptured AA causes 4-5% of all sudden deaths [6]. These significant numbers have drawn the attention of experts from various fields to understand these pathologies better.

Asymptomatic AA is mainly detected incidentally, e.g., during another exam that includes the chest or abdomen. If detected, the patient undergoes a high-risk surgery, or physicians closely monitor the aneurysm. According to the current clinical guidelines, AA is monitored by continuous measurement of its diameter and subsequent evaluation of the growth rate (in mm/year) [7]. However, evaluating the progress of AA development solely based on morphometric biomarkers has several limitations (low sensitivity and specificity). Therefore, we need to define new biomarkers, that consider additional factors. These new biomarkers should improve the early detection of aneurysms and advance the clinical assessment of its rupture risk, to prevent the fatal event to occur.

To define new biomarkers, we need to understand the aspects behind the genesis and progression of AA. For this, the research focus is shifting toward the understanding of blood flow within the aorta. Abnormal flow patterns can lead to various changes in local properties, e.g. increased wall stiffening, as previously shown for patients with Marfan syndrome and TAA, using 4D-flow magnetic resonance imaging (4D-flow MRI) [8]. However, 4D-flow MRI has a spatiotemporal limitation that prevents us from examining the flow in great detail. To go beyond the current limitations of clinically used imaging techniques, we can assess the flow using a numerical approach. The flow within the

aorta can be modeled using image-based computational fluid dynamics (CFD) with initial conditions based on 4D-flow MRI. Using this non-invasive approach, we can obtain detailed information on aberrant local flow, wall shear stress (WSS), and regional transmural blood pressure. These parameters can help define new, more accurate biomarkers to predict aneurysm formation, growth, and rupture.

In this chapter, we first discuss the biological background, which is essential to understand before defining patient-specific blood flow models in the aorta. Here, we will explain the importance and function of the circulatory system. We will discuss the structure of the arterial wall and the anatomy of the aorta. Next, we will discuss different pathologies of the aorta, especially the AA. For AA, we will focus on the current clinical guidelines for its assessment and treatment. After the biological background, we focus on a literature review concerning modeling the aorta and AA. Here we will discuss the modeling approaches for the geometry and boundary conditions, fluid properties and turbulence modeling, and aortic wall modeling - focusing on aortic wall movement and modeling of species transport within the cardiovascular system. Finally, we will briefly discuss the current definition of biomarkers that focus on flow assessment.

1.2 The Cardiovascular System

The human cardiovascular system (CVS), visualized in Fig. 1.1, is a closed-loop system that consists of two primary circuits: the small and large heart circulation. The small circulation circulates blood between the heart and lungs, while the large circulation circulates blood between the heart and the rest of the body. The circulatory system has several different functions. First, and most important, is the transport of oxygen to the whole body and removal of CO_2 Via the blood, it distributes nutrients from the digestive system to the liver and from the liver to organs. It also removes waste products through the kidneys (urine production) and skin (sweat production). It distributes hormones from the endocrine glands (endocrine glands) and heat, thereby controlling thermoregulation. By doing this, the circulatory system creates and maintains a stable internal environment [9].

In the center of the CVS is the heart. Heart acts as a constantly operating pump, assuring continuous blood distribution to the whole body. It lies on the body center line, two-thirds to the left of the midline and one-third to the right. Its weight is around 300-350 g in men and around 250-300 g in women [9]. Clinically, the heart has left and right parts, with an atrium and a ventricle on each side. The right and left hearts work together to achieve small (pulmonary) and large (body or systemic) circulation.

First, we will start with pulmonary circulation. As shown in Fig. 1.1, in the right heart, *deoxygenated blood* (from the upper and lower vena cava) leaves the right atrium through the tricuspid valve to the right ventricle. The right ventricle pumps blood at low pressure (approximately 20 mmHg) [9]. From here, it flows through the pulmonary valve and the pulmonary artery to the lungs, where the gas exchange occurs. Following the flow from the lungs, *oxygenated blood* passes through four pulmonary veins to the atrium. Next, it leaves through the mitral (or bicuspid) valve into the left ventricle. By continuous contraction during the systole, the left ventricle pumps blood under high pressure (at about 120 mmHg). Finally, from the left ventricle, the blood leaves through the aortic valve into the ascending aorta and branches into the whole body (forming systemic circulation) [9, 11].

Heart contracts (systole) and relaxes (diastole) 60 to 90 times per minute. This movement

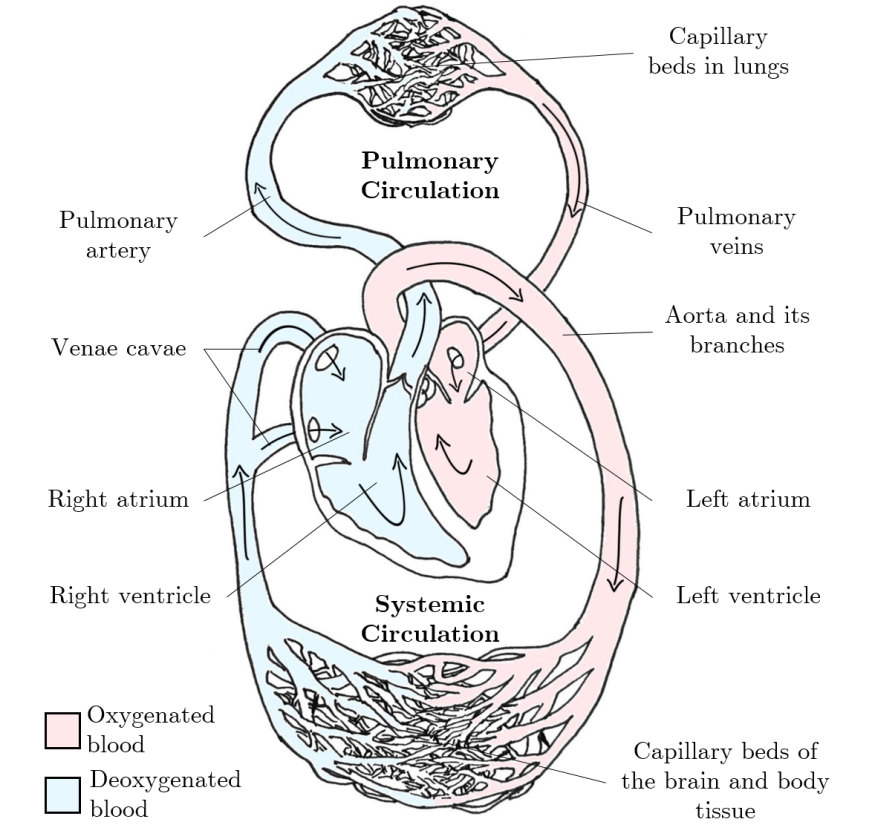

Figure 1.1: Visualization of the human cardiovascular system (hand-drawn, based on [10]).

forms a cardiac cycle. In one day, the heart pumps approximately 7,000 liters of blood via blood vessels [9, 11]. Blood vessels form an enclosed system through which blood flows. Based on their function, we can categorize vessels into three main groups: arteries, veins, and capillaries.

Arteries are the blood vessels that carry oxygenated blood from the heart to the target tissues [9], except for the pulmonary artery. The most powerful artery of the body is the aorta (visualized in Fig. 1.3). Aorta originates from the heart's left ventricle as the ascending thoracic aorta. From here, it arcs and turns to the spine (aortic arch). In the most common configuration, three arteries branch from the arch of the aorta toward the head (so-called supra-aortic arteries): the brachiocephalic trunk, the left common carotid artery, and the left subclavian artery. Next, the aortic arch continues downward as the descending thoracic aorta, and then as the abdominal aorta, from which smaller and smaller arteries emerge [9, 11].

Veins are the blood vessels that carry deoxygenated blood from the tissue to the heart - except for the pulmonary veins. The most prominent veins of the human body include the

upper and lower vena cava. Due to the lack of pressure drop in the venous system, veins contain valves in specific locations that prevent venous reflux (i.e., backward flow of blood) [9, 11]. *Capillaries* are microscopic vessels without muscular or external ligament layers. Their primary role is the exchange of respiratory gases in the organs and tissues. Their surface area in the body is more than 6,000 m^2 [9].

The inner space of vessels, in which blood flows, is called the *lumen* [11], surrounded by the arterial wall. The elastic nature of the vessel wall (especially for arteries) plays a significant role in the blood flow, where their contraction during the diastole ensures a continuous supply of blood to the whole body. The arterial vessel wall consists of three main parts: tunica intima, tunica media, and tunica externa, Fig. 1.2

Tunica intima is the inner layer of the vessels. While this layer is relatively fragile and can high shear stress can easily damage it, it has the ability to reproduce quickly. Tunica intima consists of two parts. The first part is an endothelial layer, consisting of endothelial cells in direct contact with blood and oriented in the direction of flow [12]. Second, a sub-endothelial layer that consists of collagen and fibroblast. The sub-endothelial layer is surrounded by an internal elastic membrane which is the outermost layer for most capillaries and the bridging level between the tunica intima and tunica media [13].

Tunica media is the most substantial layer of the arterial wall. It is formed mainly by circular and spirally arranged muscle cells and elastic tissue (proteoglycans, elastic, and collagen fibers). This layer's physiological function and structure highly vary in different parts of the cardiovascular system. In the great arteries, like the aorta, the primary function of tunica media is to contract during the cycle (specifically during the diastole) to help distribute the blood to the rest of the body [13]. Finally, a thin layer of elastic tissue surrounds these muscle cells - an external elastic membrane connecting the tunica media and tunica adventitia.

Tunica adventitia (or *tunica externa*) is the external layer of the arteries and vessels. It consists of connective tissue containing fibroblasts, proteoglycans, longitudinally oriented elastic, and collagen fibers. For great arteries (aorta and its branching vessels), vasa vasorum surrounds the tunica adventitia (*'vessels of the vessels'*), a system of small capillaries. The primary function of vasa vasorum is to supply oxygenated blood to the outermost layers of the arterial wall. For mammals, the vasa vasorum reduces in the abdominal aorta (compared to the thoracic aorta) [14], causing a limitation in oxygen supply for the arterial wall. The lack of vasa vasorum in the abdominal aorta is hypothesized to be the reason for the high prevalence of AAA [15]. Additionally, recently evidence was found that vasa-vasorum was also absent in TAA [16]. These findings suggest a possible correlation between the pathogenesis and progression of AA and chronic hypoxia [15].

The physiological properties of the vessel wall vary based on the specific vessel function and size. For the aorta, each layer's main parameters (i.e., porosity, permeability, and thickness) are listed in Tab. 1.1.

1.3 Aorta

Aorta is the largest and longest artery in the human body, Fig. 1.3. In healthy adults, the diameter of aorta usually does not exceed 40 mm and aorta gradually narrows downstream. The aorta expands with age at an approximate rate of 0.9 mm every ten years in men

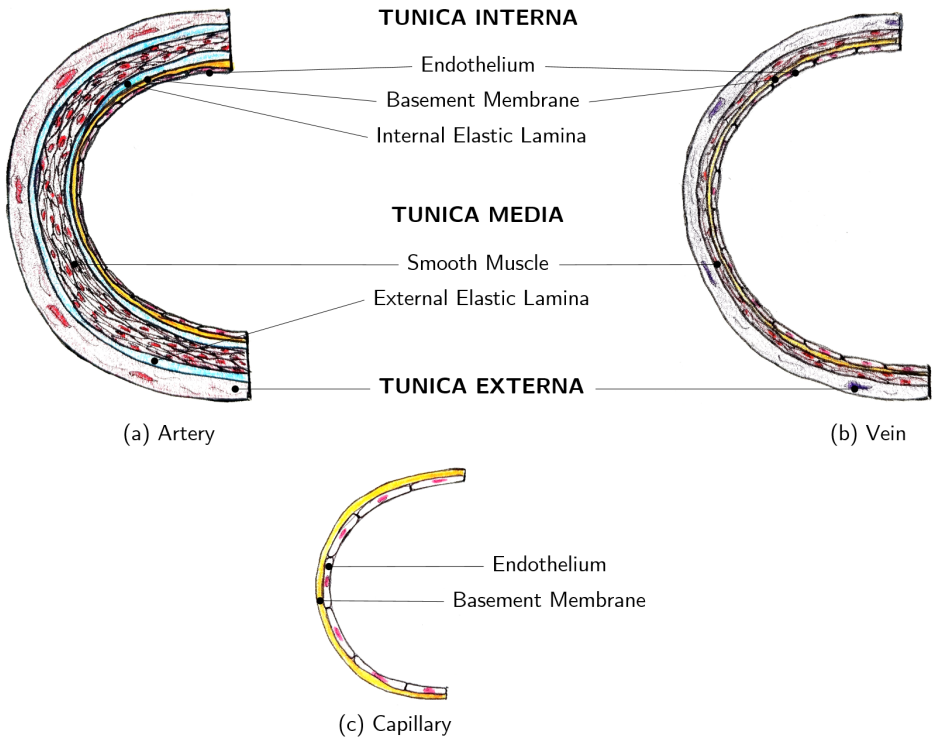

Figure 1.2: Visualization of the wall structure of the arteries (a), veins (b), and capillaries (c), hand drawn.

Table 1.1: Physiological parameters of the aortic wall.

	Porosity [-]	**Permeability** [m^2]	**Thickness** [mm]
Endothelium	5.00e-04	3.20e-21	2.00e-03
Intima	0.983	2.20e-16	0.40
Media	0.258	2.00e-18	1.20
Adventitia	0.85	3.00e-19	0.60
Homogeneous wall	0.551	4.12e-17	2.20
Ref.	[17–20]	[18]	[18, 21]

and 0.7 mm every ten years in women [7]. Except of age and gender, additional factors influencing aortic diameter are body size and blood pressure [22–27]

The primary aortic function is to distribute oxygenated blood from the left ventricle to the entire body through many branching arteries. In addition, the aorta fulfills several other roles in CVS, such as the secondary pump during diastole (via the elastic properties of the aortic wall) and the control of heart rate and systemic pressure (via the pressure-responsive receptors in the ascending aorta) [7, 22].

Aorta consists of two main sections, thoracic and abdominal, divided by the diaphragm

1

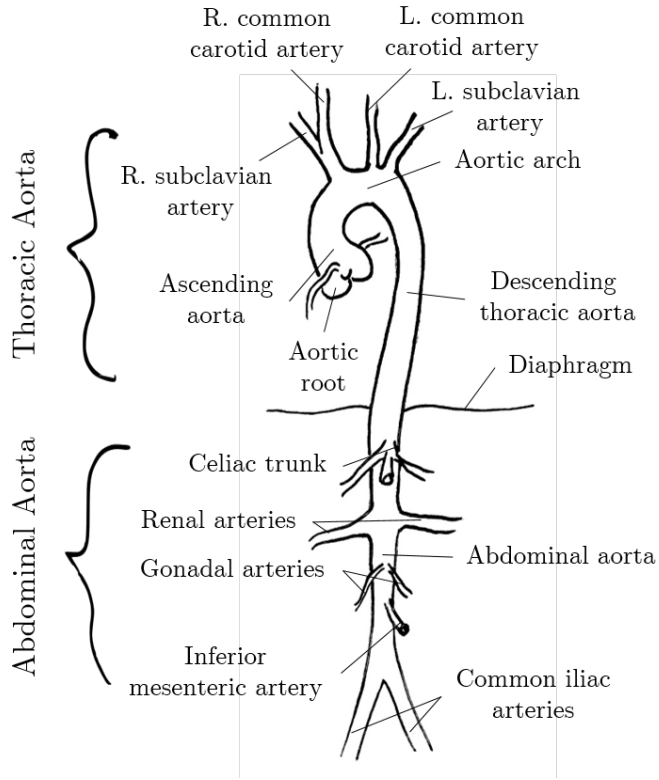

Figure 1.3: Visualization of healthy aorta with the main branching arteries (hand-drawn).

as visualized in Fig. 1.3. The ascending thoracic aorta originates from the left ventricle, where small branching vessels supply blood to the heart (coronary arteries). Then, the ascending aorta passes into the aortic arch. Here, the main branching arteries are the brachiocephalic trunk (BT), which bifurcates into the right subclavian artery (RSA), right common carotid artery (RCCA), the left common carotid artery (LCCA), and left subclavian artery (LSA). These arteries distribute blood to the head and upper limbs. While this particular configuration of the aortic arch is the most common (65-80% people) [28], several variations exist, such as the bovine arch, where BT and LCCA have identical origin [29]. This configuration increases the risk of the formation of thoracic aorta aneurysm [30].

After the arch, the small branching arteries of the descending thoracic aorta supply the respiratory tract, esophagus, pericardium, mediastinum, and intercostal arteries. After the diaphragm, the abdominal aorta supplies blood to the lower limbs and all abdominal and pelvic organs (among others) [9]. The main branching arteries in the abdominal aorta are the celiac trunk (CT), left and right renal artery (L/RRA), left and right gonadal artery (L/RGA), inferior mesenteric artery (IMA), and left and right common iliac artery (L/RCIA).

1.3.1 Aortic Pathologies

Aorta may be affected by a wide range of pathologies: AA (shown in Fig. 1.4), aortic dissection (AD), intramural hematoma, penetrating atherosclerotic ulcer, traumatic aortic injury, pseudoaneurysm, as well as genetic diseases (e.g., Marfan syndrome) and congenital abnormalities such as the coarctation of the aorta (CoA) [7]. This section will discuss AA and its rupture, aortic dissection, and Marfan syndrome in more detail.

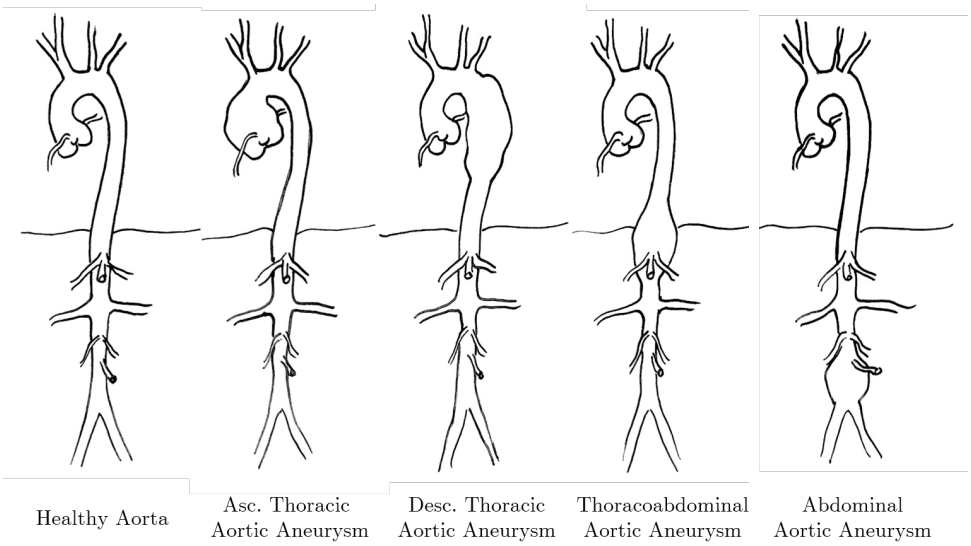

Figure 1.4: Visualization of different locations of aortic aneurysm (hand-drawn).

An *aortic aneurysm* is a severe vessel dilation with respect to its original diameter. AA can develop in different locations of the aorta as shown in Fig. 1.4. Aneurysms are classified based on location, with the highest prevalence for TAA and AAA.

Since aneurysm mainly grows asymptomatically and slowly (at a rate of 1 to 4mm per year [31–33]), the diagnosis is usually incidental during another examination of the thorax and abdomen. If a diagnosis of AA occurs, the assessment of the whole aorta is highly encouraged due to the high prevalence of secondary aneurysms. Based on a population study of 2000 patients with AAA, TAA is present in 27% of the cases [34]. The risk assessment of AA progression or rupture is predominantly based on its diameter. Therefore, based on this assessment, the clinical intervention occurs only if the diameter exceeds a maximal threshold value or escalated growth per year. The threshold varies based on other risk factors (e.g., patients with Marfan or other syndomes, age, sex, and others), but in general, it lies between ≥40 mm (AAA) to ≥50 mm (TAA) [7]. The intervention of AA is also advised if the growth rate (diameter change per year) exceeds 10 mm/year [7]. However, the diameter-based criteria to predict dissection and rupture may not be the best indicator for proper clinical evaluation [35]. While the incidence of small aneurysm rupture is low [36], a significant number of large aneurysms never rupture [37] either. These inconsistencies highlight the need to go beyond the lumen assessment and explore other risk factors, e.g., by hemodynamic analysis.

1

Aortic dissection (AD) is the disruption of a tunica media resulting from intramural hemorrhage, which leads to the separation of the layers of the aortic wall. Due to this, true lumen (TL) and false lumen (FL) develop [38, 39]. This process may be followed by rupture of the aorta (if adventitia breaches) or re-entry into the lumen of the aorta via a secondary intimal rupture [7]. According to the location of FL, the AD is classified in Stanford A dissection (with sub-types I and II, DeBakey classification) and Stanford B (DeBakey III), with the FL located in the ascending or the descending thoracic aorta respectively [7, 38, 39]. The incidence of this pathology is higher for men and increases through life. The prognosis is worse in women due to atypical symptoms and late diagnosis [7]. Patients with acute type A dissection have a 50% mortality within the first 48 hours. The progress of type B dissection is often without complications (progression or signs of rupture). Hence, the patient can be stabilized only with pharmacotherapy and closely followed-up [7].

Marfan syndrome is a genetic disorder affecting the connecting tissue [40]. It develops because of a gene mutation that controls the production of fibrillin (a protein that gives the connective tissue in the body its strength and elasticity) [41]. It affects approximately one in 4,000 people and is in 75% genetically inherited [42]. The usual signs are tall build and disproportionately long limbs and fingers [41, 42]. In addition, patients with Marfan syndrome usually have a lower life expectancy. TAA and dissection are one of the main complications connected to this pathology due to the faulty connective tissue [41]. Because of this, patients with Marfan syndrome are closely monitored for the possibility of aortic pathologies and undergo several surgeries aiming to reconstruct the aorta [41, 42].

1.4 Assessment of Aortic Pathologies

As discussed above, once the diagnosis of AA occurs, it requires a serial assessment of its diameter. The clinical guidelines suggest using non-invasive imaging methods to perform the serial assessment. These are (among others) ultrasound (US) and its variants (transthoracic echocardiography TTE, transoesophageal echocardiography - TOE), computed tomography (CT), magnetic resonance imaging (MRI), or (invasive) aortography [7]. The advantages and disadvantages of these methods are summarized in Tab. 1.2.

Table 1.2: Overview of (dis-)advantages of imaging methods with application in the aorta: transthoracic echocardiography (TTE), transoesophageal echocardiography (TOE), computed tomography (CT), magnetic resonance imaging (MRI), and aortography; - means negative note and + means positive note; adapted from [7].

Advantages/disadvantages	TTE	TOE	CT	MRI	Aortography
Ease of use	+++	++	+++	++	+
Diagnostic reliability	+	+++	+++	+++	++
Bedside/interventional use	++	++	-	-	++
Serial examination	++	+	+++	+++	-
Aortic wall visualization	+	+++	+++	+++	-
Cost	-	-	- -	- - -	- - -
Radiation	0	0	- - -	-	- -
Nephrotoxicity	0	0	- - -	- -	- - -

Until now, we have only mentioned conventionally used methods that aim to provide morphometrical information about the aorta, especially its diameter. However, to define

hemodynamical-based biomarkers, we have to be able to measure and visualize the aortic flow. Over the last few decades, the progress in imaging techniques allowed for flow acquisition using different techniques, for example, 2D phase contract MRI (2D PC-MRI) or 4D-flow MRI, among others. However, acquiring data with a sufficient spatiotemporal resolution is still challenging. Therefore, we cannot fully understand the flow's nature and the patient's condition in detail. In this case, CFD can be a helpful addition to the clinical practice by using patient-specific geometry and boundary conditions (flow measurements, pressure, heart rate, and others). Coupling CFD with imaging data can provide high spatial and temporal resolution of the velocity field and additional information such as local pressure, trans-mural pressure, WSS, turbulent kinetic energy, and others, which can assist clinicians. These parameters are complicated to obtain using conventional imaging techniques.

A key aspect in accurate aortic modeling is the patient-specific information necessary as input parameters: the geometry, movement of the aortic wall, and inlet respectively outlet flow conditions, among others. The first two mentioned are usually acquired clinically by using high spatial resolution imaging techniques such as CT or three-dimensional MRI. Another variation of MRI - 2D PC-MRI, can provide detailed information about the pulse-wave velocity and (bulk) velocity at specific locations within the aorta [8], and has been widely utilized as a source of information for computational studies. However, while this method provides a local understanding of hemodynamics, the entire velocity field, pressure drop, and WSS are still missing. Additionally, due to the multiple scans necessary to acquire the morphology and velocity data, the information can be affected by re-scan related inaccuracies. A relatively new approach is four-dimensional flow MRI (4D flow-MRI) and more recently even four-dimensional flow CT (4D flow-CT) [43, 44]. Using both of these techniques, a time-resolved 3D velocity field can be acquired, and its subsequent post-processing can yield the geometry, wall motion, and flow with its derived variables (such as WSS). However, these techniques are expensive, involve a long acquisition time, and are not typical for clinical practice [45], especially 4D-flow CT which is in early stages of development [43, 44]. Here, image-based CFD can play an important role, where we could create patient-specific computational models based on the information provided by these advanced imaging techniques. Coupling 4D-flow MRI and CFD could lead to a higher degree of flow accuracy, aiding in a better understanding of aortic pathologies.

1.5 Aorta modeling

As with any mathematical representation of a complex system, we must find a balance between the model's accuracy in describing the nature of the system and its efficiency. As spoken by A. Einstein: *"Make everything as simple as possible, but not simpler."* This postulate also holds for CFD applied in medical diagnosis. The aorta is a highly complex biological system, and trying to model its every aspect could lead to unnecessary complexity, resulting in inaccurate results. The amount of patient-specific information necessary for an accurate description of such a model causes this and often showcases non-linear behavior. Additionally, the acquisition and application of each necessary data increase the uncertainty in the simulations, which also grows non-linearly. Finally, this patient-specific information is only sometimes readily available, and simplifications in the models are often necessary. Hence, we should constantly tailor the model to the requirements of the particular study.

If we look at the different goals of various studies focusing on the aorta, we can summarize them into four main categories. First, to define the most accurate models to capture aortic behavior, like the movement of the aortic wall, studying the turbulence in the flow, or accurate prescription of boundary conditions. These studies often involve simplified geometries, in which the models can be adequately verified and validated. Second, to understand the pathology's genesis, progression, and outcome, for which the computational time is not crucial, and more complex models are often considered and applied. Third are population studies. Population studies are crucial in correctly understanding the pathogenesis and definition of possible biomarkers since the aorta varies highly within the general population and from patient to patient. Finally, fourth, use the simulations as a clinical tool to understand the current stage of the pathology and make predictions for possible outcomes. For the latter mentioned, researchers usually consider many assumptions in the model since it is crucial that the tool is easy to use and computational time is clinically relevant.

In the following sections, we will focus on understanding the different aspects connected to the modeling of blood flow in arteries, with a particular interest in their application to the aorta. We will present them in the order they are usually encountered when preparing a simulation. Hence, we will start with defining the computational domain and its boundary conditions. Then we will touch upon the modeling of blood as a fluid (e.g., physical properties and nature of the flow), followed by wall modeling and species transfer within CVS. Finally, we will conclude with a short overview of possible hemodynamical and biochemical biomarkers to predicts the rupture of AA.

1.5.1 Definition of the Computational Domain

The morphology is one of the most crucial aspects of the simulation setup. Usually, researchers adopt two approaches in modeling aortic pathologies - idealized (or simplified) and patient-specific geometry. For the latter, essential aspects of the morphology are:

1. The length of the geometry
2. The inclusion of the major branching arteries (in particular for the aorta)
3. The quality of the acquired morphology

In the next section, we will discuss the definition of the computational domain in detail.

The idealized or simplified geometries are (mainly) used for validating the models using a combination of CFD and experimental techniques (e.g., particle image velocimetry - PIV) [46, 47]. This approach minimizes the influence of any variables that might affect the validity of CFD (e.g., uncertainties in morphology, boundary conditions, and other patient-specific variables); hence, the focus of the studies is solely on the validation of the computational model. Simplified geometries are also widely utilized for parametric studies. The geometry is modified to analyze the effect of different actors on the genesis or progression of aortic pathologies. In modelling of aortic blood flow, studies often utilize a simplified curved pipe as a representation of aortic arch [48, 49]. In the case of AA, parametric models are primarily used to study the AAA. For the AAA, the studies usually assume one (or more) bulges in a straight pipe as the idealized model of the morphology [50–52].

While idealized or simplified geometries help understand the basic hemodynamics in aortic pathologies and testing of advanced computational models, their results are not suitable for drawing general conclusions. Usually, these geometries cannot fully mimic the realistic behavior of arteries, and we must consider many simplifications (e.g., rigid behavior). Additionally, the complicated nature and variability of the aorta make it impossible to generalize results based on simplified cases for the whole population. Due to this, most aorta numerical studies focus on flow simulation in image-based morphologies of volunteers or patient-specific cases with various pathologies.

Patient-specific simulations usually focus on the examination of the current state of the pathology [53], its progress [54], or to compare the pre-operation and post-operation status [55]. Additionally, in recent years, the focus shifted to simulations with many volunteers and patients - population studies. A crucial aspect of all types of patient-specific simulations is the investigated domain. To obtain proper understanding of the flow in the different variations of aortic morphologies, their adequate representations must be retrieved using one of the imaging methods.

As discussed in Section 1.3, the aorta is the largest artery in the human body with many branching arteries. Therefore, it is difficult to obtain an accurate high-resolution image incorporating its entire length and the majority of the branching arteries. In addition, simulation time grows significantly for more complex domains. Due to this, the numerical studies performed on realistic geometries often focus on one part of the aorta. [53, 56, 57]. Simulating just a fraction of the geometry, rather than evaluating the hemodynamics in the whole aorta, may lead to variations and discrepancies in the flow. In the case of TAA, the aberrant flow pattern might lead to a second aneurysm downstream the thoracic (or abdominal) aorta [7] and therefore, not considering the abdominal part in the simulations may lead to underestimating the progress of this pathology. On the other hand, if the thoracic part is omitted, the flow entering the abdominal aorta may be underestimated since the aortic arch creates significant secondary flow structures and the typical helical flow pattern [58].

Another often-made simplification of patient-specific geometries is neglecting the branching arteries. As discussed in Sec. 1.3, the aorta has many branching arteries, varying in size and throughput. While omitting the smallest branching vessels is justifiable (negligible throughput), we should pay attention to major branching arteries. In earlier studies, simulations were performed on an aorta without the supra-aortic arteries [59, 60]. This assumption is often made due to the inconceivable segmentation of these arteries caused by the low contrast close to the aortic arch during image acquisition. However, this approximation may cause significant discrepancies in the simulated flow field since approximately 15%-30% of the blood leaves the aorta through these arteries. Because of this, the hemodynamical parameters, including flow rate and WSS downstream of the aortic arch, are highly overestimated, and the WSS profiles in the arch itself are not resolved correctly. On the one hand, these simplifications are justifiable when the ascending aorta is studied upstream of the aortic arch only [57]. However, if the simulations focus on the effect of flow in the descending part, the results might be compromised.

Next, a significant aspect in evaluating the patient-specific results is the influence of reconstruction accuracy from imaging techniques, e.g., CT and MRI, on CFD results. Van der Palen et al. [61] evaluated the effect of different image reconstruction techniques and

1

scan-rescan variability of the aortic morphology on the flow and wall shear stress derived from the 4D flow MRI. Comparing data from ten volunteers at five-time instances of the cardiac cycle, for which four different segmented images were available, they found that the variability in the geometry may lead to differences in wall shear stress as high as 30% [61]. However, such an extensive analysis is not yet available for CFD studies. Abraham et al. showed in one example that small changes to arterial geometries considerably affect the predicted hemodynamics [62]. Bertier et al. presented similar conclusions for a realistic coronary artery, with three different segmentations, where pressure, WSS, and velocity profiles were severely affected by the geometry [63]. Finally, the real-world intracranial aneurysm segmentation variability was shown in a comprehensive study by Berg et al. [64]. In this study, researchers around the world were asked to segment the proved data set with their own tools. The study showed high variation in the segmented volume (up to 20%) as well as surface area (up to 30%) [64], among other morphometric parameters. These studies highlight that we should be cautious when interpreting image-based patient-specific flow based on CFD.

Finally, an essential step in geometry preparation for simulation is pre-processing. Here, we must execute several steps to prepare the geometry acquired from CT, 4D-flow MRI, or other, which often contains imperfections. These are (at least):

- Clipping of arterial inlets and outlets
- Smoothing and surface subdivision
- Adding the flow extensions

Regarding the first-mentioned item, as we have discussed, as much of the acquired morphology should be used as possible. For the aorta, this step is essential in the ascending part, specifically in the proximity of the root. Here, as much information as possible should be preserved. The next step, smoothing, is the most important during the geometry pre-processing, as it can potentially have a similar effect on the results of the simulations as described in the previous paragraph. From the available smoothing algorithms, perhaps the most used one is the Taubin smoothing filter. Compared to other methods, the Taubin smoothing procedure ensures proper smoothing of regions with high variations in surface curvature and avoids extensive shrinkage of the surface [65]. While the smoothing can potentially cause the morphology to deviate from its actual shape (e.g. due to the shrinking), Celi et al. showed that the uncertainty brought to the simulations due to the smoothing is relatively small compared to the other possible sources (e.g., segmentation) [66]. Next, the surface mesh (triangular) should be subdivided to ensure better surface definition for 3D mesh creation. Butterfly method [67], among others, provides a proper surface subdivision. Lastly, we need to add the flow extensions on (at least) the outlets. The preferred length of the flow extensions should assure a full development of the flow for the stability of the simulations. This length can be estimated based on the entrance length (corresponding to the hydraulic entrance region, as visualized in Fig. 1.5 for a straight cylinder. The length of the hydrodynamic entrance region (L_h) in a cylinder with diameter D can be estimated for laminar flow as [68]:

$$L_{h,laminar} = 0.0575ReD \tag{1.1}$$

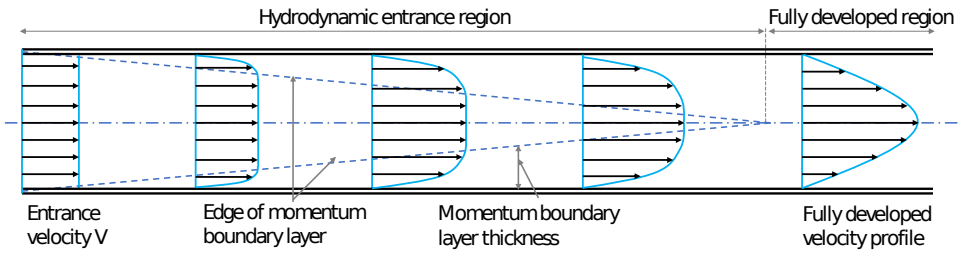

Figure 1.5: Schematics of the developing velocity profile in a straight cylinder.

where Re corresponds to the Reynolds number. Hence, considering maximal Reynolds number $Re_{max} \sim 100$ in the supra-aortic arteries [13], the extension length should equal approximately $5D_i$, with D_i being the diameter of each particular outlet artery.

1.5.2 Boundary Conditions

The most in-depth studied area in modeling CVS is the choice of boundary conditions; therefore, we will include a thorough overview of the available approaches and models in this section. The necessary boundaries to be defined in the computational domain are the wall, inlet, and outlet(s). Many studies suggest that an increase in subject-specific information will result in a more accurate model [69]. However, the information is only sometimes readily available, and many assumptions must be made, especially for the aortic wall. The most common assumption for the wall is the *'rigid wall'* - hence, no modeling of movement is considered. This assumption is often utilized due to the complexity of simulations with wall motion. More on this topic later. The research community often pays special attention to an adequate definition of the domains inlets and outlets. The proper definition of flow boundaries is essential due to the influence of down- and upstream vasculature in CVS. Various approaches have been proposed and used to simulate the effects of CVS on the flow in the aorta. They will be discussed in the following sections starting with the treatment of the inlet and followed by the definition of outlet boundary conditions.

Treatment of Inlet

Most studies consider the subject-specific flow rate for the inlet boundary condition, [60, 70–74]. Although, at the same time, some studies do not use the subject-specific input [48, 49, 75–78] due to the lack of input data. The precise inlet boundary condition is essential to obtain accurate results [79]. The best option would be to directly apply the velocity field extracted from PC-MRI, 4D-flow MRI, or another appropriate imaging method [70, 80–85]. Especially for the aorta, where the tricuspid aortic valve and movement of the aorta heavily influence the velocity profile at the inlet. However, these data are often unavailable, and slight geometrical modifications applied during CFD pre-processing make this process more difficult. If the detailed velocity profile is unknown, the shape of the inlet velocity profile needs to be defined.

The easiest option for inlet profile definition is to apply a uniform velocity at the inlet - a plug profile [48, 49, 76, 86–89]. While this approach is straightforward, it leads to an

1

inaccurate velocity field in the ascending thoracic aorta. Nevertheless, for simplicity, studies that include wall motion [59, 90] often assume a flat velocity profile. With a moving wall, the challenge lies in mapping the velocity profile on a moving surface. However, in recent years, the advantages of directly prescribing the measured velocity profile were highlighted for aortas with and without movement of its wall [83–85]. Still, many numerical studies often assume a flat profile if velocity information is not available.

An alternative approach is to prescribe an analytical velocity profile on the inlet - either parabolic or a Womersley velocity profile ($W(r,t)$), which is defined for axial velocity component in a specific time of the cycle as:

$$W(r,t) = \frac{2B_0}{\pi R^2}\left[1-\left(\frac{r}{R}\right)^2\right] + \sum_{n-1}^{N}\left\{\frac{2B_n}{\pi R^2}\left[\frac{1-\frac{J_0\left(\alpha_n \frac{r}{R} i^{3/2}\right)}{J_0\left(\alpha_n i^{3/2}\right)}}{1-\frac{2J_1\left(\alpha_n i^{3/2}\right)}{\alpha_n i^{3/2} J_0\left(\alpha_n i^{3/2}\right)}}\right]\right\} \tag{1.2}$$

where B_n is the Fourier coefficient, R is the radius, J_0 and J_1 are the Bessel functions of the first kind of zeroth and first order, respectively, and α_n is the non-dimensional Womersley number defined as:

$$\alpha_n = R\sqrt{\frac{n\omega}{\nu}} \tag{1.3}$$

where ω is the fundamental frequency and ν is the kinematic viscosity. The Fourier coefficient B_n are obtained from solving $Q(t) \approx \sum_{n=0}^{N} B_n e^{in\omega t}$ using fast Fourier transform (FFT).

It still needs to be determined whether the definition of velocity as parabola improves the accuracy of the results [80], particularly if the computational domain includes an artificial inlet extension. The inlet extensions usually account for more than $2D_i$, with D_i being the diameter of the inlet. Hence, we expect a slight difference between parabolic and plug since the flow has enough time to develop.

However, the Womersley velocity profile is justified if the simulation is for just a section of the aorta, especially the descending part. The flow is usually developed in the descending aorta and is less influenced by the downstream aorta. Hence, in this case, the application of the Womersley velocity profile at the inlet leads to an accurately predicted flow behavior through the cycle [50]. Because of this, the Womersley profile is often utilized in studies involving idealized geometries [50, 91]. Here, the application of this profile more closely simulates the pulsating nature of flow behavior during the cardiac cycle. Thanks to this, the (parametric) studies can more accurately predict the nature of flow in different geometries, resulting in more realistic conclusions and applicable to the actual aorta.

Finally, more recently, the inclusion of a moving tricuspid aortic valve as an inlet was investigated in a model of aortic root [92] or integrated into a fully patient-specific model [93]. A realistic velocity profile was simulated using a moving valve based on a clinically used artificial model for both of these. Since a fluid-structure interaction model has to be used to simulate the motion of leaflets, which is very time-consuming, this approach is currently not applicable to clinical practice. However, it brings valuable insights, especially for developing prosthetic aortic valves.

To conclude, various studies propose many different models for treating inlet boundary conditions. If the flow data are available, the subject-specific velocity component is the option for the inlet boundary condition. The application of measured data is essential for the aorta since the presence of the aortic valve and the movement of the root highly influence the flow at its inlet.

Treatment of Outlets

Choosing the proper boundary condition for the outlet arteries is complicated since the outlets are highly dependent on other factors of the CVS. The selection of proper outlet boundary conditions is crucial to capture velocity field and pressure waves accurately [94]. Perhaps the best approach is the application of the flow rate extracted from the patient-specific measurements for both inlets and outlets [81, 94, 95]. However, acquiring this data often involves 4D-flow MRI or multiple 2D PC-MRI scans at the exact locations. Hence, CFD studies with inlets and outlets defined based on the measurements are rare. Additionally, defining all flow boundary conditions using measured data poses a risk of overly defining the fluid domain due to the uncertainty in the measurements. For example, in 4D-flow MRI, the spatial resolution causes relatively poor velocity acquisition capabilities in the branching arteries of the aorta. In this case, the combination of inlet and outlet boundary conditions can cause convergence problems in the simulations.

Because of these reasons, several alternative approaches exist to define the outlet boundary conditions. Most studies involving the aorta use constant pressure for all outlets (usually zero) or flow splitting (Murray's law, based on measured data, and others). Another possibility is using lower-order modeling of the remaining CVS, such as 0D (Windkessel) or 1D modeling. This section will discuss the (dis-)advantages of all of these methods. The main point of our discussion will be the ability of the method to capture the phase shift in aortic blood flow. The phase shift in flow occurs due to the simultaneous effects of its pulsating nature and vasomotion. It is one of the main defining factors in arterial flow and should always be accounted for in the simulations.

The most often used assumption for the outlet boundary condition (especially in the early development of modeling aortic flow) is the application of constant pressure for all outlets. While assuming the constant pressure at each outlet is simple, it is an extreme simplification of reality. The pressure at each branch is never equal since it depends on the inlet, the position within the aorta, and the downstream vasculature [96]. Additionally, aortic compliance causes a phase shift in the flow. Therefore, these assumptions lead to overestimating the flow through the branching arteries. Hence, this approach should not be employed, and more advanced boundary conditions should be chosen for the outlets to accurately describe the physiological nature of the flow [94, 97].

Instead of using constant pressure, flow-splitting based on previous literature data [86] or Murray's law are often utilized as an alternative [98–100]. When using Murray's law, the information at the outlets is completely missing, and the flow through the branching arteries is assumed to be proportional to its diameter:

$$\frac{q_0}{q_{D_i}} = \left(\frac{R_0}{R_{D_i}}\right)^{1/3} \tag{1.4}$$

where q_0 stands for the volumetric flow through the mother artery with radius R_0 and q_{D_i} for the through the i-th daughter artery with radius R_{D_i}. Calculations based on Murray's

1

law show that the flow leaving each branch is approximately 5-10% of the inlet flow [101]. Therefore, 15-30% of the flow leaves through the supra-aortic arteries, which agrees relatively well with measurements. Additionally, this approach heavily depends on the goodness of the segmentation (due to the necessity of radii for the calculations), which is usually challenging for the branching arteries. While Murray's law is a better assumption than constant pressure, it still does not account for the influence of the upstream and downstream vasculature on the flow. Finally, due to its nature of estimating the outflow rates based on radii, it may be challenging to empoy this approach in simulations involving arterial kinematics.

If the velocity field is available (e.g. 4D-flow MRI), an alternative approach to Murray's law can be utilizing these data to define the boundary conditions in the branching arteries and, by this, minimize the influence of incorrect radii estimation. Here, the relative net flow of each outlet (with respect to the inlet) can be estimated from the flow data at the outlets or after each bifurcation. The advantage of this approach is its ability to account for phase shifts in the flow. However, using this approach, only the current state of the aorta can be simulated since it cannot predict the changes in the flow (e.g., due to the exercise) or vasculature (e.g., caused by surgery or genesis and progress of a certain pathology).

To simultaneously resolve the flow phase shift and dynamic changes in the computational domain, the zero-dimensional modeling (0D), Windkessel model, has been introduced [102]. The remaining vasculature is modeled using the electrical analog to CVS in this model. This approach models both the compliant and resistive nature of the arteries. The electrical circuits' equivalents to the biological properties are shown in Tab. 1.3.

Table 1.3: The biological analogs of the components of electrical circuit.

Electrical Circuit		Biological System	
$i(t)$	current	$Q(t)$	blood flow
$V(t)$	voltage	$P(t)$	pressure
R	resistance	R	peripheral resistance
Z	impedance	Z	impedance of the proximal valve
C	capacitance	C	arterial compliance
L	inductance	L	inertia of the blood flow

Several Windkessel models exist (with increasing complexity) based on electrical analogs. Namely, the two-element, three-element, and four-element Windkessel model. They are defined as (in increasing order):

$$i(t) = \frac{V(t)}{R} + C\frac{dV(t)}{dt} \tag{1.5}$$

$$\left(1 + \frac{Z}{R}\right) i(t) + ZC\frac{di(t)}{dt} = \frac{V(t)}{R} + C\frac{dV(t)}{dt} \tag{1.6}$$

$$\left(1 + \frac{Z}{R}\right) i(t) + \left(ZC + \frac{L}{R}\right) \frac{di(t)}{dt} + LC\frac{d^2i(t)}{dt^2} = \frac{V(t)}{R} + C\frac{dV(t)}{dt} \tag{1.7}$$

The simplest, two-element model accounts only for arterial compliance and peripheral resistance. The three-element model introduces the impedance of the proximal valve, and

the four-element model also accounts for the inertia of the blood flow. Several studies have coupled the 0D model to the outlets of a 3D geometry to account for the pressure drop in downstream vasculature [72, 74, 103–107]. Because of the relative simplicity of this approach, it is gaining much attention and becoming a baseline for defining dynamic outlet boundary conditions. However, applying the Windkessel model involves tuning the unknown parameters (R, Z, C, L - see Tab. 1.3. The tuning process is similar in most studies and involves an initial assumption. Antonuccio et al. recently showed that the choice of the initial tuning parameter significantly affects the simulated flow wave and pressure gradient [108]. Hence, the tuning process should be done carefully to obtain a realistic flow representation.

While the 0D model can predict the behavior of the flow in time, its main limitation is the tuning process and the adaptability to patient-specific values. Additionally, the 0D model does not include the nonlinear convective term. An alternative approach is used to overcome these limitations: 1D model [96, 109–112], which accounts for the length and circumference of the most prominent arteries. The main system of equations for the 1D model consists of the conservation of mass:

$$\frac{\partial A}{\partial t} + \frac{\partial A\mathbf{u}}{\partial x} = 0 \tag{1.8}$$

where A is the cross-sectional area of the particular artery and $\mathbf{u}$ is the velocity dependent on x and t. Secondly, the conversation of momentum is expressed as

$$\frac{\partial \mathbf{u}}{\partial t} + \mathbf{u}\frac{\partial \mathbf{u}}{\partial x} + \frac{1}{\rho}\frac{\partial p}{\partial x} + \frac{2\pi\nu}{\delta}\mathbf{u} = 0 \tag{1.9}$$

where p is the pressure within the system, ν is the kinematic viscosity, and δ is the boundary layer thickness. The system of equations is completed by assuming static radial equilibrium in the radial direction of the cylindrical tube. Then, the pressure of the vessel p can be expressed using an algebraic relationship between the external pressure p_{ext} and vessel cross-sectional area A, as:

$$p = p_{ext} + \beta\left(\sqrt{A} - \sqrt{A_0}\right) \tag{1.10}$$

Where β is a measure of the vessel stiffness in $dyne/cm^3$. A_0 is the cross-sectional area of the vessel in cm^2 determined at equilibrium state $(p, u) = (p_{ext}, 0)$, and p_{ext} is the external pressure in $dyne/cm^2$. These equations are applied to a model of an arterial system with a tree-like structure. Usually, the system includes at least 55 of the main arteries; however, more accurate models with a higher number of those considered also exist.

The 1D model accurately predicts the velocity and pressure waves in different parts of the CVS through the cardiac cycle. While some studies directly applied the pressure waves at the outlets, either by estimating them or directly applying the ones reported by Olufsen et al. for a healthy individual [96], the 1D-3D coupling also allows for a patient-specific prediction of the outlets [53, 112–115]. In this case, the model modification directly introduces the diseased section of the studied artery in the whole 1D approximation of CVS. One disadvantage of 1D/3D coupling is the added complexity. In this case, many parameters (among others, wall elasticity, number of considered arteries, arterial diameter, and length) are based on previous literature rather than taken subject-specific. These assumptions decrease the patient-specific nature of the coupled system.

1

One of the biggest challenges for patient-specific computational modeling is to know the actual pressure in the aorta. Unfortunately, to the authors' knowledge, there has yet to be a study incorporating the actual patient pressure into the simulation. Instead, the studies focused on evaluating the pressure drop alongside the aorta. However, a recent study showed a method to tune the 0D-based boundary conditions for a given systolic and diastolic pressure [105] and, by that, account for the effects of pressure changes throughout the cycle on the flow.

To conclude, there is no consensus within the research community on which approach is the most accurate to model the outlet boundary conditions if the measured data are unavailable. Instead, the models are constantly improving with the influx of new information from more detailed measurements. These measurements can also provide adequate validation for the simulated flow field, which is essential in accepting the image-based CFD in arteries as a potential clinical tool. Finally, as previously mentioned, the boundary condition for the wall is mainly assumed to be rigid (i.e., no movement is modeled). While this assumption is valid in smaller arteries, the aorta moves considerably, especially the ascending thoracic aorta, due to its connection to the heart and compliant nature. More on modeling the aortic wall will be discussed in one of the following sections.

1.5.3 Blood flow modeling

To account for the continuity of mass and momentum, the blood flow is modeled using the incompressible Navier-Stokes equations:

$$\nabla \cdot \mathbf{u} = 0 \tag{1.11}$$

$$\rho \left(\frac{\partial \mathbf{u}}{\partial t} + \mathbf{u} \cdot \nabla \mathbf{u} \right) = -\nabla p + \nabla \cdot (\mu \nabla \mathbf{u}) + \mathbf{F} \tag{1.12}$$

where $\mathbf{u}$ is the velocity vector, ρ is the fluid density, p is the pressure, $\mathbf{F}$ accounts for other external forces (e.g. gravitational force), and μ is the fluid viscosity. Since blood shows non-Newtonian behavior, the approaches to model the viscosity and other physical properties are discussed in the next section.

Blood and Its Viscosity

Blood is one of the most essential fluids in the human body. It is a colloidal suspension consisting of erythrocytes (red blood cells), leucocytes (white blood cells), and thrombocytes (platelets) suspended in plasma. Plasma consists mainly of water with additional proteins, and inorganic constituents [13]. The physical properties of blood are highly dependent on the temperature and the hematocrit level - the volume percentage of the erythrocytes in the blood [116]. Typical density of blood at 25°C is $\rho_{blood} = 1060$ kg/m^3. The most usual hematocrit level in the human population is 45% for men and 40% for women [117]. Blood rheology highly depends on the hematocrit level, as shown in Fig. 1.6. With increasing hematocrit levels, the viscosity increases as well. Additionally, blood exhibits highly shear-thinning behavior due to the interaction of the different blood components. While the viscosity of plasma is essentially constant due to the shape and interaction of erythrocytes, the blood viscosity changes with applied shear-rate ($\dot{\gamma}$). At lower shear-rates, erythrocytes aggregate (forming rouleaux), while at higher shear-rates, erythrocytes stretch in the

direction of the flow. The creation of rouleaux causes a high portion of the applied shear is used to break down the aggregates [118], causing the typical viscosity behavior of blood [117]. The shear-thinning properties of blood are reflected in the underdevelopment of the velocity profile since it does not exhibit the typical parabolic shape but rather a flattened curve.

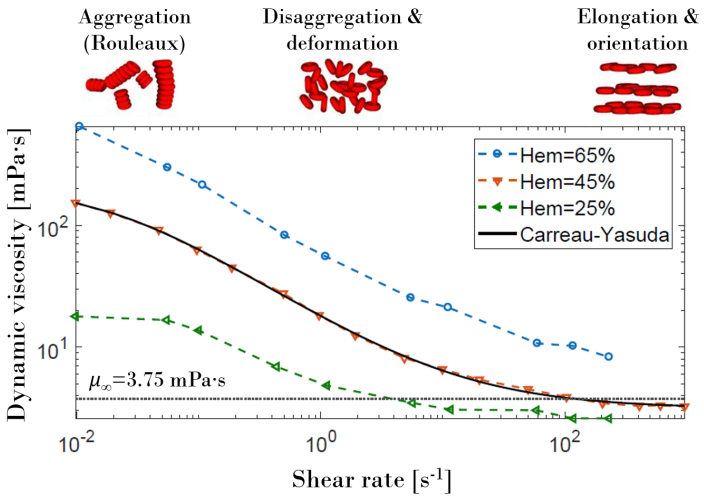

Figure 1.6: Measured values of blood viscosity for different hematocrit levels, namely 25%, 45% and 65% [119, 120], with a fitted Carreau-Yasuda model for the most common hematocrit level of 45%, and viscosity at infinity shear rate μ_p; additionally, the different behavior of erythrocytes is visualized for various range of shear rate.

Since the shear-dependent behavior of blood can significantly affect the flow's behavior, we have to focus on its definition in simulations. Several empirical models were developed to adequately model the non-Newtonian behavior of blood, shown with the expressions in Tab. 1.4.

The viscosity models focus on shear thinning, yield stress (or a combination of the two), and viscoelasticity to model the non-Newtonian properties of blood. The viscosity models have their (dis-)advantages and represent well the specific blood behavior they were designed for. However, it is difficult to determine which of the approaches models the complex blood behavior most closely. These difficulties are also due to the need for experimental data on blood viscosity at different combination hematocrit levels and shear rates. However, the Carreau-Yassuda model with parameters based on a comprehensive study of Gijsen et al. [132] seems to be the most used model for non-Newtonian blood behavior.

In CFD studies concerning blood flow in large arteries, blood is often modeled as Newtonian for simplicity. In these studies, the viscosity is assumed to be constant, with a value close to viscosity at infinite shear rate μ_∞ [133, 134]. While this is a sufficient approximation for large vessels with high to medium shear rates, simplification should not be made if the artery suffers from some pathological condition. For example, Alimohamadi et al. [73] showed that for the case of aortic dissection, high variability in blood viscosity is

1

Table 1.4: Models for non-Newtonian behavior of blood.

Approach	Model	Expression	Ref.
shear thinning	Carreau-Yasuda	$\mu(\dot{\gamma}) = \mu_\infty + (\mu_0 - \mu_\infty)\left[1 + (\lambda\dot{\gamma})^\alpha\right]^{\frac{n-1}{\alpha}}$	[121]
	Power law	$\tau(\dot{\gamma}) = k\dot{\gamma}^n$	[122]
	Cross	$\mu(\dot{\gamma}) = \mu_\infty + \frac{\mu_0 - \mu_\infty}{1 + (\lambda\dot{\gamma})^m}$	[123]
	Quemada	$\mu(\dot{\gamma}) = \mu_p\left(1 - \frac{k_0 + k_\infty\sqrt{\dot{\gamma}/\dot{\gamma}_0}}{\sqrt{\dot{\gamma}/\dot{\gamma}_c}}\Phi\right)^{-2}$	[124]
	Yeleswarapu	$\mu(\dot{\gamma}) = \mu_\infty + (\mu_0 - \mu_\infty)\frac{1 + \ln(1 + \lambda\dot{\gamma})}{1 + \lambda\dot{\gamma}}$	[125]
	Powell-Eyring	$\mu(\dot{\gamma}) = \mu_\infty + \frac{(\mu_0 - \mu_\infty)\sinh^{-1}(\lambda\dot{\gamma})}{\lambda\dot{\gamma}}$	[126]
	Ree-Eyring	$\tau(\dot{\gamma}) = \tau_c \sinh^{-1}\left(\frac{\mu_0\dot{\gamma}}{\tau_c}\right)$	[127]
shear thinning, yield stress	Herschel-Bulkley	$\tau(\dot{\gamma}) = k\dot{\gamma}^n + \tau_0$	[128]
yield stress	Casson	$\tau(\dot{\gamma})^{1/2} = (k\dot{\gamma})^{1/2} + \tau_0^{1/2}$	[129]
	Bingham	$\tau(\dot{\gamma}) = k\dot{\gamma} + \tau_0$	[130]
viscoelasticity	Oldroyd-B	$\tau(\dot{\gamma}) + \lambda_1 \overset{\triangledown}{\tau}(\dot{\gamma}) = \mu_0\left(\dot{\gamma} + \lambda_2 \overset{\triangledown}{\dot{\gamma}}\right)$	[131]

Explanation of (some) symbols: $\overset{\triangledown}{\tau}$ and $\overset{\triangledown}{\dot{\gamma}}$: the upper-convected time derivative of stress and shear tensor respectively; Φ: the volume fraction of rigid particles in suspension (hematocrit level).

present, especially in the false lumen, where the shear-rate is lower. Similar observations were also made for TAA [135], where the flow patterns observed in an idealized model TAA located just after the arc were strongly altered by varying viscosity. In the case of TAA, the aberrant flow in the aneurysm (resulting from the morphological changes) most probably causes the viscosity variation. Additionally, the pulsating nature of the flow drives the shear-rate to vary during the cycle. This behavior also affects the blood viscosity, as shown by Prahl-Wittberg et al. for aortas of patients with the Turner syndrome [136]. Hence, the non-Newtonian effects should always be accounted for when modeling the flow in arteries.

Turbulence in Aorta

Modeling the flow in the aorta poses a big question: *"Should we model the aortic flow as laminar, transitional, or turbulent?"* During turbulence, random eddies occur in the flow, creating the so-called energy cascade. In this cascade, the energy is transferred from the largest eddies to the smaller scales. Finally, the energy dissipates in the form of heat for the eddies in order of the Kolmogorov length scale.

To distinguish between the three regimes, the flow is usually characterized by the

Reynolds number (*Re* - the ratio of inertial to viscous forces) as:

$$Re = \frac{D_0 \overline{v} \rho}{\mu} \tag{1.13}$$

with D_0 being the characteristic length scale, $\overline{v}$ is the average velocity, ρ is the liquid density, and μ is the dynamic viscosity (here assumed constant). For a steady flow in a straight pipe, laminar flow occurs for *Re* below ≈2,000, and turbulence occurs for *Re* above ≈4,000 [137]. For *Re* in the range of 2,000 to 4,000, the flow is transitional, generally unstable [137], and little is known about this regime in more complicated domains, like the aorta. The characteristic values of *Re* for aorta vary during the cardiac cycle, from $Re \propto 1$ for diastole and well above 4,000 for peak systole.

However, aortic flow is often assumed to be within the range of laminar regime [138, 139]. This assumption is motivated by the pulsating nature of the flow in arteries. Due to the pulsating flow, the turbulence may need more time to develop during the high-*Re* part of the cycle fully; hence, only small oscillations can occur. For the aorta, the systolic range of *Re* much higher than 2,000 accounts for less than 10% of the total cycle time. For turbulence to be fully developed, either the duration of the high-*Re* regime has to be longer, or the limit for turbulent *Re* is higher than the usual range. Peacock et al. estimated the emergence of turbulence for $Re > 5500 \sim 9800$ [140] for a pulsating flow in a straight pipe. Therefore, much higher *Re* is usually considered critical for the onset of turbulence in aortic flow [77, 140, 141].

To relate the nature of pulsativity with the nature of blood flow, it was shown that the critical value of *Re* in the aorta increases with increasing Womersley number (Wo) [138, 140] as well as Strouhal number (St) [140]. *Womersley number* relates the transient inertial forces to the viscous forces as:

$$Wo = \frac{\omega D_0^2}{\mu \rho^{-1}} \tag{1.14}$$

where ω is the angular frequency of the flow oscillations. Womersley number is highly dependent on the arterial diameter. In the aorta, the usual range of Wo varies between seven to seventeen [142] (depending on the particular segment, highest in ascending thoracic aorta and lowest in the abdominal aorta). Hence, the critical $Re \propto Wo$ and therefore different per subject.

Strouhal number relates the oscillations of the flow (caused by the inertial forces) to the velocity variation (caused by the convective flow acceleration) [143] as:

$$St = \frac{\omega D_0}{\overline{v}} \tag{1.15}$$

For low St, no oscillations occur in flow, and the flow is laminar. On the other hand, if St is very high, oscillations dominate in the turbulent flow [143]. For a medium range of St, the vortex shedding occurs [143], as shown in simulations and experiments within AAA of a mouse [144], an aortic dissection [145], as well as for stenosed arteries [146–149].

Peacock et al. utilized Buckingham Pi analysis to derive the dimensionless groups for transition to turbulence within physiological pulsating flow [140]. Their empirical analysis

1

yielded a relationship for peak critical Re (Re^c_{peak}) based on Wo and St as:

$$Re^c_{peak} = 169\,Wo^{0.83}\,St^{-0.27} \tag{1.16}$$

This correlation was later used in a study by Stalder et al. to analyze aortic flow using 2D PC MRI [150]. They show that the measured peak Re was, on average lower than the estimated Re^c_{peak} in each segment of the aorta.

Finally, the aortic morphology can also affect the onset of turbulence. Due to the curved shape of the aorta, secondary flow occurs in the arch caused by the centripetal forces. This flow contains two counter-rotating vortices, the so-called Dean vortices. The onset of these vortices can be estimated by looking at the *Dean number* (De), which relates the inertial and centripetal forces to the viscous forces as:

$$De = Re\left(\frac{D_0}{2R_c}\right)^{1/2} \tag{1.17}$$

where R_c is the radius of the curvature for the studied artery. The counter-rotating vortices emerge for $De > 64 \sim 75$, and flow becomes fully turbulent for $De > 400$ [151] in a 90° bend. Several analyses and experimental studies showed that due to the curvature, the onset of turbulence occurs at higher Re [13, 152–154].

Using the reasoning of this combined phenomena (i.e., pulsating flow in curved arteries), many studies use the assumption of laminar flow to study aortic hemodynamics [80, 86, 94, 95, 155–158]. Nevertheless, the transitional flow (in some instances even localized turbulence) has been reported for healthy aorta, especially for young adults, as well as for different aortic pathologies [159–167]. Vergara et al. [166] showed the presence of flow disturbances in AAA and reported a considerable effect of turbulence on the estimated WSS. The level of flow disturbances is impacted by age-related changes in the aorta as well [168]. Additionally, the level of turbulent kinetic energy in the aorta increases with applied stress (e.g., due to exercise) [169], which can also be a potential factor behind the pathogenesis of AA. Finally, several other studies on disturbed flow in intracranial aneurysms reported transitional and turbulent regimes even for $Re \ll 2{,}000$ [170–172], with the peak systolic Re for intracranial aneurysm $Re \sim 400$. Therefore, it is essential to identify a proper viscous model for studies involving turbulence or cycle-to-cycle instabilities in the aorta or other arteries.

The turbulence models range from the simplest Reynolds-Averaged Navier Stokes (RANS) models like $k-\epsilon$ [173] or $k-\omega$ [174], through the combination of these two, so-called Shear-Stress Transport (SST) model [155, 175], to the Large Eddy Simulations (LES) [166, 176, 177]. Instead of modeling the turbulence, few studies resolved both the spatial and temporal resolution enough to perform Direct Numerical Simulations (DNS) of the flow and, by that, resolve all of the scales of eddies [172, 178–181]. To do this, the spatiotemporal domain has to be small enough to satisfy the Kolmogorov length (η) and time (τ_η) scales:

$$\eta = \left(\frac{\nu^3}{\epsilon}\right)^{1/4} \tag{1.18}$$

$$\tau_\eta = \left(\frac{\nu}{\epsilon}\right)^{1/2} \tag{1.19}$$

where ν represents the kinematic viscosity and ϵ represents the average dissipation rate. For flow in the aorta, the estimated typical Kolmogorov microscales are $\eta \propto 10^{-5}$ m and $\tau_\eta \propto 10^{-4}$ s [1].

While DNS is the best approach concerning the accuracy of the simulations, the method is computationally costly due to its spatiotemporal requirements. Therefore, the usage is questionable in a clinical setting. Additionally, we must consider the order of the smallest scales of eddies in turbulent blood flow. According to Antiga et al., the limiting length scale is the size of RBCs rather than η, and the blood flow should be regarded a dense suspension [182]. Hence, other approaches than DNS, e.g., LES or RANS, might be more appropriate to model flow in the aorta.

To summarize this section, at the moment, it is not very easy to adequately answer the question posed at the beginning. While many studies have performed simulations involving turbulence modeling in the aorta, two aspects still remain unanswered:

1. Does turbulence in aorta occur?
2. What is the most appropriate model to account for it?

To answer the first, more measured flow data are necessary for a broad population of healthy controls and a variety of aortic pathologies. While for the second, a rigorous analysis (with proper validation and verification) is necessary to determine the adequate turbulence model (especially in a clinical setup).

1.5.4 Modeling of Aortic Wall

When modeling the aortic wall, we must consider two features: (1) movement and (2) tissue. First, we must understand the movement of the aortic wall and its effects on the flow since each cardiac cycle, the aorta experiences significant changes in the radial shape, with diameter expanding or reducing as much as 5% during the peak systole and the diastole [183, 184]. Additionally, due to the heart's movement, the aorta (especially the ascending thoracic aorta) experiences additional movement in both horizontal and vertical directions. The second-mentioned modeling of the aortic wall tissue is essential if we want to understand how the tissue responds to various (mechano-)biological stimuli, e.g., the transport and consumption of oxygen, nitric oxide, or drugs. In this section, we will more closely elaborate on both of these subjects.

Movement of Aortic Wall

Several studies focused on modeling the aorta with an aneurysm using the finite element (FE) method, which involves just the solid modeling [185–188]. However, since these studies do not simulate hemodynamics, they are not considered further for our approach.

The *'simplest'* approach to model the interplay of fluid dynamics and solid mechanics is the fluid-structure interaction (FSI), where the fluid and solid parts of the domain are computed at the same time. Alimohamadi et al. [73] compared FSI with the rigid wall assumption in a dissected aorta. They reported that while the differences in the flow field were not too significant, they found a major variation could in the derived variables (such

[1] These order of magnitude values were estimated based upon an analysis of RANS simulations of turbulent blood flow in the aorta.

as WSS) and the pressure difference between the false and true lumen [73]. Reymond et al. [111] reported similar results in an aorta of a healthy subject; they found that CFD with rigid wall assumption significantly overestimates the values of WSS alongside the whole aorta in comparison to FSI. On the other hand, they found the pressure wave to be slightly lower in the case of FSI. Brown et al. [104] reported similar results for a healthy aorta.

For FSI, special attention has to be given to the definition of the solid part in the simulations. The most common assumptions are the constant thickness of the aortic wall, isotropic properties, and Young modulus taken from literature. Hence, the defining parameters are often based on something other than subject-specific data. Nevertheless, all the previously mentioned parameters are essential for correctly modeling the compliant vessels, especially if a specific pathology is present [189–191]. However, these patient-specific data are often not readily available for the simulations. Because of this, FSI modeling may bring uncertainty to the results due to many assumptions in the solid part [185].

The wall motion can be prescribed rather than modeled to reduce the number of assumptions made by FSI simulations. For example, Bonfanti et al. [105] modeled the motion of the aortic wall in a dissected aorta using a moving mesh approach with the prescribed motion of the wall. The motion was prescribed based on the pressure distribution on the wall. This approach was shown to be relatively fast and appropriate for the problem as the results from their simulations, especially the motion of the wall, were in close agreement with the data from non-invasive imaging. However, several discrepancies still could be found since they made several assumptions due to the not-existing data about the systolic and diastolic pressure and the distensibility of the aortic wall. Especially the need to input the distensibility of the aortic wall causes a problem for the patient-specific application of this method since this parameter is difficult to obtain. Hence, while this model shows progress toward patient-specific modeling of aortic wall motion, several improvements are still necessary for a widespread application.

An option for the simultaneous modeling of aortic wall motion and flow is the direct use of imaging data. In such a case, the wall position is obtained from measurements (e.g., MRI) and interpolated through the cycle. This approach was shown in the simulation of a small section of the thoracic ascending aorta [57] as well as the left ventricle [192]. Prescribing the wall motion has excellent potential since no assumptions have to be made, resulting in an entirely subject-specific model. However, this method still faces certain obstacles if applied to simulations of the whole aorta. In this case, the treatment of moving inlet and multiple branching arteries has to be solved.

Representation of Aortic Wall Tissue

While aortic wall tissue can be simplified for wall motion simulations, we need to properly define it for other applications, e.g., studying the transfer of various species and drugs within the wall. To do this, the tissue's physiological properties must be understood and adequately translated into the models. As mentioned in Sec. 1.3, the aortic wall consists of several layers with different functions, compositions, and physical properties. Here we will discuss how these layers can be represented in mathematical models and often made simplifications.

The most accurate representation of the aortic wall is to model each layer separately. In the so-called *'multi-layer model'*, the different layers are modeled as porous media with

their respective physical properties. Within the porous media, the flow is defined using the superficial velocity:

$$S_i = -\left(\frac{\mu}{\alpha_w}\mathrm{v_i} + \mathrm{C_{2w}}\frac{1}{2}\rho|\mathbf{v}|\mathrm{v_i}\right) \tag{1.20}$$

where S_i is the source term for the $\mathrm{i^{th}}$ (x, y, or z) momentum equation, α_w is the aortic wall permeability, and C_{2w} is the inertial resistance. The permeability and inertial resistance vary for the different layers[17–21]. While the superficial velocity can adequately model the flow through intima, media, and adventitia, a different mathematical representation has to account for the resistive effects of the endothelium and internal/external elastic membrane. Here, the pressure drop across these layers can be described using a simplified one-dimensional representation of a thin membrane:

$$\Delta p = -\left(\frac{\mu}{\alpha_m}\mathbf{v} + \mathrm{C_{2m}}\frac{1}{2}\rho\mathrm{v}^2\right)\Delta m \tag{1.21}$$

with α_m being the permeability of the membrane, C_{2m} being the pressure jump coefficient, and Δm being the membrane thickness [17–21].

Simulations with this model of the aortic wall were considered in several studies for mass transfer of species, mainly in simplified geometries [17–20]. However, multiple thin layers can cause many complications, especially during meshing. This is due to the significant difference between the aortic diameter and the typical thickness of the wall layers. The diameter of the aorta is usually 10 (for adventitia) to 10,000 (for endothelium) times larger than the different layers within the wall. Hence, the mesh has to be adequately scaled in these domains, resulting in a very large number of cell elements. Because of this, most studies involving realistic arteries consider the simplified, one-layer assumption of aortic wall [193–195]. Here, only a single layer of the aortic wall is considered, usually with physical properties based on averages of the entire wall.

1.5.5 Transport of Species

Most of the studies mentioned before modeled blood as a single-phase fluid, Newtonian or non-Newtonian, with the density and viscosity reported by the literature. However, blood is a multi-phase fluid containing several different species, and its primary purpose is to carry oxygen and other nutrients to organs and tissue. Therefore, for many pathologies, it is essential to understand the local variations in the concentration of different species.

A convection-diffusion equation characterizes the transport of species i in CVS:

$$\frac{\partial c^{(i)}}{\partial t} = \nabla\cdot\left(\mathscr{D}\nabla c^{(i)}\right) - \nabla\cdot\left(\mathbf{v}\mathrm{c}^{(\mathrm{i})}\right) + R^{(i)} \tag{1.22}$$

with $c^{(i)}$ representing concentration of species i, $\mathscr{D}$ diffusivity, and $R^{(i)}$ the source/sink term for the species. While the dilute approximation does not hold for the transport of larger molecules, it has been widely utilized in studies concerning species transport in CVS.

Several numerical studies focused on understanding the mass transfer of various species in CVS using numerical techniques. These start from 1D simulations of species transport in the whole body to determine the global changes in the species concentration [196–198],

1

to accurate 3D modeling of mass transport in realistic arteries. Additionally, studies focus on the modeling of different species and molecules. For example, many studies focused on modeling the mass transfer of large molecules such as LDL, which is essential for understanding the pathogenesis of atherosclerosis [78, 199]. For different applications, the mass transfer of oxygen has been accounted for either in idealized models of arteries [193, 200–208] or realistic computational domains obtained from different imaging techniques [209–211]. In general, the studies conclude that using CFD techniques is possible to predict accurately the distribution of different species in the diverse parts of the human body.

While studying the aorta, we have to focus on understanding oxygen distribution. Studies on AA patients found that the aorta's diseased portion has a different wall structure than the healthy sections [212]. These regions were stiffer due to the lack of collagen and elastin fibers [212, 213]. In addition, the degradation of the extracellular matrix (ECM - composed of collagen and elastin) was correlated to the insufficient supply of oxygen [214]. Several CFD studies found that aberrant blood flow causes low oxygen concentration due to fluid side limitations. Most of these studies modeled oxygen as a free species in plasma (dilute approximation) [196, 200, 201, 204, 207, 208, 211]. However, this is a substantial simplification since the majority of oxygen in CVS (98%) is bound to hemoglobin in RBCs, specifically its heme group. One heme group can carry up to four molecules of oxygen according to the following reaction mechanism:

$$\begin{aligned} \mathrm{Hb} + \mathrm{O_2} &\xrightarrow{\mathrm{K_1}} \mathrm{HbO_2} \\ \mathrm{HbO_2} + \mathrm{O_2} &\xrightarrow{\mathrm{K_2}} \mathrm{Hb(O_2)_2} \\ \mathrm{Hb(O_2)_2} + \mathrm{O_2} &\xrightarrow{\mathrm{K_3}} \mathrm{Hb(O_2)_3} \\ \mathrm{Hb(O_2)_3} + \mathrm{O_2} &\xrightarrow{\mathrm{K_4}} \mathrm{Hb(O_2)_4} \end{aligned}$$

with K_1, K_2, K_3 and K_4, being the reaction constants. Studies that considered oxygen transported as bounded species to hemoglobin [205, 206, 209, 210, 215, 216] concluded that the inclusion of hemoglobin to the transport of oxygen is essential to obtain an accurate distribution of the species in CVS.

Other than oxygen, other small molecules can affect the development of AA. In a recent study, increased nitric oxide (NO) values were present in the thoracic aorta of patients with the Marfan syndrome [217]. As we have discussed, many patients with this particular syndrome often suffer from TAA. Hence, an accurate understanding of the relationship between NO mass transfer and the development of TAA is needed.

To model NO mass transfer, we can again use the convection-diffusion equation. However, in this case, we need to focus on the treatment of the source term that represents NO production. Endothelium produces NO, which is driven by the changes in shear stress [218]. Several empirical approaches were proposed to model this relationship, with two mainly used relationships: linear and hyperbolic. First, the linear relationship between NO production and WSS [219], defined as:

$$r_{NO-linear} = r_{ref} \frac{|\tau_w|}{\tau_{ref}} \tag{1.23}$$

where r_{ref} is the reference production rate of NO (r_{ref} = 150 μMs^{-1}) and τ_{ref} is the reference WSS (τ_{ref}=2.4 Pa). Second, the hyperbolic model proposed as[220]:

$$r_{NO-hyp} = r_{basal} + r_{max} \frac{|\tau_w|}{|\tau_w| + a} \tag{1.24}$$

with r_{basal} being the NO production rate at no shear-rate (r_{basal}=2.13 nMs^{-1}), r_{max} being the maximal NO production rate (r_{basal}=457.5 nMs^{-1}), and a being a fitting parameter (a=3.5 Pa). As reported by Liu et al., the latter approach showed to be more accurate in representing the physiological nature of NO production since the simulated values were close to measured data ($\mathcal{O}(nM)$) [194]. However, a more thorough analysis of the modeling of NO production is necessary.

To conclude, many species (e.g., NO and O_2) can affect the development of arterial pathologies, including AA. Therefore, a proper understanding of the variation in local concentration is necessary. While these specific mechanisms cannot be studied using conventional imaging techniques, image-based CFD can provide these data. Finally, understanding the species distribution in AA can help define biomarkers for predicting progression and rupture. Currently, most of the studies focus mainly on defining predictive biomarkers based on impaired hemodynamics in AA, which could be improved by including species transport. The following section will discuss more on the biomarkers based on hemodynamical properties.

1.6 Biomarkers for Rupture of an Aneurysm

Several studies aimed to predict the rupture site of an aneurysm based on the hemodynamical criteria only. The hemodynamical criteria are usually based on WSS and its variants. WSS for a non-Newtonian fluid with viscosity $\mu(\dot{\gamma})$ is defined as:

$$\overrightarrow{\tau_w} = \mu(\dot{\gamma}) \left.\frac{\partial \mathbf{v}}{\partial n}\right|_{\text{wall}} \tag{1.25}$$

WSS affects the endothelial cells (ECs) that form the first layer of the arterial wall and are in direct contact with the blood flowing in the lumen. While ECs form just a small portion of the arterial wall, they are integral to a healthy artery since they attend to several critical homeostatic functions. These functions are vascular remodeling, modulation of hemostasis and thrombosis, mediation of inflammatory responses, and regulation of vascular contraction [221]. Due to its essential function, we must investigate the effect of the flow on the turnover of ECs. The regions of the arterial wall with laminar flow show a significantly lower reproduction rate of ECs [222] than those with disturbed or oscillating flow [223]. The behavior of ECs in disturbed flow can significantly increase the chance of lesions, aortic wall remodeling, or both [221]. Hence, WSS has a high potential to be a predictive biomarker for different aortic pathologies.

Since blood flow in the human body changes considerably during the cardiac cycle, time-averaged quantities are often utilized to understand its cumulative effects. These are either time-averaged wall shear stress (TAWSS):

$$TAWSS = \frac{1}{T} \int_0^T \left|\overrightarrow{\tau_w}\right| dt \tag{1.26}$$

1

where T is the cycle length or oscillatory shear index (OSI):

$$OSI = \frac{1}{2}\left(\frac{\left|\int_0^T \overrightarrow{\tau_w}\, dt\right|}{\int_0^T \left|\overrightarrow{\tau_w}\right| dt}\right) \tag{1.27}$$

While TAWSS shows the regions of the maximal or minimal averaged WSS during the whole cycle, high OSI represents the rate change of direction of the WSS vector during the cycle from the most dominant flow direction.

Using these (and other) hemodynamic parameters, several studies have investigated the effect of blood flow on the development of aneurysms and tried to propose new biomarkers for diagnosing this pathology. Xiang et al. [224] found that the aneurysm rupture site correlates with the combination of very low local values of WSS and OSI. However, Cebral et al. [225] outcomes were different. They found the rupture site in an area with high values of WSS and concentrated impingement regions. The reviews by Meng et al. [226] and Xiang et al. [227] presented that both low and high values of WSS might affect the rupture site. These contrasting outcomes brought attention to understanding an aneurysm rupture, resulting in the *CFD rupture challenge*. Here, different groups tried to estimate the rupture site of an intracranial aneurysm (located in the brain vasculature) using their respective techniques [79, 228]. From all of the participating groups, 81% could correctly predict which of the two presented aneurysms has ruptured [228]. However, the groups varied in the estimated rupture site location and considered hemodynamical criteria. Some combinations of different hemodynamical criteria were: low WSS and elevated pressure, high WSS only, low WSS and high OSI, and finally, an impingement zone with associated high WSS and high-pressure [79, 228]. Hence, this study did not bring more consensus on the hemodynamical processes behind the rupture.

Therefore, a unified idea about the genesis and development of an aneurysm still needs to be introduced. To overcome this, we have to thoroughly analyze blood flow in healthy aortas and AAs to look for potential biomarkers. Here, blood flow modeling can bring great advantages, since we can relatively quickly analyze a wide variety of pathologies, focusing on multiple aspects of blood flow.

1.7 Objective and Outline

The research presented in this thesis aims to develop a patient-specific model for flow in CVS, focusing on the aorta and AA. The model has to be accurate, i.e., it has to be sufficiently detailed to describe the physiological behavior of the aortic flow correctly. However, the model has to be also numerically efficient due to the relatively fast diagnostic requirements in the clinical setting. Hence, we can summarize several main objectives of this thesis:

1. What is the level of uncertainty brought to the simulations by the input data?
2. How can the flow, and aortic wall motion be modeled?
    - What is the most efficient yet accurate model to account for the instantaneous and localized turbulence of the blood flow?
    - How can the patient-specific nature of aortic wall movement be defined?
3. What are the predominant factors in the pathogenesis of AA?
    - What is the role of hemodynamics in AA formation and rupture?
    - What is the role of biochemical parameters in AA formation and rupture?
4. How can the models be used in other parts of the cardiovascular system?

Outline

To achieve these objectives, this thesis consists of five studies, each forming a chapter:

In *Chapter 2*, we will evaluate the level of variability in the calculated flow due to variability in the input geometry. The currently used segmentation protocol of 4D-flow MRI images includes manual adjustments of the aortic geometry. These can cause variations in input geometry for CFD. To understand the level of inaccuracy in the simulations, we will present a population study based on ten healthy subjects. Each of the volunteer aortas will be segmented four times: (1) and (2) based on two different scans with a set amount of time between them (scan-rescan variability), (3) based on two different segmentations of the same person (inter-observer variability), (4) and based on segmentation of two different people.

In *Chapter 3*, we will unravel the turbulence modeling of flow in the aorta, specifically in CoA. We present a comprehensive comparison of three RANS models and the validation of a simulated field with the measured flow (using 4D-flow MIR) in a phantom of simplified geometry representing CoA. The advantage of working first with a phantom for this study rather than analyzing the flow in a real geometry is the deep understanding of the turbulent behavior in (curved) pipes with an obstruction. By doing this, we will be able to assess which computational model is the most suitable for capturing the turbulent behavior in the CoA. Finally, we will apply the same principle to modeling turbulent flow in patient-specific CoA.

Chapter 4 will focus on the effects of aortic wall motion and inlet definition on the simulated flow field. To do this, we will present a comprehensive model that includes the motion of the wall and automatic registration of a 4D-flow MRI-based inlet velocity profile

as the boundary condition. We will utilize the prescribed mesh movement approach to define the wall motion. We will present a novel method using Radial Basis Function (RBF) interpolation of several geometries through the cardiac cycle segmented from 4D-flow MRI. Finally, to assess the uncertainty brought to the simulations due to rigid wall assumption, we will compare the static (rigid-wall assumption) and dynamic (RBF-based movement) simulations for healthy control and a patient with big root TAA.

In *Chapter 5*, we will bring more insights into the hemodynamical and biochemical (O_2 and NO) determinants behind the pathogenesis of AA. We will present a model for simultaneous NO and O_2 mass transfer in the lumen and aortic wall. We will first show how to create an aortic wall representation using a homogeneous single-layer approximation. We will discuss the complex mechanisms of O_2 and NO mass transfer within the CVS and the most appropriate models to capture their transfer within the lumen and the arterial wall. To understand the difference between a TAA and a healthy aorta, we will present an analysis of hemodynamical (TAWSS, OSI, and ECAP) and biochemical (distribution of O_2 and NO) parameters. In doing this, we will define a few biomarkers to include during population studies.

In *Chapter 6*, we will provide the application of image-based CFD in a different part of the CVS - the Circle of Willis (CoW). The CoW is an integral part of the blood distribution within the cerebrovascular system. Hence, different pathologies (e.g., atherosclerosis and aneurysm) can strongly impair blood distribution and the essential nutrients and species carried by blood within the brain. In this chapter, we hypothesize that oxygen's lumen-side mass transfer resistance can lead to an impaired function of vascular and brain tissue in this region of CVS due to hypoxia. Prolonged hypoxia can lead to the development of atherosclerosis, aneurysm, or dementia. We will present an efficient method for modeling oxygen mass transfer by blood and outline an approach to evaluating regions with limited lumen-side mass transfer, i.e., the locations of CoW suffering from hypoxia.

Finally, in *Chapter 7*, we will summarize the main conclusions of this thesis, provide recommendations for future work, and present our view on the direction of this field.

References

[1] WHO, *Cardiovascular diseases (cvds),* (2019).

[2] R. Gouveia e Melo, G. Silva Duarte, A. Lopes, M. Alves, D. Caldeira, R. Fernandes e Fernandes, and L. Mendes Pedro, *Incidence and prevalence of thoracic aortic aneurysms: A systematic review and meta-analysis of population-based studies,* Seminars in Thoracic and Cardiovascular Surgery **34**, 1 (2022).

[3] D. P. J. Howard, A. Banerjee, J. F. Fairhead, A. Handa, L. E. Silver, P. M. Rothwell, and O. V. Study, *Population-based study of incidence of acute abdominal aortic aneurysms with projected impact of screening strategy,* Journal of the American Heart Association **4** (2015), 10.1161/JAHA.115.001926.

[4] W. D. Clouse, J. W. Hallett, Jr, H. V. Schaff, P. C. Spittell, C. M. Rowland, D. M. Ilstrup, and L. J. Melton, 3rd, *Acute aortic dissection: population-based incidence compared with degenerative aortic aneurysm rupture,* Mayo Clin Proc **79**, 176 (2004).

[5] N. Abdallah, C. Mouchati, C. Crowley, L. Hanna, R. Goodall, J. Salciccioli, D. Marshall, R. Gibbs, and J. Shalhoub, *Trends in mortality from aortic dissection analyzed from the world health organization mortality database from 2000 to 2017,* International Journal of Cardiology **360**, 83 (2022).

[6] M. L. Schermerhorn, R. P. Bensley, K. A. Giles, R. Hurks, A. J. Omalley, P. Cotterill, E. Chaikof, and B. E. Landon, *Changes in abdominal aortic aneurysm rupture and short-term mortality, 1995-2008: a retrospective observational study,* Annals of Surgery **256**, 651 (2012).

[7] *2014 ESC Guidelines on the diagnosis and treatment of aortic diseases,* European Heart Journal **35**, 2873 (2014).

[8] J. J. Westenberg, A. J. Scholte, Z. Vaskova, R. J. van der Geest, M. Groenink, G. Labadie, P. J. van den Boogaard, T. Radonic, Y. Hilhorst-Hofstee, B. J. Mulder, L. J. Kroft, J. H. Reiber, and A. de Roos, *Age-related and regional changes of aortic stiffness in the marfan syndrome: Assessment with velocity-encoded MRI,* Journal of Magnetic Resonance Imaging **34**, 526 (2011).

[9] E. Marieb and K. Hoehn, *Human Anatomy & Physiology* (Pearson, 2013).

[10] *How does blood flow through the heart?: https://www.newhealthadvisor.com/Blood-Flow-Through-the-Heart.html, Accessed: 2021-12-10,* .

[11] M. Ross and W. Pawlina, *Histology: A Text and Atlas : with Correlated Cell and Molecular Biology* (Wolters Kluwer, 2016).

[12] J.-L. Gade, *Mechanical Properties of Arteries: Identification and Application* (Licentiate dissertation, Linkopig University Electronic Press, 2019).

[13] C. G. Caro, T. J. Pedley, R. C. Schroter, and W. A. Seed, *The Mechanics of the Circulation* (Oxford University Press, 1978) p. 527.

[14] H. Tanaka, N. Zaima, T. Sasaki, T. Hayasaka, N. Goto-Inoue, K. Onoue, K. Ikegami, Y. Morita, N. Yamamoto, Y. Mano, M. Sano, T. Saito, K. Sato, H. Konno, M. Setou, and N. Unno, *Adventitial vasa vasorum arteriosclerosis in abdominal aortic aneurysm,* PloS one **8**, e57398 (2013), 23460850[pmid].

[15] M. Billaud, J. C. Hill, T. D. Richards, T. G. Gleason, and J. A. Phillippi, *Medial hypoxia and adventitial vasa vasorum remodeling in human ascending aortic aneurysm,* Frontiers in Cardiovascular Medicine **5** (2018), 10.3389/fcvm.2018.00124.

[16] A. Y. Son, N. M. DeMarais, S. C. Malaisrie, J. W. Lomasney, M. Pradella, L. D. Wilsbacher, B. A. Allen, M. Markl, and R. Avery, *Complete regional absence of vasa vasorum in an ascending aortic aneurysm,* Circulation: Cardiovascular Imaging **14**, e012312 (2021).

[17] S. Chung and K. Vafain, *Effect of the fluid–structure interactions on low-density lipoprotein transportwithin a multi-layered arterial wall,* Journal of Biomechanics **45**, 371 (2012).

[18] L. Ai and K. Vafai, *A coupling model for macromolecule transport in a stenosed arterial wall,* International Journal of Heat and Mass Transfer **49**, 1568 (2006).

[19] G. Pontrelli and F. de Monte, *A multi-layer porous wall model for coronary drug-eluting stents,* International Journal of Heat and Mass Transfer **53**, 3629 (2010).

[20] G. Pontrelli, A. Di Mascio, and F. de Monte, *Local mass non-equilibrium dynamics in multi-layered porous media: application to the drug-eluting stent,* International Journal of Heat and Mass Transfer **66**, 844 (2013).

[21] M. Bukač and M. Alber, *Multi-component model of intramural hematoma,* Journal of Biomechanics **50**, 42 (2017).

[22] R. B. Devereux, G. de Simone, D. K. Arnett, L. G. Best, E. Boerwinkle, B. V. Howard, D. Kitzman, E. T. Lee, T. H. Mosley, A. Weder, and M. J. Roman, *Normal limits in relation to age, body size and gender of two-dimensional echocardiographic aortic root dimensions in persons ≥15 years of age,* The American Journal of Cardiology **110**, 1189 (2012).

[23] M. J. Roman, R. B. Devereux, R. Kramer-Fox, and J. O'Loughlin, *Two-dimensional echocardiographic aortic root dimensions in normal children and adults,* The American Journal of Cardiology **64**, 507 (1989).

[24] H. Kälsch, N. Lehmann, S. Möhlenkamp, A. Becker, S. Moebus, A. Schmermund, A. Stang, A. A. Mahabadi, K. Mann, K.-H. Jöckel, R. Erbel, and H. Eggebrecht, *Body-surface adjusted aortic reference diameters for improved identification of patients with thoracic aortic aneurysms: Results from the population-based heinz nixdorf recall study,* International Journal of Cardiology **163**, 72 (2013).

[25] I. S. Rogers, J. M. Massaro, Q. A. Truong, A. A. Mahabadi, M. F. Kriegel, C. S. Fox, G. Thanassoulis, E. M. Isselbacher, U. Hoffmann, and C. J. O'Donnell, *Distribution,*

determinants, and normal reference values of thoracic and abdominal aortic diameters by computed tomography (from the framingham heart study), The American Journal of Cardiology **111**, 1510 (2013).

[26] C. S. Lam, V. Xanthakis, L. M. Sullivan, W. Lieb, J. Aragam, M. M. Redfield, G. F. Mitchell, E. J. Benjamin, and R. S. Vasan, *Aortic root remodeling over the adult life course,* Circulation **122**, 884 (2010).

[27] O. Vriz, C. Driussi, M. Bettio, F. Ferrara, A. D'Andrea, and E. Bossone, *Aortic root dimensions and stiffness in healthy subjects,* The American Journal of Cardiology **112**, 1224 (2013).

[28] N. L. Mligiliche and N. D. Isaac, *A three branches aortic arch variant with a bi-carotid trunk and a retro-esophageal right subclavian artery,* International Journal of Anatomical Variations (2009).

[29] K. Layton, D. Kallmes, H. Cloft, E. Lindell, and V. Cox, *Bovine aortic arch variant in humans: Clarification of a common misnomer,* American Journal of Neuroradiology **27**, 1541 (2006).

[30] C. Malone, T. Urbania, S. Crook, and M. Hope, *Bovine aortic arch: A novel association with thoracic aortic dilation,* Clinical Radiology **67**, 28 (2012).

[31] R. R. Davies, L. J. Goldstein, M. A. Coady, S. L. Tittle, J. A. Rizzo, G. S. Kopf, and J. A. Elefteriades, *Yearly rupture or dissection rates for thoracic aortic aneurysms: simple prediction based on size,* Ann Thorac Surg **73**, 17 (2002).

[32] D. Oladokun, B. O. Patterson, J. Sobocinski, A. Karthikesalingam, I. Loftus, M. M. Thompson, and P. J. Holt, *Systematic review of the growth rates and influencing factors in thoracic aortic aneurysms,* Eur J Vasc Endovasc Surg **51**, 674 (2016).

[33] G. Weininger, M. Mori, S. Yousef, D. J. Hur, R. Assi, A. Geirsson, and P. Vallabhajosyula, *Growth rate of ascending thoracic aortic aneurysms in a non-referral-based population,* Journal of Cardiothoracic Surgery **17**, 14 (2022).

[34] R. A. Chaer, R. Vasoncelos, L. K. Marone, G. Al-Khoury, R. Y. Rhee, J. S. Cho, and M. S. Makaroun, *Synchronous and metachronous thoracic aneurysms in patients with abdominal aortic aneurysms,* Journal of Vascular Surgery **56**, 1261 (2012).

[35] J. A. Elefteriades, A. Sang, G. Kuzmik, and M. Hornick, *Guilt by association: paradigm for detecting a silent killer (thoracic aortic aneurysm),* Open Heart **2**, e000169 (2015).

[36] J. Powell, S. Gotensparre, M. Sweeting, L. Brown, F. Fowkes, and S. Thompson, *Rupture rates of small abdominal aortic aneurysms: A systematic review of the literature,* European Journal of Vascular and Endovascular Surgery **41**, 2 (2011).

[37] F. A. Lederle, G. R. Johnson, S. E. Wilson, D. J. Ballard, W. D. Jordan, Jr, J. Blebea, F. N. Littooy, J. A. Freischlag, D. Bandyk, J. H. Rapp, A. A. Salam, and for the Veterans Affairs Cooperative Study #417 Investigators, *Rupture Rate of Large Abdominal Aortic Aneurysms in Patients Refusing or Unfit for Elective Repair,* JAMA **287**, 2968 (2002).

[38] R. Erbel, F. Alfonso, C. Boileau, O. Dirsch, B. Eber, A. Haverich, H. Rakowski, J. Struyven, K. Radegran, U. Sechtem, J. Taylor, C. Zollikofer, W. Klein, B. Mulder, and L. Providencia, *Diagnosis and management of aortic dissection: Task Force on Aortic Dissection, European Society of Cardiology,* European Heart Journal **22**, 1642 (2001).

[39] T. Gudbjartsson, A. Ahlsson, A. Geirsson, J. Gunn, V. Hjortdal, A. Jeppsson, A. Mennander, I. Zindovic, and C. Olsson, *Acute type a aortic dissection – a review,* Scandinavian Cardiovascular Journal **54**, 1 (2020), pMID: 31542960.

[40] A. M. Kolonics-Farkas, B. Agg, K. Benke, B. Odler, A. Bohacs, Z. Kovats, Z. Szabolcs, and V. Müller, *Lung function changes are more common in marfan patients who need major thoracic surgery,* Lung **197**, 465 (2019).

[41] *Marfan syndrome: https://www.mayoclinic.org/diseases-conditions/marfan-syndrome/symptoms-causes/syc-20350782, Accessed: 2022-02-18,* .

[42] *Marfan syndrome: https://www.nhlbi.nih.gov/health-topics/marfan-syndrome, Accessed: 2022-02-18,* .

[43] J. Lantz, V. Gupta, L. Henriksson, M. Karlsson, A. Persson, C.-J. Carlhäll, and T. Ebbers, *Intracardiac flow at 4D CT: Comparison with 4D flow MRI,* Radiology **289**, 51 (2018), pMID: 29944089.

[44] U. J. Schoepf and A. Varga-Szemes, *4D flow meets CT: Can it compete with 4D flow MRI?* Radiology **289**, 59 (2018), pMID: 29944084.

[45] B. Stemkens, E. S. Paulson, and R. H. N. Tijssen, *Nuts and bolts of 4D-MRI for radiotherapy,* Physics in Medicine & Biology **63**, 21TR01 (2018).

[46] T. Puiseux, A. Sewonu, O. Meyrignac, H. Rousseau, F. Nicoud, S. Mendez, and R. Moreno, *Reconciling PC-MRI and CFD: An in-vitro study,* NMR in Biomedicine **32**, e4063 (2018), e4063 nbm.4063, https://onlinelibrary.wiley.com/doi/pdf/10.1002/nbm.4063 .

[47] B. Becsek, L. Pietrasanta, and D. Obrist, *Turbulent systolic flow downstream of a bioprosthetic aortic valve: Velocity spectra, wall shear stresses, and turbulent dissipation rates,* Frontiers in Physiology **11** (2020), 10.3389/fphys.2020.577188.

[48] F. Gao, M. Watanabe, and T. Matsuzawa, *Stress analysis in a layered aortic arch model under pulsatile blood flow,* BioMedical Engineering OnLine **5**, 25 (2006).

[49] D. Mori and T. Yamaguchi, *Computational fluid dynamics modeling and analysis of the effect of 3-D distortion of the human aortic arch,* Computer Methods in Biomechanics and Biomedical Engineering **5**, 249 (2010), pMID: 12186717.

[50] S. S. Gopalakrishnan, B. Pier, and A. Biesheuvel, *Dynamics of pulsatile flow through model abdominal aortic aneurysms,* Journal of Fluid Mechanics **758**, 150–179 (2014).

[51] E. A. Finol and C. H. Amon, *Flow-induced wall shear stress in abdominal aortic aneurysms: Part ii - pulsatile flow hemodynamics,* Computer Methods in Biomechanics and Biomedical Engineering **5**, 319 (2002), pMID: 12186711, https://doi.org/10.1080/1025584021000009751 .

[52] Y. G. Stergiou, A. G. Kanaris, A. A. Mouza, and S. V. Paras, *Fluid-structure interaction in abdominal aortic aneurysms: Effect of haematocrit,* Fluids **4** (2019), 10.3390/fluids4010011.

[53] E. Soudah, E. Y. K. Ng, T. H. Loong, M. Bordone, U. Pua, and S. Narayanan, *CFD modelling of abdominal aortic aneurysm on hemodynamic loads using a realistic geometry with ct,* Comput Math Methods Med **2013**, 472564 (2013), 23864906[pmid].

[54] F. Joly, G. Soulez, D. Garcia, S. Lessard, and C. Kauffmann, *Flow stagnation volume and abdominal aortic aneurysm growth: Insights from patient-specific computational flow dynamics of lagrangian-coherent structures,* Computers in Biology and Medicine **92**, 98 (2018).

[55] F. Auricchio, M. Conti, A. Lefieux, S. Morganti, A. Reali, F. Sardanelli, F. Secchi, S. Trimarchi, and A. Veneziani, *Patient-specific analysis of post-operative aortic hemodynamics: a focus on thoracic endovascular repair (TEVAR),* Computational Mechanics **54**, 943 (2014).

[56] M. Simão, J. Ferreira, A. C. Tomás, J. Fragata, and H. Ramos, *Aorta ascending aneurysm analysis using CFD models towards possible anomalies,* Fluids **2** (2017), 10.3390/fluids2020031.

[57] K. Capellini, E. Gasparotti, U. Cella, E. Costa, B. M. Fanni, C. Groth, S. Porziani, M. E. Biancolini, and S. Celi, *A novel formulation for the study of the ascending aortic fluid dynamics with in vivo data,* Medical Engineering & Physics **91**, 68 (2021).

[58] P. Blanco, M. Pivello, S. Urquiza, and R. Feijóo, *On the potentialities of 3D–1D coupled models in hemodynamics simulations,* Journal of Biomechanics **42**, 919 (2009).

[59] M. Y. Chong, B. Gu, C. H. Armour, S. Dokos, Z. C. Ong, X. Y. Xu, and E. Lim, *An integrated fluid–structure interaction and thrombosis model for type b aortic dissection,* Biomechanics and Modeling in Mechanobiology **21**, 261 (2022).

[60] Z. Cheng, C. Juli, N. Wood, R. Gibbs, and X. Xu, *Predicting flow in aortic dissection: Comparison of computational model with PC-MRI velocity measurements,* Medical Engineering & Physics **36**, 1176 (2014).

[61] R. L. F. van der Palen, A. A. W. Roest, P. J. van den Boogaard, A. de Roos, N. A. Blom, and J. J. M. Westenberg, *Scan–rescan reproducibility of segmental aortic wall shear stress as assessed by phase-specific segmentation with 4D flow MRI in healthy volunteers,* Magnetic Resonance Materials in Physics, Biology and Medicine **31**, 653 (2018).

[62] J. Abraham, E. Sparrow, and R. Lovik, *Unsteady, three-dimensional fluid mechanic analysis of blood flow in plaque-narrowed and plaque-freed arteries,* International Journal of Heat and Mass Transfer **51**, 5633 (2008), biomedical-Related Special Issue.

[63] B. Berthier, R. Bouzerar, and C. Legallais, *Blood flow patterns in an anatomically realistic coronary vessel: influence of three different reconstruction methods,* Journal of Biomechanics **35**, 1347 (2002).

[64] P. Berg, S. Voß, S. Saalfeld, G. Janiga, A. W. Bergersen, K. Valen-Sendstad, J. Bruening, L. Goubergrits, A. Spuler, N. M. Cancelliere, D. A. Steinman, V. M. Pereira, T. L. Chiu, A. C. O. Tsang, B. J. Chung, J. R. Cebral, S. Cito, J. Pallarès, G. Copelli, B. Csippa, G. Paál, S. Fujimura, H. Takao, S. Hodis, G. Hille, C. Karmonik, S. Elias, K. Kellermann, M. O. Khan, A. L. Marsden, H. G. Morales, S. Piskin, E. A. Finol, M. Pravdivtseva, H. Rajabzadeh-Oghaz, N. Paliwal, H. Meng, S. Seshadhri, M. Howard, M. Shojima, S.-i. Sugiyama, K. Niizuma, S. Sindeev, S. Frolov, T. Wagner, A. Brawanski, Y. Qian, Y.-A. Wu, K. D. Carlson, D. Dragomir-Daescu, and O. Beuing, *Multiple aneurysms anatomy challenge 2018 (match): Phase i: Segmentation,* Cardiovascular Engineering and Technology **9**, 565 (2018).

[65] G. Taubin, *Curve and surface smoothing without shrinkage,* in *Proceedings of IEEE International Conference on Computer Vision* (1995) pp. 852–857.

[66] S. Celi, E. Vignali, K. Capellini, and E. Gasparotti, *On the role and effects of uncertainties in cardiovascular in silico analyses,* Frontiers in Medical Technology **3** (2021), 10.3389/fmedt.2021.748908.

[67] N. Dyn, D. Levine, and J. A. Gregory, *A butterfly subdivision scheme for surface interpolation with tension control,* ACM Trans. Graph. **9**, 160–169 (1990).

[68] T. Bergman, T. Bergman, F. Incropera, D. DeWitt, and A. Lavine, *Fundamentals of Heat and Mass Transfer* (Wiley, 2011).

[69] L. Grinberg, T. Anor, J. Madsen, A. Yakhot, and G. Karniadakis, *Large-scale simulation of the human arterial tree,* Clinical and Experimental Pharmacology and Physiology **36**, 194 (2009).

[70] P. van Ooij, W. V. Potters, A. Guédon, J. J. Schneiders, H. A. Marquering, C. B. Majoie, E. vanBavel, and A. J. Nederveen, *Wall shear stress estimated with phase contrast MRI in an in vitro and in vivo intracranial aneurysm,* Journal of Magnetic Resonance Imaging **38**, 876 (2013).

[71] A. Arzani, A. S. Les, R. L. Dalman, and S. C. Shadden, *Effect of exercise on patient specific abdominal aortic aneurysm flow topology and mixing,* International Journal for Numerical Methods in Biomedical Engineering **30**, 280 (2014), https://onlinelibrary.wiley.com/doi/pdf/10.1002/cnm.2601 .

[72] M. Alimohammadi, O. Agu, S. Balabani, and V. Díaz-Zuccarini, *Development of a patient-specific simulation tool to analyse aortic dissections: Assessment of mixed patient-specific flow and pressure boundary conditions,* Medical Engineering and Physics **36**, 275 (2014), cited By 22.

[73] M. Alimohammadi, J. M. Sherwood, M. Karimpour, O. Agu, S. Balabani, and V. Díaz-Zuccarini, *Aortic dissection simulation models for clinical support: fluid-structure interaction vs. rigid wall models,* BioMedical Engineering OnLine **14**, 34 (2015), 25881252[pmid].

[74] J. Alastruey, N. Xiao, H. Fok, T. Schaeffter, and C. A. Figueroa, *On the impact of modelling assumptions in multi-scale, subject-specific models of aortic haemodynamics,* Journal of The Royal Society Interface **13**, 20160073 (2016).

[75] V. Pereira, O. Brina, A. Marcos Gonzales, A. Narata, P. Bijlenga, K. Schaller, K. Lovblad, and R. Ouared, *Evaluation of the influence of inlet boundary conditions on computational fluid dynamics for intracranial aneurysms: A virtual experiment,* Journal of Biomechanics **46**, 1531 (2013).

[76] D. Chen, M. Müller-Eschner, D. Kotelis, D. Böckler, Y. Ventikos, and H. von Tengg-Kobligk, *A longitudinal study of type-b aortic dissection and endovascular repair scenarios: Computational analyses,* Medical Engineering & Physics **35**, 1321 (2013).

[77] K. M. Tse, P. Chiu, H. P. Lee, and P. Ho, *Investigation of hemodynamics in the development of dissecting aneurysm within patient-specific dissecting aneurismal aortas using computational fluid dynamics (CFD) simulations,* Journal of Biomechanics **44**, 827 (2011).

[78] S. Kenjeres and A. de Loor, *Modeling and simulation of low-density-lipoprotein (ldl) transport through multi-layered wall of an anatomically realistic carotid artery bifurcation,* Journal of the Royal Society Interface **11**, 1 (2014).

[79] P. Berg, D. A. Steinman, G. Janiga, and et al., *The computational fluid dynamics rupture challenge 2013–phase ii: Variability of hemodynamic simulations in two intracranial aneurysms,* Journal of Biomechanical Engineering **137**, 121008 (2015).

[80] U. Morbiducci, R. Ponzini, D. Gallo, C. Bignardi, and G. Rizzo, *Inflow boundary conditions for image-based computational hemodynamics: Impact of idealized versus measured velocity profiles in the human aorta,* Journal of Biomechanics **46**, 102 (2013).

[81] F. Condemi, S. Campisi, M. Viallon, T. Troalen, G. Xuexin, A. J. Barker, M. Markl, P. Croisille, O. Trabelsi, C. Cavinato, A. Duprey, and S. Avril, *Fluid- and biomechanical analysis of ascending thoracic aorta aneurysm with concomitant aortic insufficiency,* Annals of Biomedical Engineering **45**, 2921 (2017).

[82] P. Youssefi, A. Gomez, C. Arthurs, R. Sharma, M. Jahangiri, and C. Alberto Figueroa, *Impact of Patient-Specific Inflow Velocity Profile on Hemodynamics of the Thoracic Aorta,* Journal of Biomechanical Engineering **140** (2017), 10.1115/1.4037857, 011002.

[83] S. Chandra, S. S. Raut, A. Jana, R. W. Biederman, M. Doyle, S. C. Muluk, and E. A. Finol, *Fluid-Structure Interaction Modeling of Abdominal Aortic Aneurysms: The Impact of Patient-Specific Inflow Conditions and Fluid/Solid Coupling,* Journal of Biomechanical Engineering **135** (2013), 10.1115/1.4024275, 081001.

[84] C. H. Armour, B. Guo, S. Pirola, S. Saitta, Y. Liu, Z. Dong, and X. Y. Xu, *The influence of inlet velocity profile on predicted flow in type b aortic dissection,* Biomechanics and Modeling in Mechanobiology **20**, 481 (2021).

[85] C. Schubert, J. Brüning, L. Goubergrits, A. Hennemuth, F. Berger, T. Kühne, and M. Kelm, *Assessment of hemodynamic responses to exercise in aortic coarctation using MRI-ergometry in combination with computational fluid dynamics,* Scientific Reports **10**, 18894 (2020).

[86] A. Benim, A. Nahavandi, A. Assmann, D. Schubert, P. Feindt, and S. Suh, *Simulation of blood flow in human aorta with emphasis on outlet boundary conditions,* Applied Mathematical Modelling **35**, 3175 (2011).

[87] A. Arzani, G.-Y. Suh, R. L. Dalman, and S. C. Shadden, *A longitudinal comparison of hemodynamics and intraluminal thrombus deposition in abdominal aortic aneurysms,* American Journal of Physiology-Heart and Circulatory Physiology **307**, H1786 (2014), pMID: 25326533, https://doi.org/10.1152/ajpheart.00461.2014 .

[88] A. Arzani, A. M. Gambaruto, G. Chen, and S. C. Shadden, *Lagrangian wall shear stress structures and near-wall transport inhigh-Schmidt-number aneurysmal flows,* Journal of Fluid Mechanics **790**, 158–172 (2016).

[89] J. Biasetti, F. Hussain, and T. C. Gasser, *Blood flow and coherent vortices in the normal and aneurysmatic aortas: a fluid dynamical approach to intra-luminal thrombus formation,* Journal of The Royal Society Interface **8**, 1449 (2011), https://royalsocietypublishing.org/doi/pdf/10.1098/rsif.2011.0041 .

[90] J. H. Leung, A. R. Wright, N. Cheshire, J. Crane, S. A. Thom, A. D. Hughes, and Y. Xu, *Fluid structure interaction of patient specific abdominal aortic aneurysms: a comparison with solid stress models,* BioMedical Engineering OnLine **5**, 33 (2006).

[91] A. N. Impiombato, G. La Civita, F. Orlandi, F. S. Franceschini Zinani, L. A. Oliveira Rocha, and C. Biserni, *A simple transient poiseuille-based approach to mimic the Womersley function and to model pulsatile blood flow,* Dynamics **1**, 9 (2021).

[92] J. Sigüenza, D. Pott, S. Mendez, S. J. Sonntag, T. A. S. Kaufmann, U. Steinseifer, and F. Nicoud, *Fluid-structure interaction of a pulsatile flow with an aortic valve model: A combined experimental and numerical study,* Int J Numer Method Biomed Eng **34**, e2945 (2018).

[93] A. A. Basri, M. Zuber, E. I. Basri, M. S. Zakaria, A. F. A. Aziz, M. Tamagawa, and K. A. Ahmad, *Fluid structure interaction on paravalvular leakage of transcatheter aortic valve implantation related to aortic stenosis: A Patient-Specific case,* Comput Math Methods Med **2020**, 9163085 (2020).

[94] S. Pirola, Z. Cheng, O. Jarral, D. O'Regan, J. Pepper, T. Athanasiou, and X. Xu, *On the choice of outlet boundary conditions for patient-specific analysis of aortic flow using computational fluid dynamics,* Journal of Biomechanics **60**, 15 (2017).

[95] D. Gallo, G. De Santis, F. Negri, D. Tresoldi, R. Ponzini, D. Massai, M. A. Deriu, P. Segers, B. Verhegghe, G. Rizzo, and U. Morbiducci, *On the use of in vivo measured flow rates as boundary conditions for image-based hemodynamic models of the human aorta: Implications for indicators of abnormal flow,* Annals of Biomedical Engineering **40**, 729 (2012).

[96] M. S. Olufsen, C. S. Peskin, W. Y. Kim, E. M. Pedersen, A. Nadim, and J. Larsen, *Numerical simulation and experimental validation of blood flow in arteries with structured-tree outflow conditions,* Annals of Biomedical Engineering **28**, 1281 (2000).

[97] S. Madhavan and E. M. C. Kemmerling, *The effect of inlet and outlet boundary conditions in image-based CFD modeling of aortic flow,* BioMedical Engineering OnLine **17**, 66 (2018).

[98] C. Chnafa, O. Brina, V. Pereira, and D. Steinman, *Better than nothing: a rational approach for minimizing the impact of outflow strategy on cerebrovascular simulations,* American Journal of Neuroradiology **39**, 337 (2018).

[99] M. McElroy and A. Keshmiri, *Impact of using conventional inlet/outlet boundary conditions on haemodynamic metrics in a subject-specific rabbit aorta,* Proceedings of the Institution of Mechanical Engineers, Part H: Journal of Engineering in Medicine **232**, 103 (2018).

[100] L. Johnston, R. Allen, P. Hall Barrientos, A. Mason, and A. Kazakidi, *Hemodynamic abnormalities in the aorta of turner syndrome girls,* Frontiers in Cardiovascular Medicine **8** (2021), 10.3389/fcvm.2021.670841.

[101] N. Shahcheraghi, H. Dwyer, A. Cheer, A. Barakat, and T. Rutaganira, *Unsteady and three-dimensional simulation of blood flow in the human aortic arch,* Journal of biomechanical engineering **124**, 378—387 (2002).

[102] K. Sagawa, R. K. Lie, and J. Schaefer, *Translation of Otto Frank's paper;Die Grundform des arteriellen Pulses; Zeitschrift für Biologie 37;526 (1899),* Journal of Molecular and Cellular Cardiology **22**, 253 (1990).

[103] H. J. Kim, I. E. Vignon-Clementel, C. A. Figueroa, J. F. LaDisa, K. E. Jansen, J. A. Feinstein, and C. A. Taylor, *On coupling a lumped parameter heart model and a three-dimensional finite element aorta model,* Annals of Biomedical Engineering **37**, 2153 (2009).

[104] A. G. Brown, Y. Shi, A. Marzo, C. Staicu, I. Valverde, P. Beerbaum, P. V. Lawford, and D. R. Hose, *Accuracy vs. computational time: Translating aortic simulations to the clinic,* Journal of Biomechanics **45**, 516 (2012).

[105] M. Bonfanti, S. Balabani, J. P. Greenwood, S. Puppala, S. Homer-Vanniasinkam, and V. Díaz-Zuccarini, *Computational tools for clinical support: a multi-scale compliant model for haemodynamic simulations in an aortic dissection based on multi-modal imaging data,* Journal of The Royal Society Interface **14**, 20170632 (2017).

[106] R. M. Romarowski, A. Lefieux, S. Morganti, A. Veneziani, and F. Auricchio, *Patient-specific CFD modelling in the thoracic aorta with PC-MRI–based boundary conditions: A least-square three-element windkessel approach,* International Journal for Numerical Methods in Biomedical Engineering **34**, e3134 (2018), e3134 cnm.3134.

[107] S. Saitta, S. Pirola, F. Piatti, E. Votta, F. Lucherini, F. Pluchinotta, M. Carminati, M. Lombardi, C. Geppert, F. Cuomo, C. A. Figueroa, X. Y. Xu, and A. Redaelli, *Evaluation of 4D flow MRI-based non-invasive pressure assessment in aortic coarctations,* Journal of Biomechanics **94**, 13 (2019).

[108] M. N. Antonuccio, A. Mariotti, B. M. Fanni, K. Capellini, C. Capelli, E. Sauvage, and S. Celi, *Effects of uncertainty of outlet boundary conditions in a patient-specific case of aortic coarctation,* Annals of Biomedical Engineering **49**, 3494 (2021).

[109] K. H. Parker and C. Jones, *Forward and backward running waves in the arteries: analysis using the method of characteristics,* (1990).

[110] S. J. Sherwin, L. Formaggia, J. Peiró, and V. Franke, *Computational modelling of 1D blood flow with variable mechanical properties and its application to the simulation of wave propagation in the human arterial system,* International Journal for Numerical Methods in Fluids **43**, 673.

[111] P. Reymond, P. Crosetto, S. Deparis, A. Quarteroni, and N. Stergiopulos, *Physiological simulation of blood flow in the aorta: Comparison of hemodynamic indices as predicted by 3-D FSI, 3-D rigid wall and 1-D models,* Medical Engineering & Physics **35**, 784 (2013).

[112] Z. Duanmu, W. Chen, H. Gao, X. Yang, X. Luo, and N. A. Hill, *A one-dimensional hemodynamic model of the coronary arterial tree,* Frontiers in Physiology **10** (2019), 10.3389/fphys.2019.00853.

[113] E. Soudah, R. Rossi, S. Idelsohn, and E. Oñate, *A reduced-order model based on the coupled 1D-3D finite element simulations for an efficient analysis of hemodynamics problems,* Computational Mechanics **54**, 1013 (2014).

[114] P. J. Blanco, C. A. Bulant, L. O. Müller, G. D. M. Talou, C. G. Bezerra, P. A. Lemos, and R. A. Feijóo, *Comparison of 1D and 3D models for the estimation of fractional flow reserve,* Scientific Reports **8**, 17275 (2018).

[115] F. Caforio, C. Augustin, J. Alastruey, M. Gsell, and G. Plank, *A coupling strategy for a 3D-1D model of the cardiovascular system to study the effects of pulse wave propagation on cardiac function,* Computational Mechanics **70**, 703 (2022).

[116] *Blood: https://www.kenhub.com/en/library/anatomy/the-blood, Accessed: 2022-04-20,* .

[117] R. Fournier, *Basic Transport Phenomena In Biomedical Engineering*, Chemical Engineering Series (Taylor & Francis, 1998).

[118] R. L. Replogle, H. J. Meielman, and E. W. Merril, *Special article,* Circulation **36**, 148 (1967).

[119] S. Chien, *Shear dependence of effective cell volume as a determinant of blood viscosity,* Science **168**, 977 (1970).

[120] S. Chien, *Chapter 26 - Biophysical behavior of red cells in suspensions,* in *The Red Blood Cell (Second Edition)*, edited by D. M. Surgenor (Academic Press, 1975) second edition ed., pp. 1031 – 1133.

[121] P. Carreau, *Rheological equations from molecular network theories,* Journal of Rheology **16**, 99 (1972).

[122] J. W. Gooch, ed., *Encyclopedic Dictionary of Polymers* (Springer New York, New York, NY, 2007) pp. 781–781.

[123] M. M. Cross, *Relation between viscoelasticity and shear-thinning behaviour in liquids,* Rheologica Acta **18**, 609 (1979).

[124] D. Quemada, *Rheology of concentrated disperse systems and minimum energy dissipation principle,* Rheologica Acta **16**, 82 (1977).

[125] K. Yeleswarapu, M. Kameneva, K. Rajagopal, and J. Antaki, *The flow of blood in tubes: theory and experiment,* Mechanics Research Communications **25**, 257 (1998).

[126] R. E. Powell and H. Eyring, *Mechanisms for the relaxation theory of viscosity,* Nature **154**, 427 (1944).

[127] T. Ree and H. Eyring, *Theory of non-newtonian flow. i. solid plastic system,* Journal of Applied Physics **26**, 793 (1955), https://doi.org/10.1063/1.1722098 .

[128] W. H. Herschel and R. Bulkley, *Konsistenzmessungen von gummi-benzollösungen,* Kolloid-Zeitschrift **39**, 291 (1926).

[129] N. Casson, *Rheology of Disperse Systems: Proceedings of a Conference Organized by the British Society of Rheology and Held at the University College of Swansea in September 1957* (Symposium Publications Division, Pergamon Press, 1959).

[130] E. Bingham, *Fluidity and Plasticity - Scholar's Choice Edition* (Creative Media Partners, LLC, 2015).

[131] J. G. Oldroyd and A. H. Wilson, *On the formulation of rheological equations of state,* Proceedings of the Royal Society of London. Series A. Mathematical and Physical Sciences **200**, 523 (1950).

[132] F. Gijsen, F. van de Vosse, and J. Janssen, *The influence of the non-newtonian properties of blood on the flow in large arteries: steady flow in a carotid bifurcation model,* Journal of Biomechanics **32**, 601 (1999).

[133] A. Arzani, *Accounting for residence-time in blood rheology models: do we really need non-newtonian blood flow modelling in large arteries?* Journal of The Royal Society Interface **15**, 20180486 (2018).

[134] H. Liu, L. Lan, J. Abrigo, H. L. Ip, Y. Soo, D. Zheng, K. S. Wong, D. Wang, L. Shi, T. W. Leung, and X. Leng, *Comparison of newtonian and non-newtonian fluid models in blood flow simulation in patients with intracranial arterial stenosis,* Frontiers in Physiology **12** (2021), 10.3389/fphys.2021.718540.

[135] X. Wang and X. Li, *Computational simulation of aortic aneurysm using FSI method: Influence of blood viscosity on aneurismal dynamic behaviors,* Computers in Biology and Medicine **41**, 812 (2011).

[136] L. Prahl Wittberg, S. van Wyk, L. Fuchs, E. Gutmark, P. Backeljauw, and I. Gutmark-Little, *Effects of aortic irregularities on blood flow,* Biomechanics and Modeling in Mechanobiology **15**, 345 (2016).

[137] P. J. LaNasa and E. L. Upp, *1 - introduction,* in *Fluid Flow Measurement (Third Edition)*, edited by P. J. LaNasa and E. L. Upp (Butterworth-Heinemann, Oxford, 2014) third edition ed., pp. 1–17.

[138] Y. C. Fung, *Biomechanics: circulation*, 2nd ed. (Springer, 1997).

[139] K. A. Barbee, *Role of subcellular shear–stress distributions in endothelial cell mechanotransduction,* Annals of Biomedical Engineering **30**, 472 (2002).

[140] J. Peacock, T. Jones, C. Tock, and R. Lutz, *The onset of turbulence in physiological pulsatile flow in a straight tube,* Experiments in Fluids **24**, 1 (1998).

[141] G. S. Fung, S. Lam, S. W. Cheng, and K. Chow, *On stent-graft models in thoracic aortic endovascular repair: A computational investigation of the hemodynamic factors,* Computers in Biology and Medicine **38**, 484 (2008).

[142] O. San and A. E. Staples, *An improved model for reduced-order physiological fluid flows,* Journal of Mechanics in Medicine and Biology **12**, 1250052 (2012).

[143] N. D. Katopodes, *Chapter 5 - viscous fluid flow,* in *Free-Surface Flow*, edited by N. D. Katopodes (Butterworth-Heinemann, 2019) pp. 324–426.

[144] M. D. Ford, U. Piomelli, R. Y. Cao, C. D. Funk, and A. Pollard, *Numerical Simulations of the Intra-Aneurysmal Vortex Shedding in Induced Mouse Abdominal Aortic Aneurysms,* in *ASME 2010 3rd Joint US-European Fluids Engineering Summer Meeting: Volume 1, Symposia – Parts A, B, and C*, Fluids Engineering Division Summer Meeting (ASME, 2010) pp. 2181–2190.

[145] N. de Hoon, K. Lawonn, A. Jalba, E. Eisemann, and A. Vilanova, *Inkvis: A high-particle-count approach for visualization of phase-contrast magnetic resonance imaging data,* in *Eurographics Workshop on Visual Computing for Biology and Medicine* (The Eurographics Association, 2019).

[146] P. K. Pandey, R. Agrawal, P. Mukul, and M. K. Das, *Study on pulsatile blood flow in cerebral stenosed artery,* in *Fluid Mechanics and Fluid Power*, edited by T. Prabu, P. Viswanathan, A. Agrawal, and J. Banerjee (Springer Singapore, Singapore, 2021) pp. 581–588.

[147] J. Brum, M. Bernal, N. Barrere, C. Negreira, and C. Cabeza, *Vortex dynamics and transport phenomena in stenotic aortic models using Echo-PIV,* Physics in Medicine & Biology **66**, 055026 (2021).

[148] A. Bit, D. Ghagare, A. A. Rizvanov, and H. Chattopadhyay, *Assessment of influences of stenoses in right carotid artery on left carotid artery using wall stress marker,* BioMed Research International **2017**, 2935195 (2017).

[149] N. Kumar, S. M. A. Khader, R. Pai, S. Khan, and P. Kyriacou, *Fluid structure interaction study of stenosed carotid artery considering the effects of blood pressure,* International Journal of Engineering Science **154**, 103341 (2020).

[150] A. F. Stalder, A. Frydrychowicz, M. F. Russe, J. G. Korvink, J. Hennig, K. Li, and M. Markl, *Assessment of flow instabilities in the healthy aorta using flow-sensitive MRI,* Journal of Magnetic Resonance Imaging **33**, 839 (2011).

[151] P. M. Ligrani, *A Study of Dean Vortex Development and Structure in a Curved Rectangular Channel with Aspect Ratio of 40 at Dean Numbers up to 430* (NASA, 1994).

[152] G. I. Taylor, *The criterion for turbulence in curved pipes,* Proceedings of the Royal Society of London. Series A, Containing Papers of a Mathematical and Physical Character **124**, 243 (1929).

[153] A. Kalpakli, R. Örlü, N. Tillmark, and P. H. Alfredsson, *Pulsatile turbulent flow through pipe bends at high Dean and Womersley numbers,* Journal of Physics: Conference Series **318**, 092023 (2011).

[154] J. H. Siggers and S. L. Waters, *Unsteady flows in pipes with finite curvature,* Journal of Fluid Mechanics **600**, 133–165 (2008).

[155] D. Chen, M. Müller-Eschner, H. von Tengg-Kobligk, D. Barber, D. Böckler, R. Hose, and Y. Ventikos, *A patient-specific study of type-b aortic dissection: evaluation of true-false lumen blood exchange,* BioMedical Engineering OnLine **12**, 65 (2013).

[156] A. Qiao, W. Yin, and B. Chu, *Numerical simulation of fluid–structure interaction in bypassed debakey iii aortic dissection,* Computer Methods in Biomechanics and Biomedical Engineering **18**, 1173 (2015), pMID: 24533642, https://doi.org/10.1080/10255842.2014.881806 .

[157] Y. Qiao, Y. Zeng, Y. Ding, J. Fan, K. Luo, and T. Zhu, *Numerical simulation of two-phase non-Newtonian blood flow with fluid-structure interaction in aortic dissection,* Computer Methods in Biomechanics and Biomedical Engineering **22**, 620 (2019), pMID: 30822150.

[158] S. Singh, X. Xu, N. Wood, J. Pepper, C. Izgi, T. Treasure, and R. Mohiaddin, *Aortic flow patterns before and after personalised external aortic root support implantation in marfan patients,* Journal of Biomechanics **49**, 100 (2016).

[159] P. Dyverfeldt, M. D. Hope, E. E. Tseng, and D. Saloner, *Magnetic resonance measurement of turbulent kinetic energy for the estimation of irreversible pressure loss in aortic stenosis,* JACC: Cardiovascular Imaging **6**, 64 (2013).

[160] P. Dyverfeldt, M. Bissell, A. J. Barker, A. F. Bolger, C.-J. Carlhäll, T. Ebbers, C. J. Francios, A. Frydrychowicz, J. Geiger, D. Giese, M. D. Hope, P. J. Kilner, S. Kozerke, S. Myerson, S. Neubauer, O. Wieben, and M. Markl, *4D flow cardiovascular magnetic resonance consensus statement,* Journal of cardiovascular magnetic resonance : official journal of the Society for Cardiovascular Magnetic Resonance **17**, 72 (2015), 26257141[pmid].

[161] A. Arzani, P. Dyverfeldt, T. Ebbers, and S. C. Shadden, *In vivo validation of numerical prediction for turbulence intensity in an aortic coarctation,* Annals of Biomedical Engineering **40**, 860 (2011).

[162] J. Lantz, T. Ebbers, J. E. Engvall, and M. Karlsson, *Validation of turbulent kinetic energy in an aortic coarctation before and after intervention - MRI vs. CFD,* Journal of Cardiovascular Magnetic Resonance **15**, E46 (2013).

[163] F. Tan, A. Borghi, R. Mohiaddin, N. Wood, S. Thom, and X. Xu, *Analysis of flow patterns in a patient-specific thoracic aortic aneurysm model,* Computers & Structures **87**, 680 (2009), fifth MIT Conference on Computational Fluid and Solid Mechanics.

[164] K. Khanafer and R. Berguer, *Fluid–structure interaction analysis of turbulent pulsatile flow within a layered aortic wall as related to aortic dissection,* Journal of Biomechanics **42**, 2642 (2009).

[165] S.-W. Lee, L. Antiga, J. D. Spence, and D. A. Steinman, *Geometry of the carotid bifurcation predicts its exposure to disturbed flow,* Stroke **39**, 2341 (2008).

[166] C. Vergara, D. L. Van, M. Quadrio, L. Formaggia, and M. Domanin, *Large eddy simulations of blood dynamics in abdominal aortic aneurysms,* Medical Engineering & Physics **47**, 38 (2017).

[167] E. L. Manchester and X. Y. Xu, *The effect of turbulence on transitional flow in the fda's benchmark nozzle model using large-eddy simulation,* International Journal for Numerical Methods in Biomedical Engineering **36**, e3389 (2020).

[168] H. Ha, M. Ziegler, M. Welander, N. Bjarnegård, C.-J. Carlhäll, M. Lindenberger, T. Länne, T. Ebbers, and P. Dyverfeldt, *Age-related vascular changes affect turbulence in aortic blood flow,* Frontiers in Physiology **9** (2018), 10.3389/fphys.2018.00036.

[169] J. Sundin, M. Bustamante, T. Ebbers, P. Dyverfeldt, and C.-J. Carlhäll, *Turbulent intensity of blood flow in the healthy aorta increases with dobutamine stress and is related to cardiac output,* Frontiers in Physiology **13** (2022), 10.3389/fphys.2022.869701.

[170] K. Jain, J. Jiang, C. Strother, and K.-A. Mardal, *Transitional hemodynamics in intracranial aneurysms — comparative velocity investigations with high resolution lattice boltzmann simulations, normal resolution ANSYS simulations, and MR imaging,* Medical Physics **43**, 6186 (2016).

[171] *Transitional flow in intracranial aneurysms – a space and time refinement study below the Kolmogorov scales using Lattice Boltzmann Method, journal = Computers & Fluids, volume = 127, pages = 36-46, year = 2016, issn = 0045-7930, doi = https://doi.org/10.1016/j.compfluid.2015.12.011, url = https://www.sciencedirect.com/science/article/pii/S0045793015004089, author = Kartik Jain and Sabine Roller and Kent-André Mardal, keywords = Intracranial aneurysm, Lattice Boltzmann Method, Convergence, Transitional flow, .*

[172] K. Valen-Sendstad, K.-A. Mardal, M. Mortensen, B. A. P. Reif, and H. P. Langtangen, *Direct numerical simulation of transitional flow in a patient-specific intracranial aneurysm,* Journal of Biomechanics **44**, 2826 (2011).

[173] L. Mao, J. Liu, H. Hong, Q. Sun, J. Huang, J. Liu, Z. Zhu, and Q. Wang, *Hemodynamic analysis of surgical correction for patient-specific aortic coarctation with aortic arch hypoplasia by end-to-side anastomosis,* in *2014 7th International Conference on Biomedical Engineering and Informatics* (2014) pp. 446–450.

[174] A. Nikolić, M. Topalović, V. Simić, and N. Filipović, *Turbulent finite element model applied for blood flow calculation in arterial bifurcation,* Computer Methods and Programs in Biomedicine **209**, 106328 (2021).

[175] Z. Cheng, F. P. P. Tan, C. V. Riga, C. D. Bicknell, M. S. Hamady, R. G. J. Gibbs, N. B. Wood, and X. Y. Xu, *Analysis of flow patterns in a patient-specific aortic dissection model,* Journal of Biomechanical Engineering **132**, 051007 (2010).

[176] J. Lantz, J. Engvall, T. Ebbers, and M. Karlsson, *Large eddy simulation of aortic coarctation before and after surgery,* Artery Research **6**, 180 (2012).

[177] E. L. Manchester, S. Pirola, M. Y. Salmasi, D. P. O'Regan, T. Athanasiou, and X. Y. Xu, *Analysis of turbulence effects in a patient-specific aorta with aortic valve stenosis,* Cardiovascular Engineering and Technology **12**, 438 (2021).

[178] M. D. Ford and U. Piomelli, *Exploring high frequency temporal fluctuations in the terminal aneurysm of the basilar bifurcation,* Journal of Biomechanical Engineering **134**, 091003 (2012).

[179] C. Poelma, P. N. Watton, and Y. Ventikos, *Transitional flow in aneurysms and the computation of haemodynamic parameters,* Journal of The Royal Society Interface **12**, 20141394 (2015).

[180] H. Baek, M. V. Jayaraman, P. D. Richardson, and G. E. Karniadakis, *Flow instability and wall shear stress variation in intracranial aneurysms,* Journal of The Royal Society Interface **7**, 967 (2010).

[181] P. Corso, G. Giannakopoulos, U. Gülan, C. E. Frouzakis, and M. Holzner, *A novel estimation approach of pressure gradient and haemodynamic stresses as indicators of pathological aortic flow using subvoxel modelling,* IEEE Transactions on Biomedical Engineering **68**, 980 (2021).

[182] L. Antiga and D. A. Steinman, *Rethinking turbulence in blood,* Biorheology **46**, 77 (2009), 2.

[183] L. M. de Heer, R. P. J. Budde, W. P. T. M. Mali, A. M. de Vos, L. A. van Herwerden, and J. Kluin, *Aortic root dimension changes during systole and diastole: evaluation with ecg-gated multidetector row computed tomography,* Int J Cardiovasc Imaging **27**, 1195 (2011).

[184] N. Grøndal, M. Bramsen, M. Thomsen, C. Rasmussen, and J. Lindholt, *The cardiac cycle is a major contributor to variability in size measurements of abdominal aortic aneurysms by ultrasound,* European Journal of Vascular and Endovascular Surgery **43**, 30 (2012).

[185] D. A. Vorp, *Biomechanics of abdominal aortic aneurysm,* Journal of Biomechanics **40**, 1887 (2007), 17254589[pmid].

[186] M. F. Fillinger, M. Raghavan, S. P. Marra, J. L. Cronenwett, and F. E. Kennedy, *In vivo analysis of mechanical wall stress and abdominal aortic aneurysm rupture risk,* Journal of Vascular Surgery **36**, 589 (2002).

[187] S. Polzer and T. C. Gasser, *Biomechanical rupture risk assessment of abdominal aortic aneurysms based on a novel probabilistic rupture risk index,* Journal of The Royal Society Interface **12**, 20150852 (2015), https://royalsocietypublishing.org/doi/pdf/10.1098/rsif.2015.0852 .

[188] J.-S. Ren and X.-G. Yuan, *Mechanics of formation and rupture of human aneurysm,* Applied Mathematics and Mechanics **31**, 593 (2010).

[189] J. P. Vande Geest, D. H. J. Wang, S. R. Wisniewski, M. S. Makaroun, and D. A. Vorp, *Towards a noninvasive method for determination of patient-specific wall strength distribution in abdominal aortic aneurysms,* Annals of Biomedical Engineering **34**, 1098 (2006).

[190] S. R. Vallabhaneni, G. L. Gilling-Smith, T. V. How, S. D. Carter, J. A. Brennan, and P. L. Harris, *Heterogeneity of tensile strength and matrix metalloproteinase activity in the wall of abdominal aortic aneurysms,* Journal of Endovascular Therapy **11**, 494 (2004), pMID: 15298501.

[191] E. S. D. Martino, A. Bohra, J. P. V. Geest, N. Gupta, M. S. Makaroun, and D. A. Vorp, *Biomechanical properties of ruptured versus electively repaired abdominal aortic aneurysm wall tissue,* Journal of Vascular Surgery **43**, 570 (2006).

[192] F. Xu and S. Kenjereš, *Numerical simulations of flow patterns in the human left ventricle model with a novel dynamic mesh morphing approach based on radial basis function,* Computers in Biology and Medicine **130**, 104184 (2021).

[193] J. Moore and C. R. Ethier, *Oxygen mass transfer calculations in large arteries,* Journal of Biomechanical Engineering **119**, 469 (1997).

[194] X. Liu, Z. Wang, P. Zhao, Z. Fan, A. Sun, F. Zhan, Y. Fan, and X. Deng, *Nitric oxide transport in normal human thoracic aorta: Effects of hemodynamics and nitric oxide scavengers,* PLOS ONE **9**, 1 (2014).

[195] S. Qian, T. Ma, N. Zhang, X. Liu, P. Zhao, X. Li, D. Chen, L. Hu, L. Chang, L. Xu, X. Deng, and Y. Fan, *Spatiotemporal transfer of nitric oxide in patient-specific atherosclerotic carotid artery bifurcations with MRI and computational fluid dynamics modeling,* Computers in Biology and Medicine **125**, 104015 (2020).

[196] C. Ji, Y. He, and F. Liang, *A modeling study of blood flow and oxygen transport in the Circle of Willis,* Lixue Xuebao/Chinese Journal of Theoretical and Applied Mechanics **3**, 1114 (2010).

[197] F. Yan, W.-T. Jiang, Z. Xu, Q.-Y. Wang, Y.-B. Fan, and M. Zhang, *Developing transmission line equations of oxygen transport for predicting oxygen distribution in the arterial system,* Scientific Reports **8**, 5369 (2018).

[198] P. Causin and F. Malgaroli, *A mathematical and computational model of blood flow regulation in microvessels: Application to the eye retina circulation,* Journal of Mechanics in Medicine and Biology **15**, 1540027 (2015).

[199] C. Ethier, *Computational modeling of mass transfer and links to atherosclerosis,* Annals of Biomedical Engineering **30**, 461 (2002).

[200] M. Kaazempur-Mofrad, S. Wada, J. Myers, and C. Ethier, *Mass transport and fluid flow in stenotic arteries: Axisymmetric and asymmetric models,* International Journal of Heat and Mass Transfer **48**, 4510 (2005).

[201] M. Caputo, C. Chiastra, C. Cianciolo, E. Cutrì, G. Dubini, J. Gunn, B. Keller, F. Migliavacca, and P. Zunino, *Simulation of oxygen transfer in stented arteries and correlation with in-stent restenosis,* International Journal for Numerical Methods in Biomedical Engineering **29**, 1373 (2013).

[202] M. Khakpour and K. Vafai, *Critical assessment of arterial transport models,* International Journal of Heat and Mass Transfer **51**, 807 (2008).

[203] G. Coppola and C. Caro, *Oxygen mass transfer in a model three-dimensional artery,* Journal of The Royal Society Interface **5**, 1067 (2008).

[204] T. Zheng, J. Wen, W. Jiang, X. Deng, and Y. Fan, *Numerical investigation of oxygen mass transfer in a helical-type artery bypass graft,* Computer Methods in Biomechanics and Biomedical Engineering **17**, 549 (2014), pMID: 22794110.

[205] E. Murphy, A. S Dunne, D. Martin, and F. J Boyle, *Oxygen mass transport in stented coronary arteries,* Annals of Biomedical Engineering **44** (2016), 10.1007/s10439-015-1501-6.

[206] P. Causin, G. Guidoboni, F. Malgaroli, R. Sacco, and A. Harris, *Blood flow mechanics and oxygen transport and delivery in the retinal microcirculation: multiscale mathematical modeling and numerical simulation,* Biomechanics and Modelling in Mechanobiology **15** (2015), 10.1007/s10237-015-0708-7.

[207] F. Iori, L. Grechy, R. W. Corbett, W. Gedroyc, N. Duncan, C. G. Caro, and P. E. Vincent, *The effect of in-plane arterial curvature on blood flow and oxygen transport in arterio-venous fistulae,* Physics of Fluids **27**, 031903 (2015).

[208] S. Tada, *Numerical study of oxygen transport in a carotid bifurcation,* Physics in Medicine and Biology **55**, 3993 (2010).

[209] J. Chen, E. Gutmark, G. Mylavarapu, P. F. Backeljauw, and I. Gutmark-Little, *Numerical investigation of mass transport through patient-specific deformed aortae,* Journal of Biomechanics **47**, 544 (2014).

[210] F. Yan, W.-T. Jiang, R.-Q. Dong, Q.-Y. Wang, Y.-B. Fan, and M. Zhang, *Blood flow and oxygen transport in descending branch of lateral femoral circumflex arteries after transfemoral amputation: A numerical study,* Journal of Medical and Biological Engineering **37**, 63 (2017).

[211] N. Sun, J. H. Leung, N. B. Wood, A. D. Hughes, S. A. Thom, N. J. Cheshire, and X. Y. Xu, *Computational analysis of oxygen transport in a patient-specific model of abdominal aortic aneurysm with intraluminal thrombus,* The British Journal of Radiology **82**, S18 (2009), pMID: 20348531.

[212] K. Wilson, J. Lindholt, P. Hoskins, L. Heickendorff, S. Vammen, and A. Bradbury, *The relationship between abdominal aortic aneurysm distensibility and serum markers of elastin and collagen metabolism,* European Journal of Vascular and Endovascular Surgery **21**, 175 (2001).

[213] C. S. Lim, S. Kiriakidis, A. Sandison, E. M. Paleolog, and A. H. Davies, *Hypoxia-inducible factor pathway and diseases of the vascular wall,* Journal of Vascular Surgery **58**, 219 (2013).

[214] C. W. M. Ong, K. Fox, A. Ettorre, P. T. Elkington, and J. S. Friedland, *Hypoxia increases neutrophil-driven matrix destruction after exposure to mycobacterium tuberculosis,* Scientific Reports **8**, 11475 (2018).

[215] D. Liu, N. Wood, N. Witt, A. Hughes, S. A Thom, and X. Xu, *Computational analysis of oxygen transport in the retinal arterial network,* Current Eye Research **34**, 945 (2009).

[216] X. Liu, Y. Fan, and X. Deng, *Effect of spiral flow on the transport of oxygen in the aorta: A numerical study,* Annals of Biomedical Engineering **38**, 917 (2010).

[217] A. de la Fuente-Alonso, M. Toral, A. Alfayate, M. J. Ruiz-Rodríguez, E. Bonzón-Kulichenko, G. Teixido-Tura, S. Martínez-Martínez, M. J. Méndez-Olivares, D. López-Maderuelo, I. González-Valdés, E. Garcia-Izquierdo, S. Mingo, C. E. Martín, L. Muiño-Mosquera, J. De Backer, J. F. Nistal, A. Forteza, A. Evangelista, J. Vázquez, M. R. Campanero, and J. M. Redondo, *Aortic disease in marfan syndrome is caused by overactivation of sgc-prkg signaling by no,* Nature Communications **12**, 2628 (2021).

[218] P. Vallance and A. Hingorani, *Endothelial nitric oxide in humans in health and disease,* Int J Exp Pathol **80**, 291 (1999).

[219] X. Chen, D. G. Buerk, K. A. Barbee, P. Kirby, and D. Jaron, *3D network model of no transport in tissue,* Medical & Biological Engineering & Computing **49**, 633 (2011).

[220] A. M. Andrews, D. Jaron, D. G. Buerk, P. L. Kirby, and K. A. Barbee, *Direct, real-time measurement of shear stress-induced nitric oxide produced from endothelial cells in vitro,* Nitric Oxide **23**, 335 (2010).

[221] Y.-S. J. Li, J. H. Haga, and S. Chien, *Molecular basis of the effects of shear stress on vascular endothelial cells,* Journal of Biomechanics **38**, 1949 (2005).

[222] M. Levesque, R. Nerem, and E. Sprague, *Vascular endottielial cell proliferation in culture and the influence of flow,* Biomaterials **11**, 702 (1990).

[223] S. Chien, *Effects of disturbed flow on endothelial cells,* Annals of Biomedical Engineering **36**, 554 (2008).

[224] J. Xiang, S. K. Natarajan, M. Tremmel, D. Ma, J. Mocco, L. N. Hopkins, A. H. Siddiqui, E. I. Levy, and H. Meng, *Hemodynamic morphologic discriminants for intracranial aneurysm rupture,* Stroke **42**, 144 (2011).

[225] J. Cebral, F. Mut, M. Raschi, E. Scrivano, R. Ceratto, P. Lylyk, and C. Putman, *Aneurysm rupture following treatment with flow-diverting stents: Computational hemodynamics analysis of treatment,* American Journal of Neuroradiology **32**, 27 (2011).

[226] H. Meng, V. Tutino, J. Xiang, and A. Siddiqui, *High WSS or low WSS? complex interactions of hemodynamics with intracranial aneurysm initiation, growth, and rupture: Toward a unifying hypothesis,* American Journal of Neuroradiology **35**, 1254 (2014).

[227] J. Xiang, V. Tutino, K. Snyder, and H. Meng, *CFD: Computational fluid dynamics or confounding factor dissemination? the role of hemodynamics in intracranial aneurysm rupture risk assessment,* American Journal of Neuroradiology **35**, 1849 (2014).

[228] G. Janiga, P. Berg, S. Sugiyama, K. Kono, and D. Steinman, *The computational fluid dynamics rupture challenge 2013—phase i: Prediction of rupture status in intracranial aneurysms,* American Journal of Neuroradiology **36**, 530 (2015).

2

Effect of Geometrical Uncertainties

An aortic aneurysm is associated with aberrant blood flow and wall shear stress (WSS). This can be studied by coupling magnetic resonance imaging (MRI) with computational fluid dynamics (CFD). For patient-specific simulations, extra attention should be given to the variation in the segmentation of the MRI data set and its effect on WSS. We performed CFD simulations of blood flow in the aorta for ten different volunteers and provided corresponding WSS distributions. The aorta of each volunteer was segmented four times. The same inlet and outlet boundary conditions were applied for all segmentation variations of each volunteer. Steady-state CFD simulations were performed with inlet flow based on phase-contrast MRI during peak systole. We show that the commonly used comparison of mean and maximal values of WSS, based on CFD in the different segments of the thoracic aorta, yields good to excellent correlation (0.78 to 0.95) for rescan and moderate to excellent correlation (0.64 to 1.00) for intra- and interobserver reproducibility. However, the effect of geometrical variations is higher for the voxel-to-voxel comparison of WSS. With this analysis method, the correlation for different segments of the whole aorta is poor to moderate (0.43 to 0.66) for rescan and poor to good (0.48 to 0.73) for intra- and interobserver reproducibility. Therefore, we advise being critical of the CFD results based on the MRI segmentations to avoid possible misinterpretation. While the global values of WSS are similar for different modalities, the variation of results is high when considering the local distributions.

This chapter had been published as: R. Perinajová, J. F. Juffermans, J. J. Westenberg, R. L. van der Palen, P. J. van den Boogaard, H. J. Lamb, and S. Kenjereš, Geometrically induced wall shear stress variability in CFD-MRI coupled simulations of blood flow in the thoracic aortas, Computers in Biology and Medicine 133 (2021).

2.1 Introduction

Aorta pathologies such as an aortic aneurysm, dissection, and coarctation affect its function [1]. These conditions are not completely understood. However, aberrant blood flow patterns and associated hemodynamical parameters like wall shear stress (WSS) have been linked to aortic dysfunction [2, 3].

To study WSS in the aorta, we need to have information about the blood flow and the location of the aortic wall. In theory, both of these can be acquired using 4D-flow magnetic resonance imaging (MRI) [4]. While the 4D-flow MRI acquisition can produce a velocity field that closely represents the actual aortic flow [5–7], using this technique to acquire the location of the aortic wall may be incorrect [8, 9]. The irregularities in the segmented wall location can be influenced by the movement of the aorta during the cardiac cycle as well as due to its compliance [9, 10]. Besides, the segmentation of the geometry is done (partly) manually in most commercial and research tools. Therefore, the observer's lumen interpretation results in segmentation variability [10]. Van der Palen et al. [9] showed that this variability, among others, may lead to differences in MRI-estimated WSS as high as 30%. Additionally, while several methods have been proposed to calculate WSS from the 4D-flow MRI velocity field [11–14], the MRI-based WSS is underestimated due to the resolution of the flow field [3, 15]. Hence, to be able to accurately predict WSS, a different method should be used.

To do this, many studies showed that coupling MRI with computational fluid dynamics (CFD) leads to patient-specific results that closely represent reality [16–18]. An important aspect, that is often not addressed in evaluating the accuracy of patient-specific simulations is the influence of variability in geometry reconstruction from imaging techniques on numerical results. The effects of geometry variation on the calculated blood flow and associated parameters are assessed in two CFD studies focused on coronary vessels [19, 20]. Both concluded that a small variation in geometry has a considerable effect on the predicted hemodynamics. However, these conclusions were based on just one case, and hence the wide applicability is questionable. Moreover, none of these studies focused on the aorta, where the biggest variation in geometry can be expected due to its extensive motion during the cardiac cycle.

The present study aims to bridge this gap in the literature and evaluate the effect of variations in the input geometry on WSS obtained from CFD. By this, we extend the previously performed 4D flow MRI-based segmentation variability [10] and WSS variability [9], and we aim to establish a baseline for variability in CFD simulations. We perform simulations on aortas from ten volunteers at the peak systole. Four different segmented geometries are available for each volunteer. We compare the simulated WSS using statistical analysis as shown in [9], where the effect of varying geometry on WSS is evaluated based on the comparison of average values in five investigated regions - *zero-dimensional* analysis. Moreover, we extend this approach and propose two different ways of higher-dimensional comparison. First, we compare WSS between the different geometries based on its circumferential average alongside the centerline - *one-dimensional* analysis. Second, we perform a voxel-to-voxel comparison of flattened surface maps - *two-dimensional* analysis. We show the influence of the method for analysis on the agreement, where the WSS correlation between the different geometries decreases with the increasing order of the method.

2.2 Methodology

The present study is based on the data presented in our previous studies [9, 10], where ten healthy volunteers were analyzed, but it is now extended with CFD simulations. The characteristics of the volunteers, like gender, age, weight, height, and heart rate, can be found in [9], and the morphometric characteristics of the acquired aortas can be found in [10]. All volunteers gave informed consent before the MRI acquisition, and METC approval was obtained for the study of these volunteers.

2.2.1 MRI data-set

The studied data set consists of ten different volunteers with four different geometries for each. 4D-flow MRI was performed on a 3.0 T Scanner (Ingenia, Philips Medical Systems, Best, The Netherlands with Software Stream 4.1.3.0). The spatial resolution was 2.5 x 2.5 x 2.5 mm^3, and the temporal resolution was 35.1-36.5 ms. Additional details about the aortic 4D acquisition can be found in [9]. All volunteers were scanned twice, with a 30-minute interval between the scans.

Afterward, acquired 4D-flow MRI data were segmented using CAAS MR 4D flow v1.1 (Pie Medical Imaging BV, Maastricht, The Netherlands). A semi-automated segmentation algorithm was used that optimizes the location of the surface while maintaining the smoothness of the 3D surface [9]. The segmentations were manually adapted from the level of the aortic valve to the thoracic descending aorta (at the same level as the aortic valve).

The four different geometries of each volunteer were obtained with different segmentations, as follows: (i) 4D-Flow MRI was performed, and the geometry was segmented by the first observer - RvdP (geometry A - scan), (ii) the MRI scan was reproduced within 30 minutes from the first scan with consequent segmentation by RvdP (geometry B - rescan), (iii) the segmentation by RvdP was reproduced on the data from the first scan (geometry C - intraobserver), (iv) the last geometry was segmented from the first MRI data set by the second observer - PB (geometry D - interobserver). The repeated analysis was performed blindly to the results of the previous analyses. RvdP has six years of experience, and PB has fifteen years of experience in cardiovascular MRI. All geometries are shown in Fig.2.1. In this study, only the thoracic aorta without the branches is evaluated. WSS_{MRI} was estimated from the MRI velocity field using CAAS MR 4D flow v1.1 (Pie Medical Imaging BV, Maastricht, The Netherlands). For each wall point of the segmented surfaces, WSS was calculated using a quadratic approximation of the axial velocity profile perpendicular to the aortic wall.

For analysis purposes, the resulting surfaces were split into five different investigated segments using cut-planes based on anatomical landmarks, using CAAS MR 4D flow v1.1: sinotubular junction (1), mid-ascending aorta (2), the origin of the innominate artery (3), beyond the left subclavian artery (4), the mid-descending thoracic aorta (5), and the descending aorta at the level of the aortic valve (6). This resulted in five segments (from the sinotubular junction to the descending aorta): proximal ascending aorta (pAAo), distal ascending aorta (dAAo), aortic arch (Arch), proximal descending aorta (pDAo), and distal descending aorta (dDAo). The segments with the corresponding cut planes are shown in Fig.2.2a.

Figure 2.1: Geometries obtained from MRI for all ten volunteers obtained from four different segmentations: A - scan, B - rescan, C - intraobserver, D - interobserver.

2.2.2 Computer simulation setup

Geometry preparation

The raw geometry obtained directly from MRI is not suitable for performing CFD simulations, and hence it has to be pre-processed. Several improvements to the surface have to be performed, such as smoothing, capping ends, and the addition of flow extensions at the outlets and inlets. The exact parameters for the surface manipulation using Vascular Modeling Toolkit (VMTK) [21] are as follows:

- smoothing - Taubin method, passband 0.4
- surface subdivision - butterfly method
- flow extensions - adaptive length of $3R_i$, where R_i is the mean profile radius of the corresponding inlet and/or outlet

The value for smoothing was chosen to obtain a smooth surface while maintaining its size. An example of the original MRI data set and processed geometry is shown in Fig.2.2.

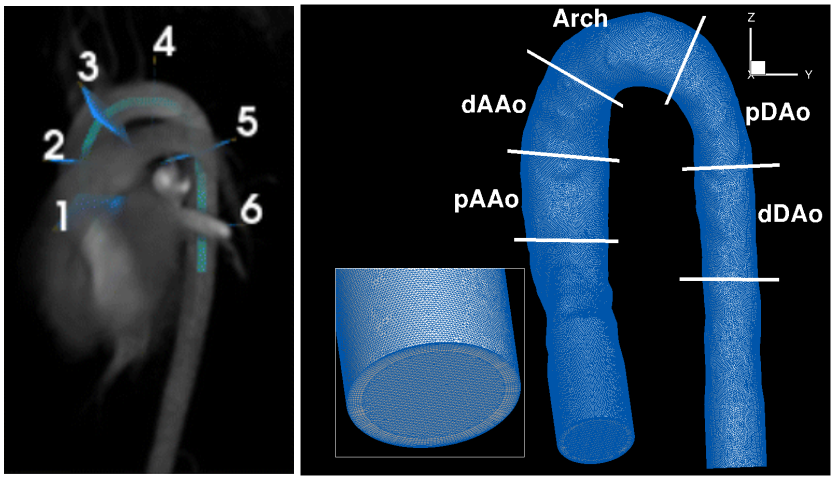

(a) (b)

Figure 2.2: (a) Images obtained from MRI for volunteer 1 with visualized cut planes 1-6 and (b) pre-processed geometry with the smoothed surface, flow extension, and tetrahedral mesh with detail of fine boundary layer and the visualization of the analyzed significantly important regions of the thoracic aorta: pAAo - proximal ascending aorta, dAAo - distal ascending aorta, Arch - aortic arch, pDAo - the proximal descending aorta and dDAo - distal descending aorta (b)

Discretization

An example of a computational mesh is shown in Fig.2.2b. The meshing is done using ICEM CFD (Ansys Inc., Canonsburg, PA, United States). For every geometry, a hybrid numerical mesh was constructed with a fine boundary layer. The boundary layers are covered by prismatic control volumes, whereas the tetrahedral elements are applied in the center region of the aorta. Note that this refined numerical mesh in the proximity of the

vessel wall is applied to be able to capture properly velocity gradients within relatively thin boundary layers. An order of magnitude estimate for usual flow in the aorta yields the boundary layer to be $\delta \sim 0.1$ mm. Therefore, the cells close to the wall should be at least of this size [22].

The boundary layer was constructed using ten layers, an exponential growth rate of 1.2, and a constant first-layer thickness of 0.01 mm. The computational mesh used for the simulations contained between three and five million control volumes. This resolution proved to be sufficient to obtain the grid-independent solutions (details can be found in appendix 2.5).

Besides, Fig.2.2 shows the cut planes which were used to divide the geometry for the analysis. Only segments between the cut planes were used for the analysis. This division is important since the original geometries (shown in Fig. 2.1) vary in the arterial length due to different segmentation.

Governing equations and Simulation setup

The steady blood flow is described by the conservation of mass and momentum (Navier-Stokes) equations for the incompressible fluid, which are written as:

$$\nabla \cdot \mathbf{u} = 0 \tag{2.1}$$

$$\rho \mathbf{u} \cdot \nabla \mathbf{u} = -\nabla p + \mu \nabla^2 \mathbf{u} \tag{2.2}$$

where $\mathbf{u}$ is the velocity vector, ρ is the density ($\rho = 1060$ kg/m^3), p is the pressure and μ is the dynamic viscosity ($\mu = 3.5$ mPa·s). The flow was assumed to be laminar, with the peak Reynolds number varying from 2024 to 3142.

The boundary condition for the inlet face was set to a mass flow inlet with a flat profile, and the value was based on the MRI measurements. The mass flow rate was exported from the reformatted 4D flow measurements and was kept the same for all four segmentations per volunteer. The outlet was set to the outflow boundary condition, with a zero diffusion flux for all flow variables. The rigid wall assumption with the no-slip velocity boundary condition was imposed at the aorta wall. All simulations were performed using Ansys Fluent 18.2 (Ansys Inc., Canonsburg, Pennsylvania, USA). The details of the numerical solver setup are listed below:

- Solver - pressure based
- Pressure-Velocity Coupling - SIMPLE
- Spatial discretization
  - Gradient - Least Squares Cell-Based
  - Pressure - Second-Order
  - Momentum - Second-Order Upwind
- Residuals - 10^{-5}

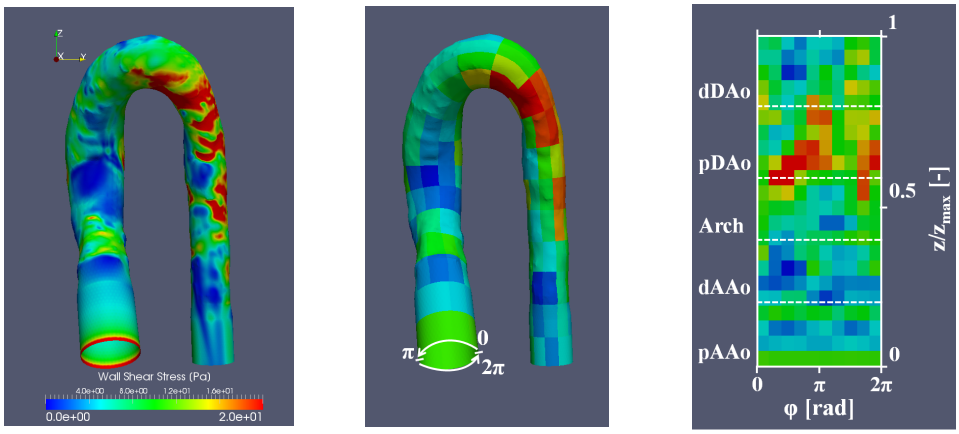

(a) (b) (c)

Figure 2.3: Visualization of the WSS mapping protocol for one of the geometries (V1, segmentation A) with the original surface showing WSS (a), the mapped and patched surface with averaged WSS in the patches and visualized unwrapping direction (b), and the projected surface representation with the visualization of the aortic regions where z/z_{max} represents the dimensionless length of the centerline (c).

2.2.3 Post-processing

To evaluate the variation between the calculated WSS in the different geometries obtained from MRI, a two-dimensional mapping approach is performed for all three-dimensional aortic walls. In this approach, the contours of WSS at the aorta wall are divided into several circumferential and longitudinal sections. In total, 100 circumferential segments were created for each surface, and the length of each segment in the longitudinal direction was 0.5 mm. The surface is then cut along the inner curvature of the aorta wall, making a simple two-dimensional projection map of the WSS distribution. The most important steps in this mapping approach are shown in Fig.2.3. Note that for illustration purposes, in this particular case, segments were significantly bigger (10 circumferential sectors with 1 cm in the longitudinal direction). In the last step, the 2D maps of the WSS from different segmentations were superimposed using an in-house image registration protocol.

2.2.4 Statistical Analysis

Statistical analysis was performed on the acquired data using an in-house code implemented in Matlab R2018b (MathWorks, Natick, MA, USA). The WSS_{mean} and WSS_{max} are presented together with the standard deviation. The acquired data were analyzed in three different ways.

First, the aorta wall surface was divided into five sections, and the mean and maximal value of WSS were calculated for each section, resulting in a single WSS parameter (consequently, we named this approach - *'Point Analysis'*). The Bland-Altman analysis was performed on these data, where the mean difference and the limits of agreement were calculated in the mean and max WSS, respectively, between the different surfaces. The limits of agreement are equal to 1.96σ (where σ is the standard deviation). Moreover, the Spearman Correlation Coefficient (ρ) was calculated for both the mean and maximal values

of WSS. This analysis was equal to the one based on the MRI data of [9].

Secondly, the circumferential average and circumferential maximal values were analyzed alongside the whole centerline of the studied aortas (we name this approach - *'Line Analysis'*). These data were subsequently analyzed similarly as the *'Point Analysis'*. Plots of the mean difference in the circumferential average or circumferential maxima were created together with the limits of agreement. Also, ρ was calculated for the five different regions of the thoracic aorta.

Lastly, the statistical analysis was performed on the created WSS maps (we name this approach - *'Surface Analysis'*). For the surfaces, WSS_{mean} and the standard deviation from the different surfaces were calculated for each of the volunteers. Afterward, the voxel-to-voxel ρ was calculated for all volunteers based on the whole surface, as well as the five investigated regions of the thoracic aorta.

For all methods, the classification of ρ was as follows: ($\rho \geq 0.95$: excellent); ($\rho \in (0.95; 0.85\rangle$: strong); ($\rho \in (0.85; 0.70\rangle$: good); ($\rho \in (0.70; 0.50\rangle$: moderate); ($\rho < 0.5$: poor). The significance level was set to $p = 0.05$; hence the analysis with p-value $p < 0.05$ is considered as statistically significant.

2.3 Results

2.3.1 Point Analysis

Tables 2.1 and 2.2 show the results from the Bland-Altman analysis, [23] for the mean and maximal values of WSS, respectively, of the investigated regions of the thoracic aorta. The analysis consists of the mean difference between the WSS for the different segmentations and corresponding limits of agreement.

Table 2.1: Bland-Altman analysis for WSS_{mean} showing the mean difference and the limits of agreement (1.96 times standard deviation σ) in the investigated regions of the thoracic aorta: proximal ascending aorta (pAAo), distal ascending aorta (dAAo), aortic arch (Arch), proximal descending aorta (pDAo), and distal descending aorta (dDAo).

	Mean Difference [Pa]					Limits of Agreement (1.96σ) [Pa]				
	pAAo	dAAo	Arch	pDAo	dDAo	pAAo	dAAo	Arch	pDAo	dDAo
A-B	-0.14	0.01	0.24	0.45	-0.24	1.71	1.60	2.20	2.17	2.36
A-C	0.66	0.72	0.58	1.24	0.65	1.77	2.51	2.54	3.10	3.68
A-D	0.29	0.50	0.41	0.92	0.77	1.87	1.62	2.30	1.84	2.71
B-C	0.81	0.71	0.34	0.79	0.90	1.86	1.53	1.53	1.64	3.27
B-D	0.44	0.49	0.17	0.47	1.01	1.44	1.24	1.93	1.53	2.67
C-D	-0.40	-0.23	-0.17	-0.32	0.12	1.01	1.75	1.89	1.61	2.76

The analysis based on the average WSS in the thoracic aorta shows a mean difference between the values in a range from 0 Pa to 1 Pa (if absolute values are taken into consideration). The limits of agreement lie between 1 Pa and 3.7 Pa. The results for WSS_{max} in the thoracic aorta sections show higher values for both the mean difference and the limits of agreement. For this case, the mean difference lies between 0 Pa and 9.74 Pa (in absolute values), and the limits of agreement are from 6 Pa to 23 Pa.

The analysis of the MRI results performed by one observer (RvdP) [9] considers just the following surface combinations: A-B (scan-rescan), A-C (intraobserver), and A-D

Table 2.2: Bland-Altman analysis for WSS_{max} showing the mean difference and the limits of agreement (1.96 times standard deviation σ) in the investigated regions of the thoracic aorta: proximal ascending aorta (pAAo), distal ascending aorta (dAAo), aortic arch (Arch), proximal descending aorta (pDAo), and distal descending aorta (dDAo).

	Mean Difference [Pa]					Limits of Agreement (1.96σ) [Pa]				
	pAAo	dAAo	Arch	pDAo	dDAo	pAAo	dAAo	Arch	pDAo	dDAo
A-B	0.16	0.18	0.31	2.87	-0.15	6.04	7.79	14.21	14.17	15.26
A-C	4.76	3.46	5.41	9.74	8.82	7.85	7.11	14.07	16.43	23.13
A-D	2.87	1.43	2.68	3.40	6.38	8.98	8.08	10.11	14.71	17.64
B-C	4.60	3.28	5.10	6.87	8.96	8.08	4.10	13.10	9.95	19.77
B-D	2.71	1.25	2.40	0.52	6.52	8.40	5.69	9.51	12.73	15.15
C-D	-1.89	-2.03	-2.73	-6.35	-2.44	3.44	4.94	7.12	7.89	11.93

Table 2.3: Spearman Correlation Coefficient as obtained from MRI and CFD for the surface combinations for the mean and maximal values of WSS in the investigated regions of the aorta: proximal ascending aorta (pAAo), distal ascending aorta (dAAo), aortic arch (Arch), proximal descending aorta (pDAo), and distal descending aorta (dDAo).

	WSS_{mean}					WSS_{max}				
	pAAo	dAAo	Arch	pDAo	dDAo	pAAo	dAAo	Arch	pDAo	dDAo
$A\text{-}B_{CFD}$	0.78	0.84	0.81	0.95	0.88	0.89	0.62	0.68	0.79	0.77
$A\text{-}B_{MRI}$	0.90	0.89	0.72	0.64	0.79	0.86	0.68	0.71	0.68	0.65
$A\text{-}C_{CFD}$	0.70	0.79	0.81	0.79	0.76	0.79	0.72	0.58	0.59	0.41
$A\text{-}C_{MRI}$	0.99	0.95	0.99	1.00	0.98	0.96	0.78	0.95	0.99	0.93
$A\text{-}D_{CFD}$	0.64	0.72	0.92	1.00	0.78	0.82	0.73	0.62	0.61	0.67
$A\text{-}D_{MRI}$	0.94	1.00	0.99	0.96	0.97	0.81	0.81	0.94	0.98	0.93
$B\text{-}C_{CFD}$	0.72	0.92	0.78	0.85	0.89	0.68	0.84	0.72	0.65	0.38
$B\text{-}D_{CFD}$	0.76	0.81	0.87	0.95	0.81	0.66	0.75	0.83	0.61	0.61
$C\text{-}D_{CFD}$	0.92	0.78	0.90	0.79	0.87	0.93	0.84	0.90	0.96	0.83
$Mean_{CFD}$	0.75	0.81	0.85	0.89	0.83	0.80	0.75	0.72	0.70	0.61

(interobserver). The results presented here show a similar trend to the ones presented by RvdP [9] The variability of WSS and the limits of agreement are higher for regional WSS_{max}. However, the results obtained from CFD show higher mean differences and limits of agreement. This is most probably related to the overall range of WSS. While the values of WSS extracted from MRI data are $\mathcal{O}(1)$, the values of WSS based on CFD are $\mathcal{O}(10)$.

Next, the Spearman Correlation Coefficient was calculated for both the mean and maximal values of WSS in the investigated regions of the thoracic aorta. The results are presented in Table 2.3. For WSS_{mean}, the correlation between the surfaces is good to strong for most of the cases. The only exceptions are surface combinations A-D in the pAAo, where the correlation is moderate, and A-D in the pDAo, where the correlation is excellent. When looking at the average values per region, the correlation increases from the pAAo (good) reaching its maximum in the pDAo (strong) and slightly decreasing in the dDAo (good). Not many differences can be found between the different surface combinations.

The maximal values of WSS show more variety, with the correlation being moderate

to strong. However, a case with excellent correlation can be found (C-D in pDAo) as well as cases with poor correlation (A-C and B-C both in dDAo). Unlike for the WSS_{mean}, the correlation does not reach its maximum in the pDAo but rather gradually decreases. The average of respective correlation for all surface representations decreases from good in the pAAo to moderate in the dDAo. This trend can be explained by the overall values for WSS. From table 2.2 can be seen that both the difference between the value of WSS_{max} as well as the limits of agreement increase downstream the aorta. A similar trend can also be seen in the actual values of WSS for each of the studied surfaces. WSS is gradually increasing from the aortic root.

From the paper by Van der Palen et. al. [9], the results show the correlation to be good to strong for WSS_{mean} and moderate to good for WSS_{max} in the case of A-B. For the surface combination A-C, the correlation was found to be good to excellent for both WSS_{mean} and WSS_{max}. Finally, results for A-D show good to excellent correlation for both WSS_{mean} and WSS_{max}.

The results from the CFD analysis show a similar correlation of mean WSS for all cases and a lower correlation of maximal values of WSS. The difference in WSS_{max} arises especially in the descending part of the thoracic aorta. While the correlation based on MRI was overall good to excellent [9], the agreement for CFD is moderate to good in these regions.

An example of the plots for the scan-rescan analysis (A-B) of WSS_{mean} and WSS_{max} based on the Bland-Altman analysis is shown in Fig. 2.4 together with the correlation plots. Plots for the other surface comparisons can be found in appendix 2.5.

2.3.2 Line Analysis

In the next step, the circumferential averages of WSS were calculated along the corresponding centerline for all geometries. Afterward, the average of WSS_{mean} per volunteer was calculated together with the standard deviation. The resulting plots for all ten volunteers can be seen in Fig.2.5.

As shown in Fig.2.5, the agreement between the geometries is better in the pAAo and dAAo than in the rest of the aorta. In the arch, the variation of WSS_{mean} shows higher discrepancies as the flow starts to be more complex. Further downstream the aorta, in the pDAo and dDAo, the agreement between WSS_{mean} obtained from different segmentations is very weak.

The Spearman correlation coefficient was calculated for the circumferential averages of WSS alongside the centerline. The values for all possible surface combinations are shown in Table 2.4. The correlation between the different surfaces is better for the circumferential averages. Mostly moderate and good correlation can be reported. The average among all volunteers shows a good correlation for A-C, A-D, and C-D and a moderate correlation for A-B, B-C, and B-D. However, the differences are relatively small. The standard deviation varies between 0.05 and 0.11, and the p-value was smaller than 0.0001 for all cases.

2.3.3 Surface Analysis

The results of the two-dimensional mapping procedure of WSS along the thoracic aorta wall are shown in Figs.2.6 and 2.7. It can be seen that WSS is lower in the ascending part and higher in the arch and the descending aorta. In the descending aorta, significant variations

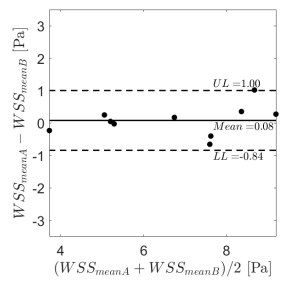

(a) Bland-Altman plot for WSS_{mean}.

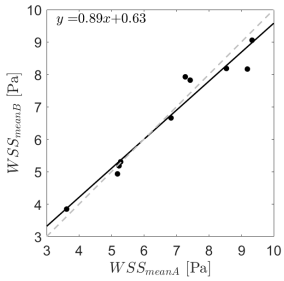

(b) Correlation plot for WSS_{mean}.

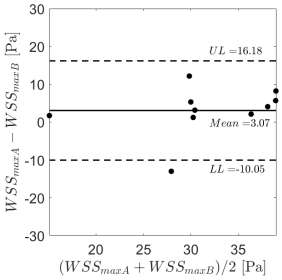

(c) Bland-Altman plot for WSS_{max}.

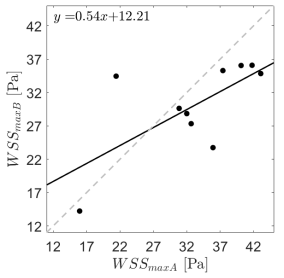

(d) Correlation plot for WSS_{max}.

Figure 2.4: Bland-Altman plots for the scan-rescan analysis (A-B) with the highlighted mean value of WSS difference and the upper (UL) and lower (LL) limits of agreement (2σ) for WSS_{mean} a) and WSS_{max} c) and correlation plots with the corresponding equation for WSS_{mean} b) and WSS_{max} d).

Table 2.4: Spearman correlation coefficient *r* based on the circumferential averages for ten volunteers (V1-V10) with the mean value and standard deviation (SD).

	V1	V2	V3	V4	V5	V6	V7	V8	V9	V10	Mean	SD
A-B	0.68	0.72	0.64	0.61	0.76	0.62	0.55	0.70	0.65	0.73	0.67	0.06
A-C	0.75	0.59	0.72	0.70	0.79	0.76	0.73	0.85	0.64	0.69	0.72	0.07
A-D	0.78	0.72	0.74	0.70	0.75	0.82	0.81	0.68	0.58	0.72	0.73	0.07
B-C	0.73	0.71	0.53	0.42	0.74	0.75	0.68	0.68	0.74	0.74	0.67	0.11
B-D	0.69	0.66	0.68	0.62	0.72	0.73	0.71	0.62	0.62	0.75	0.68	0.05
C-D	0.66	0.73	0.79	0.63	0.85	0.75	0.79	0.65	0.74	0.85	0.74	0.08

are present in local WSS for all geometries. These results agree with the circumferential averages, where the variation between the WSS was prominent in the descending aorta and suggests that the possible error in WSS based on CFD will be most prevalent in these parts.

Until this point, the WSS distributions were assessed qualitatively by visual comparison. To evaluate more quantitatively the degree of variation in WSS caused by the geometry diversity, the map of average WSS and the standard deviation was additionally created from the four segmentations (shown as the last two inserts in Figs.2.6 and 2.7). Two local maxima located between the aortic arch and the proximal descending aorta can be identified for

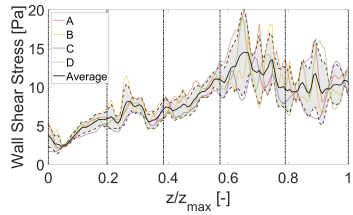

(a) Volunteer 1

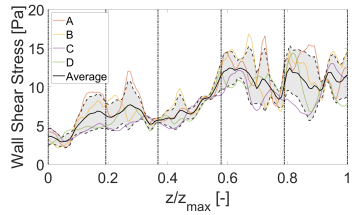

(b) Volunteer 2

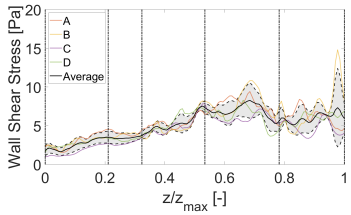

(c) Volunteer 3

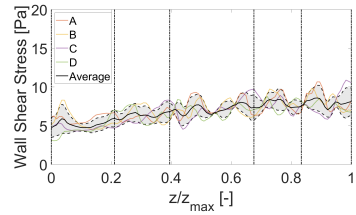

(d) Volunteer 4

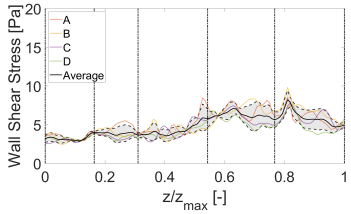

(e) Volunteer 5

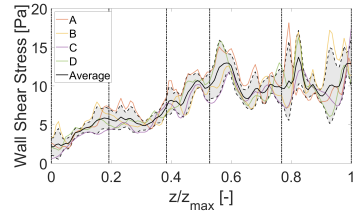

(f) Volunteer 6

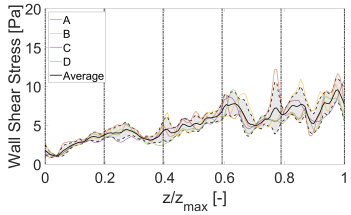

(g) Volunteer 7

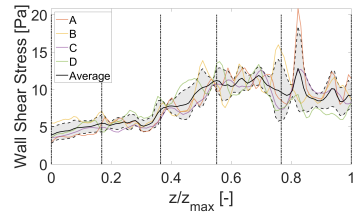

(h) Volunteer 8

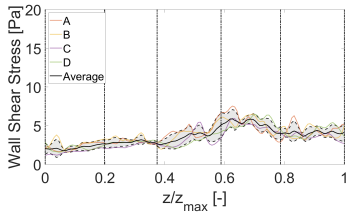

(i) Volunteer 9

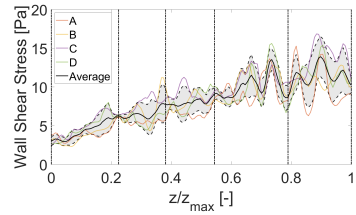

(j) Volunteer 10

Figure 2.5: Circumferential average of WSS alongside the normalized centerline length (z/z_{max}) for the four different segmentation with its mean value and standard deviation for volunteers 1-10.

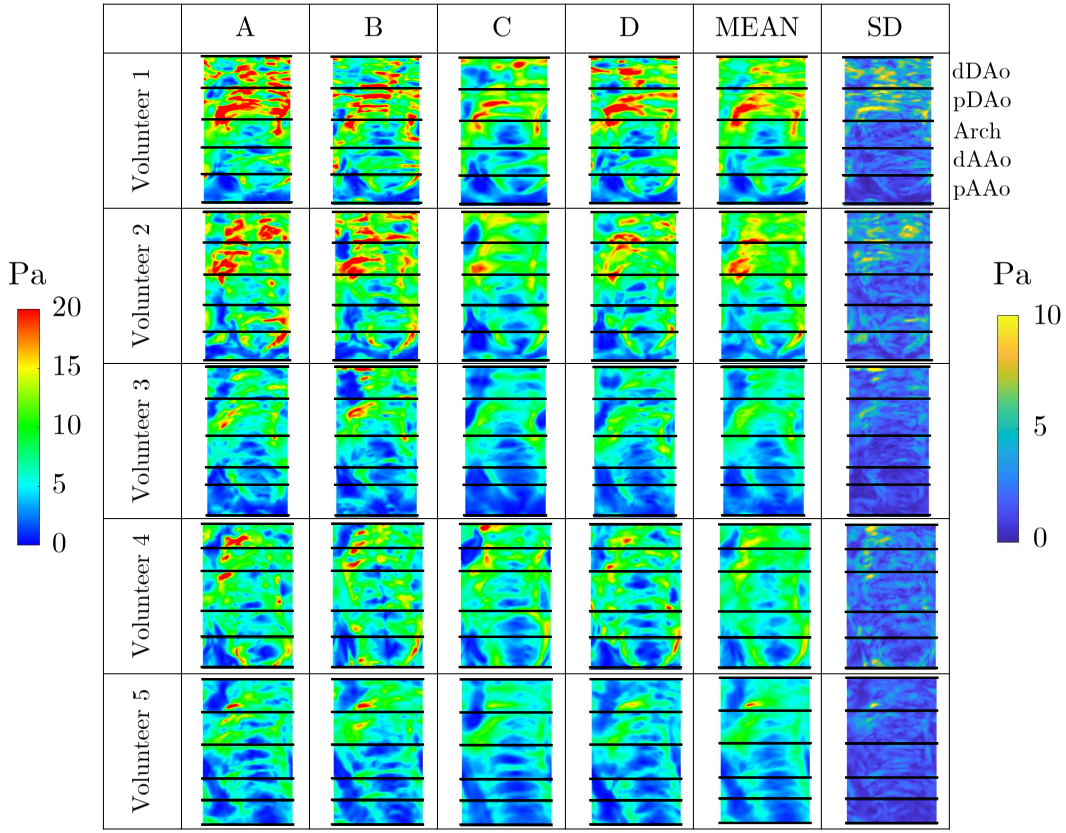

Figure 2.6: Maps of WSS for volunteers 1-5 with the mean WSS map per volunteer and the corresponding standard deviation (SD) map; all of the maps are split into the five investigated regions: pAAo - proximal ascending aorta, dAAo - distal ascending aorta, Arch - aortic arch, pAAo - proximal descending aorta, pAAo - proximal descending aorta.

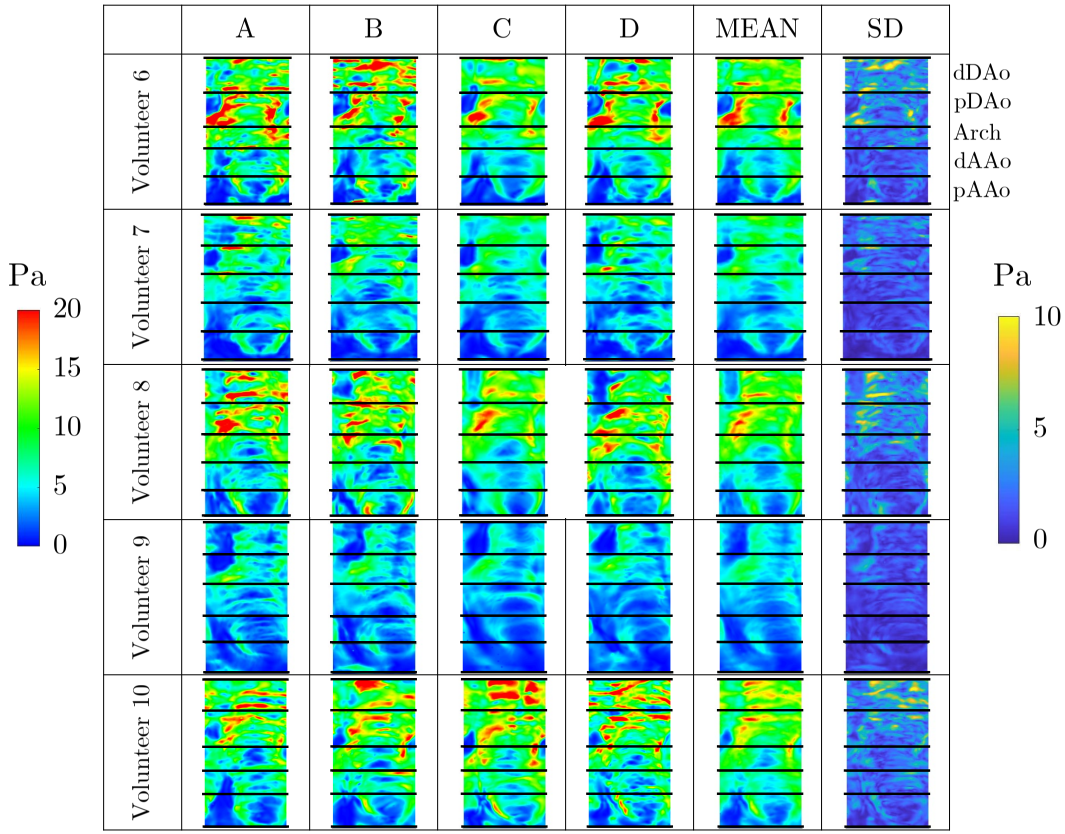

Figure 2.7: Maps of WSS for volunteers 6-10 with the mean WSS map per volunteer and the corresponding standard deviation (SD) map; all of the maps are split into the five investigated regions: pAAo - proximal ascending aorta, dAAo - distal ascending aorta, Arch - aortic arch, pAAo - proximal descending aorta, pAAo - proximal descending aorta.

all presented geometries. The plot of standard deviation shows the highest values in the descending part of the aorta as well.

The results of the Spearman correlation coefficient of WSS based on the voxel-to-voxel analysis of the whole surface representing the thoracic aorta can be found in Table 2.5. The results show that the voxel-to-voxel correlation is mostly moderate and in a few cases, good or poor. The average of all volunteers shows a moderate correlation for all possible surface comparisons. The standard deviation for the Spearman Correlation Coefficient is between 0.06 and 0.09 among the different segmentation combinations. It should also be noted the p-value for all cases was smaller than 0.0001.

Table 2.5: Spearman correlation coefficient r based on the voxel-to-voxel analysis for ten volunteers (V1-V10) with the mean value and standard deviation (SD).

	V1	V2	V3	V4	V5	V6	V7	V8	V9	V10	Mean	SD
A-B	0.55	0.60	0.58	0.43	0.66	0.61	0.49	0.63	0.60	0.54	0.57	0.07
A-C	0.63	0.53	0.67	0.53	0.62	0.71	0.68	0.73	0.49	0.54	0.61	0.09
A-D	0.63	0.54	0.55	0.58	0.53	0.68	0.68	0.54	0.49	0.48	0.57	0.07
B-C	0.63	0.62	0.60	0.49	0.54	0.65	0.62	0.64	0.52	0.67	0.60	0.06
B-D	0.57	0.51	0.55	0.42	0.52	0.59	0.60	0.53	0.48	0.63	0.54	0.06
C-D	0.59	0.70	0.68	0.53	0.64	0.73	0.71	0.58	0.68	0.68	0.65	0.07

The correlation coefficients do not show a better or worse agreement among different combinations of surfaces. All segmentations made from the scan (A, C, D) have a similar agreement. Also, the segmentation based on the re-scan (B), which was performed in slightly different physiological conditions, has a similar agreement with the scan-based surfaces, as can be seen from Table 2.5. Hence, the CFD-based WSS is not highly affected by the re-scan conditions.

The Spearman correlation coefficient based on the whole surface has lower values than the one based on the circumferential averages shown in Table 2.4. This can suggest that while the locality of WSS_{max} and WSS_{min} may differ, the mean values of the cross-sections are close to each other.

Finally, we have calculated the voxel-to-voxel Spearman correlation coefficient based on the investigated regions of the thoracic aorta (as was shown in Fig.2.2). The results for the correlation coefficient in the distinct regions can be seen in Table 2.6. A similar trend can be observed for all surfaces, where the correlation gradually decreases from the inlet to the outlet of the aorta. The highest correlation can be found at the beginning of the aorta - in the pAAo. In this region, a moderate correlation can be found for all surface combinations. In the dAAo, the agreement is lower but still moderate. In the aortic arch, the correlation is even lower, on average still being moderate but with values around 0.5. For both parts of the descending thoracic aorta, the agreement is poor.

These results confirm the findings in the comparison of the surfaces from Figs.2.6 and 2.7 as well as the graphs of circumferential averages shown in Fig.2.5. The agreement between the surfaces is lower in the pDAo and dDAo. It has to be noted that the agreement based on the voxel-to-voxel comparison is significantly lower in comparison to both the results observed for MRI by van der Palen [9] and the *'Point Analysis'* for CFD.

Table 2.6: Average of all the volunteers for Spearman correlation coefficient r within the investigated segments of the aorta.

	pAAo	dAAo	Arch	pDAo	dDAo
A-B	0.64	0.54	0.50	0.40	0.25
A-C	0.63	0.57	0.53	0.47	0.30
A-D	0.59	0.49	0.47	0.38	0.34
B-C	0.62	0.52	0.50	0.47	0.34
B-D	0.57	0.52	0.44	0.40	0.31
C-D	0.66	0.58	0.55	0.52	0.38
Mean	0.62	0.54	0.50	0.44	0.32

2.4 Discussion

Image-based CFD of arterial geometries is gaining popularity in studying various arterial diseases. While numerous advances in simulating the flow in patient-specific arteries have been developed, many questions have also been raised about the validity of such simulations. There are many factors in the aortic flow that can have a significant impact on the generated flow patterns. These include the types of inlet and outlet boundary conditions, movement of the wall, the pulsating character of the inflow, blood rheology, etc. A great majority of these factors have been previously investigated, mostly on small cohorts.

However, the base of the simulations - the geometry of the aorta - affects the flow as well, and the effects of small variations in geometry on the WSS have often been overlooked in the MRI-based CFD studies. Particularly for MRI, it was previously shown that the morphometric characteristics of segmented aorta vary between rescan, intra- and interobserver analysis [10], and this has an effect on WSS estimated based on the 4D-flow MRI velocity fields [9]. Hence, it is of great importance to understand how small variations in geometry due to the segmentation process affect the simulations. In this study, we aimed to answer this question and create a confidence interval for both the expected error as well as the method with which such variability should be investigated.

2.4.1 Evaluation Method

In MRI-based studies, the WSS variability is often evaluated based on a commonly used 'Point Analysis', in which WSS_{mean} or WSS_{max} of a few segments of the aorta are compared between the different segmentations. This leads to many studies reporting a high level of agreement in WSS between intra/interobserver and scan/rescan [7, 9, 24].

We have performed the same point analysis also on our CFD data set, which resulted in a good agreement between different surfaces, similar to MRI. While the agreement in the ascending aorta and arch are close to MRI, more differences are observed in the ascending aorta. The discrepancies between CFD and MRI variability based on the 'Point Analysis' are likely caused by higher velocities in this region due to the gradual narrowing of the artery and the omission of the branching arteries. Higher velocity causes higher WSS and steeper gradients close to the wall. Consequently, small irregularities between different

segmentations eventually lead to a worse correlation between them. Additionally, for MRI, the velocity field does not change with different segmentations (except for scan/rescan comparison). For CFD, the velocity field may slightly differ due to the differences in the geometry, which also adds to the higher disagreement in the descending aorta.

While this type of analysis is widely accepted by the medical society, considering just a few data points per segmentation and high spatial averaging of the results may lead to over-estimation of the quality of the agreement. By visual inspection of MRI-based WSS contours (Fig. 2.8b), multiple discrepancies between different segmentations can be observed, which are not represented in the results based on the 'Point Analysis'. This shows that performing simplified analysis and comparing the results just in terms of WSS_{mean} or WSS_{max} in the particular segments of the aorta is insufficient since a lot of the information is lost due to averaging.

We observed an identical trend also in WSS_{CFD}. While the 'Point Analysis' shows a high agreement, 'Line Analysis' and 'Surface Analysis' give, on average moderate and poor agreement, respectively. Both of these methods give much more information about the actual WSS trends in the aorta and can capture the local variations, which may be vital for evaluating disease progression. Additionally, the WSS correlation is lower in the descending part of the aorta, as shown in the more detailed analyses. This was not visible from the analysis of MRI results nor from the 'Point Analysis' of the CFD results.

2.4.2 Effect of Morphology on WSS

Morphology of aorta based on 4D flow MRI has a certain degree of uncertainty [10]. This also brings variability to CFD-based WSS. The three methods of the analysis show that the WSS variability gradually increases from the ascending aorta to the descending aorta. The higher value of WSS in the descending aorta is due to the smaller radius of the descending aorta compared to the ascending part [10]. Also, the flow features in this region are more complex. The complex flow features originate from interactions of recirculation zone and secondary flow structures (so-called Dean vortices [25]). While all surfaces exhibit similar distributions, some differences can be observed as well, especially comparing the segmentation C to the rest. The maps of WSS from segmentation C were smoother than the others. This is reflected in the smaller variations in maximal/minimal WSS in all parts of the aorta compared to the other segmentations.

Accurate 4D flow MRI-based segmentations are more difficult to obtain since the method is highly dependent on the spatial and temporal resolution and the velocity field. This often leads to the method not being completely automatic, and many manual adjustments need to be applied during the segmentation procedure. Consequently, the segmentations may vary, even for the same MRI data set.

This affects the simulations, and it is crucial that the error in WSS due to the segmentation variation is taken into account. Whereas the effects of the different segmentations are not high and the global WSS_{mean} and WSS_{max} correspond well, many differences can be seen in the details of WSS. Similar results were also presented for intracranial aneurysms [26, 27], where WSS varied between 28% to 51%, depending on segmentation. Because of this, a high-quality segmentation is desirable for an accurate estimation of WSS.

Additionally, as was shown for intracranial aneurysms, the branch positioning and diameter have a great effect on WSS [26, 27]. It should be noted that this study omits the

main branching arteries in the aortic arch. Consequently, the flow rate in the descending aorta is higher for CFD than for the MRI. Including the branches in the segmentation would probably lead to even higher discrepancies since both the positioning of the branching arteries as well as their diameter could be different for the four segmentations. This, in combination with more complicated boundary conditions for the branching arteries, could result in more variation in WSS between segmentations. This stresses the importance of high-quality segmentation for accurate estimations of WSS.

2.4.3 Clinical Implications

WSS is a pathophysiological stimulus at the intimal surface of the aortic vessel wall that has been shown to alter gene expression and endothelial cell function [28]. Altered shear stress, either in the longitudinal or circumferential direction, can promote endothelial changes that can create an area at risk for vascular remodeling and aneurysm growth. Accurate mapping of the variations in wall shear stress may prove to become a very relevant clinical tool, but before its introduction, the effect of accurate aortic lumen segmentation and observer- and repeated scanning-induced variations on the wall shear stress quantitation needs in-depth evaluation. In this study, we have used a combined MRI-CFD approach to study the variations in wall shear stress.

Our analyses showed more WSS variability in the descending aortic segments for the line- and voxel-to-voxel analysis compared to the point analysis. Interestingly, these segments require less manual adaptation by the observer compared to the ascending aortic segments (at least for the distal descending aortic segment). The descending aorta (beyond the arch) is more fixed to the spinal column and, therefore, not sensitive to motion, as is the ascending aorta. For the descending aorta, we attributed the observed WSS variability to a higher velocity and more complex flow in these regions (compared to the ascending aortic segments) in the healthy volunteers.

These findings are important and give rise to reflection from a clinical perspective, for instance, in patients with stenotic bicuspid aortic valves or aortic dissections. Patients with stenotic bicuspid aortic valves often have ascending aorta dilatation/aneurysm formation [29]. Next to the difficulties for an accurate ascending aorta segmentation due to motion, higher velocities and complex flow phenomena are observed in the ascending aorta in these patients [30]. For the later mentioned aortic dissection, the reconstructed geometry plays a key role in determining the complex blood flow in the true and false lumen [31]. Additionally, the presence of multiple intimal tears greatly influences the complexity of the flow in aortic dissections [32]. All of these characteristics lead to higher WSS variability depending on the applied WSS analysis method. Hence, it would be of clinical interest to perform an interobserver analysis in a subset of patients with a spectrum of aortic diseases (with and without high-velocity outflow jets) with the proposed analysis methods as a potential next step.

2.4.4 Limitations

A limitation of this study is a relatively small cohort of ten healthy volunteers with similar ages. For a more robust analysis, a larger group of volunteers with wider age differences should be considered. Also, the study did not include patients with anomalies in the aorta due to ethical concerns with repeated examination. As has been shown, the lumen

morphology has a great effect on WSS, which is often considered one of the evaluation factors for certain arterial diseases [33]. Hence, for diseased patients, it might be crucial to segment the artery as close as possible to reality. Additionally, the diseased aorta may introduce more variability, not only by pathology but also by the fact that 4D flow MRI acquisition is time-consuming, which is always a more challenging examination in patients (more heart rate variability, less cooperation, difficulty not moving, etc.) [10].

Several assumptions were made on the CFD part of this study, which may influence the results. First is the assumption of laminar flow. Our operating range of Reynolds number was in the transition region, and hence turbulence modeling should be considered and the effects of turbulence investigated.

Next, the rigid-wall assumption overestimates WSS, as demonstrated in [34]. However, this should not have influenced our results since the purpose of this study was to evaluate the WSS variability due to different segmentations in multiple volunteers. For our study, the actual movement of the aorta was similar, considering that the four compared aortas per volunteer were based on two scans taken closely after each other, and the physiological conditions (e.g., heartbeat) were very similar. Also, the segmentation was always performed at the peak systole. Additionally, the moving-wall approach is computationally very costly and requires additional patient-specific information, like the thickness of the wall and the elastic properties of the wall. All these parameters are difficult to obtain for each case, and hence, using simulation approaches like Fluid-Structure Interaction or prescribed motion may lead to additional uncertainties in the simulations [34, 35].

Third, we have considered just steady-state simulations with a blood flow simulated at the peak systole. The differences between steady simulations at the peak systole and genuine time-dependent simulations were addressed in [36]. Because of the steady-state simulations, some quantities used for the evaluation of arterial flow cannot be obtained, e.g., time-averaged WSS and oscillatory shear index. However, since we have used the same boundary conditions for all simulations, the agreement in WSS between different segmentation should not be highly affected by the steady-state approach. Therefore, for this study, the steady-state approach is sufficient.

Finally, a pre-processing procedure was applied for segmentations, which included cutting the inlets and outlets, smoothing, and adding extensions. While we have kept all parameters the same and only one person was performing this procedure, some discrepancies can still be introduced to the surfaces due to the smoothing. For example, the positioning of the cutting planes on inlets could lead to a different size of inflow extensions. For a more rigorous analysis, the variability in pre-processing should be investigated as well.

2.5 Summary and Conclusions

In the present study, we addressed the geometrically induced variability of the WSS in CFD-MRI coupled simulations. First, we adopted an approach often seen in literature, a comparison of spatially averaged WSS_{mean} in the five selected regions of the thoracic aorta (so-called '*Point Analysis*' method). For both MRI and CFD results, agreement in global WSS for the different geometries is similar, showing, on average, good to excellent correlation in all selected parts of the thoracic aorta.

Next, we performed a more detailed visual and statistical analysis of CFD results. The circumferential averages of WSS were calculated alongside the centerline (so-called '*Line*

Analysis' method), and two-dimensional mapping of the three-dimensional aorta wall values are performed to conduct voxel-to-voxel comparison (so-called '*Surface Analysis*' method). In comparison to the *'Point Analysis'*, both *'Line'* and *'Surface Analysis'* show a lower agreement between different segmentations. The correlation varies between moderate and good for the *'Line Analysis'*, while it is between poor and good for the *'Surface Analysis'* method. This reduced agreement is a consequence of minimal to no averaging in the *'Line Analysis' and 'Surface Analysis'* approach respectively. Additionally, we observed a lower correlation of WSS in the descending part of the thoracic aorta obtained from *'Surface Analysis'* for various segmentations. This trend was not visible in the *'Point Analysis'* and can be attributed to the more complex flow in this region.

Hence, our findings stress the importance of carefully analyzing the local WSS distributions of CFD simulations based on the 4D-Flow MRI segmentations. Finally, since we show that the WSS variability is similar for both rescan and intra/interobserver segmentations, CFD-MRI coupling shows the potential for studying the progression of aortic pathologies in serial follow-up scans.

Appendix A: Comparison of WSS between CFD and MRI

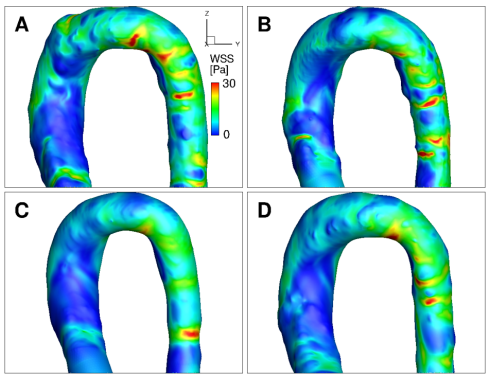

(a) CFD

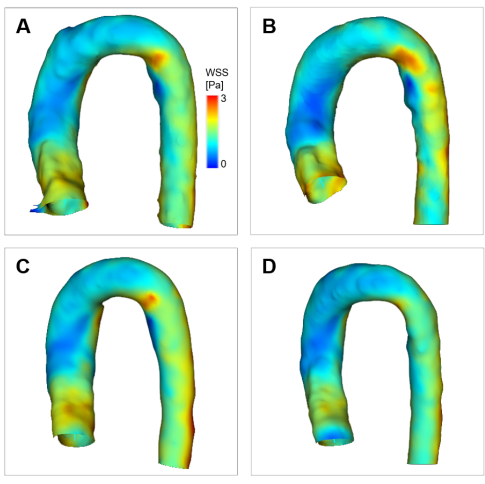

(b) MRI

Figure 2.8: Contours of WSS magnitude at peak systole for four different geometrical representations of aorta A-D of the volunteer six as obtained from simulations (a) and Magnetic Resonance Imaging was obtained using CAAS MR 4D flow v1.1 (b).

Contours of WSS for all four segmentations of one volunteer (V6) are shown in Fig.2.8 for both MRI and CFD. The scales for the contours were adjusted case-specifically: the WSS range is 0 - 30 Pa for the CFD results and 0 - 3 Pa for MRI results. Few similarities can be observed between MRI and CFD. WSS shows lower values in the ascending part of the aorta and gradually increases downstream for MRI as well as CFD. However, many differences can be found both in the localization of minima and maxima and also in the values. The maximal values of WSS reach just up to 3 Pa for the MRI, whereas for WSS based on the simulations, locations with WSS higher than 30 Pa can be found.

To establish the baseline of WSS_{CFD} we compare the simulated results to WSS_{MRI} for all four segmentations of one volunteer. Both methods lead to a similar global distribution of WSS with different absolute values (WSS_{CFD} ~ $\mathcal{O}(10)$ Pa and WSS_{MRI} ~ $\mathcal{O}(1)$ Pa). However, due to the assumptions in the simulation - rigid wall and no branching arteries - we are not able to perform a direct comparison. Both of these contribute to an overestimation of WSS_{CFD} [37, 38].

Moreover, it has been previously shown that the values of WSS_{MRI} are underestimated [15]. To calculate the gradient of the velocity at the wall, the boundary layer has to be resolved adequately. The boundary layer thickness for the pulsating flows in an artery with diameter D is expressed as [22]:

$$\delta = \sqrt{\frac{\mu D}{2\rho U}} \tag{2.3}$$

where δ is the boundary layer thickness. An order of magnitude estimate for the aorta gives the thickness of the boundary layer to be δ ~ 0.1 mm. The resolution of the MRI measurements is Δx = 2.5 mm. Hence, MRI does not have a resolution high enough to resolve the boundary layer adequately, and WSS cannot be properly estimated. Because of that, image-based WSS_{CFD} should always be considered. However, for patient-specific simulations, both the geometry as well as the boundary conditions should be considered as close to reality as possible.

Appendix B: Grid Dependency Study

In order to perform a mesh dependency study, three meshes were created for one of the cases: coarse, normal, and fine. The coarse mesh consists of 1.7 million elements, with a maximal cell size of 0.5D. The normal mesh consists of 4.2 million elements, with a maximal cell size of 0.3D. Finally, the fine mesh consists of 7.4 million elements, with a maximal cell size of 0.19D. For all meshes, the boundary layer settings were kept the same, as described in Section 2.2.2. The contours of WSS calculated on these three meshes are shown in Fig.2.9. No significant differences can be observed in the contour distribution of the WSS at the thoracic artery wall. To assess in more detail the local distributions of WSS, characteristic profiles were extracted along an arbitrarily selected line along the descending part of the thoracic aorta (as indicated by the black line), Fig.2.9. The extracted profiles of WSS are shown in Fig.2.10. Again, very small differences can be observed between the coarse and finer meshes. The maximal difference between the coarse and the normal mesh is 1.28%, and between the coarse and the fine mesh is 1.94%. The normal and the fine mesh agree well in WSS for most of the extracted data. The maximal difference between these two meshes is 0.64%. Based on all this, the normal mesh results were used for statistical analysis of the data.

Appendix C: Bland-Altman plots

Below, the Bland-Altman plots can be found for the surface combinations A-C, A-D, B-C, B-D, and C-D.

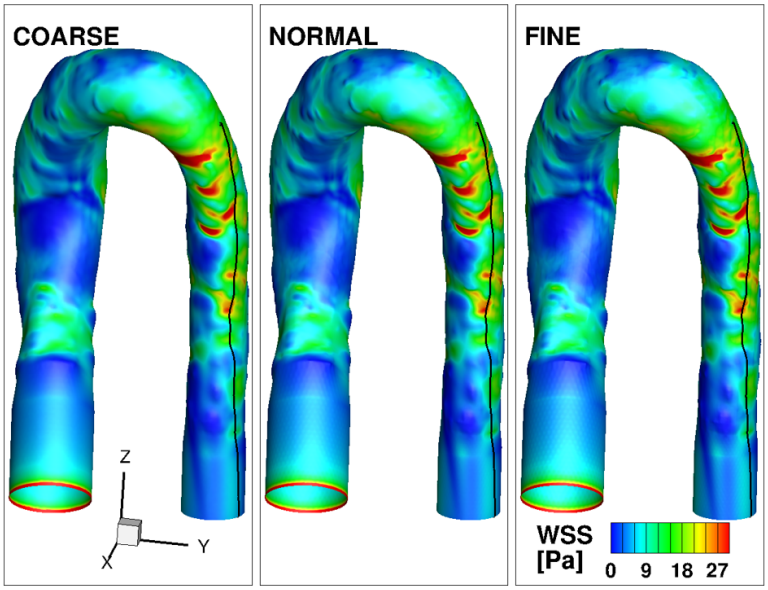

Figure 2.9: Contours of WSS and the line for the data extraction for the three different meshes - Coarse (left), Normal (middle - used in all simulations) and Fine (right) - for the geometry A of Volunteer 1.

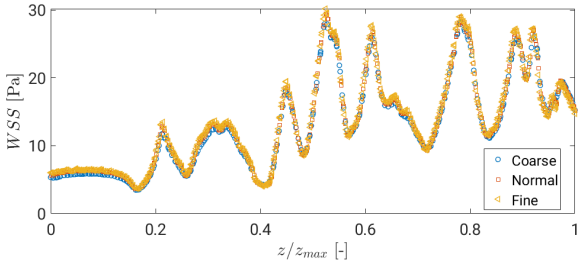

Figure 2.10: WSS alongside the out-seam in the descending thoracic aorta for three different meshes - coarse, normal, and fine - for the geometry A of Volunteer 1.

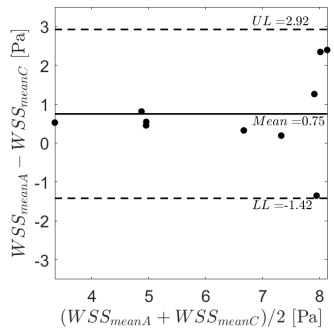

(a) Bland-Altman plot for WSS_{mean}.

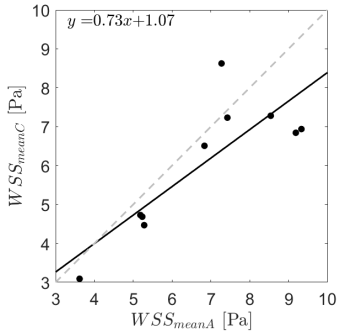

(b) Correlation plot for WSS_{mean}.

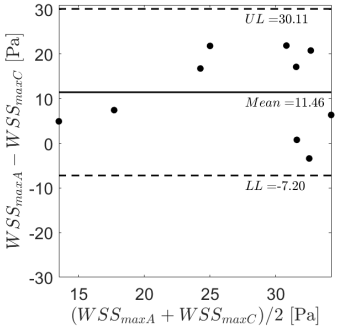

(c) Bland-Altman plot for WSS_{max}.

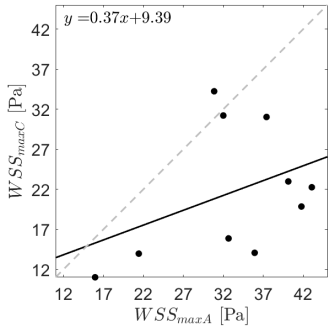

(d) Correlation plot for WSS_{max}.

Figure 2.11: Bland–Altman plots for the intraobserver analysis (A-C) with highlighted mean value of WSS difference and the upper (UL) and lower (LL) limits of agreement (2σ) for WSS_{mean} a) and WSS_{max} c) and correlation plots with the corresponding equation for WSS_{mean} b) and WSS_{max} d).

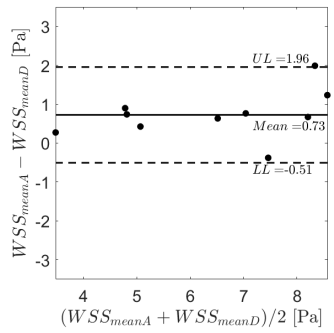

(a) Bland-Altman plot for WSS_{mean}.

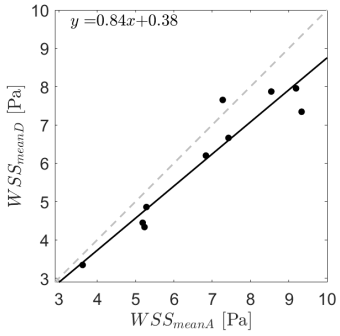

(b) Correlation plot for WSS_{mean}.

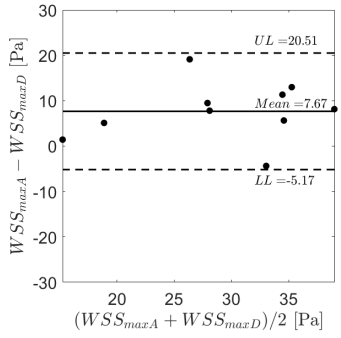

(c) Bland-Altman plot for WSS_{max}.

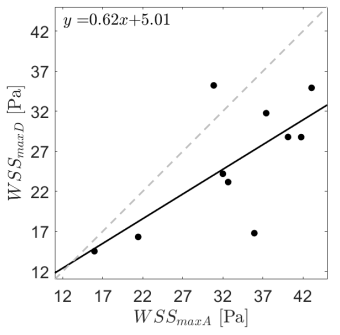

(d) Correlation plot for WSS_{max}.

Figure 2.12: Bland–Altman plots for the interobserver analysis (A-D) with highlighted mean value of WSS difference and the upper (UL) and lower (LL) limits of agreement (2σ) for WSS_{mean} a) and WSS_{max} c) and correlation plots with the corresponding equation for WSS_{mean} b) and WSS_{max} d).

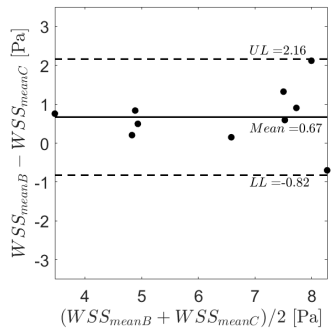

(a) Bland-Altman plot for WSS_{mean}.

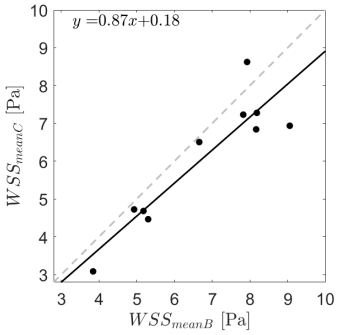

(b) Correlation plot for WSS_{mean}.

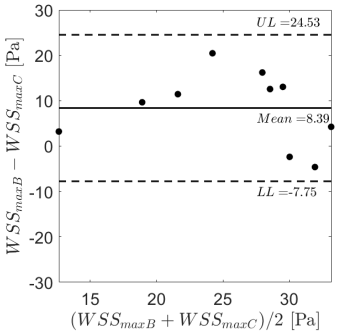

(c) Bland-Altman plot for WSS_{max}.

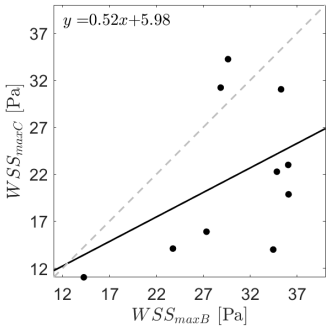

(d) Correlation plot for WSS_{max}.

Figure 2.13: Bland–Altman plots for the B-C surface analysis with highlighted mean value of WSS difference and the upper (UL) and lower (LL) limits of agreement (2σ) for WSS_{mean} a) and WSS_{max} c) and correlation plots with the corresponding equation for WSS_{mean} b) and WSS_{max} d).

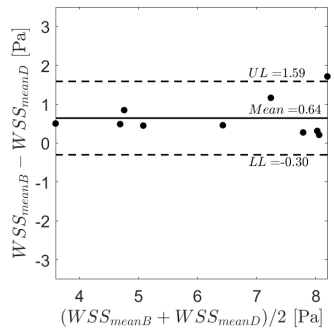

(a) Bland-Altman plot for WSS_{mean}.

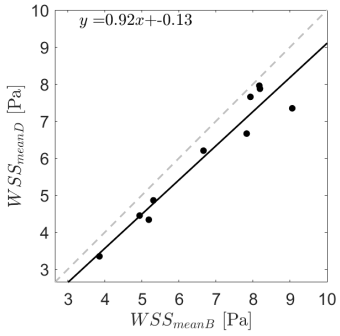

(b) Correlation plot for WSS_{mean}.

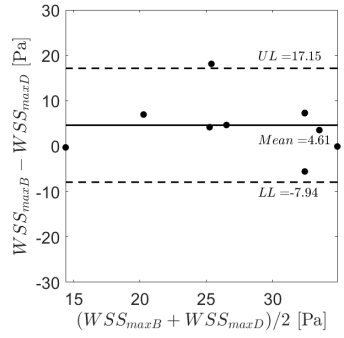

(c) Bland-Altman plot for WSS_{max}.

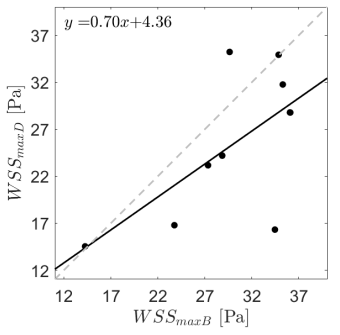

(d) Correlation plot for WSS_{max}.

Figure 2.14: Bland–Altman plots for the B-D surface analysis with highlighted mean value of WSS difference and the upper (UL) and lower (LL) limits of agreement (2σ) for WSS_{mean} a) and WSS_{max} c) and correlation plots with the corresponding equation for WSS_{mean} b) and WSS_{max} d).

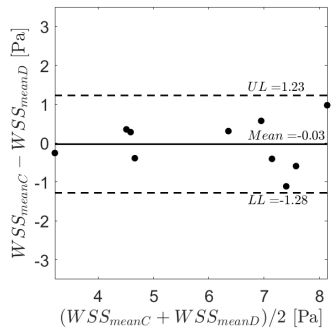

(a) Bland-Altman plot for WSS_{mean}.

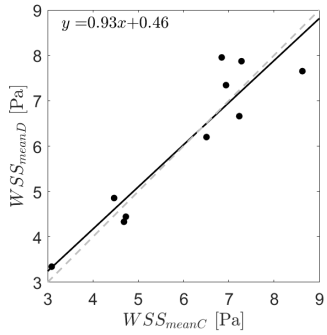

(b) Correlation plot for WSS_{mean}.

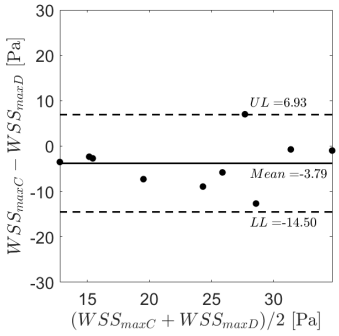

(c) Bland-Altman plot for WSS_{max}.

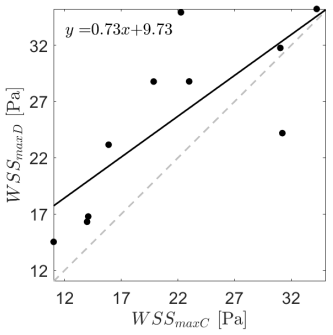

(d) Correlation plot for WSS_{max}.

Figure 2.15: Bland–Altman plots for the C-D surface analysis with highlighted mean value of WSS difference and the upper (UL) and lower (LL) limits of agreement (2σ) for WSS_{mean} a) and WSS_{max} c) and correlation plots with the corresponding equation for WSS_{mean} b) and WSS_{max} d).

References

[1] *2014 ESC Guidelines on the diagnosis and treatment of aortic diseases,* European Heart Journal **35**, 2873 (2014).

[2] C. J. François, M. Markl, M. L. Schiebler, E. Niespodzany, B. R. Landgraf, C. Schlensak, and A. Frydrychowicz, *Four-dimensional, flow-sensitive magnetic resonance imaging of blood flow patterns in thoracic aortic dissections,* The Journal of Thoracic and Cardiovascular Surgery **145**, 1359 (2013).

[3] M. Cibis, W. V. Potters, F. J. Gijsen, H. Marquering, P. van Ooij, E. vanBavel, J. J. Wentzel, and A. J. Nederveen, *The effect of spatial and temporal resolution of cine phase contrast MRI on wall shear stress and oscillatory shear index assessment,* PLOS ONE **11**, 1 (2016).

[4] B. Stemkens, E. S. Paulson, and R. H. N. Tijssen, *Nuts and bolts of 4D-MRI for radiotherapy,* Physics in Medicine & Biology **63**, 21TR01 (2018).

[5] Z. Stankovic, B. D. Allen, J. Garcia, K. B. Jarvis, and M. Markl, *4D flow imaging with MRI,* Cardiovascular Diagnosis and Therapy **4** (2014).

[6] S. Petersson, P. Dyverfeldt, A. Sigfridsson, J. Lantz, C.-J. Carlhäll, and T. Ebbers, *Quantification of turbulence and velocity in stenotic flow using spiral three-dimensional phase-contrast MRI,* Magnetic Resonance in Medicine **75**, 1249 (2016), https://onlinelibrary.wiley.com/doi/pdf/10.1002/mrm.25698 .

[7] P. van Ooij, A. L. Powell, W. V. Potters, J. C. Carr, M. Markl, and Barker, and Alex J. , *Reproducibility and interobserver variability of systolic blood flow velocity and 3D wall shear stress derived from 4D flow MRI in the healthy aorta,* Journal of Magnetic Resonance Imaging **43**, 236 (2016).

[8] P. Dyverfeldt, M. Bissell, A. J. Barker, A. F. Bolger, C.-J. Carlhäll, T. Ebbers, C. J. Francios, A. Frydrychowicz, J. Geiger, D. Giese, M. D. Hope, P. J. Kilner, S. Kozerke, S. Myerson, S. Neubauer, O. Wieben, and M. Markl, *4D flow cardiovascular magnetic resonance consensus statement,* Journal of cardiovascular magnetic resonance : official journal of the Society for Cardiovascular Magnetic Resonance **17**, 72 (2015), 26257141[pmid].

[9] R. L. F. van der Palen, A. A. W. Roest, P. J. van den Boogaard, A. de Roos, N. A. Blom, and J. J. M. Westenberg, *Scan–rescan reproducibility of segmental aortic wall shear stress as assessed by phase-specific segmentation with 4D flow MRI in healthy volunteers,* Magnetic Resonance Materials in Physics, Biology and Medicine **31**, 653 (2018).

[10] J. F. Juffermans, J. J. Westenberg, P. J. van den Boogaard, A. A. Roest, H. C. van Assen, R. L. van der Palen, and H. J. Lamb, *Reproducibility of aorta segmentation on 4D flow MRI in healthy volunteers,* Journal of Magnetic Resonance Imaging **n/a** (2020), 10.1002/jMRI.27431.

[11] U. Köhler, I. Marshall, M. B. Robertson, Q. Long, X. Y. Xu, and P. R. Hoskins, *MRI measurement of wall shear stress vectors in bifurcation models and comparison with CFD predictions,* Journal of Magnetic Resonance Imaging **14**, 563 (2001), https://onlinelibrary.wiley.com/doi/pdf/10.1002/jMRI.1220 .

[12] P. Papathanasopoulou, S. Zhao, U. Köhler, M. B. Robertson, Q. Long, P. Hoskins, X. Yun Xu, and I. Marshall, *MRI measurement of time-resolved wall shear stress vectors in a carotid bifurcation model, and comparison with CFD predictions,* Journal of Magnetic Resonance Imaging **17**, 153 (2003), https://onlinelibrary.wiley.com/doi/pdf/10.1002/jMRI.10243 .

[13] W. V. Potters, P. van Ooij, H. Marquering, E. vanBavel, and A. J. Nederveen, *Volumetric arterial wall shear stress calculation based on cine phase contrast MRI,* Journal of Magnetic Resonance Imaging **41**, 505 (2015).

[14] J. Sotelo, L. Dux-Santoy, A. Guala, J. Rodríguez-Palomares, A. Evangelista, C. Sing-Long, J. Urbina, J. Mura, D. E. Hurtado, and S. Uribe, *3D axial and circumferential wall shear stress from 4D flow MRI data using a finite element method and a laplacian approach,* Magnetic Resonance in Medicine **79**, 2816 (2018), https://onlinelibrary.wiley.com/doi/pdf/10.1002/mrm.26927 .

[15] S. Petersson, P. Dyverfeldt, and T. Ebbers, *Assessment of the accuracy of MRI wall shear stress estimation using numerical simulations,* Journal of Magnetic Resonance Imaging **36**, 128 (2012).

[16] D. A. Steinman, *Image-based computational fluid dynamics modeling in realistic arterial geometries,* Annals of Biomedical Engineering **30**, 483 (2002).

[17] L. Goubergrits, E. Riesenkampff, P. Yevtushenko, J. Schaller, U. Kertzscher, F. Berger, and T. Kuehne, *Is MRI-based CFD able to improve clinical treatment of coarctations of aorta?* Annals of Biomedical Engineering **43**, 168 (2015).

[18] F. Condemi, S. Campisi, M. Viallon, T. Troalen, G. Xuexin, A. J. Barker, M. Markl, P. Croisille, O. Trabelsi, C. Cavinato, A. Duprey, and S. Avril, *Fluid- and biomechanical analysis of ascending thoracic aorta aneurysm with concomitant aortic insufficiency,* Annals of Biomedical Engineering **45**, 2921 (2017).

[19] J. Abraham, E. Sparrow, and R. Lovik, *Unsteady, three-dimensional fluid mechanic analysis of blood flow in plaque-narrowed and plaque-freed arteries,* International Journal of Heat and Mass Transfer **51**, 5633 (2008), biomedical-Related Special Issue.

[20] B. Berthier, R. Bouzerar, and C. Legallais, *Blood flow patterns in an anatomically realistic coronary vessel: influence of three different reconstruction methods,* Journal of Biomechanics **35**, 1347 (2002).

[21] L. Antiga, M. Piccinelli, L. Botti, B. Ene-Iordache, A. Remuzzi, and D. A. Steinman, *An image-based modeling framework for patient-specific computational hemodynamics,* Medical & Biological Engineering & Computing **46**, 1097 (2008).

[22] Y. C. Fung, *Biomechanics: circulation*, 2nd ed. (Springer, 1997).

[23] J. M. Bland and D. G. Altman, *Measuring agreement in method comparison studies,* Statistical Methods in Medical Research **8**, 135 (1999), pMID: 10501650.

[24] M. Markl, W. Wallis, and A. Harloff, *Reproducibility of flow and wall shear stress analysis using flow-sensitive four-dimensional MRI,* Journal of Magnetic Resonance Imaging **33**, 988 (2011).

[25] K. Y. Chung, G. Belfort, W. A. Edelstein, and X. Li, *Dean vortices in curved tube flow: 5. 3-D MRI and numerical analysis of the velocity field,* AIChE Journal **39**, 1592 (1993).

[26] K. Valen-Sendstad, A. W. Bergersen, Y. Shimogonya, L. Goubergrits, J. Bruening, J. Pallares, S. Cito, S. Piskin, K. Pekkan, A. J. Geers, I. Larrabide, S. Rapaka, V. Mihalef, W. Fu, A. Qiao, K. Jain, S. Roller, K.-A. Mardal, R. Kamakoti, T. Spirka, N. Ashton, A. Revell, N. Aristokleous, J. G. Houston, M. Tsuji, F. Ishida, P. G. Menon, L. D. Browne, S. Broderick, M. Shojima, S. Koizumi, M. Barbour, A. Aliseda, H. G. Morales, T. Lefèvre, S. Hodis, Y. M. Al-Smadi, J. S. Tran, A. L. Marsden, S. Vaippummadhom, G. A. Einstein, A. G. Brown, K. Debus, K. Niizuma, S. Rashad, S.-i. Sugiyama, M. Owais Khan, A. R. Updegrove, S. C. Shadden, B. M. W. Cornelissen, C. B. L. M. Majoie, P. Berg, S. Saalfield, K. Kono, and D. A. Steinman, *Real-world variability in the prediction of intracranial aneurysm wall shear stress: The 2015 international aneurysm CFD challenge,* Cardiovascular Engineering and Technology **9**, 544 (2018).

[27] S. Voß, O. Beuing, G. Janiga, and P. Berg, *Multiple aneurysms anatomy challenge 2018 (match)—phase ib: Effect of morphology on hemodynamics,* PLOS ONE **14**, 1 (2019).

[28] A. M. Malek, R. Jackman, R. D. Rosenberg, and S. Izumo, *Endothelial expression of thrombomodulin is reversibly regulated by fluid shear stress.* Circulation Research **74**, 852 (1994), https://www.ahajournals.org/doi/pdf/10.1161/01.RES.74.5.852 .

[29] S. Verma and S. C. Siu, *Aortic dilatation in patients with bicuspid aortic valve,* New England Journal of Medicine **370**, 1920 (2014), pMID: 24827036, https://doi.org/10.1056/NEJMra1207059 .

[30] A. J. Barker, M. Markl, J. Bürk, R. Lorenz, J. Bock, S. Bauer, J. Schulz-Menger, and F. von Knobelsdorff-Brenkenhoff, *Bicuspid aortic valve is associated with altered wall shear stress in the ascending aorta,* Circulation: Cardiovascular Imaging **5**, 457 (2012), https://www.ahajournals.org/doi/pdf/10.1161/CIRCIMAGING.112.973370 .

[31] Z. Cheng, F. P. P. Tan, C. V. Riga, C. D. Bicknell, M. S. Hamady, R. G. J. Gibbs, N. B. Wood, and X. Y. Xu, *Analysis of flow patterns in a patient-specific aortic dissection model,* Journal of Biomechanical Engineering **132**, 051007 (2010).

[32] D. Liu, Z. Fan, Y. Li, N. Zhang, Z. Sun, J. An, A. Stalder, A. Greiser, and J. Liu, *Quantitative study of abdominal blood flow patterns in patients with aortic dissection by 4-dimensional flow MRI,* Scientific Reports **8** (2018), 10.1038/s41598-018-27249-9.

[33] R. Kadirvel, Y.-H. Ding, D. Dai, H. Zakaria, A. M. Robertson, M. A. Danielson, D. A. Lewis, H. J. Cloft, and D. F. Kallmes, *The influence of hemodynamic forces on biomarkers in the walls of elastase-induced aneurysms in rabbits,* Neuroradiology **49**, 1041 (2007).

[34] M. Alimohammadi, J. M. Sherwood, M. Karimpour, O. Agu, S. Balabani, and V. Díaz-Zuccarini, *Aortic dissection simulation models for clinical support: fluid-structure*

interaction vs. rigid wall models, BioMedical Engineering OnLine **14**, 34 (2015), 25881252[pmid].

[35] P. Rissland, Y. Alemu, S. Einav, J. Ricotta, and D. Bluestein, *Abdominal aortic aneurysm risk of rupture: Patient-specific FSI simulations using anisotropic model,* Journal of Biomechanical Engineering **131** (2008), 10.1115/1.3005200, 031001.

[36] A. J. Geers, I. Larrabide, H. G. Morales, and A. F. Frangi, *Comparison of steady-state and transient blood flow simulations of intracranial aneurysms,* in *2010 Annual International Conference of the IEEE Engineering in Medicine and Biology* (2010) pp. 2622–2625.

[37] Y. Jiang, Y. Qiu, D. Li, D. Yuan, T. Zheng, and L. Peng, *Influence of aortic branch arteries on the hemodynamics of patient-specific type b aortic dissection following TEVAR,* Medicine in Novel Technology and Devices **4**, 100028 (2019).

[38] P. H. Geoghegan, M. C. Jermy, and D. S. Nobes, *A PIV comparison of the flow field and wall shear stress in rigid and compliant models of healthy carotid arteries,* Journal of Mechanics in Medicine and Biology **17**, 1750041 (2017), https://doi.org/10.1142/S0219519417500415 .

3

Modelling of Turbulent Flow in Aorta

In this study, we analyzed turbulent flows through a phantom (a 180° bend with narrowing) at peak systole and a patient-specific coarctation of the aorta (CoA), with a pulsating flow, using magnetic resonance imaging (MRI) and computational fluid dynamics (CFD). For MRI, a 4D Flow MRI is performed using a 3T scanner. For CFD, the standard $k-\epsilon$, shear stress transport $k-\omega$, and Reynolds Stress (RSM) models are applied. A good agreement between measured and simulated velocity is obtained for the phantom, especially for CFD with RSM. The wall shear stress (WSS) shows significant differences between CFD and MRI in absolute values due to the limited near-wall resolution of MRI. However, normalized WSS shows qualitatively very similar distributions of the local values between MRI and CFD. Finally, a direct comparison between in vivo 4D Flow MRI and CFD with the RSM turbulence model is performed in the CoA. MRI can properly identify regions with locally elevated or suppressed WSS. If the exact values of the WSS are necessary, CFD is the preferred method. For future applications, we recommend the use of the combined MRI/CFD method for the analysis and evaluation of the local flow patterns and WSS in the aorta.

This chapter has been published as: R. Perinajová, J. F. Juffermans, J. L. Mercado, J.-P. Aben, L. Ledoux, J. J. M. Westenberg, H. J. Lamb, and S. Kenjereš, Assessment of turbulent blood flow and wall shear stress in aortic coarctation using image-based simulations, BioMedical Engineering OnLine 20 (2021).

3.1 Introduction

Coarctation of the aorta (CoA) is a congenital condition in which the aorta has a narrowing, usually in the thoracic descending aorta distal to the branching arteries of the aortic arch. The narrowing of the artery causes flow acceleration, where a turbulent-like flow may occur during the systolic phase [1]. It has been shown that the transitional and turbulent flow in CoA leads to aberrant blood flow in the narrowing and a vortex-like recirculation pattern distal to the stenosis [2]. Due to the stenosis and onset of turbulence, the wall shear stress (WSS) is also elevated, and the presence of turbulence may cause oscillations of its values [3] This type of flow may cause, among others, degradation of the arterial wall, initialization of an aneurysm, and atherosclerosis [4].

Several studies have assessed the hemodynamics of this pathology using Magnetic Resonance Imaging (MRI) [5, 6]. However, due to the relatively low spatial resolution of MRI, the flow velocity in the proximity of the wall and its derived quantities, such as WSS, may be incorrect [7]. Several recent studies have identified image-based computational fluid dynamics (CFD) to be a good alternative to studying blood flow in CoA [8, 9]. However, these previous studies have not addressed the important effects of locally generated turbulence in CoA, as demonstrated by Gaze et al. [10]. The turbulent flow in CoA has been simulated by using various turbulence modeling approaches: (i) the Reynolds-Averaged Navier-Stokes (RANS) ([11], (ii) Large-Eddy Simulation (LES) [12], and finally, (iii) Direct Numerical Simulation (DNS) [13] methods. The DNS and LES proved to perform very well for transient and turbulent flow regimes for arteries with stenotic regions, [14]. However, because of the huge computational costs associated with the high temporal and spatial resolution requirements of LES and DNS, these approaches are less suitable for clinical applications, [15]. To meet demands on a computationally efficient and sufficiently accurate CFD approach, we propose to employ the unsteady RANS method with an advanced second-order moments-based turbulence model (so-called Reynolds stress model, RSM). The advantage of this model lies in its ability to automatically take into account the exact production terms of the turbulent stresses (which need to be additionally modeled in the eddy-viscosity type of RANS model), as well as to predict turbulence anisotropy (in contrast to the assumption of turbulence isotropy as used in the eddy-viscosity turbulence models), which are important features of a flow in a turbulent regime.

In the present study, we will first introduce a U-bend phantom that mimics the aorta with coarctation and produces numerous flow features observed in vivo. For the phantom, we will perform a detailed comparison between experiments (performed by 4D Flow MRI) and CFD simulations. In addition to the proposed RSM turbulence model, also two widely used eddy-viscosity-based turbulence models will be introduced. We will investigate levels of agreement between CFD and phantom experiments by focusing on the mean flow features and local distributions of the wall shear stress. Finally, we will perform a comparative assessment between CFD simulation (based on the turbulence model, which performed best for the phantom study) and in vivo 4D Flow MRI for the patient-specific pulsating blood flow in CoA.

3.2 Methods

3.2.1 Studied Cases

Phantom

The phantom for this study was a 3D-printed computer-aided design object, mimicking the simplified aorta with coarctation. It represents a 180° bend structure in which obstruction is present in the distal leg, as shown in Fig.3.1a. The three-dimensional U-tube phantom is fabricated from Duraform Flex material with characteristic stiffness of a shore hardness scale of A75, manufactured by Materialise. The phantom can be considered as a rigid structure. To allow magnetic resonance imaging, the 3D U-tube phantom is placed inside a 10 l jerry can, which is filled with Gelatin. Gelatin is used instead of water to prevent the movement of the liquid due to the sound produced by the MRI system. The exact composition of the Gelatin is 9.9 l water, 600 g Gelatin, 100 ml paraben, and 1.5 ml Gadovist. The jerry can has two connectors to allow connection with the tubes through which the liquid will be pumped. A constant throughput is provided using a pump connected to the inlet tube with a prescribed flow of $\dot{Q}_0$ = 4.5 l/min. Additional morphometric and flow characteristics of the studied phantom can be found in Tab. 3.1.

Table 3.1: Morphometric, numerical mesh, and flow characteristics (showing the estimated thickness of boundary layer, Womersley number - Wo, inlet Reynolds number - Re_0, and stenotic Reynolds number - Re_{st}) for the phantom and the patient with coarctation (CoA). Note that δ_1 and δ_2 are the estimated transient boundary layer thickness ($\delta_1 = \sqrt{\nu/\omega}$) and averaged boundary layer thickness ($\delta_2 = \sqrt{\nu D_0/U}$), respectively, [16].

	Phantom	**Patient with CoA**
Morphometric Characteristics		
D_0 [cm]	2.10	1.82
D_{st}/D_0 [-]	0.62	0.60
Mesh Details		
Bulk max. element size [mm]	0.80	0.75
1^{st} prism element thickness [mm]	0.05	0.05
Exponential Growth Factor	1.20	1.20
Number of Prism Layers	10	10
Flow Characteristics		
δ_1 [mm]	-	0.06
δ_2 [mm]	0.32	0.23
Re_0 [-]	4,539	6,276
Re_{st} [-]	7,332	11,425
Wo [-]	-	28.87

Patient-specific Aorta with Coarctation

This study protocol was approved by the Medical Ethics Committee of the Leiden University Medical Center (P14.095), and informed consent was signed by both parents/guardians of the subject. The patient with CoA included in this study was female, 14.5 years old, 164cm, 51,9 kg, and had a tricuspid aortic valve. The final geometry includes both thoracic and abdominal aorta (AbAo) with six branching arteries: Brachiocephalic Trunk (BT), Left Common Carotid Artery (LCCA), Left Subclavian Artery (LSA), Celiac Trunk (CT), and

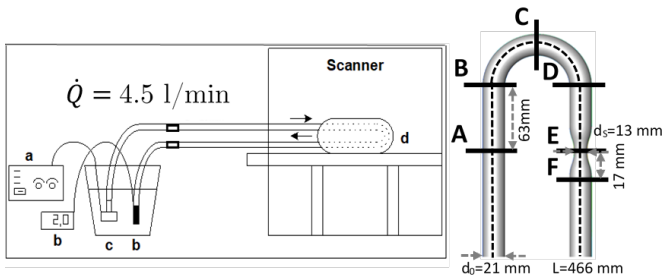

(a) Phantom experimental setup (-left) with geometrical details (-right).

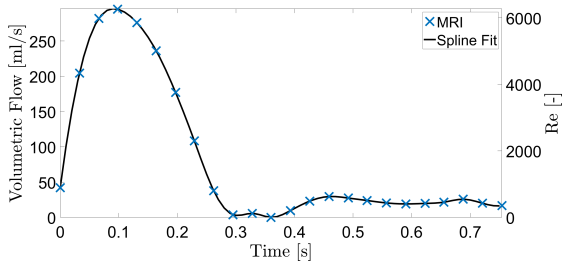

(b) The simulated cardiac cycle of the patient-specific CoA.

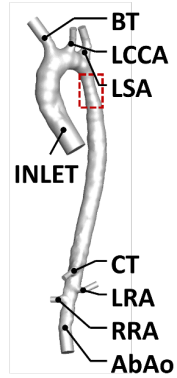

(c) The CoA geometry.

Figure 3.1: (a) Phantom experimental setup (-left) with: variable power source (**a**), flow indicator (**b**), submersible pump (**c**), flow phantom in the MRI scanner (**d**), and the phantom geometry (-right) represented with the main diameter d_0, stenotic diameter d_S, and total length of L; (b) The mass flow rate at the inlet of the patient-specific aorta with coarctation (CoA) from MRI and the fitted spline; (c) The patient-specific CoA with a highlighted position of narrowing (in red), inlet, and branching arteries: Brachiocephalic Trunk (BT), Left Common Carotid Artery (LCCA), Left Subclavian Artery (LSA), Celiac Trunk (CT), Left Renal Artery (LRA), Right Renal Artery (RRA), and the rest of the Abdominal Aorta (AbAo).

Left/Right Renal Artery (L/RRA) (visualized in Fig.3.1c. Additional morphometric and flow characteristics of the studied CoA can be found in Tab. 3.1.

3.2.2 Magnetic Resonance Imaging

For both the phantom and patient-specific CoA, 4D flow MRI was performed on a 3T MRI system (Ingenia, Philips Healthcare, Best, The Netherlands). For the patient-specific CoA, an aortic 4D flow MRI was performed using a hemidiaphragm respiratory navigator with retrospective electrocardiogram gating without echo-planar imaging. Additional information about the MRI sequences can be found in Tab. 3.2.

The acquired 4D-flow MRI data sets were afterward analyzed using CAAS MR Solutions v5.0 (Pie Medical Imaging BV, Maastricht, The Netherlands). The analysis is similar for both phantom and patient-specific CoA and the most important differences are highlighted. In both, the analysis was initialized by the manual placement of starting and ending points.

Table 3.2: Details of MRI sequence for phantom and patient with aortic coarctation.

	Phantom	Patient-specific CoA
Heart rate [bpm]	60 (simulated)	80
Velocity encoding [cm/s]	70	
Echo time [ms]	5.5	2.3
Repetition time [ms]	11	4.1
Reconstructed phases [-]	20	24
Flip angle [°]	7	10
Field of view [mm^3]	-	350×350×52.5
Acquired spatial resolution [mm^3]	1.5×1.5×1.5	2.5×2.5×2.5
Reconstructed spatial resolution [mm^3]	0.7×0.7×1.5	1.5×1.5×2.5
Echo planar imaging factor (anterior-posterior direction)	5	-
Sense factor (anterior-posterior direction)	2	2
Acquisition time (without respiratory compensation) [min]	-	5.8

For the phantom, the two points were placed at the same level in the opposite legs, whereas for the patient-specific CoA, the starting point was placed in the aortic root, and the ending points were placed in the abdominal aorta and the six branching arteries. A phase-specific 3D volume was automatically segmented for the specific phase and copied to all phases. The 3D segmentation uses a deformable model algorithm that recursively optimizes the location of the surface towards the vessel luminal boundary based on image gradients extracted from the appropriate phase within the 4D flow MRI data while simultaneously maintaining local smoothness of the 3D segmented surface, [17]. Manual delineation of the vessel lumen boundary was applied with the available adaptation tool from the software in case of segmentation incorrectness for the patient-specific CoA.

3.2.3 CFD Model

Numerical Mesh

To perform CFD simulations of the patient-specific aorta geometry (obtained from 4D Flow MRI segmentation using CAAS MR Solutions v5.0), we first used Vascular Modeling Toolkit for the geometry reconstruction, [18]. To check the sensitivity of CFD results on the imposed levels of geometry smoothing, we have used the rough (CFD_{rough}) (i.e., by using a Taubin filter with 100 iterations and passband settings of 0.4), and the smoothed geometry (CFD_{smooth}) (i.e., by using a Taubin filter with 100 iterations and passband settings of 0.01). For both geometries, cylindrical extensions were added at all outlets with a length of $1.5d_0$ (where d_0 is the diameter of the individual blood vessel where the outlet is located). For both phantom and patient-specific aorta simulations, we have employed a hybrid numerical mesh containing prismatic elements in the proximity of the wall (to resolve characteristic boundary layers properly), while the tetrahedrons were used in the central part of the domain. Details about the mesh sizing are shown in Tab. 3.1.

We have performed a mesh-independency study, and the final numerical mesh for the phantom case was approximately 14 million control volumes, while approximately 7 million control volumes were used for the aorta case. Note that the larger number of control volumes for the phantom geometry was due to the addition of a segment with a length of $10d_0$ to have a proper capture of the post-stenotic flow region (not shown in Fig.

3.1a).

Governing Equations

Since we are dealing with a fully (the phantom case) or a partially (the aorta case) developed turbulent flow regimes, we adopt an unsteady RANS approach to model turbulence. We apply three different classes of turbulence models: two based on the eddy-viscosity concept (standard $k-\epsilon$ and shear-stress transport (SST) $k-\omega$ model), and an advanced turbulence model based on solving a complete set of turbulent stress components (the full RSM). Despite its superior theoretical foundation when compared to the eddy-viscosity turbulence models [19], applications of the RSM model are very scarce in bio-medical flow applications. Here we propose the use of the RSM as an alternative to a high-fidelity DNS or LES approach. The following set of governing equations is introduced for the above-mentioned turbulence models:

- the standard eddy-viscosity $k-\epsilon$ model with enhanced wall treatment, [20]: PDEs for $(U_i - p - k - \varepsilon)$
- the low-Reynolds Shear Stress Transport (SST) $k-\omega$ model, [21]: PDEs for $(U_i - p - k - \omega)$
- the Reynolds Stress Model (RSM) with the linear pressure strain term and enhanced wall treatment, [22]: PDEs for $(U_i - p - \overline{u_i u_j} - \varepsilon)$

where U_i is the velocity vector, p is the pressure, k is turbulent kinetic energy, ε is dissipation rate, ω is turbulent frequency, and $\overline{u_i u_j}$ is turbulent stress tensor.

Boundary and Initial Conditions

For the phantom, the imposed volumetric flow rate of 4.5 l/min is identical to the experimental conditions and corresponds to the inlet Reynolds number of $Re = 4539$ ($Re = V_0 \cdot D_0/\nu$). For the patient-specific aorta, the time-dependent inlet conditions are matched with MRI measurements during the entire cardiac cycle. We have extracted the measured volumetric flow rate at the inlet plane (Q_0) and converted it to the characteristic mass flow rate ($\dot{m} = Q_0 \cdot \rho_{\text{blood}}$). The mass flow rates were fitted with a smooth spline with piecewise polynomial (with a smoothing parameter $p = 0.99999947$ and $R^2 = 0.9995$), Fig.3.1b, which gives the following range of the inlet Reynolds number, $0 \leq Re \leq 6276$, and corresponding Womersley number of $Wo = D_0 \left(\omega_f/\nu\right)^{1/2} = 29$. In total, we have simulated five cardiac cycles to obtain results without the influence of initial conditions. Only the last cycle was used for the analysis. For all turbulence parameters, the uniform inlet values were imposed with the following specifications: the intensity of turbulence of 5%, the ratio of turbulent and molecular viscosity (μ_t/μ) of 10, the isotropic assumption of normal turbulent stress components ($\overline{u_i u_i} = 2/3k$), and zero values of the turbulent shear stress components ($\overline{u_i u_j} = 0$). At outlets, a zero diffusion flux was imposed for all transport variables. For the patient-specific aorta, a pre-defined fixed (MRI-based) percentage of the inlet flow rate was prescribed. The no-slip velocity boundary condition was imposed on the walls of blood vessels, and the model was assumed to be rigid.

Physical Properties and Simulation Setup

For the phantom, water was used as a working fluid (ρ = 998 kg/m^3, μ = 1.003 mPa·s). For the aorta, the real blood properties were assumed for the simulations (ρ = 1060 kg/m^3, μ = 3.5 mPa·s). It was previously demonstrated that the assumption of constant blood viscosity is adequate for aortic blood simulations, [23]. The simulations were performed using Ansys Fluent 19.1 (Ansys Inc., Canonsburg, Pennsylvania, USA) with the following simulation settings:

- Solver - pressure based
- Pressure-Velocity Coupling - SIMPLE
- Spatial discretization
  - Gradient - Least Squares Cell-Based
  - Pressure - Second Order
  - Momentum - Second-Order Upwind
  - Turbulence Variables - Second-Order Upwind
- Temporal discretization (CoA case)
  - fully implicit second-order scheme
  - time step Δt = 0.0005s
- Residuals (all)- 10^{-5}

3.2.4 Analysis

Downsizing and Mapping

For additional analysis and voxel-to-voxel comparison, the phantom CFD velocity data were down-sampled by applying a bilinear interpolation on two different equidistant meshes (DCFD):

- $\text{DCFD}_{0.7\times0.7\times1.5}$: voxel resolution $0.7 \times 0.7 \times 1.5$ mm^3 (identical to MRI)
- $\text{DCFD}_{0.2\times0.2\times0.2}$: voxel resolution $0.2 \times 0.2 \times 0.2$ mm^3

Both downsized CFD velocity fields were analyzed using CAAS MR Solutions v5.0 (Pie Medical Imaging BV, Maastricht, The Netherlands) to obtain WSS. Additionally, the WSS distribution along the vessel walls was mapped on a 2D surface where the horizontal axis indicates the non-dimensional radial distance from the vessel centerline ($-\pi \leq r \leq +\pi$), and the vertical axis indicates the non-dimensional arc length of the vessel ($0 \leq l/l_0 \leq 1$). This mapping was done by an originally developed in-house tool in Matlab R2019a (MathWorks, Inc., Natick, Massachusetts, U.S.A.). This approach has provided an easy and objective comparison between different results.

Vorticity Calculation

Vorticity ($\boldsymbol{\omega}$) was calculated from MRI-based velocity components using Matlab R2019a (MathWorks, Inc., Natick, Massachusetts, U.S.A.) as

$$\boldsymbol{\omega} = \nabla \times \boldsymbol{u} \tag{3.1}$$

where $\boldsymbol{u}$ is the velocity vector. In the numerical procedure, the partial derivatives were calculated using a central differencing scheme for the interior points and a single-sided (forward) difference scheme for the edges.

Wall Shear Stress Calculation

The WSS for MRI and the downsized CFD data sets were calculated based on the extracted velocity profile perpendicular to the phase-specific segmented 3D surface using CAAS MR Solutions v5.0. After factorizing the velocity profile into its component parallel to the lumen wall, WSS was computed by the first derivative of a quadratic approximation of that velocity profile at the location of the lumen wall as

$$\tau_w = \mu \frac{\partial U_{\parallel}}{\partial n}\bigg|_{\text{wall}} \tag{3.2}$$

where $U_{\parallel}$ is the wall-parallel velocity component and n is the wall-normal direction. For the CFD simulations involving turbulence models, the wall shear stress is directly available from calculations of the wall-parallel velocity component based on the enhanced wall treatment:

$$\tau_w = \rho u^* u_\tau \tag{3.3}$$

where u^* is the friction velocity, and u_τ is the wall friction velocity. The u^* is blended between the viscous sub-layer and logarithmic region as

$$u^* = \left[\left(\frac{\mu U_{\parallel}}{\Delta y} + C_\mu^{1/2} \rho k \right) \frac{1}{\rho} \right]^{1/2} \tag{3.4}$$

and u_τ is blended as [24]

$$u_\tau = U_{\parallel} \left[\left(u^+_{lam} \right)^{-4} + \left(u^+_{turb} \right)^{-4} \right]^{1/4} \tag{3.5}$$

3.3 Results

3.3.1 Phantom

4D-flow MRI Flow Rate

The volumetric flow rate was extracted from eleven different locations distributed evenly along the length of the phantom using CAAS MR Solutions v5.0 to test the performance of the MRI acquisition. We calculated the error between the set inlet volumetric flow Q_0 and the flow extracted at the different cut planes Q_i. The average error in flow rate was $0.25 \pm 2.11\%$.

Comparison of Turbulence Models

Next, we moved toward a detailed comparison of the MRI and CFD simulations performed with various turbulence models by comparing the non-dimensional velocity (v/v_0, where v_0 is the mean inlet velocity) magnitude profiles at six characteristic locations: inlet (A), the start of the bend (B), middle of bend (C), end of the bend (D), middle of narrowing (E), and distal to narrowing (F), as shown in Fig.3.2 and Fig.3.3. The differences between the models emerge in the middle of the bend, i.e., at location C. This location is particularly sensitive due to the generation of the secondary flows (Dean vortices) and flow acceleration along the outer wall curvature. Additionally, at the post-stenotic location (location F), numerical simulations captured well the recirculation region; however, the $k-\varepsilon$ model underestimated the velocity magnitude in the center, whereas both SST and RSM models are showing a very good agreement with MRI in the wall vicinity, with a slight overprediction in the center.

The observed changes in the distributions of the velocity profiles for CFD with considered turbulence models are due to different predictions of turbulence levels. To illustrate this, we plot a series of the profiles of the non-dimensional turbulent kinetic energy (k/v_0^2) at identical locations as previously analyzed for the velocity profiles (locations A-F), Figs.3.3a-3.3f. All turbulence models give similar profiles at inlet segment location (A), with almost identical values in the center and symmetrical peak values in the proximity of the wall, and are in good agreement with the previously reported results [25]. The symmetrical distribution is, with elevated turbulence levels in the proximity of the outer wall, due to the presence of the bent (B-D). It is interesting to note that in the center of stenosis (location E), despite a big over-prediction of turbulent kinetic energy by the $k-\varepsilon$ model, resulting velocity magnitudes still agree very well due to the dominance of convective term in the momentum equation (due to a sudden flow acceleration). Finally, it can be seen that the post-stenotic region (location F) is characterized by the highest levels of turbulence caused by combined effects of a flow acceleration. (in the center) and flow recirculation (in the wall proximity).

Voxel-to-Voxel Velocity and Vorticity Comparisons

As the next step, we will compare in more detail (voxel-to-voxel) the results of CFD (with the best-performing turbulence model, RSM) against MRI. The contours of the velocity magnitude in the central horizontal cross-section (y = 0) are shown in Fig.3.4. Here we present the velocity magnitude distribution on the original CFD resolution (CFD), downsized CFD resolution (DCFD, where downsizing is done to match original MRI resolution), original measurements (MRI), and the absolute difference between downsized CFD and MRI (DCFD-MRI), respectively. It can be seen that an overall good agreement is obtained between DCFD and MRI and that the most salient flow features are well captured with both techniques. The small deviations are located in the proximity of the walls (in the curved part) and central stenotic and post-stenotic regions.

To compare secondary flow patterns, we plot the contours of the out-of-plane vorticity component for all cases at characteristic selected cross-sections (A-F), Fig.3.5. Note that the out-of-plane vorticity component (defined in here adopted coordinate system as $\omega_x = \partial w/\partial y - \partial v/\partial z$) is a sensitive flow parameter since it captures gradients of both velocity components in the particular plane perpendicular to the flow direction. At the inlet segment

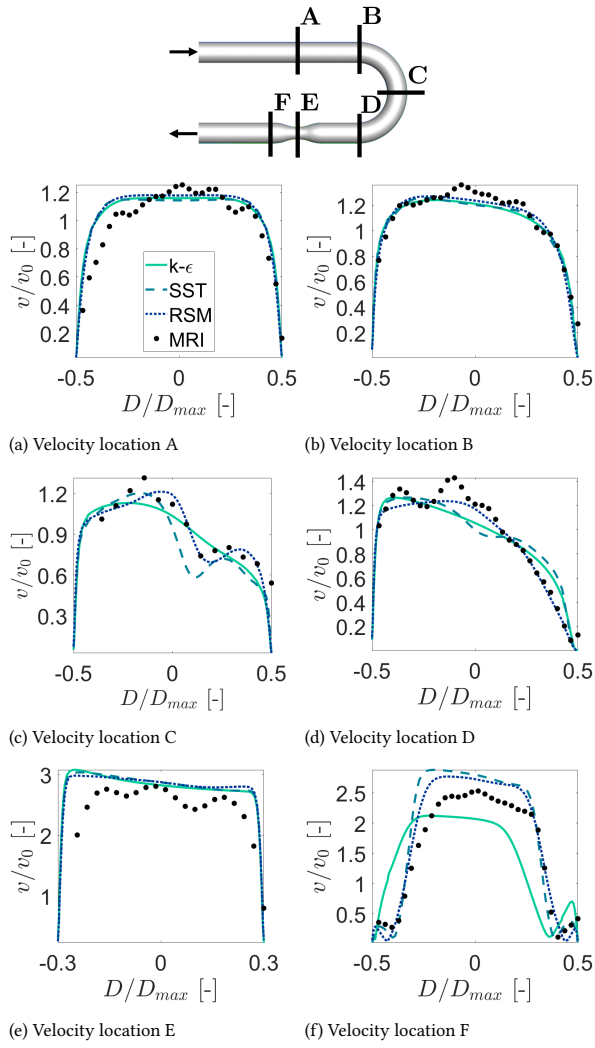

(a) Velocity location A

(b) Velocity location B

(c) Velocity location C

(d) Velocity location D

(e) Velocity location E

(f) Velocity location F

Figure 3.2: Comparison of measured (4D Flow MRI) and simulated (CFD) normalized velocity magnitude (v/v_0, where v_0 is the mean inlet velocity) profiles at characteristic locations along the bend tube (A-F) (profiles extracted in the middle). The lines indicate various turbulence models: standard $k-\varepsilon$, SST (Shear Stress Transport), and RSM (Reynolds Stress Model), respectively.

location (A), there should not yet be any significant appearance of the secondary motions, as confirmed by CFD and DCFD results. The MRI contours show a more noisy distribution, but their levels are relatively small. By entering the bend curvature (location B), the vorticity starts to be generated. Here, due to limited spatial resolution, the MRI just partially captures some of the secondary flow features. The agreement is much better at the most interesting location in the center of the bend (location C), where all cases captured the well-detailed structure of the Dean vortices. The traces of Dean vortices are still visible at the end of

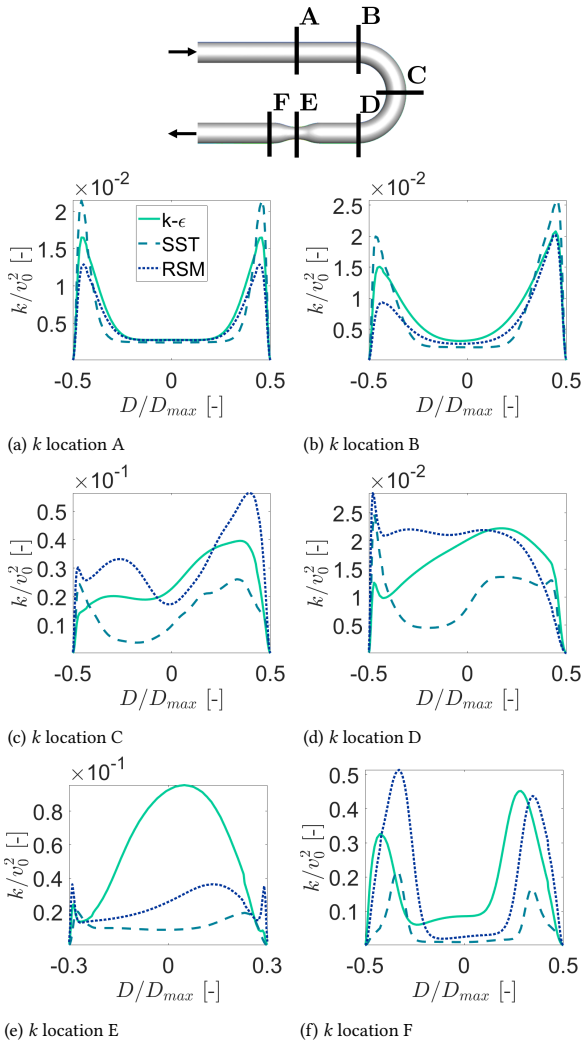

(a) k location A (b) k location B

(c) k location C (d) k location D

(e) k location E (f) k location F

Figure 3.3: Comparison of turbulent kinetic energy k/v_0^2 profiles at characteristic locations along the bend tube (A-F) (profiles extracted in the middle). The lines indicate various turbulence models: standard $k-\varepsilon$, SST (Shear Stress Transport), and RSM (Reynolds Stress Model), respectively.

the curved bend (location D), where a satisfactory agreement between CFD and MRI is obtained. A similar level of agreement is also obtained in the stenosis center (location E). Some visible deviations are observed in the post-stenotic region (location F), where the differences in vorticity magnitude are more pronounced.

Wall Shear Stress

The contours of the wall shear stress along the phantom walls for the original CFD (obtained with the RSM turbulence model), downsized CFD results ($DCFD_{0.2\times0.2\times0.2}$ and

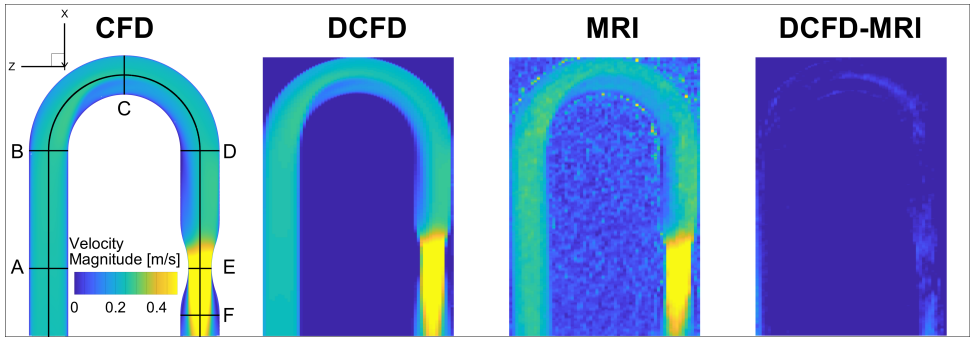

Figure 3.4: The contours of the velocity magnitude ($|v|$) in the central horizontal plane for CFD (original resolution), DCFD (downsized resolution), and MRI (original resolution), where the last contour indicates the absolute difference between DCFD and MRI.

$DCFD_{0.7\times0.7\times1.5\ mm^3}$), and original MRI are shown in Fig.3.6a. To provide a complete distribution of the WSS along the phantom wall, we generated two-dimensional maps of WSS, where the horizontal coordinate represents the non-dimensional circumference (expressed in angles, $-\pi \le r \le +\pi$, where $r = 0$ indicates the inner curve and $r = \pm\pi$ indicate the outer phantom curve), while the vertical coordinate represents the non-dimensional enveloped arc length of the phantom ($0 \le l/l_0 \le 1$, where 0 and 1 correspond to the start and the end of the phantom, and l_0 is the centerline length), Fig.3.6b. The non-dimensional WSS maps (WSS/WSS_{mean}, where WSS_{mean} indicates the spatially-averaged WSS over the entire phantom surface, given in Tab.3.3) are shown in Fig.3.6c. Finally, profiles of the circumferentially averaged non-dimensional WSS are shown in Fig.3.7.

The agreement between CFD and MRI is good in the inlet leg of the phantom. The differences emerge in the bent and stenotic regions. Here, with the decreasing resolution, the absolute values of WSS decrease. It can be seen that all cases predicted high values of WSS in the stenotic region (within the dashed lines), but lowering the spatial resolution of the CFD results and MRI produced a slight shift of the location where WSS reached its maximum value.

Table 3.3: The maximal values of WSS during peak systole in the stenosis (WSS_{st}), spatially averaged values of WSS during peak systole (WSS_{mean}) and its standard deviation for the simplified phantom for MRI, $DCFD_{0.7\times0.7\times1.5mm^3}$, $DCFD_{0.2\times0.2\times0.2mm^3}$, original CFD, and the peak shift (normalized by the inlet diameter d_0) in MRI and downsized CFD (in respect with the original CFD).

	WSS_{st} [Pa]	WSS_{mean} [Pa]	Standard Deviation [Pa]	Peak Shift* [-]
MRI	0.60	0.18	0.09	$0.39d_0$
$DCFD_{0.7\times0.7\times1.5mm^3}$	1.10	0.25	0.17	$0.22d_0$
$DCFD_{0.2\times0.2\times0.2mm^3}$	2.35	0.45	0.41	$0.11d_0$
CFD	4.99	0.68	0.80	-

* The shift is calculated with respect to the original resolution CFD.

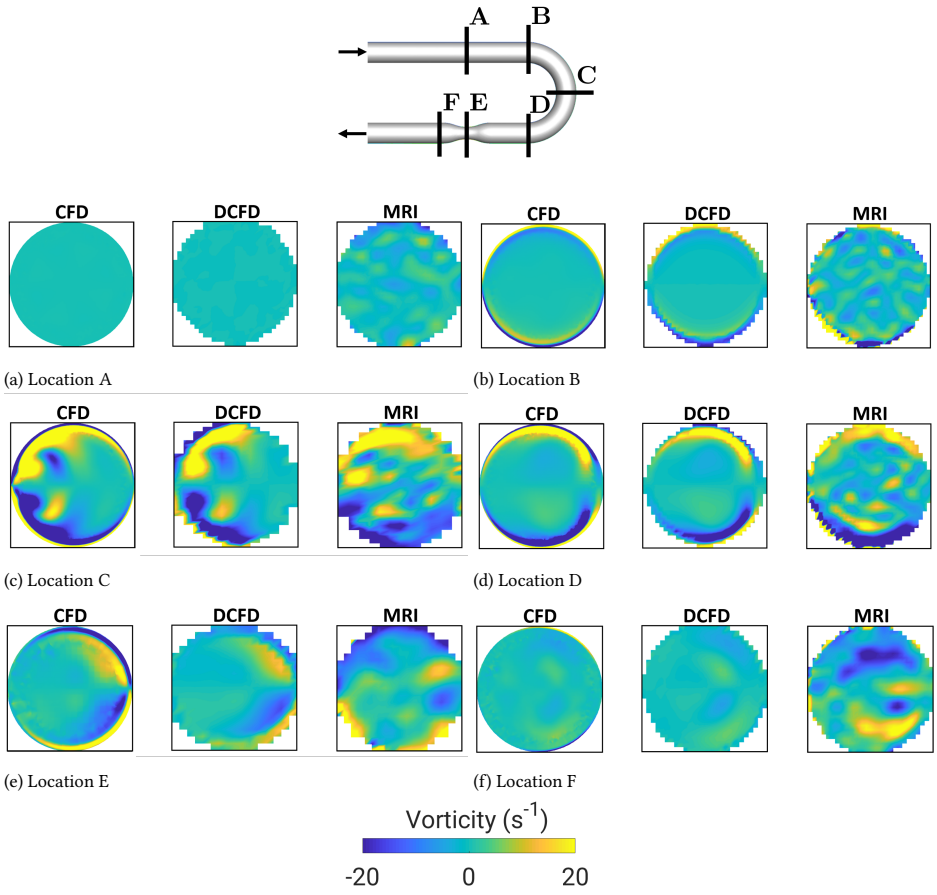

Figure 3.5: The contours of the out-of-plane vorticity component at selected cross-sections (A-F) - comparison of CFD (original spatial resolution), DCFD (downsized spatial resolution), and MRI.

3.3.2 Patient-specific CoA: In Vivo MRI and CFD based on RSM turbulence model

After demonstrating that CFD with the RSM turbulence model was sufficient to predict the characteristic flow features in the phantom, we next moved to the patient-specific aorta geometry with coarctation, for which in vivo 4D Flow MRI measurements are available, Fig.3.1c. The resulting flow pattern, presented in the form of stream traces colored by the velocity magnitude at the peak systole, is shown in Fig.3.8a. It can be seen that a good agreement between MRI and CFD is obtained in capturing important flow features: a strong helical pattern in the aortic arch and sudden flow acceleration in the coarctation. A summary of the direct comparison between CFD and MRI in predicting the peak and spatially averaged (mean) values of the WSS is provided in Table 3.4. It can be seen that in vivo MRI underestimated the local values of WSS, similar to our previous findings in the phantom geometry. The effect of the surface smoothing revealed relatively small

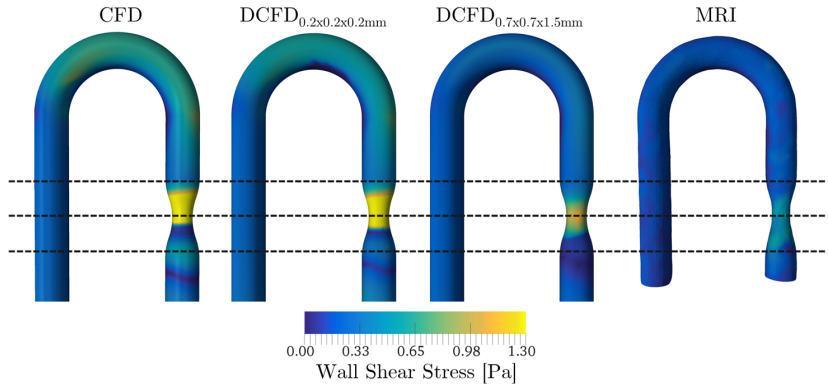

(a)

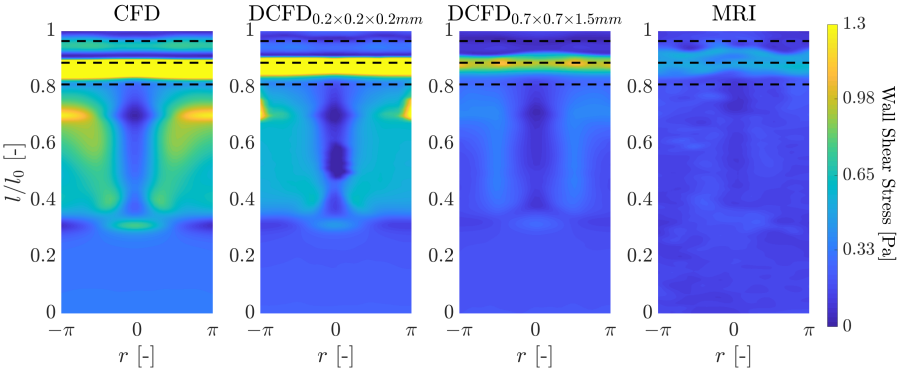

(b)

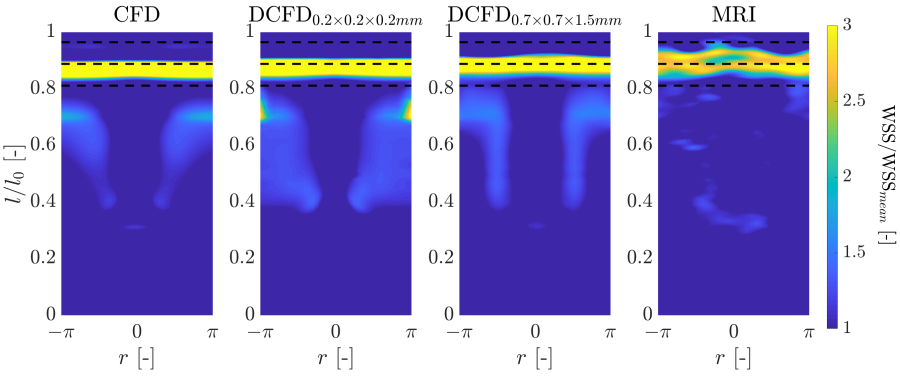

(c)

Figure 3.6: (a) The contours of the WSS at the phantom surface: CFD (original), DCFD (downsized), and MRI results; (b) The two-dimensional representation of the WSS at the phantom surface; (c) The two-dimensional map of the normalized WSS (WSS/WSS_{mean}), where WSS_{mean} is a spatially averaged mean WSS calculated for each modality.

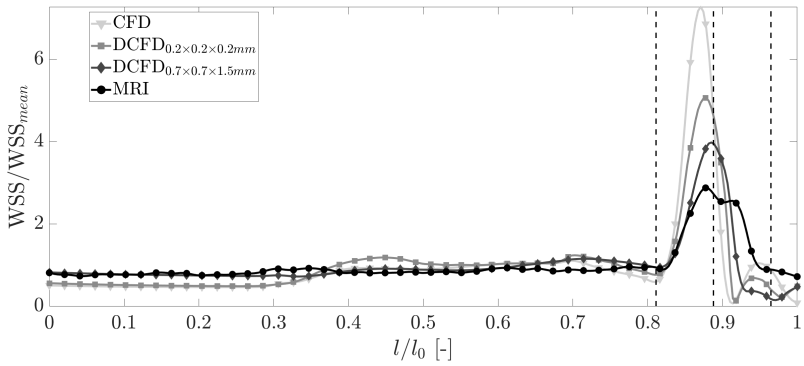

Figure 3.7: Profiles of the non-dimensional circumferentially averaged wall shear stress (WSS/WSS$_{\text{mean}}$) obtained from original and downsized CFD results and MRI.

differences between the rough and smoothed geometries. Note that present CFD results agree well with similar numerical studies reported in the literature, e.g., [26–28] Instead of focusing on the local differences in WSS from MRI and CFD in their absolute terms, we proceed with qualitative comparisons between simulations and experiments by identifying regions along aorta walls characterized by locally elevated or lowered values of WSS to their spatially averaged mean values (averaged over the entire aorta wall). The contours of the non-dimensional WSS distribution (WSS/WSS$_{\text{mean}}$) for CFD (both rough and smoothed geometry) and MRI are given in Fig.3.8b. It can be seen that an overall good agreement is obtained, especially when considering the smoothed CFD and MRI distributions in the coarctation and the descending part of the aorta. This is additionally illustrated by showing 2D maps of the local non-dimensional WSS, where the entire surface of the aorta wall is mapped, Figs.3.8c and 3.8d. The blank spaces in the mapped surfaces represent the branching arteries that were removed during the mapping procedure. Due to the proximity of the first two branching arteries (i.e., Brachiocephalic Trunk and Left Common Carotid Artery), they are merged on the mapped surface.

Finally, the scatter plots (symbols) and circumferentially averaged non-dimensional WSS profiles (lines) are shown in Fig.3.9. Similar to comparisons in the phantom geometry, qualitatively good agreement is obtained with distinct peak values in the coarctation. A shift in the location of the maximal WSS for the MRI is also observed. Note that larger peaks of WSS from CFD at $l/l_0 = 0.9$ locations are due to the secondary side branches of the aorta, which are not properly resolved in MRI.

3.4 Discussion

The present study investigated the flow and WSS for a specific aorta pathology - aortic coarctation - using a combined 4D Flow MRI and CFD techniques for simplified (phantom) and patient-specific geometry. For both studied geometries, the flow is in a fully (phantom) or a partially developed (CoA) turbulent regime. The importance of selected turbulence models for CFD is demonstrated by performing a comparative assessment between two

Table 3.4: The maximal values of WSS in the stenosis (WSS_{st}), mean values of WSS (WSS_{mean}) and its standard deviation of the patient-specific Aortic Coarctation (without branches) for MRI, CFD, smoothed CFD (CFD_{sm}), and the peak shift normalized by the inlet diameter d_0 in MRI with respect to CFD_{sm}.

	WSS_{st} [Pa]	WSS_{mean} [Pa]	Standard Deviation [Pa]	Peak Shift* [-]
MRI	7.73	2.12	0.97	$0.52d_0$
CFD	48.95	15.06	12.43	-
CFD_{sm}	45.87	14.00	10.00	-

* The shift is calculated with respect to CFD_{sm}.

types of eddy-viscosity models and RSM for the phantom configuration.

3.4.1 Comparison of Turbulence Models with MRI

The differences in the cross-section averaged velocity magnitude profiles (at A-F locations) between MRI and CFD with the RSM model did not exceed 15% in the stenotic region and 7% in the rest of the phantom. In contrast, the maximum disagreement between CFD with the $k-\varepsilon$ model and MRI was 45% for the post-stenotic region, while this disagreement reached 18% in the stenotic region for the SST model. The overall best performances of the RSM turbulence models can be explained in terms of the theoretical foundation behind this model. The exact treatment of production terms of the individual turbulent stress components plays a crucial importance in complex three-dimensional flows (e.g., the curved part of the phantom followed by a stenotic region) as presented here. In comparison with the eddy-viscosity models, the RSM predicts well the secondary motions and captures well flow adaptation to sudden changes of the cross-sectional area, [19]. This was also shown in terms of streamwise velocity and turbulent kinetic energy in a 60° bend tube [29], where RSM performed best in comparison to other commonly used eddy-viscosity models. Especially for turbulent kinetic energy, while the eddy-viscosity models tend to under-predict the DNS-based values, RSM can capture the behavior better. We have also shown this in our results, where RSM-based turbulent kinetic energy showed slightly higher peaks in the curved part of the phantom. Based on this and the direct comparison of performances of turbulence models with MRI measurements in the phantom, we conclude that the RSM turbulence model is the most suitable to capture the most important flow features properly. Additionally, in terms of computational efficiency, although a larger number of transport equations needs to be solved by the RSM turbulence model when compared to the eddy-viscosity-based models, its computational costs are still much smaller when compared to high-fidelity LES or DNS methods (i.e., $\mathcal{O}(10^2 - 10^3)$ faster, respectively), which makes it a good choice for patient-specific clinical applications.

3.4.2 Wall Shear Stress Based on CFD and MRI

Two main points need to be addressed when comparing simulations (CFD) and experiments (MRI): (i) the absolute values of the WSS, and (ii) the local distributions of the WSS, respectively. Generally, we observed consistently lower values of WSS from MRI in comparison to CFD results. This can be explained in terms of the lower spatial resolution of MRI - especially in the proximity of the wall. The absolute values of the spatially-averaged WSS_{mean} from CFD simulations for the phantom are 3.7× (CFD), 2.5× ($DCFD_{0.2\times0.2\times0.2mm^3}$), and 1.4×

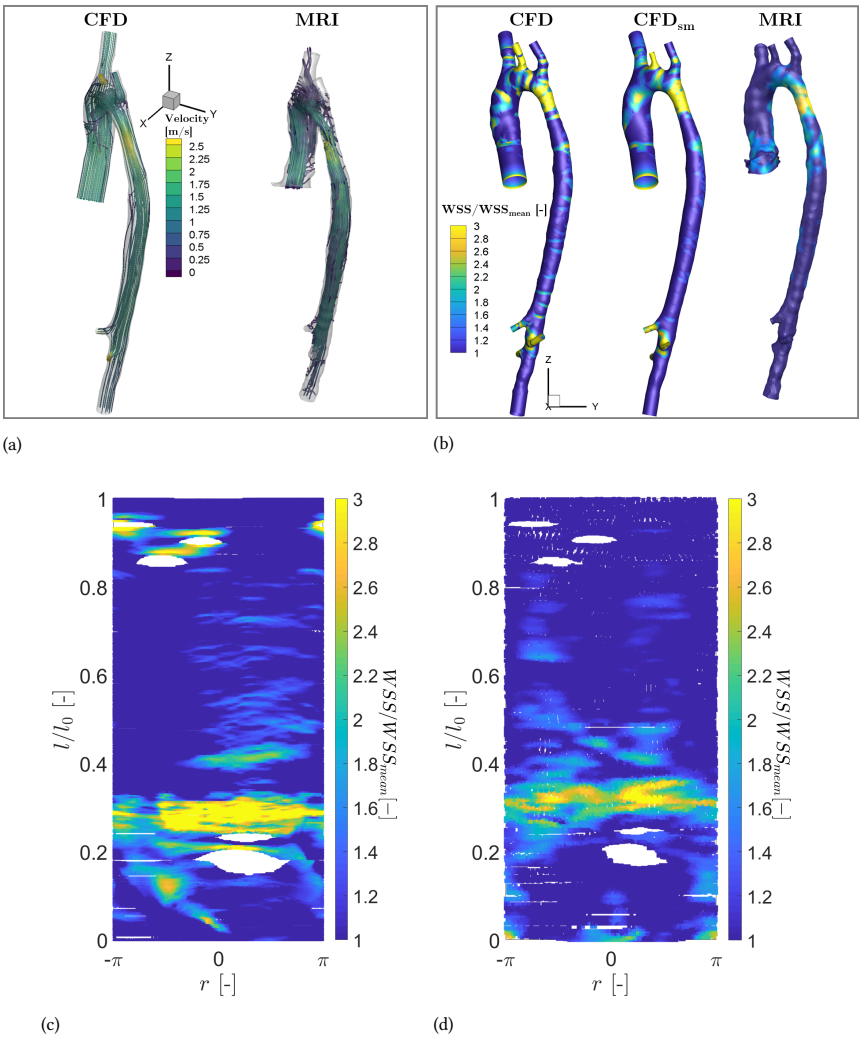

Figure 3.8: The patient-specific CoA case: The stream traces colored by the velocity magnitude at the peak systole for CFD and 4D Flpw MRI (a); The contours of the non-dimensional WSS (WSS/WSS$_{mean}$) at the aorta wall (b); The 2D map of WSS distribution for CFD$_{sm}$ (c) and 4D Flow MRI (d).

(DCFD$_{0.7\times0.7\times1.5mm^3}$) higher than the MRI values, respectively. Similarly, the peak WSS in the stenotic region (WSS$_{st}$) for CFD simulations are 8.3× (CFD), 3.9× (DCFD$_{0.2\times0.2\times0.2mm^3}$), and 1.83× (DCFD$_{0.7\times0.7\times1.5mm^3}$) higher than the MRI values. Note that the stenotic region is the most sensitive one due to a sudden flow acceleration, and a reduction of the number of voxels (since the spatial resolution of MRI is fixed). In contrast, the CFD wall resolution in this region is increased since the identical number of control volumes for the healthy segment is now distributed over the reduced area of the stenotic cross-section. It can be seen that the reduction of spatial resolution of CFD lowers values of WSS. A similar

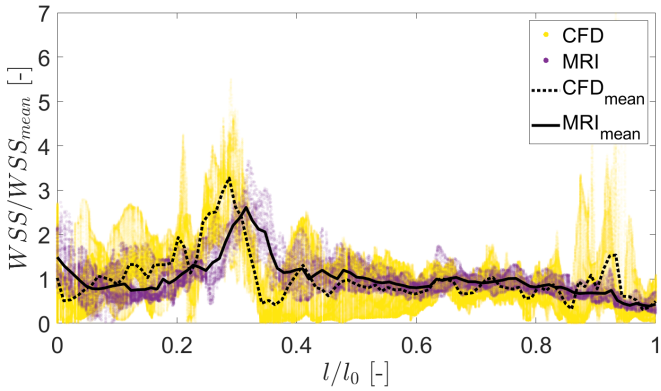

Figure 3.9: Circumferentially averaged profiles (lines) of the non-dimensional WSS for 4D Flow MRI and CFD_{sm}.

systemic undersolving of WSS by MRI was also reported in [7].

In contrast to the absolute values of WSS, the local distributions of WSS calculated from CFD and measured by MRI exhibit more similarities. To illustrate this, we scaled the local WSS with the spatially averaged mean WSS (WSS_{mean}) of each modality, as shown in Fig.3.6c. This approach enables us to compare variations of WSS associated with locally elevated or suppressed distributions for the reference averaged value. The circumferentially averaged mean WSS profiles, shown in Fig.3.7, show a good agreement except at the stenotic region. It can be seen that the reduction of spatial resolution of CFD reduced the peak values but also introduced a shift of the peak location. Similar behavior was also shown in a related study of [30], but these findings were not addressed. This shift should be taken into account when analyzing cases where the exact location of the peak WSS is of importance.

3.4.3 Effect of Assumptions in CFD

The reliability and accuracy of CFD simulations in studying blood flow in patient-specific conditions are directly connected to realistic representations of vessel geometry, as well as the imposed boundary conditions. The geometry representation can affect the simulations by not including all of the side branches [31] and due to the segmentation variability [32]. For the aortic coarctation studies, the choice of proper inlet and outlet side-branching boundary conditions was highlighted in [28] and [33], respectively. Finally, the assumption of rigid-wall in patient-specific simulations can lead to differences up to 30% [34].

Our approach to perform analysis for a simplified phantom is based on a step-by-step elimination process of specific contributions (e.g., exact wall geometry with all side branches, the exact specification of the inlet and outlet boundary conditions, and wall elasticity) which makes a fair comparison between CFD and MRI for patient-specific cases difficult. By eliminating the effects of the above-mentioned limitations, we have achieved identical phantom working conditions for simulations and experiments. Despite achieving a good agreement between CFD and MRI for the mean velocity profiles at various cross-sections of the phantom, the local distribution of the WSS still exhibited significantly

different values. A similar level of disagreement was also reported in the literature, [26, 27]. Based on the above-presented arguments, we conclude that the major contributor to disagreement between MRI and CFD is due to limitations in spatial resolution of MRI in the proximity of the aortic wall.

The effect of pre-processing on the outcomes of simulations is also highlighted in the patient-specific CoA. For this case, a more drastic smoothing of the aortic wall resulted in a decrease in mean WSS of 7.3%, bringing the value closer to MRI. However, this decrease is still relatively small, compared to almost an order-of-magnitude difference in WSS between MRI and CFD, and both simulations resulted in very similar global distributions of WSS.

Our thorough comparison of blood flow and WSS based on MRI and CFD showed that the blood flow, in general, agreed well with both techniques. However, the derived variables, like WSS, deviate much more. The reasons behind the deviation can be found on both sides. As demonstrated in the phantom, the underestimation of WSS is mostly due to MRI not being able to capture the steep gradients in a region with sudden flow acceleration. However, the boundary condition treatment and preparation of the geometry in CFD has also a big effect. Patient-specific CoA showed that the application of a flat parabolic profile leads to discrepancies in the ascending aorta, and using arterial geometry without adequate smoothing slightly overestimates CFD-based WSS. Hence, when evaluating the WSS differences between MRI and CFD, attention should be given to the limitation of both techniques.

3.4.4 Clinical Applications

While in this work, we present the MRI-CFD coupling using 4D-flow MRI data, the technique can be coupled with different imaging techniques for the acquisition of the anatomy - e.g., MRA imaging. Nevertheless, PC-MRI at the inlet is still necessary for an accurate definition of boundary conditions, [28]. With this integrated CFD-MRI approach, where CFD is based on the advanced RSM turbulence model, it is possible to generate simulation results with high spatial resolution and a high level of accuracy within a few hours. This may lead to several interesting clinical applications of the image-based CFD framework for diseased arteries. Potential examples include pre- and post-operative follow-up for patients suffering from CoA, [12]. Furthermore, by studying a wider population of patients, biomarkers for re-stenosis could be identified similarly as was done for femoropopliteal arteries [35], which could lead to a predictive method for potential complications connected to CoA.

The proposed approach is not only limited to coarctation or aorta. It can be easily applied also in other aortic diseases (e.g., aneurysm and dissection) or to study the blood flow in different parts of the cardiovascular system. Examples of these applications have already been tested, for example, in cerebral aneurysms [36], stenosis of major arteries [37], and pulmonary arteries [38], and show very good promise.

Finally, it is important to touch upon the feasibility of using image-based CFD in the clinical application. As we showed with this study, the methods have a great potential to study the long-term effects of diseases or to model the progression and predict the outcomes of chronic vascular diseases. However, the state of the methods at the moment does not allow for implementation in acute decision-making. This is especially due to the fact that the simulations and their preparation is time-consuming and requires expert knowledge. Most medical doctors do not have adequate training to perform such simulations, and therefore,

experts in computational fluid dynamics should be involved. Hence, until improvements in automatizing the image-based CFD are made, for example, by implementing mesh-less methods (e.g., Solid Particle Hydrodynamics [39]), the usage of MRI or other imaging methods for diagnostics of acute cases is necessary.

3.4.5 Limitations

For the MRI measurements in the simplified phantom, the 4D Flow MRI with non-segmented gradient-echo and echo planar imaging (EPI) acceleration has been used. In contrast to that, for in vivo patient-specific CoA, the 4D Flow MRI with segmented gradient-echo without EPI has been applied. As a result, some minor differences in accuracy in velocity quantitation may be present between these two experiments. Additionally, water was used as a working fluid for the flow in the phantom instead of blood-mimicking fluid with non-Newtonian viscosity, e.g., as proposed by Cheng et al. [40]. Use of such a fluid would represent the blood flow more adequately [40]; however, since the shear rate in the aorta was relatively high, the non-Newtonian effects should be minimal. The CFD simulations of the patient-specific CoA have been performed with the rigid walls assumption. The dynamic movement of the aorta is present in vivo 4D Flow MRI, which can produce differences in local distributions of WSS along the arterial wall. To circumvent the effects of the dynamic movement of the aorta during the cardiac cycle, the simplified phantom geometry has been considered too. Despite the relatively high Reynolds number of flow in the patient-specific aorta, some local non-Newtonian effects can take place, which is currently not taken into account in CFD simulations. We have considered a single case of the patient-specific CoA and have performed a comparative assessment of 4D Flow MRI and CFD-RSM as a first proof-of-concept. This study can be easily extended with a larger number of patient-specific aorta conditions.

3.5 Conclusions

With this study, we showed that MRI-based CFD simulations are a good alternative tool to use in studying the blood flow in CoA. Using MRI and MRI-based simulations, we assessed the blood flow in a phantom representing a simplified CoA and in a patient-specific aorta with coarctation.

Due to the narrowing and relatively high Re, the flow in the phantom was of turbulent nature. Because of this, a choice of turbulent model had to be made. We have compared $k-\epsilon$, SST, and RSM. The differences between the turbulence model arise after the bend – where the flow gets more complex. The lower-order CFD models ($k-\epsilon$, SST) cannot accurately model the secondary flow motion that naturally appears in these types of geometries, as is shown in the results obtained from MRI. However, the RSM model can predict these motions, as was shown for both velocity magnitude as well as out-of-plane vorticity. Thanks to using the phantom, where the boundary conditions between MRI and CFD are identical, we were able to accurately study WSS, an important parameter that is often regarded as a bio-marker for CoA. We showed that WSS based on MRI is approximately four times lower than WSS based on CFD; however, it agrees well in terms of the local distribution.

Finally, we have applied MRI-CFD coupling on patient-specific CoA to demonstrate the

usability of the technique for clinical applications. The agreement between 4D-flow MRI and CFD was good in terms of velocity. For WSS, simulations showed higher values than MRI again; however, the local regions of high/low WSS agree well between the different techniques. However, the simulations bring several advantages, like higher resolution and better prediction of the absolute values of WSS. This shows that image-based simulations are a good technique to asses the state of this pathology.

Appendix: Numerical Mesh and Mesh Dependency Studies

In table 3.5, we give an overview of the Grid Convergence Index (GCI) analysis for the two studied cases. We have based the analysis on mean WSS since WSS was the main study objective in this research. Three meshes, with tetrahedral elements and a prism layer close to the wall, were created for each of the cases:

- Fine (mesh 1) - phantom (14.1 million), patient CoA (9.3 million)
- Medium (mesh 2) - phantom (7.0 million), patient CoA (4.7 million)
- Coarse (mesh 3) - phantom (3.6 million), patient CoA (2.3 million).

Both the Richardson extrapolation and the test of whether the studied parameter lies in the asymptotic range show that the medium mesh is sufficient. Based on the analysis, we have proceeded with mesh 2 (medium) for all presented results. The details of the final numerical meshes that were used for the two studied geometries are shown in Fig.3.10.

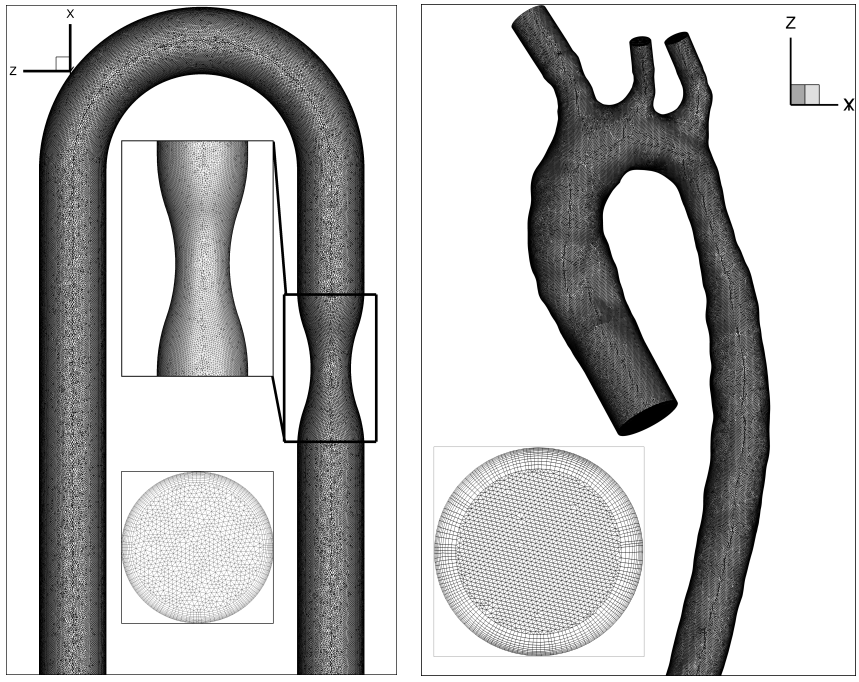

(a) Phantom (b) Aorta with Coarctation

Figure 3.10: The hybrid mesh containing the prismatic elements in the wall proximity and tetrahedra in the center of the domain with details of the inlet and stenosed region for phantom (a) and patient-specific aorta (b).

Table 3.5: The mesh dependency analysis for Phantom and Patient geometries, with corresponding wall shear stress for three different meshes (fine - 1, medium - 2, coarse - 3), refinement ratio r, Richardson Extrapolation ($f_{h=0}$, Grid Convergence Index ($GCI_{1,2}$ fine-medium, $GCI_{2,3}$ medium-coarse), and the test whether the studied variables lie in the asymptotic range.

	Phantom	Patient
WSS_1 [Pa]	0.684	14.054
WSS_2 [Pa]	0.679	14.000
WSS_3 [Pa]	0.669	13.690
r	2.018	1.999
$f_{h=0}$ [Pa]	0.689	14.065
$GCI_{1,2}$ [%]	0.912	0.101
$GCI_{2,3}$ [%]	1.812	0.584
Asymptotic?	1.007	1.004

References

[1] T. Yamaguchi, S. Kikkawa, K. Tanishita, and M. Sugawara, *Spectrum analysis of turbulence in the canine ascending aorta measured with a hot-film anemometer,* Journal of Biomechanics **21**, 489 (1988).

[2] R. A. Krasuski and F. Fouad-Tarazi, *Chapter 74 - coarctation of the aorta,* in *Comprehensive Hypertension*, edited by G. Y. Lip and J. E. Hall (Mosby, 2007) pp. 923 – 930.

[3] H. Abe, H. Kawamura, and H. Choi, *Very large-scale structures and their effects on the wall shear-stress fluctuations in a turbulent channel flow up to re_τ=640,* Journal of Fluids Engineering **126**, 835 (2004).

[4] Yixiang Feng, S. Wada, K. Tsubota, and T. Yamaguchi, *A model-based numerical analysis in the early development of intracranial aneurysms,* in *2005 IEEE Engineering in Medicine and Biology 27th Annual Conference* (2005) pp. 607–610.

[5] P. Dyverfeldt, M. D. Hope, E. E. Tseng, and D. Saloner, *Magnetic resonance measurement of turbulent kinetic energy for the estimation of irreversible pressure loss in aortic stenosis,* JACC: Cardiovascular Imaging **6**, 64 (2013).

[6] J. F. Juffermans, I. Nederend, P. J. van den Boogaard, A. D. J. ten Harkel, M. G. Hazekamp, H. J. Lamb, A. A. W. Roest, and J. J. M. Westenberg, *The effects of age at correction of aortic coarctation and recurrent obstruction on adolescent patients: MRI evaluation of wall shear stress and pulse wave velocity,* European Radiology Experimental **3**, 24 (2019).

[7] J. Zimmermann, D. Demedts, H. Mirzaee, P. Ewert, H. Stern, C. Meierhofer, B. Menze, and A. Hennemuth, *Wall shear stress estimation in the aorta: Impact of wall motion, spatiotemporal resolution, and phase noise,* Journal of Magnetic Resonance Imaging **48**, 718 (2018).

[8] A. Rinaudo, G. D'Ancona, R. Baglini, A. Amaducci, F. Follis, M. Pilato, and S. Pasta, *Computational fluid dynamics simulation to evaluate aortic coarctation gradient with contrast-enhanced ct,* Computer Methods in Biomechanics and Biomedical Engineering **18**, 1066 (2015), pMID: 24460213.

[9] Y. Zhu, R. Chen, Y.-H. Juan, H. Li, J. Wang, Z. Yu, and H. Liu, *Clinical validation and assessment of aortic hemodynamics using computational fluid dynamics simulations from computed tomography angiography,* BioMedical Engineering OnLine **17**, 53 (2018).

[10] D. Gaze, *Congenital Heart Disease* (IntechOpen, 2018).

[11] F. Yang, B. Zhai, L.-G. Hou, Q. Zhang, and J. Wang, *Computational fluid dynamics in the numerical simulation analysis of end-to-side anastomosis for coarctation of the aorta,* Journal of Thoracic Disease **10** (2018).

[12] M. Andersson, J. Lantz, T. Ebbers, and M. Karlsson, *Quantitative assessment of turbulence and flow eccentricity in an aortic coarctation: Impact of virtual interventions,* Cardiovascular Engineering and Technology **6**, 281 (2015).

[13] A. Arzani, P. Dyverfeldt, T. Ebbers, and S. C. Shadden, *In vivo validation of numerical prediction for turbulence intensity in an aortic coarctation,* Annals of Biomedical Engineering **40**, 860 (2011).

[14] R. Gårdhagen, J. Lantz, F. Carlsson, and M. Karlsson, *Large eddy simulation of stenotic flow forwall shear stress estimation - validation and application,* WSEAS Transactions on Biology and Biomedicine **8**, 86 (2011).

[15] B. Wols, *Computational Fluid Dynamics in Drinking Water Treatment*, KWR Watercycle Research Institute Series (IWA Publishing, 2011).

[16] Y. C. Fung, *Biomechanics: circulation*, 2nd ed. (Springer, 1997).

[17] H. Delingette, *General object reconstruction based on simplex meshes,* International Journal of Computer Vision **32**, 111 (1999).

[18] L. Antiga, M. Piccinelli, L. Botti, B. Ene-Iordache, A. Remuzzi, and D. A. Steinman, *An image-based modeling framework for patient-specific computational hemodynamics,* Medical & Biological Engineering & Computing **46**, 1097 (2008).

[19] K. Hanjalić and B. Launder, *Modelling Turbulence in Engineering and the Environment: Second-Moment Routes to Closure* (Cambridge University Press, 2011).

[20] B. E. Launder and D. B. Spalding, *Lectures in mathematical models of turbulence [by] B. E. Launder and D. B. Spalding* (Academic Press London, New York, 1972) pp. 7, 169 p.

[21] F. R. Menter, *Two-equation eddy-viscosity turbulence models for engineering applications,* AIAA Journal **32**, 1598 (1994), https://doi.org/10.2514/3.12149 .

[22] M. M. Gibson and B. E. Launder, *Ground effects on pressure fluctuations in the atmospheric boundary layer,* Journal of Fluid Mechanics **86**, 491–511 (1978).

[23] A. A. Soares, S. Gonzaga, C. Oliveira, A. Simões, and A. I. Rouboa, *Computational fluid dynamics in abdominal aorta bifurcation: non-newtonian versus newtonian blood flow in a real case study,* Computer Methods in Biomechanics and Biomedical Engineering **20**, 822 (2017), pMID: 28367643.

[24] I. ANSYS, ed., *Ansys fluent theory guide,* (2017) Chap. 4, pp. 39–91.

[25] A. Malhotra and K. H. Mousa, *Turbulence modelling in pipe flow,* Mathematical and Computer Modelling **14**, 755 (1990).

[26] J. Szajer and K. Ho-Shon, *A comparison of 4D flow MRI-derived wall shear stress with computational fluid dynamics methods for intracranial aneurysms and carotid bifurcations — a review,* Magnetic Resonance Imaging **48**, 62 (2018).

[27] S. Miyazaki, K. Itatani, T. Furusawa, T. Nishino, M. Sugiyama, Y. Takehara, and S. Yasukochi, *Validation of numerical simulation methods in aortic arch using 4D flow MRI,* Heart and Vessels **32**, 1032 (2017).

[28] L. Goubergrits, R. Mevert, P. Yevtushenko, J. Schaller, U. Kertzscher, S. Meier, S. Schubert, E. Riesenkampff, and T. Kuehne, *The impact of MRI-based inflow for the hemodynamic evaluation of aortic coarctation,* Annals of Biomedical Engineering **41**, 2575 (2013).

[29] X. Yang and P. G. Tucker, *Assessment of turbulence model performance: Large streamline curvature and integral length scales,* Computers & Fluids **126**, 91 (2016).

[30] T. Puiseux, A. Sewonu, O. Meyrignac, H. Rousseau, F. Nicoud, S. Mendez, and R. Moreno, *Reconciling PC-MRI and CFD: An in-vitro study,* NMR in Biomedicine **32**, e4063 (2019), e4063 nbm.4063.

[31] P. Yevtushenko, F. Hellmeier, J. Bruening, T. Kuehne, and L. Goubergrits, *Numerical investigation of the impact of branching vessel boundary conditions on aortic hemodynamics,* Current Directions in Biomedical Engineering **3**, 321 (01 Sep. 2017).

[32] R. Perinajová, J. F. Juffermans, J. J. Westenberg, R. L. van der Palen, P. J. van den Boogaard, H. J. Lamb, and S. Kenjereš, *Geometrically induced wall shear stress variability in CFD-MRI coupled simulations of blood flow in the thoracic aortas,* Computers in Biology and Medicine **133**, 104385 (2021).

[33] S. Madhavan and E. M. C. Kemmerling, *The effect of inlet and outlet boundary conditions in image-based CFD modeling of aortic flow,* BioMedical Engineering OnLine **17**, 66 (2018).

[34] J. LANTZ, J. RENNER, and M. KARLSSON, *Wall shear stress in a subject specific human aorta — influence of fluid-structure interaction,* International Journal of Applied Mechanics **03**, 759 (2011).

[35] C. Gökgöl, N. Diehm, L. Räber, and P. Büchler, *Prediction of restenosis based on hemodynamical markers in revascularized femoro-popliteal arteries during leg flexion,* Biomechanics and Modeling in Mechanobiology **18**, 1883 (2019).

[36] M. Castro, C. Putman, and J. Cebral, *Computational fluid dynamics modeling of intracranial aneurysms: Effects of parent artery segmentation on intra-aneurysmal hemodynamics,* American Journal of Neuroradiology **27**, 1703 (2006).

[37] D. Zhang, P. Xu, H. Qiao, X. Liu, L. Luo, W. Huang, H. Zhang, and C. Shi, *Carotid dsa based CFD simulation in assessing the patient with asymptomatic carotid stenosis: a preliminary study,* BioMedical Engineering OnLine **17**, 31 (2018).

[38] F. M. Rijnberg, S. F. S. van der Woude, H. C. van Assen, J. F. Juffermans, M. G. Hazekamp, M. R. M. Jongbloed, S. Kenjeres, H. J. Lamb, J. J. M. Westenberg, J. J. Wentzel, and A. A. W. Roest, *Non-uniform mixing of hepatic venous flow and inferior vena cava flow in the fontan conduit,* Journal of The Royal Society Interface **18**, 20201027 (2021).

[39] A. Caballero, W. Mao, L. Liang, J. Oshinski, C. Primiano, R. McKay, S. Kodali, and W. Sun, *Modeling left ventricular blood flow using smoothed particle hydrodynamics,* Cardiovascular Engineering and Technology **8**, 465 (2017).

[40] A. L. Cheng, C. P. Wee, N. M. Pahlevan, and J. C. Wood, *A 4D flow MRI evaluation of the impact of shear-dependent fluid viscosity on in vitro fontan circulation flow,* American journal of physiology. Heart and circulatory physiology **317**, H1243 (2019).

4

Modelling of Aortic Wall Movement

A proper understanding of the origin and progression of the thoracic aortic aneurysm (TAA) can help prevent its growth and rupture. For a better understanding of this pathogenesis, the aortic blood flow has to be studied and interpreted in great detail. We can obtain detailed aortic blood flow information using Magnetic Resonance Imaging (MRI) based computational fluid dynamics (CFD) with a prescribed motion of the aortic wall. We performed two different types of simulations - static (rigid wall) and dynamic (moving wall) for healthy control and a patient with a TAA. For the latter, we have developed a novel morphing approach based on the Radial Basis Function (RBF) interpolation of the segmented 4D-flow MRI geometries at different time instants. Additionally, we have applied reconstructed 4D-flow MRI velocity profiles at the inlet with an automatic registration protocol. The simulated RBF-based movement of the aorta matched well with the original 4D-flow MRI geometries. The wall movement was most dominant in the ascending aorta, accompanied by the highest variation of the blood flow patterns. The resulting data indicated significant differences between the dynamic and static simulations, with a relative difference for the patient of 7.47±14.18% in time-averaged wall shear stress and 15.97±43.32% in the oscillatory shear index (for the whole domain). In conclusion, the RBF-based morphing approach proved to be numerically accurate and computationally efficient in capturing complex kinematics of the aorta, as validated by 4D-flow MRI. We recommend this approach for future use in MRI-based CFD simulations in broad population studies. Performing these would bring a better understanding of the onset and growth of TAA.

This chapter has been submitted to BioMedical Engineering OnLine.

4.1 Introduction

Rupture of Thoracic Aortic Aneurysm (TAA) is an acute medical condition, with a fatality rate of almost 95% [1]. Because of the high fatality, properly diagnosing and treating this dangerous condition is of utmost importance. However, the conventional guidelines that focus on the diameter and growth rate of TAA were shown to be inadequate in many cases [2, 3]. This emphasizes the need for new biomarkers that aim for patient-specific prediction of TAA rupture and look beyond the analysis based solely on the aorta geometry [4]. The blood flow information must be assessed to establish new predicting biomarkers. Such information can be obtained from 4D flow Magnetic Resonance Imaging (MRI); however, its spatial and temporal resolution is limited [5]. In recent years, the clinical image-based computational fluid dynamics (CFD) [6] was successfully applied to provide the patient-specific blood flow features in great detail, for example, flow in aorta [7–9] and TAA [10] as well as in wider population studies [11, 12]. However, one important aspect of modeling the aorta or TAA is often omitted in the literature - the movement of the aorta (i.e., aorta kinematic). Because of the beating heart during the cardiac cycle, the aortic root moves downwards during systole and returns to its original position during diastole. This movement was reported to be approximately nine millimeters in the downward direction [13] with a clockwise twist up to twenty degrees [14]. Furthermore, the aortic compliance causes the wall to expand and contract radially during the cardiac cycle due to the changing transmural pressure gradient over time [15]. It was reported that changes in the thoracic aorta diameter were in the 1.7 to 3.6 mm range [16]. These combined effects of the aortic wall kinetics can significantly affect the blood flow simulations, and consequently, they should be included in the CFD simulation [17].

To model the blood vessel movement, two simulation strategies have been applied in previous studies in the literature: (i) the fully coupled fluid-structure interaction (FSI), and (ii) the predefined wall displacement. The FSI studies of aorta hemodynamics were applied in [17–21]. However, the FSI method for patient-specific situations suffers from numerous limitations. These include the lack of detailed information on the aortic wall properties (i.e., non-homogeneous thickness and elasticity), difficulties with the physiological boundary conditions (for example, pressure), as well as the quite intensive computational costs (for example, iterative pre-stressing procedure, fluid/structure mechanics coupling). The estimation of the aorta motion was the focus of several studies in the literature [22–24]. Dynamic computed tomography (CT) was used to characterize the aortic wall motion in patients with aortic dissection [22]. It was demonstrated that this technique could provide segmentation of the aorta and its distensibility. On the other hand, there was no information regarding the aorta hemodynamics (blood velocity and flow rates). A simplified method for the aortic wall motion was proposed in [24]. The developed moving-boundary method (MBM) tuned with the non-invasive clinical images (2D cine-MRI) provided a good agreement with the FSI results. The MBM method was also less computationally expensive. However, due to several parameters that still need to be based on theoretical estimates (especially the distensibility), these methods lack the potential to be fully patient-specific.

More recently, the mesh morphing approach based on radial basis function (RBF) was proposed for mimicking the motion of biological tissue, e.g., aortic valve [25], left ventricle with mitral valve [26], and thoracic aorta [27, 28]. The RBF-based mesh morphing tools proved to be potentially numerically efficient and accurate in various applications. They

could cope with many data formats and large-size unstructured meshes, [29–32]. In the case of RBF application in the aorta, Capellini et al. [27, 28] presented an approach where only the ascending thoracic aorta (excluding root) was considered dynamic, and the rest of the domain was assumed to be rigid. Additionally, only a simplified inlet velocity boundary condition was implemented. These assumptions bring considerable simplifications to the complexity of motion and flow in the aorta.

To bridge these simplifications, we propose a proof-of-concept approach for a fully coupled 4D-flow MRI-CFD model of the aorta. This approach will be validated for the healthy control subject and patient-specific aorta with a large root aneurysm. For both cases, the movement of the aorta and all inlet and outlet boundary conditions will be extracted from the corresponding 4D-flow MRI scans. The dynamic behavior of the aorta will be mimicked by a morphing approach based on the radial basis function (RBF) interpolation based on Xu and Kenjereš [26]. We adapt the method to account for the motion of the whole thoracic aorta. To define the motion, we utilize 4D-flow MRI data at several points of the cardiac cycle. In addition, we present an automatic registration protocol of the 4D-flow MRI-derived velocity profile at the inlet for the moving aorta.

4.2 Methods

4.2.1 Studied Cases

Two subjects were included in this study - a healthy control (HC) and a patient (P). The patient had a root aortic aneurysm with a diameter $D = 50$ mm and aortic valve regurgitation of 33%. Additional characteristics for both subjects can be found in Tab. 4.1.

Table 4.1: Characteristics of the healthy control and patient.

		Healthy Control	Patient
Gender		male	female
Age	**[yr]**	43	26
Weight	**[kg]**	85	67
Height	**[cm]**	195	187
Blood pressure	**[mmHg]**	115/67	83/46
Mean arterial pressure	**[mmHg]**	85	63
Heart rate	**[bpm]**	61	49

4.2.2 MRI Acquisition and Data Processing

For both subjects, 4D-flow MRI was performed on a 3T MRI system (Elition, Philips Healthcare, Best, The Netherlands) using a hemidiaphragm respiratory navigator with retrospective electrocardiogram gating without echo-planar imaging. Additional parameters in the MRI sequence can be found in Tab. 4.2

The acquired 4D-flow MRI data sets were segmented using CAAS MR Solutions v5.2. (Pie Medical Imaging BV, Maastricht, The Netherlands). The protocol for segmentation is identical for both studied subjects. The analysis is initialized by manually placing starting and ending points of the domain at peak systole. The starting point is placed in the aortic root, and the ending points are placed in all major branching arteries of the

Table 4.2: Details of 4D-flow MRI sequence for healthy control and patient.

		Healthy Control	Patient
Velocity encoding	**[cm/s]**	150	160
Reconstructed temporal resolution	**[ms]**	30	38
Echo time	**[ms]**	2.6	2.7
Repetition time	**[ms]**	4.5	4.6
Flip angle	**[°]**	10	10
Acquired isotropic resolution	**[mm]**	2.5	2.7
Field of view	**[mm3]**	350x78x160	450x60x150
Turbo field echo factor	**[-]**	2	2
Parallel imaging factor	**[-]**	2.5x1.2	2.5x1.2

arch (Brachiocephalic Trunk, Left Common Carotid Artery, and Left Subclavian Artery) and in the abdominal aorta. Subsequently, a 3D volume at peak systole is automatically segmented and manually adjusted (if discrepancies are observed). The manual adjustments for the peak-systolic phase are mostly necessary for the regions with flow recirculation, i.e., in the proximity of the aortic root and downstream the aortic arch. After successful segmentation, the peak systolic 3D volume is copied to the next phase of interest and manually adjusted for the movement. In this case, the manual interventions are more complex and time-consuming (up to three hours per phase) due to the arterial movement, both caused by the compliance of the aortic wall as well as the movement of the heart. This process is especially time-consuming in the ascending aorta due to its complex movement through the cardiac cycle. The segmentation procedure is then repeated for all of the phases of interest (in total, four instants of the cardiac cycle were extracted - mid-rising systole, peak systole, mid-decreasing systole, and beginning of diastole).

4.2.3 Geometry pre-processing

The initial surface obtained via segmentation of 4D-flow MRI is not suitable for CFD due to the relative 'roughness' of the surface mesh (i.e., variation of the normal vector direction of the segmented surface from its ideal form due to segmentation errors) and inconsistent boundary faces of inlets and outlets. To remove these imperfections, we performed pre-processing of the extracted surfaces using Vascular Modelling Toolkit (VMTK) [33]. The initial (4D-flow MRI) and final surface after pre-processing for peak systole are shown in Fig. 4.1; note that while the whole aorta was extracted for HC, only the thoracic part was considered for the further simulations and analysis.

To obtain the final surface, the following steps are executed: First, the surface inlet and outlets are cut perpendicular to the arterial centerline. Next, the smoothing step is performed. In this step, the most optimal smoothing should account for the regions with high variation of the normal vectors while preserving the total volume. We have utilized the Taubin smoothing, with pass-band 0.1 and 100 iterations. Compared to other methods, the Taubin smoothing procedure ensures proper smoothing of regions with high variations in surface curvature and avoids extensive shrinkage of the surface [34]. Next, the surface mesh (triangular) is subdivided using the Butterfly method [35] to ensure better surface definition for the computational model. Finally, we added cylindrical extensions on the inlet

Figure 4.1: Initial surface obtained from 4D-flow MRI (white) and the geometry after the final step of pre-processing (red) for healthy control (left) and patient (right).

and outlets in the normal direction of the respective planes. The diameter and the length of the extension are determined based on the diameter of the respective boundary (D_i). The length was kept constant for all outlets ($5 \cdot D_i$), and only a very short flow extension was created for the inlet ($0.5 \cdot D_i$) to assure the reliability of the applied inlet velocity profile while ensuring the stability of the moving mesh implementation.

4.2.4 Computational Model

The case-specific computational model was developed to take into account the detailed aorta geometry (and its movement), as well as the inlet and boundary conditions (BC) from the 4D-flow MRI scans. The entire algorithm is illustrated in the flow chart shown in Fig. 4.2. We have performed simulations with the rigid (static) and moving (dynamic) aortic wall for both subject- and patient-specific geometries. For the latter, additional algorithm details are given in Fig. 4.2b and will be discussed below.

4.2.5 Fluid Dynamics

In the present work, we adopt the ALE (Arbitrary Lagrangian-Eulerian) formulation for conservation of mass and momentum for a moving numerical mesh, for which the following governing equations are solved [36]:

$$\frac{\partial \rho}{\partial t} + \nabla \cdot \left[\rho \left(\mathbf{v} - \mathbf{v}_g \right) \right] = 0 \tag{4.1}$$

$$\frac{\partial (\rho \mathbf{v})}{\partial t} + \nabla \cdot \left[\rho \mathbf{v} \left(\mathbf{v} - \mathbf{v}_g \right) \right] = -\nabla p + \nabla \cdot \overline{\overline{\tau}} \tag{4.2}$$

where ρ is the fluid density, $\mathbf{v}$ is the fluid velocity, $\mathbf{v}_g$ is the grid (or mesh) velocity, p is the pressure, and $\overline{\overline{\tau}}$ is the viscous stress tensor $\left(\overline{\overline{\tau}} = \mu \left(\nabla \mathbf{v} + \nabla \mathbf{v}^T \right) \right)$, with μ as the dynamic viscosity of the fluid. Note that for the static simulations (the rigid wall assumption), we

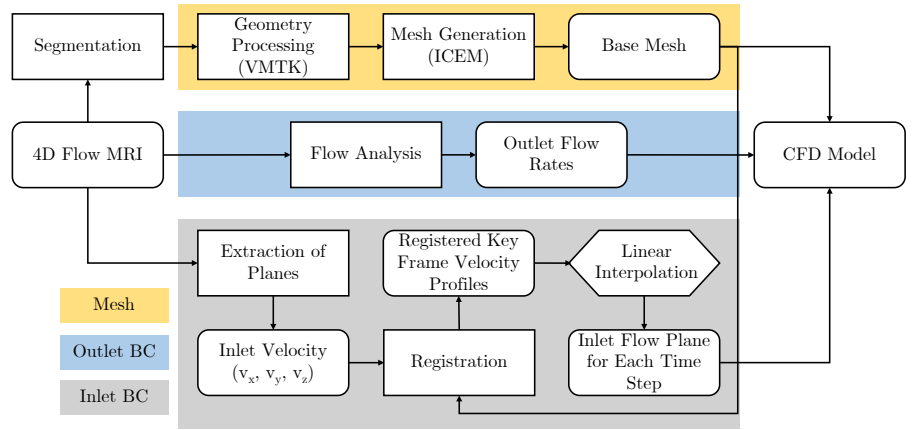

(a)

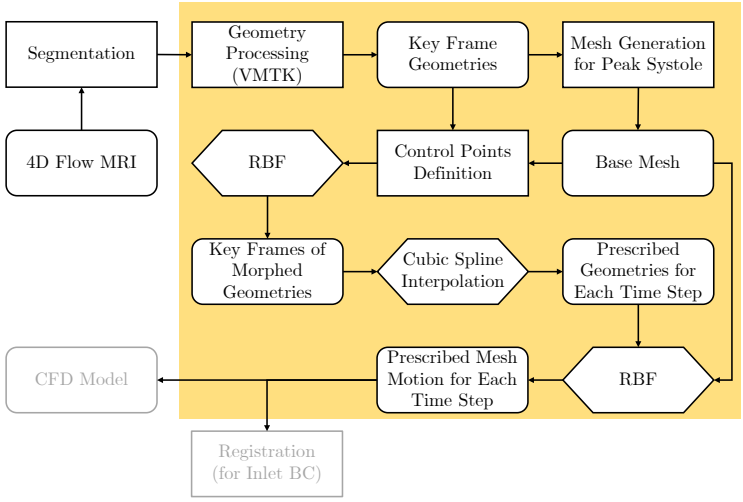

(b)

Figure 4.2: Schematic flow-chart showing the main CFD model inputs (mesh, outlet boundary conditions, and inlet boundary conditions) for the static simulations (a) and the details of the dynamic mesh morphing of the aortic wall for the dynamic simulations (b).

have $\mathbf{v}_g = 0$. Additionally, since we employed a moving grid approach for part of our simulations, we need to define the space conservation law as follows:

$$\frac{dV}{dt} = \int_{\partial V} \mathbf{v}_g \cdot \mathbf{A} = \sum_{j}^{n_f} \mathbf{v}_{\mathbf{g},\mathbf{j}} \cdot \mathbf{A}_j \tag{4.3}$$

where dV/dt is the volume derivative of the arbitrary control volume V, ∂V is the boundary of control volume V, $\mathbf{A}$ is the face vector area, n_f is the number of faces j. Finally,

the dot product on the right-hand side is calculated from

$$\mathbf{v}_{\mathrm{gj}} \cdot \mathbf{A}_j = \frac{\partial V_j}{\delta t} \tag{4.4}$$

where ∂V_j denotes the volume swept out by the control volume, face j over each time step [37].

4.2.6 Boundary and Initial Conditions

The inlet plane boundary condition was specified as a velocity inlet where all three velocity components at particular instants of the cardiac cycle were extracted from the reconstructed 4D-flow MRI (similarly to other studies [38–41]). This was done using an in-house developed software tool for proper time registration and interpolation of the clinical data. All steps of this procedure are shown in the flow-chart diagram shown in Fig. 4.2a, and can be summarized as:

1. Using an in-house developed tool for 4D-flow MRI data analysis, all three velocity components $\mathbf{v}\left(v_x, v_y, v_z\right)$ are extracted from the reconstructed 4D-flow MRI data at the inlet plane of the studied case for each acquired time step (n = 34 for the healthy control, and n = 32 for the patient-specific acquisitions, respectively).

2. Velocity data are linearly interpolated for each (n) and (n+1) time step, where time-step size (Δt) is based on the requirements of CFD (in the present work, we have Δt = 1 ms, for both cases).

3. Inlet (represented by the CFD mesh) is imported from the base mesh (at peak systole), and the interpolated velocity profile is registered on this mesh; for dynamic simulations, the inlet is imported for each time step from the generated moving mesh.

4. The velocity components are then interpreted in the CFD software as a *Profile* and interpolated and projected on the inlet mesh using Inverse-distance interpolation.

An example of the inlet flow rate and the interpolated velocity profiles at peak systole for the HC and P cases can be seen in Fig. 4.3. Outlet boundary conditions were treated as outflow with a pre-defined fraction of mass flow per outlet. The outflow boundary condition assumes zero-diffusive flux for all flow variables and a mass balance correction at the outlet. The flow fractions at each outlet (w_n) were defined based on the 4D-flow MRI measurements. Since the 4D-flow data in the supra-aortic arteries are unreliable due to a low number of voxels, we have exported planes in the upstream and downstream proximity of each bifurcation and, by that, estimated the net flow leaving through each outlet. Afterward, the fractions at each time step were calculated as follows:

$$w_n = \frac{Q_n}{Q_i} \frac{1}{\sum_{n=1}^{m} w_n} \tag{4.5}$$

where w_n and Q_n are the flow fractions and the net flow of the respective outlets, Q_i is the net flow at the inlet and m is the total number of outlets. Each outlet flow fraction is scaled by the sum of all of the fractions to satisfy $\sum_{n=1}^{m} Q_i \cdot w_n = Q_i$. Applying the measured

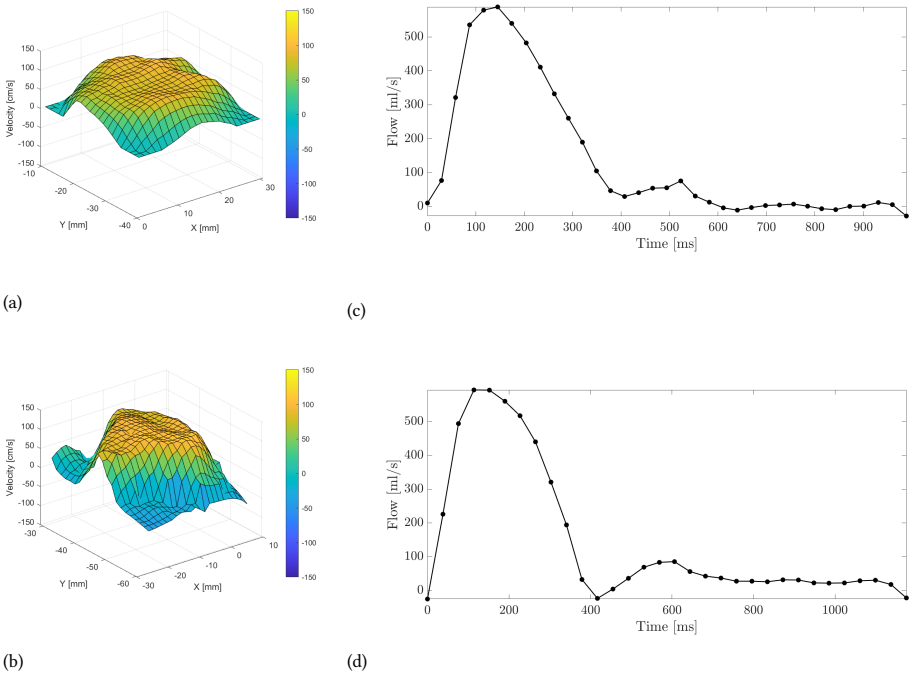

Figure 4.3: Interpolated inlet velocity profile at peak systole based on 4D-flow MRI for healthy control (a) and patient (b) and the volumetric flow at the inlet for one cycle for healthy control (c) and patient (d).

data at each time-step proved to be more accurate in the definition of the patient-specific simulations, as shown previously by Gallo et al. [42].

The no-slip condition was applied at the wall for both static and dynamic simulations. The definition of wall movement for the dynamic simulations is discussed in detail in the next section. The transient simulations were initialized using the steady-state solution at the peak systole. In total, we have simulated three cardiac cycles to eliminate the influence of initial conditions. We have used only results from the last cardiac cycle for the final analysis.

4.2.7 Moving Wall

In the present study, for dynamic simulations, we have adopted a predefined moving wall approach as shown in Fig. 4.2b. The wall motion was defined from four key-frame geometries (i.e., geometries of interest) extracted from the 4D-flow MRI (as previously described in MRI Acquisition and Segmentation section). The full process of the moving mesh generation over the entire cardiac cycle can be summarized as:

1. The 4D-flow-based geometries at key-frames are pre-processed using VMTK (as described in Sec. 4.2.3) yielding the initial surface of the aorta (in .stl format)

2. For the geometry at the peak systole, various cross-section markers (planes) are

introduced to separate the static (branching arteries) and dynamic (the rest of the aorta) segments

3. The three-dimensional numerical mesh is created for this aortic geometry (base mesh), with a refinement close to the wall

4. The control points are introduced for the peak systole and all key-frames by the following procedure:

   (i) Control points for the inlet and outlet are defined (circumferential equidistant distribution)

   (ii) A finite number of the planes perpendicular to the flow direction with uniform longitudinal distances are selected; in each of these planes, the radial distances are defined similarly to (i);

   (iii) Additional manually adjusted control points are introduced at locations in the proximity of the branching arteries

   (iv) The final form of the structured control points matrices are established with $i \times j$ control points (i = number of planes, j = control points per plane), for HC = 19×6 and P = 18×6

5. The base mesh (generated in step 3) is morphed using Radial Basis Function (RBF) interpolation of the control points (defined in the previous step), resulting in the morphed surface geometries for all selected key-frames

6. The surface coordinates of key-frames geometries are then interpolated in time over the entire cardiac cycle using spline interpolation with smoothing parameter $p = 0.999$, resulting in a total of n=1018 and 1212 frames; Note that we assumed no aortic movement during diastole

7. The generated surface geometries at each time step alongside the base mesh are then used as input for the RBF-based mesh-morphing during the simulations

RBF Interpolation - Mathematical view

Fig. 4.4 depicts the surface points (both HC and P) for the reference phase (peak systole - red) and for one of the RBF-generated frames (mid acceleration - blue) together with the control points for the two respective phases.

RBF interpolation is based on source points, i.e. the nodal points of the original geometry, and target points which are the nodal points of the deformed geometry. It assumes an unknown smooth function f that is given via the set of source and target points. This function is then approximated by an interpolant $s(x)$ of which the general form is defined as:

$$s(x) = \sum_{i=1}^{N} \gamma_i \varphi(||x - x_{k_i}||) + h(x), \quad x \in \mathbb{R}^n \tag{4.6}$$

where $s(x)$ is the approximating smooth function, N the source points, γ_i the weights of the radial basis, φ the radial basis function, $x_{k_i} = [x_{k_i}, y_{k_i}, z_{k_i}]$ the coordinates of the source

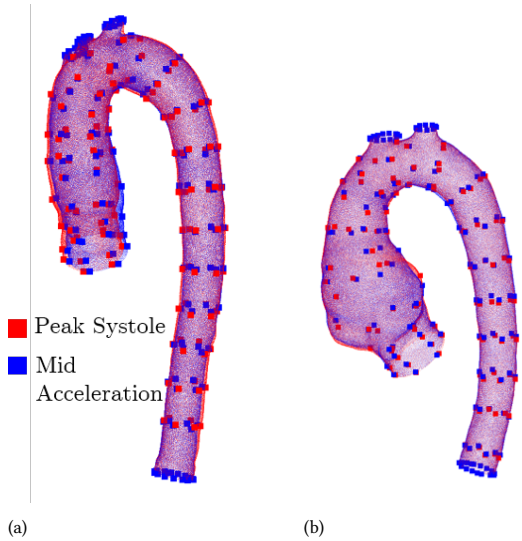

Figure 4.4: Surface points and control points (bigger) at peak systole (red) and mid acceleration (blue) for healthy control (a) and patient (b).

points, and $h(x)$ a polynomial part of which the degree depends on the type of radial basis function used. The polynomial part is added to guarantee the existence and uniqueness of the solution. The parameters γ_i and the polynomial coefficients are determined by solving a linear system of equations, with the order equal to N. This is defined by the passage- and orthogonality condition

$$\begin{cases} s(x_{k_i}) = g_{k_i} & 1 \leq i \leq N \\ \sum_{i=1}^{N} \gamma_i q(x_{k_i}) = 0, \end{cases} \tag{4.7}$$

where g_i are known discrete values of displacement of the source points x_{k_i}, and q polynomials with a degree less than or equal to the degree of polynomial h. The first criterion ensures that $s(x)$ go through the given values g_{k_i}. Secondly, the summation of the product of the weights and the polynomial at the source points x_{k_i} equals zero which satisfies the orthogonality condition. The values of γ_i and polynomial coefficients β_i are found by solving

$$\begin{bmatrix} M_{k_i} & H_{k_i} \\ H_{k_i}^T & 0 \end{bmatrix} \begin{bmatrix} \gamma \\ \beta \end{bmatrix} = \begin{bmatrix} g_{k_i} \\ 0 \end{bmatrix} \tag{4.8}$$

where M_{k_i} is the interpolation matrix containing the evaluation of the radial function based on the source points, and H_{k_i} the coordinate matrix in which the i-th row is $\begin{bmatrix} 1 & x_{k_i} & y_{k_i} & z_{k_i} \end{bmatrix}$. Finally, the displacement of the non-source points s_m is calculated by

$$s_m = \begin{bmatrix} M_m & H_m \end{bmatrix} \begin{bmatrix} \gamma \\ \beta \end{bmatrix} \tag{4.9}$$

where M_m is the evaluated matrix based on basis function $M_{mij} = \varphi(\|x_{mj} - x_{k_i}\|)$, and H_m is the coordinate matrix with i-th row $[1\ x_{m_i}\ y_{m_i}\ z_{m_i}]$.
We used the Multi-quadratics method for the radial basis function, which is defined as:

$$\varphi(r) = \sqrt{r^2 + c^2} \tag{4.10}$$

where r is the euclidean distance between the source (x) and non-source (x_{k_i}) points ($\|x - x_{k_i}\|$) and c is the shape parameter. The shape parameter was estimated based on the mean distance between the source points and their farthest neighbor normalized by the distance to their nearest neighbor. The estimated shape parameters for this study were $c_{HC} = 3.2 \times 10^{-3}$ for HC and $c_P = 4.0 \times 10^{-3}$ for P.

4.2.8 Physical and Solver Setup

The blood rheology was accounted for by applying the Carreau-Yasuda model:

$$\mu_{app} = \mu_\infty + (\mu_0 - \mu_\infty)\left[1 + (\lambda\dot{\gamma})^\alpha\right]^{\frac{n-1}{\alpha}} \tag{4.11}$$

where μ_{app} is the apparent viscosity, μ_∞ the viscosity at infinite shear, μ_0 the viscosity at zero shear, λ the relaxation time, $\dot{\gamma}$ the shear rate, α a shape parameter, and n the power-law index. The values for these parameters are adopted from [43], and are μ_∞ = 2.2 mPa·s, μ_0 = 22 mPa·s, λ = 0.110 s, α = 0.644, and n = 0.392. The blood density was kept constant (ρ = 1060 kg/m^3).

The initial mesh was identical for static and dynamic simulations and consisted of tetrahedral elements with refinement close to the wall. We have performed a mesh dependency study for the peak-systolic flow conditions (all details shown in the Appendix). Based on the mesh dependency study, the final mesh consisted of $n = 1.58 \cdot 10^6$ elements for the HC case and $n = 1.47 \cdot 10^6$ elements for the P case. Specifically for the dynamic simulations, the smoothing and re-meshing of the 3D mesh were conducted if element skewness was higher than 0.9. We have used the spring-based smoothing with the spring constant factor of one and a maximum of 250 iterations allowed. For re-meshing, the minimal and maximal allowed cell size for the whole domain varied between 1.76×10^{-4} m and 5.76×10^{-3} m.

The simulations were performed using Ansys Fluent 2019 R3 (Ansys, Canonsburg, Pennsylvania, USA). The main computational settings used in this study were: the pressure-based solver, PISO for pressure-velocity coupling, the second-order upwind scheme used for the discretization of convective terms, the second-order central differencing scheme (CDS) used for the discretization of diffusive terms, the time integration was performed by the second-order fully implicit scheme, and the convergence criterion per time step of 10^{-5} was used for all quantities.

4.2.9 Post-processing

The near-wall hemodynamic effects were studied by introducing several quantities averaged over the entire cardiac cycle:

$$\text{TAWSS} = \frac{1}{T}\int_0^T \left|\overrightarrow{\tau_w}\right| \ dt \tag{4.12}$$

where $TAWSS$ is the time-averaged wall shear stress, T is the length of a cardiac cycle, and $\overrightarrow{\tau_w}$ is the wall shear stress,

$$\mathrm{OSI} = \frac{1}{2}\left(1 - \frac{\left|\int_0^T \overrightarrow{\tau_w} dt\right|}{\int_0^T \left|\overrightarrow{\tau_w}\right| dt}\right) \tag{4.13}$$

where OSI is the oscillatory shear index. For the dynamic simulations, the values of TAWSS and OSI were projected and visualized on the surface geometry at the peak systole. Additionally, we have calculated the percentage difference ($\Delta\Phi$) between $\mathrm{CFD}_{\mathrm{static}}$ and $\mathrm{CFD}_{\mathrm{dynamic}}$ for above-defined quantities as:

$$\Delta\phi = \frac{\phi_{stat} - \phi_{dyn}}{0.5(\phi_{stat} + \phi_{dyn})} \times 100 \quad (\text{in } \%) \tag{4.14}$$

where ϕ_{stat} and ϕ_{dyn} are the TAWSS or OSI for the static and dynamic CFD simulations, respectively.

4.3 Results

4.3.1 MRI-based Wall Movement

First, we want to assess the quality of the prescribed movement. The image-based movement of the aortic wall for both HC and P is shown in Fig. 4.5. To validate the results of the RBF-based interpolation, we compare geometries extracted from the 4D-flow MRI (blue isosurface) and RBF-based reconstruction (red isosurface) - both at the mid acceleration time instant, Fig. 4.5a. Furthermore, we also compare characteristic circumferential wall profiles at various cross-sections: (1) proximal Ascending Aorta (pAscAo), (2) distal Ascending Aorta (dAscAo), (3) proximal Descending Aorta (pDescAo), and (4) distal Descending Aorta (dDescAo), respectively. Additionally, in Fig. 4.5b, we show the time-evolution of the RBF-based circumferential profiles in identical cross-sections (i.e., planes (1-4)) at the four key-frames (black- mid acceleration, red- peak systole, blue- mid deceleration, green- early diastole). Finally, we have calculated the absolute Euclidean distance between each point of RBF-generated surfaces and the MRI segmentations. These data are shown for HC and P (at each key-frame) in Fig. 4.6, and the median and mean values alongside the standard deviation of the whole domain are reported in Tab. 4.3.

Table 4.3: Median, mean, and standard deviation (std) for the absolute difference between RBF and MRI surface vertices (based on Fig. 4.5c) for healthy control (HC) and patient (P) at four key-frames (KF): KF1 - mid acceleration, KF2 - peak systole, KF3 - mid deceleration, and KF4 - early diastole.

			KF 1	KF 2	KF 3	KF 4
HC	**Median**	**[mm]**	0.63	0.46	0.62	0.62
	Mean		0.69	0.45	0.70	0.70
	std		0.35	0.18	0.41	0.43
P	**Median**	**[mm]**	0.57	0.46	0.59	0.63
	Mean		0.63	0.46	0.70	0.85
	std		0.36	0.20	0.43	0.72

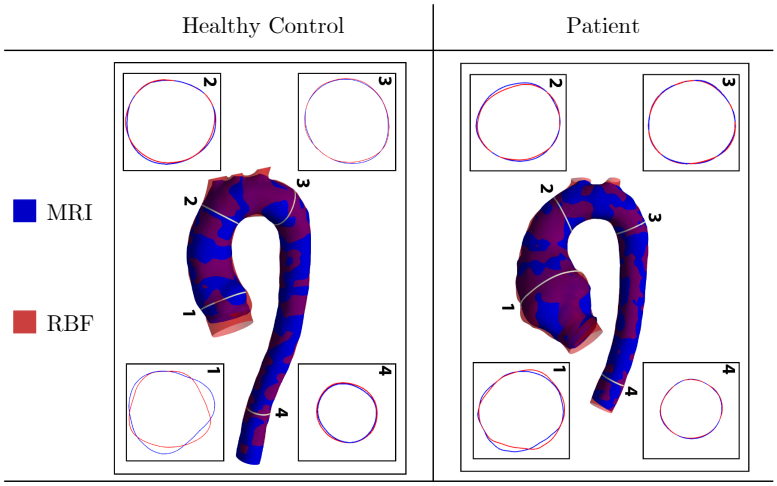

(a)

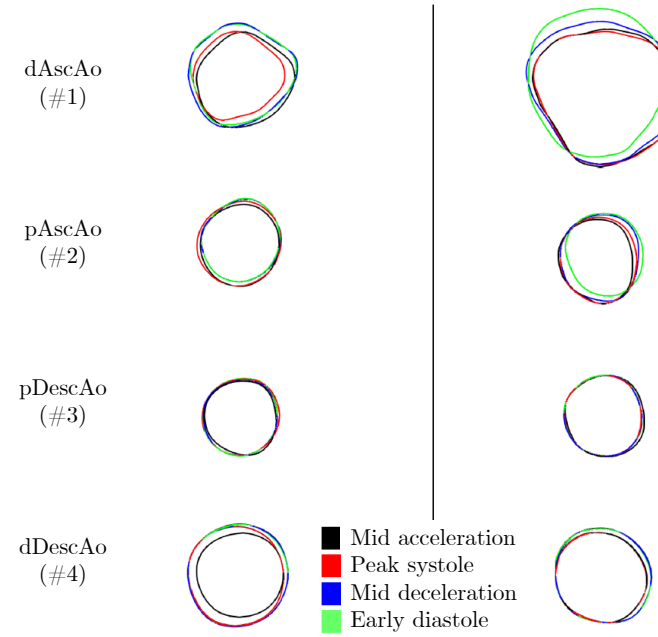

(b)

Figure 4.5: Comparison of the geometry for healthy control (HC) and patient (P) at mid acceleration for MRI (blue) and RBF (red) a) for the whole aorta and cross-sections at Proximal Ascending Aorta (pAscAo - 1), Distal Ascending Aorta (dAscAo - 2), Proximal Descending Aorta (pDescAo - 3), and Distal Descending Aorta (dDescAo - 4); the evolution of RBF-based cross-sections at the key-frames (mid acceleration - black, peak systole - red, mid deceleration - blue, and early diastole - green) for the four locations b).

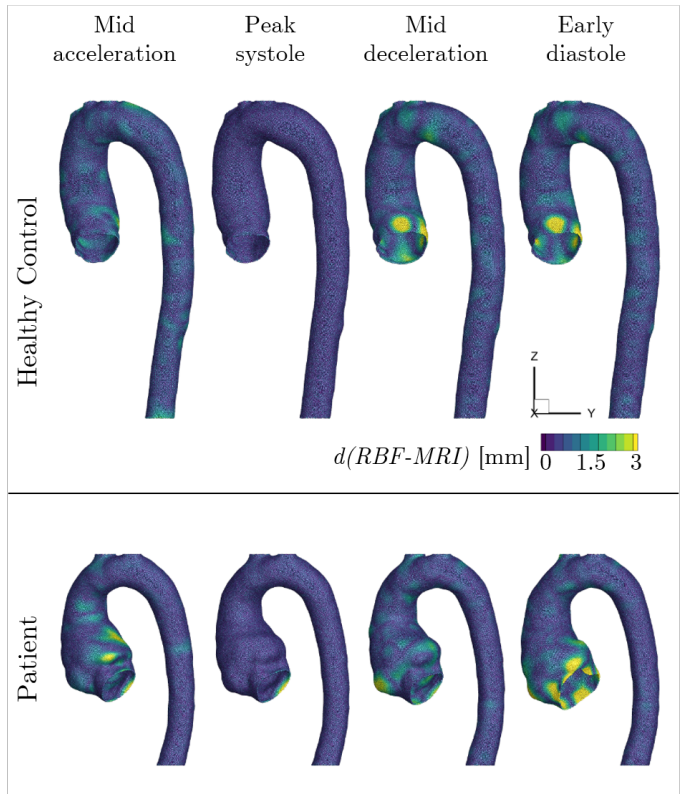

Figure 4.6: The Euclidean distance between the RBF and MRI surface vertices $d(RBF - MRI)$ for HC and P at each key-frame.

To quantify the level of the aorta movement, the normalized time-averaged aortic wall displacements (magnitude and corresponding coordinate directions) are shown in Fig. 4.7. The normalization was done using the radius of the inlet plane (i.e. $r_{\mathrm{HC}}^{\mathrm{in}} = 1.49 \cdot 10^{-2}$ m, and $r_{\mathrm{P}}^{\mathrm{in}} = 1.58 \cdot 10^{-2}$ m).

4.3.2 Computational Time

To compare the effect of the wall motion on the computational time for three simulated cycles, we report the wall time for one of the cases (HC). Both static and dynamic simulations (for this comparison) were run on 16 processors of AMD Opteron 6234. The reported wall time for static simulation was 33:07:59 (in [h:min:s]), and for the dynamic simulations, 38:29:31. The main differences were in the I/O intensive tasks (reading the prescribed mesh).

4.3.3 Effect of Wall Movement on Blood Flow

Contours of the velocity magnitude at the pre-selected cross-sections (dAscAo, pAscAo, and pDescAo) at four time instants of the cardiac cycle (mid acceleration, peak systole,

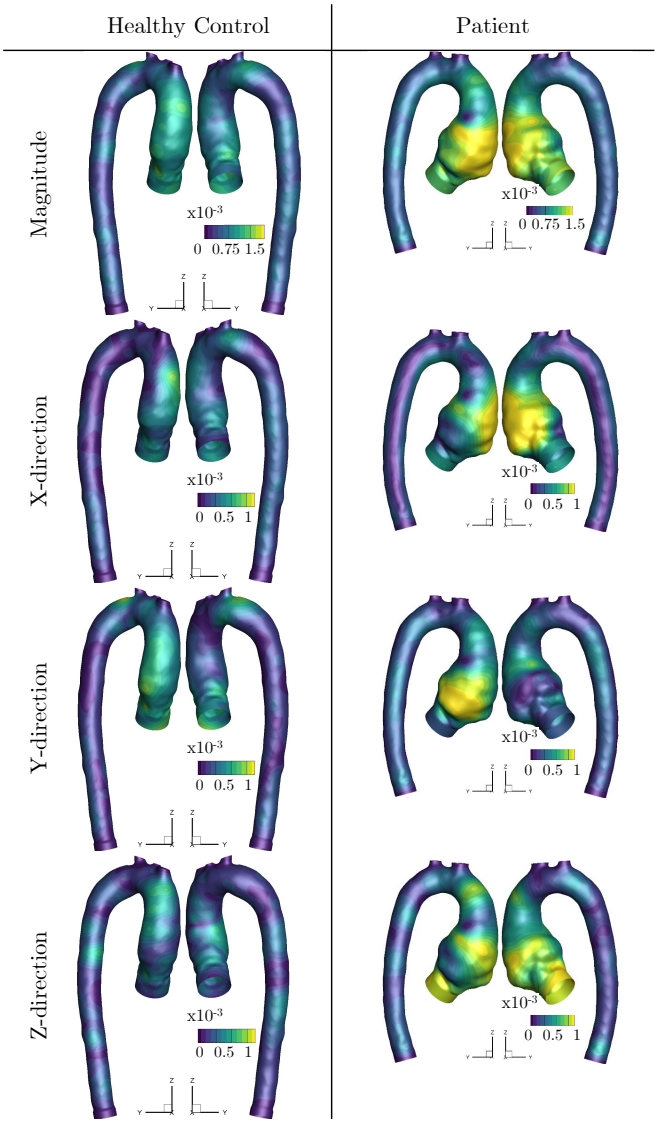

Figure 4.7: The time-average displacement (magnitude, x-direction, y-direction, and z-direction) during the cycle.

mid deceleration, and early diastole), for the healthy and patient-specific cases (both with static and dynamic simulations) are shown in Fig. 4.8 and Fig. 4.9, respectively. For MRI, the velocity field was reconstructed from 4D-flow MRI data extracted in planes in the flow direction. Note that for better visualization, used color maps are specifically adjusted for different cross-sections and time steps.

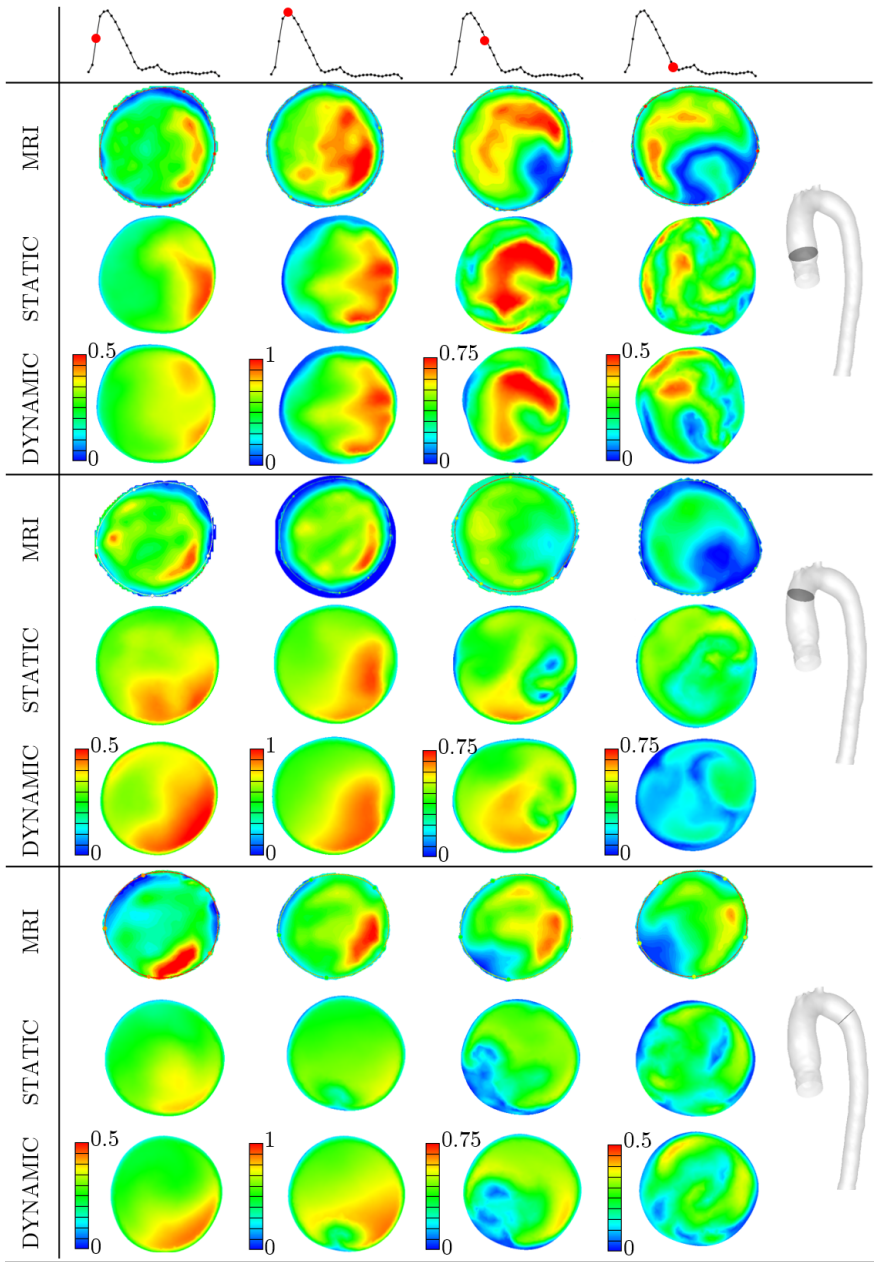

Figure 4.8: Velocity magnitude [m/s] at the visualized cross-sections of interest (Proximal Ascending Aorta (pAscAo - 1), Distal Ascending Aorta (dAscAo - 2), Proximal Descending Aorta (pDescAo - 3)) based on MRI, static, and dynamic CFD for healthy control (HC) at mid acceleration, peak systole, mid-deceleration, and early diastole; the scale of velocity magnitude is adjusted per plane/time-step.

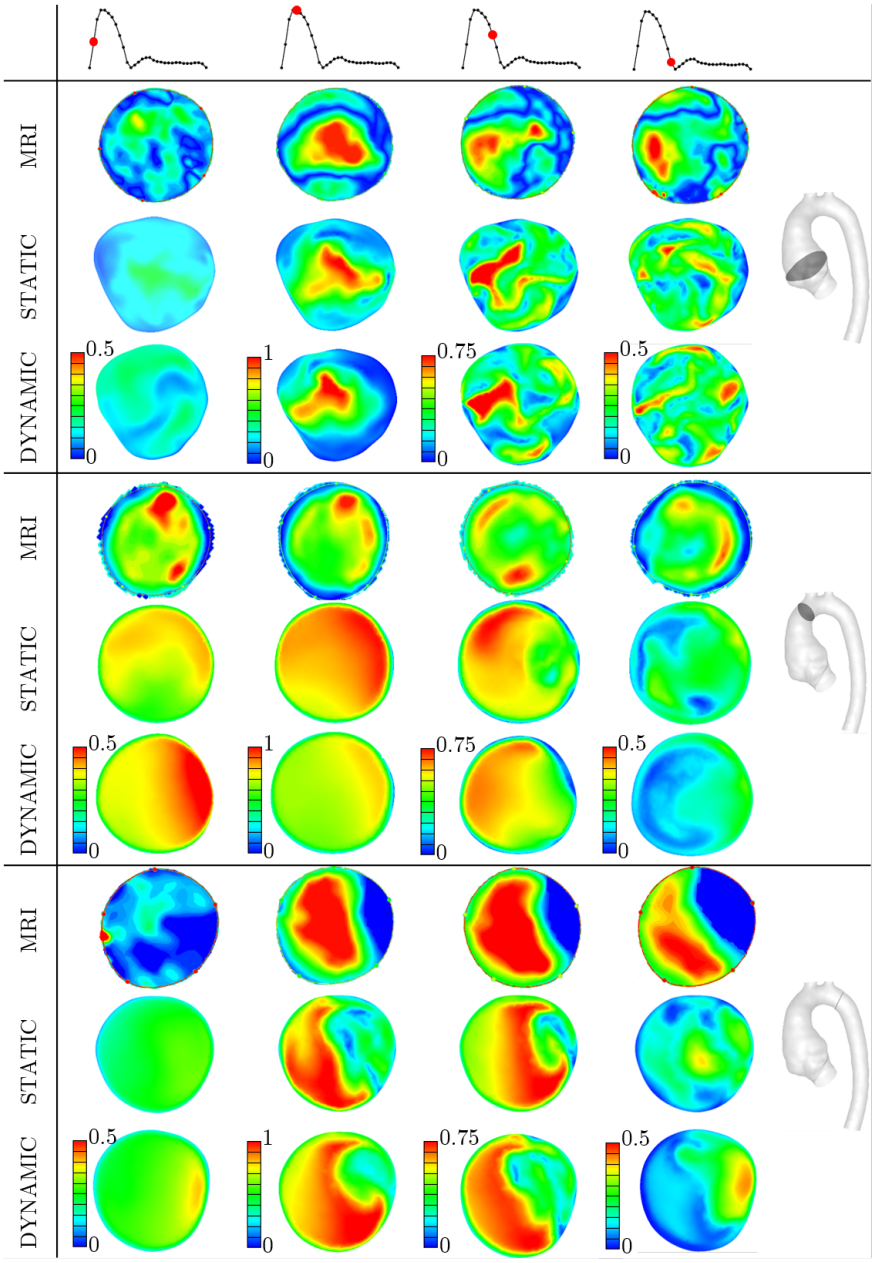

Figure 4.9: Velocity magnitude [m/s] at the visualized cross-sections of interest (Proximal Ascending Aorta (pAscAo - 1), Distal Ascending Aorta (dAscAo - 2), Proximal Descending Aorta (pDescAo - 3)) based on MRI, static, and dynamic CFD for the patient (P) at mid acceleration, peak systole, mid deceleration, and early diastole; the scale of velocity magnitude is adjusted per plane/time-step.

4.3.4 Effect of Wall Movement on TAWSS and OSI

Time-averaged wall shear stress (TAWSS) and oscillatory shear index (OSI) are two important flow-derived quantities often mentioned in the literature as potential biomarkers to evaluate the progression of aortic aneurysms. The contours of the TAWSS and OSI for the CFD_{static} and $CFD_{dynamic}$ simulations are shown in Fig. 4.10. To make the comparison between the static and dynamic simulations easier, we also provided contours of the percentage differences ΔTAWSS and ΔOSI. Note that for the dynamic simulation contours of the TAWSS and OSI are shown for the peak-systole geometry. Next, we have also calculated the mean values of the absolute difference over the whole aorta surface (without side branches) for TAWSS and OSI. The mean value of absolute ΔTAWSS for the healthy control was $\Delta TAWSS_{HC} = 2.72 \pm 4.93\%$ Pa, and $\Delta TAWSS_{P} = 7.47 \pm 14.18\%$ Pa for the patient-specific geometry. For the OSI difference, the mean value (of absolute ΔOSI) was $\Delta OSI_{HC} = 12.87 \pm 43.92\%$ for the former, and $\Delta OSI_{P} = 15.97 \pm 43.32\%$ for the later.

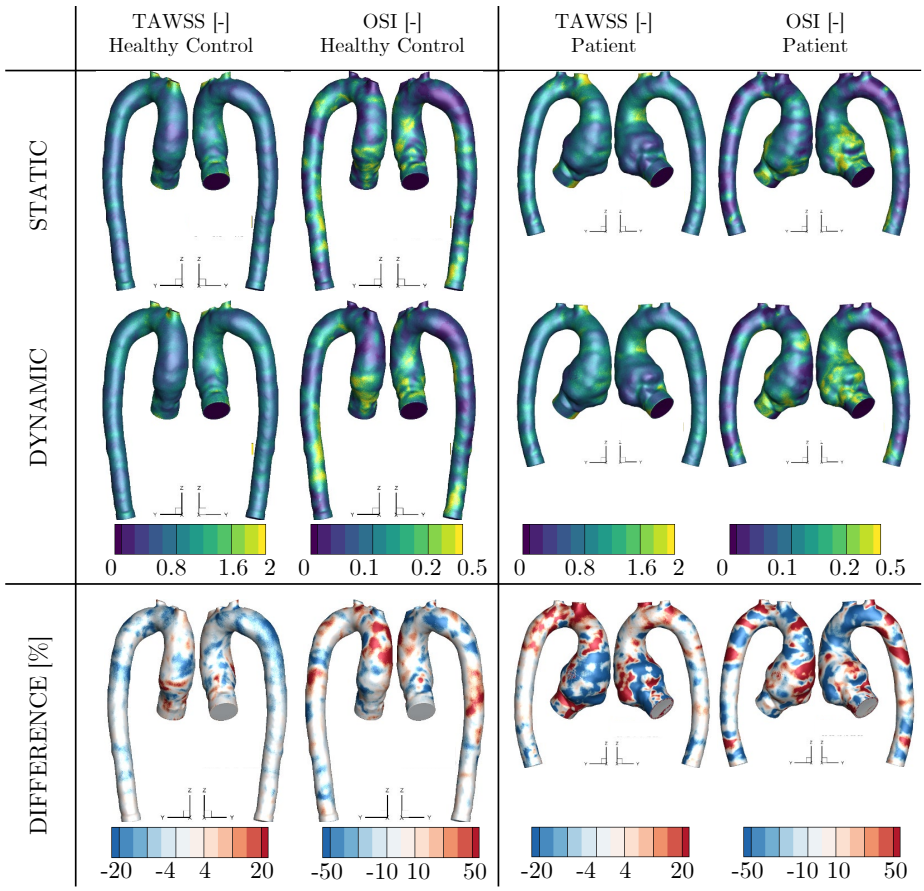

Figure 4.10: Time-averaged wall shear stress (TAWSS [Pa]) and Oscillatory Shear Index (OSI [-]) based on static and dynamic simulations and the absolute percentage difference for the respective quantities between static and dynamic simulations for healthy control and patient.

Finally, while we can understand the spatial distribution of ΔTAWSS and ΔOSI based on the surface plots, they are unable to show the locality of the highest differences between static and dynamic simulations with respect to the range of TAWSS and OSI. To overcome this, Fig. 4.11 shows the correlation between the dynamic TAWSS or OSI and the respective percentage difference (ΔTAWSS or ΔOSI [%]) for HC and P. In addition, we have plotted the average value of $\Delta\phi$ for each of the assessed quantities and a binned average for the OSI. In the case of the binned average, the data were grouped based on a specific range of OSI values (0.01) for the whole domain and average for the outliers with high OSI (i.e. when the number of points within a range of OSI was less than 100).

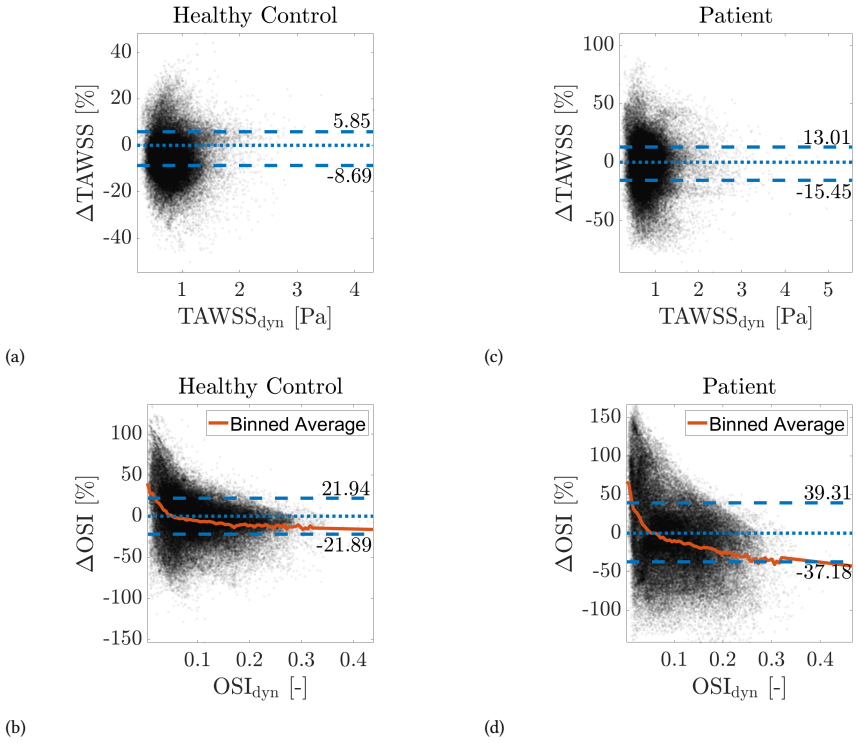

Figure 4.11: Correlation of time-averaged wall shear stress (TAWSS [Pa]) and oscillatory shear index (OSI [-]), both extracted from the dynamic simulations, with the respective percentage differences between static and dynamic simulations (ΔTAWSS or ΔOSI [%]) for TAWSS a) and OSI b) for the healthy control and TAWSS c) and OSI d) for the patient; we highlight the positive/negative average values of the differences (blue) and for OSI only, the binned average based on the OSI values (orange).

4.4 Discussion

In the present work, we proposed an image-based method for prescribing the motion of the aortic wall for CFD using RBF. The RBF method was chosen since it proved to be a viable approach to represent the complex motion of the aorta. By performing simulations with the pre-defined motion of the blood vessels, we avoid the necessity of obtaining detailed

information regarding the vessel wall (i.e., elasticity and thickness). This information is usually not readily available, making the patient-specific studies challenging for the traditional FSI methods [18–20, 22–24]. Additionally, the computational time of simulations with prescribed motion is comparable with static simulations, as can be seen from our results. This is an important factor, especially considering the clinical applications with larger population studies. We have performed static and dynamic simulations for two geometries: the healthy-control (HC) and patient-specific case (P) with a large TAA located close to the aortic root.

The prescribed RBF-based motion of the thoracic aorta matched well with the 4D-flow MRI, as illustrated in Fig. 4.5a for mid-acceleration. Some differences could be observed in the proximity of the aortic root. Close to the aortic root, the displacement is also the largest, as visualized in Fig. 4.5b and 4.7. In this region (ascending aorta), the motion is rather complex and is a result of the superposition of the axial and radial displacements. The longitudinal displacement (in the feet-head (FH) direction) generated by the physiological strain from the heart, makes an important contribution to the total displacement, as previously reported in several studies on aortic kinematics [13, 14, 44]. It is important to note that this FH-component of aortic motion is not included in the FSI studies of the aorta ([18–20]), nor in the studies that model the pre-defined aorta motion on the basis of its wall compliance ([22–24]), which can have a significant impact on the final results. In contrast to the ascending aorta, the descending aorta is less susceptible to motion due to the presence of the spinal column, and its displacement is dominantly in the radial direction [44].

The discrepancies between RBF and MRI in the proximity of the aortic root can also be found for the other key-frame geometries, Fig. 4.6. The agreement between the original segmentation and RBF, in terms of distance between the surface vertices, is good for most of the investigated aortic domain (as seen in Tab. 4.3), except for the root. While this could (potentially) be avoided by locally increasing the density of the control points, the final moving geometry does not have to improve with respect to realistic aortic kinematics. This is caused by the accuracy of the original segmentation, which decreases for key-frames further from the peak systole [45], (Fig. 4.6). The segmentation variability can be high, especially close to the root, as shown previously for healthy aortas [46]. Additionally, a similar argument can also be made for including more key-frame geometries. Currently, we only considered four geometries for the proof-of-concept study. This choice was motivated by the segmentation procedure being very time-consuming, with many manual adjustments necessary. Hence, including more details in the RBF procedure can, on the contrary, increase the amount of uncertainty and degrade our simulations.

Although we have only segmented a limited number of geometries to prescribe the movement, the selected key-frames probably contain the most radial expansion during the cycle. This allows us to capture most of the movement with the least amount of information required. Additionally, the ability of the proposed method to capture the movement based on only a limited number of segmentations is an important advantage for clinical use. In this case, the observer does not need to segment all the phases, saving valuable clinical practice time.

While the limitations behind the segmentation of 4D-flow MRI are well-known [45–47], our choice to use this method was motivated by the direct availability of measured flow data.

This allows us to obtain accurate inlet and outlet boundary conditions and an estimation of the moving domain from a singular measurement. As shown previously by several studies [38–41] and in 4.5, velocity profile from measurements should always be imposed as an inlet boundary condition, if available. Additionally, Gallo et al. [42] showed the importance of including as much patient-specific information as possible on all of the outlets of the studied domain to obtain accurate results. By utilizing 4D-flow MRI to obtain all of these, we are able to create a well-informed, fully patient-specific model of the moving aorta without the necessity of additional measurements on the subjects.

To validate the proposed model, we can directly utilize the 4D flow MRI. As can be seen in Fig. 4.8 for HC and in Fig. 4.9 for P, the computed profiles resemble well the ones acquired by MRI. Some differences can be observed, especially for lower velocity values (i.e., further from peak systole). These discrepancies could originate from the computational model (e.g., inaccurate inlet plane for boundary conditions [48]), as well as 4D-flow MRI. For these phases, a higher noise-to-signal ratio is present due to the static VENC. This can cause limited velocity field acquisition [49] for these phases. However, in general, the simulations can predict the blood flow behavior in the studied aortas correctly.

Since an increasing number of studies are investigating the effect of aberrant blood flow on the development and rupture of aortic aneurysms, we highlight here the effects of the aorta motion on changes in blood flow patterns. Based on the presented results, certain differences in blood flow patterns were obtained with the static (a rigid wall assumption) and dynamic (predefined aorta motion) simulations, Fig. 4.8 and Fig. 4.9. The latter showed slightly better agreement, qualitatively, with the 4D-Flow MRI measurements, especially during the decelerating part of the systole and early diastole. For example, in plane 2 for HC, during mid-deceleration and early diastole, the dynamic simulations were more accurate in capturing the velocity profile measured with 4D flow MRI. While these observations are only qualitative, they clearly show the effect of the aortic movement on the flow.

The flow-derived variables such as the TAWSS and OSI are often used as potential biomarkers to indicate the onset and growth of aortic aneurysm [5]. Elevated regions of WSS were related to more rapid degradation of the extracellular matrix [50]. This causes weakening of the aortic wall (due to lack of elastin), and it was linked to the growth of the TAA [50]. On the other end of the spectrum, low TAWSS may lead to endothelial dysfunction, correlated with thickening of the aortic wall [9, 51] Furthermore, high OSI affects the response of the endothelial cells, and it was connected to the onset of atherosclerosis [52], a condition with high prevalence in patients with aortic aneurysms [53]. Our simulations revealed significant differences between TAWSS and OSI calculated from the static and dynamic simulations for both geometries, Fig. 4.10. In static simulations, TAWSS is over-predicted, and OSI is under-predicted. This observation is in accordance with other studies in the literature that considered the aorta movement - either by FSI [17] or by prescribed motion [24, 28].

Additionally, we observed that aortic wall movement has a considerable effect on the whole range of TAWSS and OSI, Fig. 4.11. For OSI, it can be seen that the error introduced by the simulations is highest in the regions with low OSI. On the other hand, for higher values of OSI, which are physiologically important [52], the difference between static and dynamic simulation is lower, yet, still as high as 21% for HC and 37% for P. In the case of TAWSS, for which both low and high TAWSS are physiologically important[9, 50, 51],

we could not observe such a clear correlation, Here, the difference between static and dynamic simulations is similarly dominant for the whole range of TAWSS. These findings highlight the importance of including aortic wall motion in the simulations to prevent misinterpretation of the results.

We also found that the differences between static and dynamic CFD for both TAWSS and OSI are correlated with the magnitude of displacement, Fig. 4.7. The differences in both variables were most significant in the proximity of the aortic root and the ascending part of the aorta, i.e., in the regions where displacement is most prominent. In the arch and descending aorta, the differences between static and dynamic simulations and resulting TAWSS and OSI were smaller. Capellini et al. [28] presented an approach where only a portion of the aorta (ascending thoracic aorta) is considered moving, and the rest of the domain is static. For this case, they showed that the differences downstream of the moving region are negligible. Contrary, as shown in the presented study, the movement in the arch and descending aorta still affects the flow considerably and should not be omitted. In conclusion, the aspects of the movement of the whole aorta should be included in the new generation of CFD simulations for accurate modeling of blood flow.

Finally, we need to contextualize our findings with respect to other possible sources of uncertainty in the simulations. As shown in our previous study, WSS is highly affected by the segmentation variability, with a local deviation of up to 50% (at peak systole) [46]. Similar or higher uncertainty as found for OSI and TAWSS in our results was also reported due to inflow rates [54, 55] and outflow boundary conditions [42]. Nevertheless, due to a lack of data for dynamic simulations, specifically for simulations with prescribed motion, it is not possible to generalize whether rigid assumption for the aorta is sufficient in terms of uncertainty, unlike for other parts of the cardiovascular system [56]. For this, a more thorough follow-up study is necessary, including a larger number of pathologies.

Next, we address several limitations of the present work. To demonstrate the proof-of-concept of the adopted RBF-based morphing approach in mimicking the aortic motion, we have considered two geometries: the healthy control and the patient-specific TAA. Future studies can include significantly larger numbers of both subject and patient-specific cases. Moreover, the patient-specific cases should include additional aortic pathologies such as dissection and coarctation [57]. Nevertheless, our work aimed to investigate the feasibility, accuracy, and numerical efficiency of the proposed method. Since we have selected an advanced stage of TAA as one of the test cases, it is expected that the method will also perform well for less-developed pathologies. We also assumed that there was no aortic movement during the diastole. This assumption was a consequence of the unattainable segmentation of the 4D-flow MRI scans due to very low blood flow intensity during this period of the cardiac cycle. However, this assumption is valid since the aortic motion during diastole is limited [16], and we do not expect significant deviations from our findings. Finally, the presented simulation method with aortic motion was coupled with the 4D-flow MRI clinical data; here, we need to address two points: (1) The 4D-flow MRI acquisition is affected by several acquisition parameters such as efficient respiratory motion compensation, VENC, and Sense factor that reflects the amount of parallel imaging for acceleration. All of these can have an effect on the signal-to-noise ratio and hence the segmented data. (2) The current segmentation procedure requires significant manual adjustments to properly capture the exact wall position at particular time instants of the

cardiac cycle. We also addressed some of this segmentation variability on the calculated WSS in our previous study [46], where we observed significant variability in WSS due to the segmentation procedure. Since a similar protocol was also used in this study, this could also affect the prescribed wall movement. Additionally, using this technique hinders proper capturing of the aortic dilatation since the absolute difference between the root diameter of systolic and diastolic phase can be lower than the resolution of 4D-flow MRI, as reported by De Heer et al. [58]. However, here developed numerical simulation methodology can be directly integrated with other clinical imaging procedures as well (US, MRA, CT), which would improve the segmentation variability and the resolution to capture the motion properly.

4.5 Conclusions

In the present work, we showed how the aortic wall motion can be simulated by applying an efficient image-based geometry morphing approach based on the radial basis function (RBF) interpolation. The simulated aortic motion was in good agreement with the 4D-flow MRI extracted geometries. The developed method proved to be accurate and numerically robust for both considered cases: the healthy-control and the patient-specific aorta with an aneurysm in the aortic root. The computational time for dynamic simulations (with moving aortic walls) was similar to their static (with rigid wall assumption) counterparts, confirming the numerical efficiency of the proposed method. Effects of wall motion in the dynamic simulations were most prominent in the ascending aorta and this improved agreement with the 4D-flow MRI in comparison to the static simulations. We also report on the largest differences between the calculated TAWSS and OSI for static and dynamic simulations in the ascending part of the aorta. This shows the importance and necessity to include aortic wall motion in the CFD simulations in obtaining more accurate flow and flow-derived biomarkers, such as the TAWSS and OSI. Based on here presented proof-of-concept study on two geometries and improved agreement with the 4D-flow MRI, we propose to apply the presented moving wall approach on larger cohorts of patient-specific cases with various aortic pathologies.

Appendix A: Mesh Dependency

To investigate the mesh dependency of the simulations, we created three different meshes for HC (coarse - 0.83×10^6, medium - 1.58×10^6, and fine - 3.00×10^6 control volumes) and performed simulations at the peak-systolic flow conditions. Fig. 4.12 shows WSS for all three meshes and data extracted alongside a line following the aorta for all three meshes.

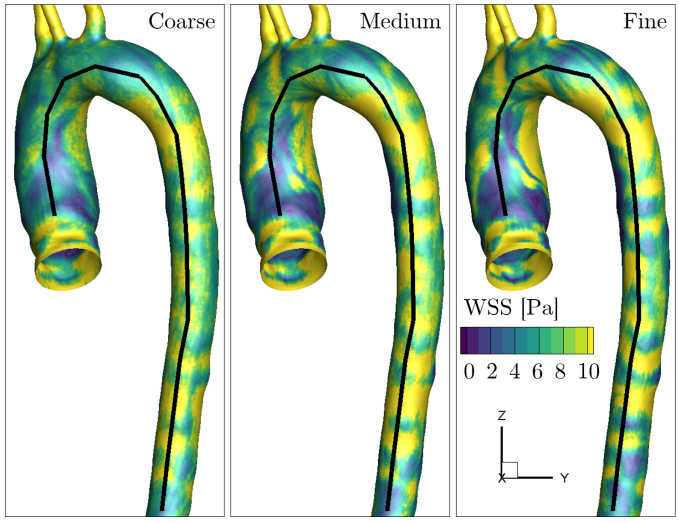

(a)

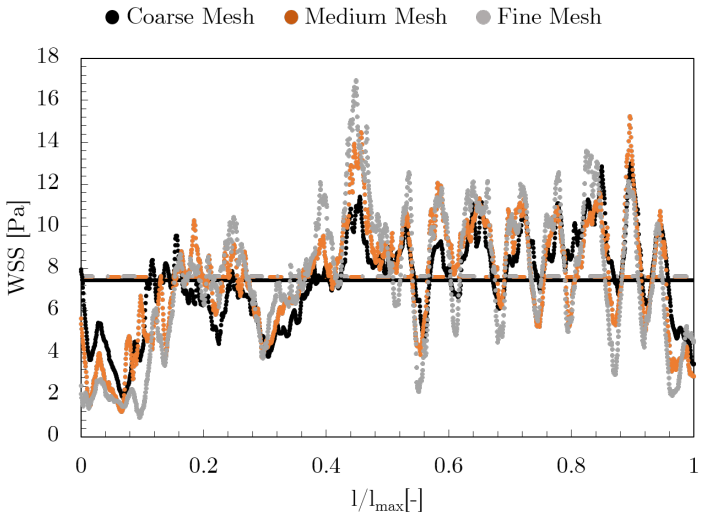

(b)

Figure 4.12: Wall shear stress (WSS [Pa]) for healthy control as obtained for coarse, medium, and fine mesh with visualized extraction line (a) and the data extracted alongside the line with normalized line distance (l/l_{max}) starting from the root with the respective averaged data (b) (coarse - black, medium - orange, fine - grey).

We have also estimated the Grid Convergence Index (GCI) [59]. The results of the GCI analysis are given in Tab.4.4.

Table 4.4: The total number of elements and resolution for mesh sizes coarse, medium, and fine are displayed. Furthermore, the average and maximum WSS over the extracted line, are given. GCI_a and GCI_b are calculated based on the average and maximum WSS respectively.

Mesh		Coarse	Medium	Fine
# cells	**[$\times 10^6$]**	0.83	1.58	3.00
Resolution	**[mm3]**	2	1.8	1.6
WSS_{mean}	**[Pa]**	7.45	7.60	7.63
GCI_a	**[%]**	N/A	0.076	0.014
WSS_{max}	**[Pa]**	13.01	15.24	16.93
GCI_b	**[%]**	N/A	2.095	1.347

Appendix B: Effect of Inlet Boundary Conditions

To study the possible effects of various inlet boundary conditions (BC) on the flow and WSS distribution we have performed three simulations (for the static aortic wall) with the following velocity profiles in the inlet plane: the MRI-based, parabolic, and plug. The MRI-based inlet was defined using a reconstructed plane at the inlet from the 4D-flow MRI data. The uniform (plug) and parabolic velocity profiles were reconstructed such that their averaged velocity profiles give the corresponding MRI-based inlet flow rate. Using these settings, we have performed simulations for both the healthy control and the patient-specific geometries and obtained WSS distributions (and differences between the inlet BCs) are shown in Fig. 4.13 and Fig. 4.14. To make an easier distinction, the range of the WSS contours and particular WSS differences (the color map values) were adjusted per the considered case. Additionally, we have extracted two characteristic profiles along the ascending (line A) and descending (line B) parts of the aortic wall, to analyze the results in detail. Due to the complexity of the mowing wall model, the inlet boundary conditions used in the literature are often simplified and defined as either plug or parabolic profiles. In the present work, we have demonstrated that the effects of the various specifications of the inlet velocity profiles were significant in the ascending aorta. In contrast, in descending part of the aorta, the impact of the various inlet velocity profiles was much less significant. Additionally, the quality of the segmentation in the proximity of the aortic inlet can have a significant impact on the calculated WSS distribution.

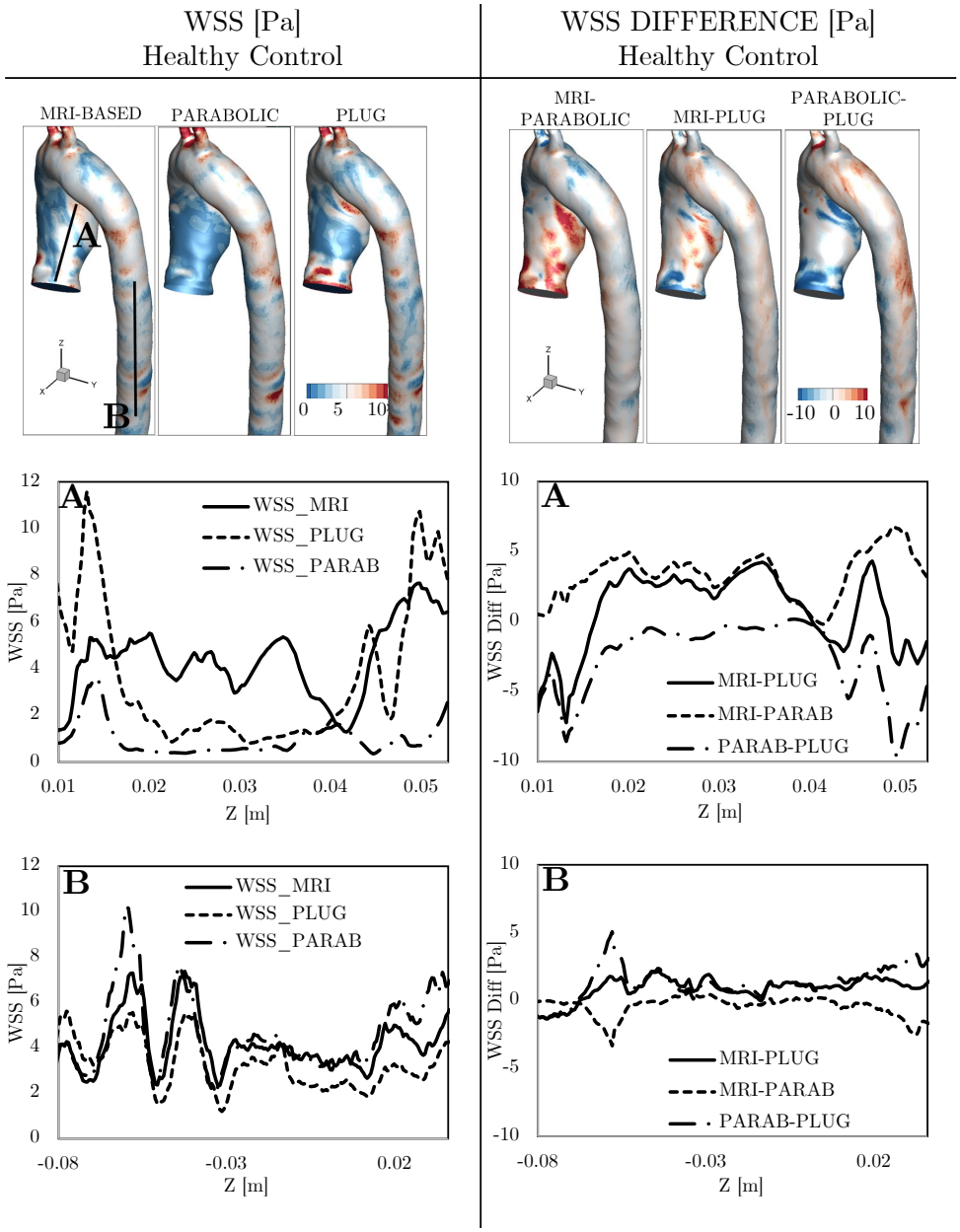

Figure 4.13: Comparison of wall shear stress (WSS in Pa) from CFD simulations with a varying inlet (MRI-based, parabolic, and plug) for healthy control and the absolute difference between MRI-based and parabolic, MRI-based and plug, and parabolic and plug. Detailed information was also extracted alongside lines (A - ascending aorta, B - descending aorta).

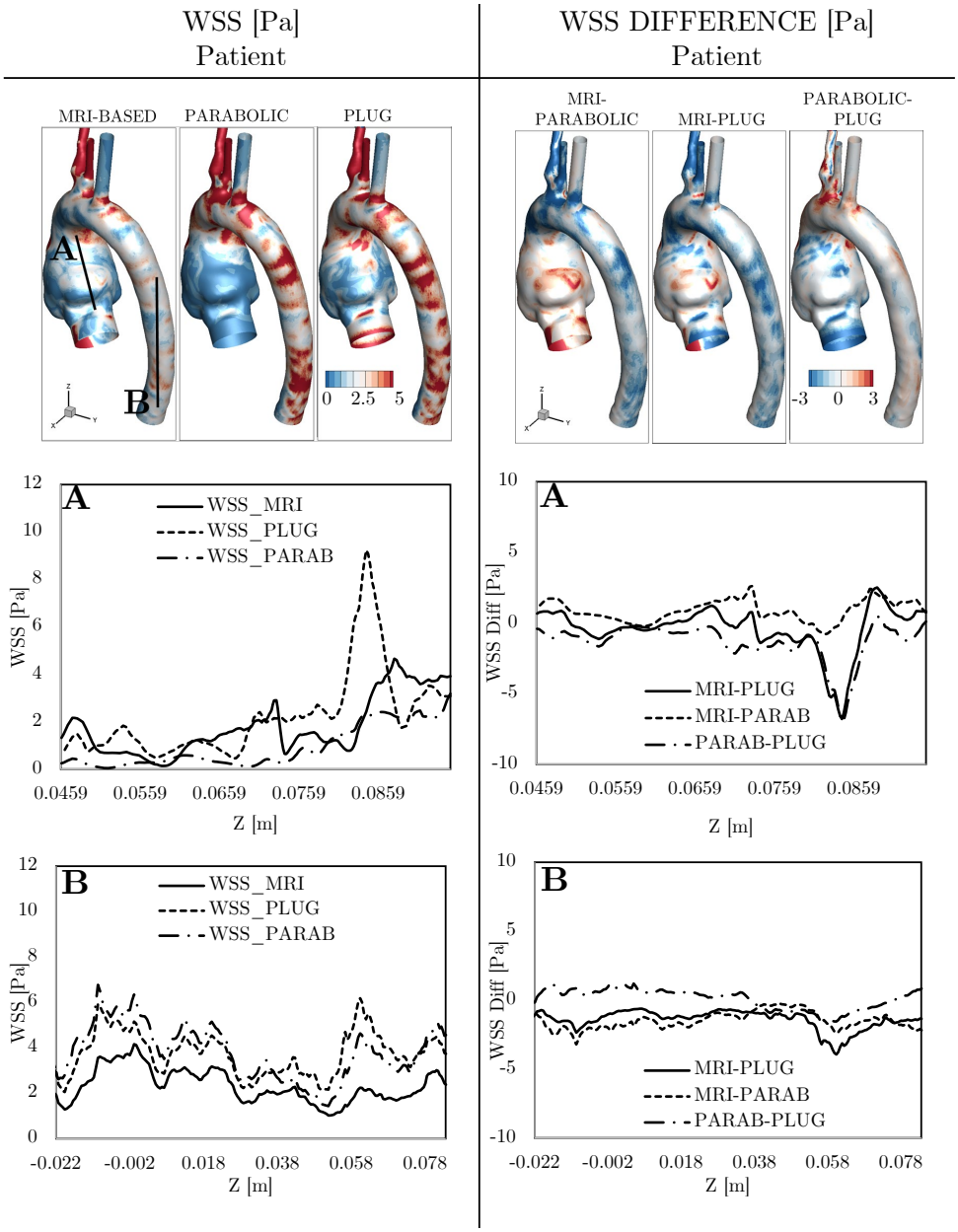

Figure 4.14: Comparison of wall shear stress (WSS in Pa) from CFD simulations with a varying inlet (MRI-based, parabolic, and plug) for the patient and the absolute difference between MRI-based and parabolic, MRI-based and plug, and parabolic and plug. Detailed information was also extracted alongside lines (A - ascending aorta, B - descending aorta).

References

[1] G. Johansson, U. Markström, and J. Swedenborg, *Ruptured thoracic aortic aneurysms: A study of incidence and mortality rates,* Journal of Vascular Surgery **21**, 985 (1995).

[2] L. A. Pape, T. T. Tsai, E. M. Isselbacher, J. K. Oh, P. T. O'Gara, A. Evangelista, R. Fattori, G. Meinhardt, S. Trimarchi, E. Bossone, T. Suzuki, J. V. Cooper, J. B. Froehlich, C. A. Nienaber, and K. A. Eagle, *Aortic diameter ≥5.5 cm is not a good predictor of type a aortic dissection,* Circulation **116**, 1120 (2007).

[3] M. J. Sweeting, S. G. Thompson, L. C. Brown, and o. b. o. t. R. c. Powell, J T, *Meta-analysis of individual patient data to examine factors affecting growth and rupture of small abdominal aortic aneurysms,* British Journal of Surgery **99**, 655 (2012).

[4] S. Pasta, V. Agnese, A. Gallo, F. Cosentino, M. Di Giuseppe, G. Gentile, G. M. Raffa, J. F. Maalouf, H. I. Michelena, D. Bellavia, P. G. Conaldi, and M. Pilato, *Shear stress and aortic strain associations with biomarkers of ascending thoracic aortic aneurysm,* The Annals of Thoracic Surgery **110**, 1595 (2020).

[5] M. Cibis, W. V. Potters, F. J. Gijsen, H. Marquering, P. van Ooij, E. vanBavel, J. J. Wentzel, and A. J. Nederveen, *The effect of spatial and temporal resolution of cine phase contrast MRI on wall shear stress and oscillatory shear index assessment,* PLOS ONE **11**, 1 (2016).

[6] S. Kenjereš, *On recent progress in modelling and simulations of multi-scale transfer of mass, momentum and particles in bio-medical applications,* Flow, Turbulence and Combustion **96**, 837 (2016).

[7] K. M. Tse, P. Chiu, H. P. Lee, and P. Ho, *Investigation of hemodynamics in the development of dissecting aneurysm within patient-specific dissecting aneurismal aortas using computational fluid dynamics (CFD) simulations,* Journal of Biomechanics **44**, 827 (2011).

[8] R. Perinajová, J. F. Juffermans, J. L. Mercado, J.-P. Aben, L. Ledoux, J. J. M. Westenberg, H. J. Lamb, and S. Kenjereš, *Assessment of turbulent blood flow and wall shear stress in aortic coarctation using image-based simulations,* BioMedical Engineering OnLine **20**, 84 (2021).

[9] S. Jamaleddin Mousavi, R. Jayendiran, S. Farzaneh, S. Campisi, M. Viallon, P. Croisille, and S. Avril, *Coupling hemodynamics with mechanobiology in patient-specific computational models of ascending thoracic aortic aneurysms,* Computer Methods and Programs in Biomedicine **205**, 106107 (2021).

[10] R. Jayendiran, S. Campisi, M. Viallon, P. Croisille, and S. Avril, *Hemodynamics alteration in patient-specific dilated ascending thoracic aortas with tricuspid and bicuspid aortic valves,* Journal of Biomechanics **110**, 109954 (2020).

[11] Y. Zhu, R. Chen, Y.-H. Juan, H. Li, J. Wang, Z. Yu, and H. Liu, *Clinical validation and assessment of aortic hemodynamics using computational fluid dynamics simulations from computed tomography angiography,* BioMedical Engineering OnLine **17**, 53 (2018).

[12] Q. Lu, W. Lin, R. Zhang, R. Chen, X. Wei, T. Li, Z. Du, Z. Xie, Z. Yu, X. Xie, and H. Liu, *Validation and diagnostic performance of a CFD-based non-invasive method for the diagnosis of aortic coarctation,* Frontiers in Neuroinformatics **14**, 59 (2020).

[13] G. W. Burggraf, M. T. Mathew, and J. O. Parker, *Aortic root motion determined by ultrasound: Relation to cardiac performance in man,* Catheterization and Cardiovascular Diagnosis **4**, 29 (1978).

[14] M. Stuber, M. B. Scheidegger, S. E. Fischer, E. Nagel, F. Steinemann, O. M. Hess, and P. Boesiger, *Alterations in the local myocardial motion pattern in patients suffering from pressure overload due to aortic stenosis,* Circulation **100**, 361 (1999).

[15] T. Nosek, *Essentials of Human Physiology* (Gold Standard Multimedia Incorporated, 1998).

[16] J.-P. Guo, X. Jia, Z. Sai, Y.-Y. Ge, S. Wang, and W. Guo, *Thoracic aorta dimension changes during systole and diastole: Evaluation with ecg-gated computed tomography,* Annals of Vascular Surgery **35**, 168 (2016).

[17] M. Alimohammadi, J. M. Sherwood, M. Karimpour, O. Agu, S. Balabani, and V. Díaz-Zuccarini, *Aortic dissection simulation models for clinical support: fluid-structure interaction vs. rigid wall models,* BioMedical Engineering OnLine **14**, 34 (2015), 25881252[pmid].

[18] P. Reymond, P. Crosetto, S. Deparis, A. Quarteroni, and N. Stergiopulos, *Physiological simulation of blood flow in the aorta: Comparison of hemodynamic indices as predicted by 3-D FSI, 3-D rigid wall and 1-D models,* Medical Engineering & Physics **35**, 784 (2013).

[19] Y. Qiao, Y. Zeng, Y. Ding, J. Fan, K. Luo, and T. Zhu, *Numerical simulation of two-phase non-Newtonian blood flow with fluid-structure interaction in aortic dissection,* Computer Methods in Biomechanics and Biomedical Engineering **22**, 620 (2019), pMID: 30822150.

[20] R. Pons, A. Guala, J. F. Rodríguez-Palomares, J. C. Cajas, L. Dux-Santoy, G. Teixidó-Tura, J. J. Molins, M. Vázquez, A. Evangelista, and J. Martorell, *Fluid-structure interaction simulations outperform computational fluid dynamics in the description of thoracic aorta haemodynamics and in the differentiation of progressive dilation in marfan syndrome patients,* Royal Society Open Science **7**, 191752 (2020).

[21] E. Vignali, E. Gasparotti, S. Celi, and S. Avril, *Fully-coupled FSI computational analyses in the ascending thoracic aorta using patient-specific conditions and anisotropic material properties,* Frontiers in Physiology **12** (2021), 10.3389/fphys.2021.732561.

[22] M.-K. Ganten, T. F. Weber, H. von Tengg-Kobligk, D. Böckler, W. Stiller, P. Geisbüsch, G. W. Kauffmann, S. Delorme, M. Bock, and H.-U. Kauczor, *Motion characterization of aortic wall and intimal flap by ecg-gated CT in patients with chronic b-dissection,* European Journal of Radiology **72**, 146 (2009), imaging of Soft Tissue Sarcomas II.

[23] M. Bonfanti, S. Balabani, J. P. Greenwood, S. Puppala, S. Homer-Vanniasinkam, and V. Díaz-Zuccarini, *Computational tools for clinical support: a multi-scale compliant model for haemodynamic simulations in an aortic dissection based on multi-modal imaging data,* Journal of The Royal Society Interface **14**, 20170632 (2017).

[24] M. Bonfanti, S. Balabani, M. Alimohammadi, O. Agu, S. Homer-Vanniasinkam, and V. Díaz-Zuccarini, *A simplified method to account for wall motion in patient-specific blood flow simulations of aortic dissection: Comparison with fluid-structure interaction,* Medical Engineering & Physics **58**, 72 (2018).

[25] L. Geronzi, E. Gasparotti, K. Capellini, U. Cella, C. Groth, S. Porziani, A. Chiappa, S. Celi, and M. E. Biancolini, *Advanced radial basis functions mesh morphing for high fidelity fluid-structure interaction with known movement of the walls: Simulation of an aortic valve,* in *Computational Science – ICCS 2020*, edited by V. V. Krzhizhanovskaya, G. Závodszky, M. H. Lees, J. J. Dongarra, P. M. A. Sloot, S. Brissos, and J. Teixeira (Springer International Publishing, Cham, 2020) pp. 280–293.

[26] F. Xu and S. Kenjereš, *Numerical simulations of flow patterns in the human left ventricle model with a novel dynamic mesh morphing approach based on radial basis function,* Computers in Biology and Medicine **130**, 104184 (2021).

[27] K. Capellini, E. Vignali, E. Costa, E. Gasparotti, M. E. Biancolini, L. Landini, V. Positano, and S. Celi, *Computational Fluid Dynamic Study for aTAA Hemodynamics: An Integrated Image-Based and Radial Basis Functions Mesh Morphing Approach,* Journal of Biomechanical Engineering **140** (2018), 10.1115/1.4040940.

[28] K. Capellini, E. Gasparotti, U. Cella, E. Costa, B. M. Fanni, C. Groth, S. Porziani, M. E. Biancolini, and S. Celi, *A novel formulation for the study of the ascending aortic fluid dynamics with in vivo data,* Medical Engineering & Physics **91**, 68 (2021).

[29] N. Di Domenico, C. Groth, A. Wade, T. Berg, and M. Biancolini, *Fluid structure interaction analysis: vortex shedding induced vibrations,* Procedia Structural Integrity **8**, 422 (2018), aIAS2017 - 46th Conference on Stress Analysis and Mechanical Engineering Design, 6-9 September 2017, Pisa, Italy.

[30] A. de Boer, M. van der Schoot, and H. Bijl, *Mesh deformation based on radial basis function interpolation,* Computers & Structures **85**, 784 (2007), fourth MIT Conference on Computational Fluid and Solid Mechanics.

[31] M. E. Biancolini, U. Cella, C. Groth, and M. Genta, *Static aeroelastic analysis of an aircraft wind-tunnel model by means of modal RBF mesh updating,* Journal of Aerospace Engineering **29**, 04016061 (2016).

[32] C. Groth, M. E. Biancolini, E. Costa, and U. Cella, *Validation of high fidelity computational methods for aeronautical FSI analyses,* in *Flexible Engineering Toward Green Aircraft* (Springer, 2020) pp. 29–48.

[33] L. Antiga, M. Piccinelli, L. Botti, B. Ene-Iordache, A. Remuzzi, and D. A. Steinman, *An image-based modeling framework for patient-specific computational hemodynamics,* Medical & Biological Engineering & Computing **46**, 1097 (2008).

[34] G. Taubin, *Curve and surface smoothing without shrinkage,* in *Proceedings of IEEE International Conference on Computer Vision* (1995) pp. 852–857.

[35] N. Dyn, D. Levine, and J. A. Gregory, *A butterfly subdivision scheme for surface interpolation with tension control,* ACM Trans. Graph. **9**, 160–169 (1990).

[36] S. S. Khalafvand, F. Xu, J. Westenberg, F. Gijsen, and S. Kenjeres, *Intraventricular blood flow with a fully dynamic mitral valvle model,* Computers in Biology and Medicine **104**, 197 (2019).

[37] I. ANSYS, ed., *Ansys fluent theory guide,* (2017) Chap. 4, pp. 39–91.

[38] U. Morbiducci, R. Ponzini, D. Gallo, C. Bignardi, and G. Rizzo, *Inflow boundary conditions for image-based computational hemodynamics: Impact of idealized versus measured velocity profiles in the human aorta,* Journal of Biomechanics **46**, 102 (2013).

[39] P. Youssefi, A. Gomez, C. Arthurs, R. Sharma, M. Jahangiri, and C. Alberto Figueroa, *Impact of Patient-Specific Inflow Velocity Profile on Hemodynamics of the Thoracic Aorta,* Journal of Biomechanical Engineering **140** (2017), 10.1115/1.4037857.

[40] S. Pirola, O. A. Jarral, D. P. O'Regan, G. Asimakopoulos, J. R. Anderson, J. R. Pepper, T. Athanasiou, and X. Y. Xu, *Computational study of aortic hemodynamics for patients with an abnormal aortic valve: The importance of secondary flow at the ascending aorta inlet,* APL Bioengineering **2**, 026101 (2018).

[41] C. H. Armour, B. Guo, S. Pirola, S. Saitta, Y. Liu, Z. Dong, and X. Y. Xu, *The influence of inlet velocity profile on predicted flow in type b aortic dissection,* Biomechanics and Modeling in Mechanobiology **20**, 481 (2021).

[42] D. Gallo, G. De Santis, F. Negri, D. Tresoldi, R. Ponzini, D. Massai, M. A. Deriu, P. Segers, B. Verhegghe, G. Rizzo, and U. Morbiducci, *On the use of in vivo measured flow rates as boundary conditions for image-based hemodynamic models of the human aorta: Implications for indicators of abnormal flow,* Annals of Biomedical Engineering **40**, 729 (2012).

[43] F. Gijsen, F. van de Vosse, and J. Janssen, *The influence of the non-newtonian properties of blood on the flow in large arteries: steady flow in a carotid bifurcation model,* Journal of Biomechanics **32**, 601 (1999).

[44] A. M. Sailer, B. A. J. M. Wagemans, M. Das, M. W. de Haan, P. J. Nelemans, J. E. Wildberger, and G. W. H. Schurink, *Quantification of respiratory movement of the aorta and side branches,* Journal of Endovascular Therapy **22**, 905 (2015).

[45] J. F. Juffermans, J. J. Westenberg, P. J. van den Boogaard, A. A. Roest, H. C. van Assen, R. L. van der Palen, and H. J. Lamb, *Reproducibility of aorta segmentation on 4D flow MRI in healthy volunteers,* Journal of Magnetic Resonance Imaging **n/a** (2020), 10.1002/jMRI.27431.

[46] R. Perinajová, J. F. Juffermans, J. J. Westenberg, R. L. van der Palen, P. J. van den Boogaard, H. J. Lamb, and S. Kenjereš, *Geometrically induced wall shear stress variability in CFD-MRI coupled simulations of blood flow in the thoracic aortas,* Computers in Biology and Medicine **133**, 104385 (2021).

[47] P. A. Corrado, A. L. Wentland, J. Starekova, A. Dhyani, K. N. Goss, and O. Wieben, *Fully automated intracardiac 4D flow MRI post-processing using deep learning for biventricular segmentation,* European Radiology **32**, 5669 (2022).

[48] M. E. Casciaro, A. F. Pascaner, F. N. Guilenea, J. Alcibar, U. Gencer, G. Soulat, E. Mousseaux, and D. Craiem, *4D flow MRI: impact of region of interest size, angulation and spatial resolution on aortic flow assessment,* Physiol Meas **42** (2021).

[49] L. E. Ma, M. Markl, K. Chow, A. Vali, C. Wu, and S. Schnell, *Efficient triple-venc phase-contrast MRI for improved velocity dynamic range,* Magnetic Resonance in Medicine **83**, 505 (2020).

[50] D. G. Guzzardi, A. J. Barker, P. van Ooij, S. C. Malaisrie, J. J. Puthumana, D. D. Belke, H. E. Mewhort, D. A. Svystonyuk, S. Kang, S. Verma, J. Collins, J. Carr, R. O. Bonow, M. Markl, J. D. Thomas, P. M. McCarthy, and P. W. Fedak, *Valve-related hemodynamics mediate human bicuspid aortopathy: Insights from wall shear stress mapping,* Journal of the American College of Cardiology **66**, 892 (2015).

[51] J. E. Carroll, E. S. Colley, S. D. Thomas, R. L. Varcoe, A. Simmons, and T. J. Barber, *Tracking geometric and hemodynamic alterations of an arteriovenous fistula through patient-specific modelling,* Computer Methods and Programs in Biomedicine **186**, 105203 (2020).

[52] A. Chakraborty, S. Chakraborty, V. R. Jala, B. Haribabu, M. K. Sharp, and R. E. Berson, *Effects of biaxial oscillatory shear stress on endothelial cell proliferation and morphology,* Biotechnology and Bioengineering **109**, 695 (2012).

[53] D. Reed, C. Reed, G. Stemmermann, and T. Hayashi, *Are aortic aneurysms caused by atherosclerosis?* Circulation **85**, 205 (1992).

[54] S. Bozzi, U. Morbiducci, D. Gallo, R. Ponzini, G. Rizzo, C. Bignardi, and G. Passoni, *Uncertainty propagation of phase contrast-MRI derived inlet boundary conditions in computational hemodynamics models of thoracic aorta,* Computer Methods in Biomechanics and Biomedical Engineering **20**, 1104 (2017).

[55] A. Marzo, P. Singh, I. Larrabide, A. Radaelli, S. Coley, M. Gwilliam, I. D. Wilkinson, P. Lawford, P. Reymond, U. Patel, A. Frangi, and D. R. Hose, *Computational hemodynamics in cerebral aneurysms: The effects of modeled versus measured boundary conditions,* Annals of Biomedical Engineering **39**, 884 (2011).

[56] D. A. Steinman and V. M. Pereira, *How patient specific are patient-specific computational models of cerebral aneurysms? an overview of sources of error and variability,* Neurosurgical Focus FOC **47**, E14 (2019).

[57] R. Erbel, *Diseases of the thoracic aorta,* Heart **86**, 227 (2001).

[58] L. M. de Heer, R. P. J. Budde, W. P. T. M. Mali, A. M. de Vos, L. A. van Herwerden, and J. Kluin, *Aortic root dimension changes during systole and diastole: evaluation with ecg-gated multidetector row computed tomography,* Int J Cardiovasc Imaging **27**, 1195 (2011).

[59] P. J. Roache, K. N. Ghia, and F. M. White, *Editorial Policy Statement on the Control of Numerical Accuracy,* Journal of Fluids Engineering **108**, 2 (1986).

5

Modelling of NO and O_2 mass transfer in aorta

There is a pressing need to establish novel biomarkers to predict the progression of thoracic aortic aneurysm (TAA) dilatation. Aside from hemodynamics, the roles of oxygen (O_2) and nitric oxide (NO) in TAA pathogenesis are potentially significant. As such, it is imperative to comprehend the relationship between aneurysm presence and species distribution in both the lumen and aortic wall. Given the limitations of existing imaging methods, we propose the use of patient-specific computational fluid dynamics (CFD) to explore this relationship. We have performed CFD simulations of O_2 and NO mass transfer in the lumen and aortic wall for two cases: a healthy control (HC) and a patient with TAA, both acquired using 4D-flow magnetic resonance imaging (MRI). The mass transfer of O_2 was based on active transport by hemoglobin, while the local variations of the wall shear stress (WSS) drove NO production. Comparing hemodynamic properties, the time-averaged WSS was considerably lower for TAA, while the oscillatory shear index and endothelial cell activation potential were notably elevated. O_2 and NO showed a non-uniform distribution within the lumen and an inverse correlation between the two species. We identified several locations of hypoxic regions for both cases due to lumen-side mass transfer limitations. In the wall, NO varied spatially, with a clear distinction between TAA and HC. In conclusion, the hemodynamics and mass transfer of NO in the aorta exhibit the potential to serve as a diagnostic biomarker for TAA. Furthermore, hypoxia may provide additional insights into the onset of other aortic pathologies.

This chapter had been published as: R. Perinajová, J. F. Juffermans, C. Borrás Álvarez-Cuevas, J. J. Westenberg, H. J. Lamb, S. Kenjereš, Influence of aortic aneurysm on the local distribution of NO and O_2 using image-based computational fluid dynamics, Computers in Biology and Medicine 160 (2023).

5.1 Introduction

Thoracic aortic aneurysm (TAA) is a progressive pathology of the aorta characterized by vessel dilatation, dysfunction of vascular smooth muscle cells, and remodeling of the extracellular matrix, as described by the European Society of Cardiology [1]. Given that this disease is primarily asymptomatic, the rupture of TAA is associated with high mortality rates [2]. Therefore, it is crucial to define new biomarkers to identify the genesis, growth, and rupture of TAA. Recent studies have suggested that the distribution of Oxygen (O_2) and Nitric Oxide (NO) in the aorta could be potential new biomarkers for TAA. TAA tissue exhibits O_2 deficiency (hypoxia) [3]. Moreover, an insufficient supply of O_2 to the aortic wall was linked to the genesis of abdominal aortic aneurysm (AAA) [4, 5], likely due to the scarcity of vasa vasorum in this section of the aorta [6]. NO is a regulator in vascular homeostasis and was proposed as a potential key indicator for the development of TAA in patients with Marfan syndrome [7, 8]. Elevated NO pathways were observed in individuals with this genetic condition [7], and NO was found to be a significant contributor to the development of TAA in animal models and patients [8]. Therefore, analyzing the behavior of these two molecules in patients with TAA could lead to the identification of direct biochemical markers that estimate the risk of disease progression and rupture.

However, the potential measurement methods for non-invasive assessment of O_2 and NO concentration in the lumen and aortic wall currently do not have a sufficient spatial resolution, as reported in recent studies [9–12]. As a viable alternative, we have previously demonstrated the usefulness of image-based computational fluid dynamics (CFD) in providing insights into blood flow dynamics in the aorta [13, 14]. Here, we have to emphasize the subject- and patient-specific nature of simulations, where the geometry and boundary conditions should be based on actual measurements, such as 4D-flow magnetic resonance imaging (4D-flow MRI). By utilizing a patient-specific model based on 4D-flow MRI, we can expand the CFD model to account for the mass transfer of these species. However, it is imperative to consider the complex interplay between O_2, NO, and various actors in the vascular system to ensure a physiologically accurate representation of the model.

O_2 is transferred within the cardiovascular system by two distinct mechanisms: diffusion as free species in plasma and binding to hemoglobin, a protein in the erythrocytes. The latter process is the primary mode and contributes to over 98% of total O_2 transport. However, at low shear rates, O_2 is released from the hemoglobin, and free diffusion becomes dominant. This process is particularly pronounced in the capillaries and the proximity of the arterial walls in (the low-shear region) of the great vessels. Therefore, modeling both mechanisms simultaneously is essential [15]. Within the arterial wall, O_2 is supplied by both the lumen and the vasa vasorum and consumed by the tissue. For modeling NO, the focus must be on three primary mechanisms: production, transport, and consumption. First, NO production occurs mainly in the endothelial layer of the arterial wall and is moderated by local wall shear stress (WSS) [16, 17] due to the activation of endothelial cells. The second mechanism involves NO transport from the endothelial layer to the smooth muscle cells and into the arterial wall, mainly driven by diffusion. In the opposite direction, NO is transported within the lumen by combined diffusion and convection. Finally, the primary NO sink is its reaction with hemoglobin to form a complex and oxidation to nitrate in the lumen. The reaction with cytoglobin is the major contributor to NO consumption in

the arterial wall [16, 17].

Numerous investigations have been conducted on modeling the transport processes of O_2 [15, 18] and NO [19–23] in idealized or large arteries, such as the aorta. However, the combined effects of hemodynamics and both species were not examined in the aorta. As reported by Allen et al., hypoxia can stimulate the release of NO from red blood cells [24] and, by that, affect vasodilation. Thus, understanding the relationship between the distribution of O_2 and NO can yield valuable insights into the hemodynamic regulation of arterial behavior. Finally, although most studies demonstrated the limitations of O_2 and NO transport in the lumen, the effect on the aortic wall and its remodeling are usually omitted due to the increased complexity of the computational model.

In this study, we put forth the hypothesis that the distribution of O_2 and NO in the aorta is significantly influenced by hemodynamics and the presence of an aneurysm and may serve as an indicator for aneurysm pathogenesis. To investigate this hypothesis, we simulated the interplay between blood flow and mass transfer in the aorta and its wall for two molecules: O_2 and NO. To model the aortic wall, we employed a single-layer approximation with averaged properties to incorporate the effect of intima, media, and adventitia. We developed a model for mass transfer of O_2 within the aorta and aortic wall and its consumption by the wall. In addition, we introduce a model for NO production, which is driven by local hemodynamics and biochemical reactions in the blood and aortic tissue. By using this computational framework, we were able to simulate and comprehend the processes that occur within the aorta and aortic wall in greater detail. We conducted simulations of blood flow with the mass transfer of both studied species in two case-specific geometries: a healthy control (HC) and a patient (P) with a root aneurysm. Finally, based on the analysis of hemodynamics and mass transfer properties of these two cases, we propose potential biomarkers that may indicate TAA pathogenesis.

5.2 Methods

5.2.1 Studied Cases

The Medical Ethics Committee approved this study protocol of the Leiden University Medical Center (G20.149 for P and P18.034 for HC). Moreover, informed consent was signed by both of the subjects. We have studied two different subjects - a healthy control (HC, Fig. 5.1a) and a patient with a root aneurysm with D_{max} = 5 cm (P, Fig. 5.1b)).

5.2.2 MRI Data

Both P (female, 67 years old, heart rate during acquisition: 48 bpm) and HC (male, 80 years old, heart rate during acquisition: 62 bpm) were examined using 4D-flow MRI on a 3T system (Elition, Philips Healthcare, Best, The Netherlands). The MRI acquisition protocol used a hemidiaphragm respiratory navigator with retrospective electrocardiogram gating. All of the additional details about the MRI sequence can be found in Tab. 5.1

The subject-specific domain for the lumen-only simulations was obtained by segmenting the 4D-flow MRI data set using CAAS MR Solutions v5.2. (Pie Medical Imaging, Maastricht, The Netherlands). The segmentation protocol is identical for both studied subjects, and the details can be found in our previous study [14]. The segmented geometries, after additional pre-processing using the Vascular Modeling Toolkit (VMTK), can be found in Fig. 5.1 with

Table 5.1: Parameters of 4D-flow MRI sequence for healthy control and patient.

		Healthy Control	Patient
Velocity encoding	**[cm/s]**	150	160
Reconstructed temporal resolution	**[ms]**	28	38
Echo time	**[ms]**	2.6	2.7
Repetition time	**[ms]**	4.5	4.6
Flip angle	**[°]**	10	10
Acquired isotropic resolution	**[mm]**	2.5	2.7
Field of view	**[mm^3]**	430x70x280	350x80x220
Turbo field echo factor	**[-]**	2	2
Parallel imaging factor	**[-]**	2.5x1.2	2.5x1.2

highlighted locations of interest - ascending aorta (AscAo), aortic arch (Arch), descending aorta (DescAo), and for P only thoracic aortic aneurysm (TAA).

To create the domain for lumen-wall simulations, the surface of the segmented geometry was offset in the normal direction using Autodesk Meshmixer v3.5 (Autodesk, Inc., California, United States) by the uniform wall thickness T_w = 2.20 mm, based on values typically used in literature [25, 26].

5.2.3 Computational Model

Fluid Dynamics

The conservation of mass and momentum for the blood flow in the aorta is:

$$\frac{\partial \rho}{\partial t} + \nabla \cdot (\rho \mathbf{v}) = 0 \tag{5.1}$$

$$\frac{\partial \rho \mathbf{v}}{\partial t} + \nabla \cdot (\rho \mathbf{v} \otimes \mathbf{v}) = -\nabla p + \nabla \cdot (\mu[\nabla \mathbf{v} + (\nabla \mathbf{v})^{\mathrm{T}}]) \tag{5.2}$$

where $\mathbf{v}$ is the fluid velocity, ρ is the fluid density, μ the fluid dynamic viscosity, and p is the pressure.

Mass transport of O_2

Oxygen transport by plasma (*'passive'* oxygen transport) can be described by the dilute approximation. For this, the convection-diffusion equation for O_2 can be written as:

$$\frac{\partial c^{\mathrm{O_2}}}{\partial t} + \nabla \cdot \left(\mathbf{v} c^{\mathrm{O_2}}\right) = \nabla \cdot \left(\mathscr{D}_f^{\mathrm{O_2}} \nabla c^{\mathrm{O_2}}\right) + r^{\mathrm{O_2}} \tag{5.3}$$

where $c^{\mathrm{O_2}}$ is the concentration of O_2, $\mathscr{D}_f^{\mathrm{O_2}}$ is the O_2 diffusion coefficient in fluid, and $r^{\mathrm{O_2}}$ is the source/sink which is neglected for the case of passive oxygen transport. For the *'active'* oxygen transport (transport of oxygen bound to hemoglobin) $r^{\mathrm{O_2}}$ reflects the complex reaction process of binding and releasing O_2 from the hemoglobin. For simplification, we assume that the concentration of free O_2 is dependent on the hemoglobin (Hb) saturation as:

$$\mathrm{S} = \frac{\mathrm{pO_2^n}}{\mathrm{pO_2^n} + \mathrm{P_{50}^n}} \tag{5.4}$$

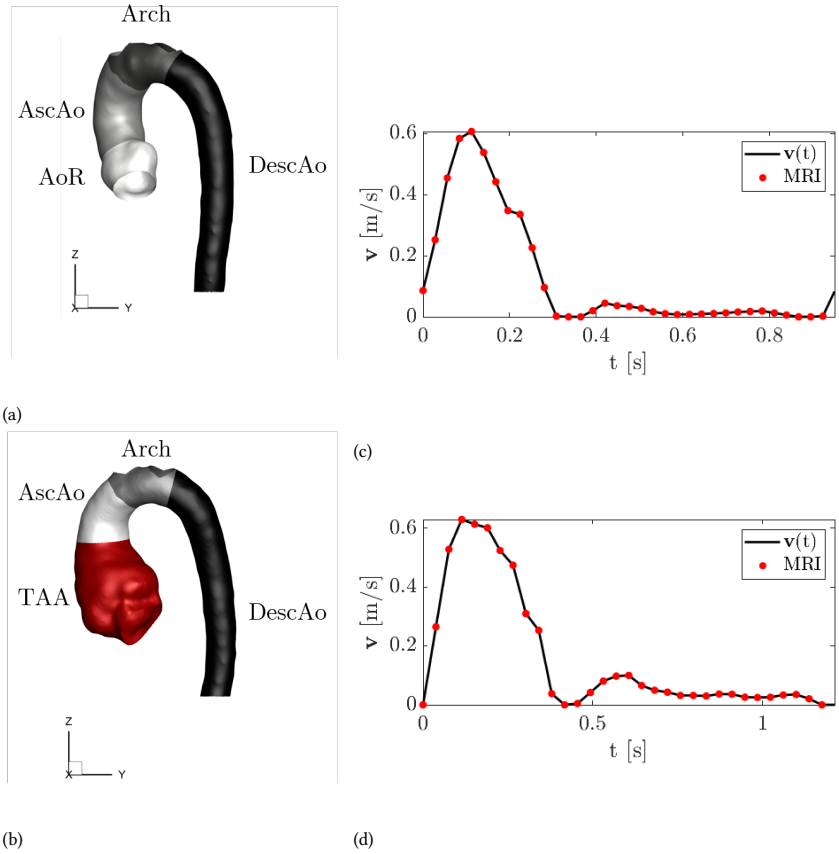

Figure 5.1: Pre-processed geometry of healthy control (a) and patient (b) with highlighted regions for analysis (ascending aorta - AscAo, aortic arch - Arch, descending aorta - DescAo, aortic root - AoR (for healthy control only), and thoracic aortic aneurysm - TAA (for the patient only)) and the 4D-flow MRI extracted mean velocity at the inlet with the interpolated velocity **v**(t) for healthy control (c) and patient (d).

where S is the saturation of hemoglobin by O_2 (from 0 to 100%), pO_2 is the partial pressure of O_2, n is the Hill's coefficient (n = 2.7) and P_{50} is the partial pressure of O_2 for saturation of 50% (P_{50} = 26.6 mmHg).

Using the O_2 saturation curve and concentration of saturated Hb, and performing a linearization assumption of the $\frac{dS}{dpO_2}$ term as shown by Moore et al. [15], the mass transfer for O_2 is defined as:

$$\left(1+\frac{[\mathrm{Hb}]}{\alpha}\frac{n\bar{S}}{\overline{pO_2}}\left(1-\bar{S}\right)\right)\left(\frac{\partial pO_2}{\partial t}+\mathbf{u}\cdot\nabla pO_2\right)= \nabla\cdot\left[\mathscr{D}_f^{O_2}\left(1+\frac{[\mathrm{Hb}]}{\alpha}\frac{\mathscr{D}_c}{\mathscr{D}_f^{O_2}}\frac{n\bar{S}}{\overline{pO_2}}\left(1-\bar{S}\right)\right)\nabla pO_2\right] \tag{5.5}$$

where α is the solubility coefficient of oxygen, $\mathscr{D}_f^{O_2}$ is the oxygen diffusion coefficient in blood, [Hb] is oxygen carrying capacity of hemoglobin in blood, and $\mathscr{D}_c$ is the oxyhemoglobin diffusion coefficient in blood. In this equation, the coefficient on the right-hand side is a non-constant diffusivity of oxygen and the coefficient on the left-hand side as a non-constant carrying capacity of oxygen, respectively.

For the O_2 transport in the aortic wall, the convection term is omitted, and we model the process by only considering pure diffusion:

$$\alpha_T \frac{\partial \mathrm{pO_2}}{\partial t} = \alpha_T \nabla \cdot \left(\mathscr{D}_w^{O_2} \nabla \mathrm{pO_2} \right) - r_w^{O_2} \tag{5.6}$$

where α_T is the O_2 solubility in the wall, $\mathscr{D}_w^{O_2}$ is the O_2 diffusion coefficient in the wall, and $r_w^{O_2}$ is the volumetric O_2 consumption rate by the wall.

Mass transport of NO

Production of NO occurs in the endothelial layer of the wall and is moderated by local WSS. We have assumed a linear dependency of NO production (r_{NO}) on WSS, defined similarly to Chen et. al. [20]:

$$r^{\mathrm{NO}} = r_{ref} \frac{\left| \overrightarrow{\tau_w} \right|}{\tau_{ref}} \tag{5.7}$$

where r_{ref} is the reference production rate, $\left| \overrightarrow{\tau_w} \right|$ is the WSS magnitude at the wall, and τ_{ref} is the reference wall shear stress. The mass transport of NO in the lumen is modeled using the convection-diffusion equation:

$$\frac{\partial c^{\mathrm{NO}}}{\partial t} + \nabla \cdot \left(\mathrm{v} c^{\mathrm{NO}} \right) = \nabla \cdot \left(\mathscr{D}_f^{\mathrm{NO}} \right) - r_f^{\mathrm{NO}} \tag{5.8}$$

where c^{NO} is the NO concentration, $\mathscr{D}_f^{\mathrm{NO}}$ is the diffusion coefficient of NO in blood, and r_f^{NO} is the consumption rate of NO by erythrocytes and oxygenation with oxygen, defined as:

$$r_f^{\mathrm{NO}} = k_{\mathrm{O_2}} c_{\mathrm{NO}}^2 + k_{\mathrm{ery}} c_{\mathrm{NO}} \tag{5.9}$$

where $k_{\mathrm{O_2}}$ is the auto-oxidative NO reaction rate and k_{ery} is the NO reaction rate with erythrocytes. The NO flux from the endothelium to the lumen (J_f^{NO}) was determined using:

$$J_f^{NO} = A \mathscr{D}_f^{NO} \left. \frac{dc^{NO}}{dr} \right|_{r=w} \tag{5.10}$$

Finally, in the wall, the NO transport is assumed to be diffusion driven:

$$\frac{\partial c^{NO}}{\partial t} = \nabla \cdot \left(\mathscr{D}_w^{NO} \nabla c^{NO} \right) - r_w^{NO} \tag{5.11}$$

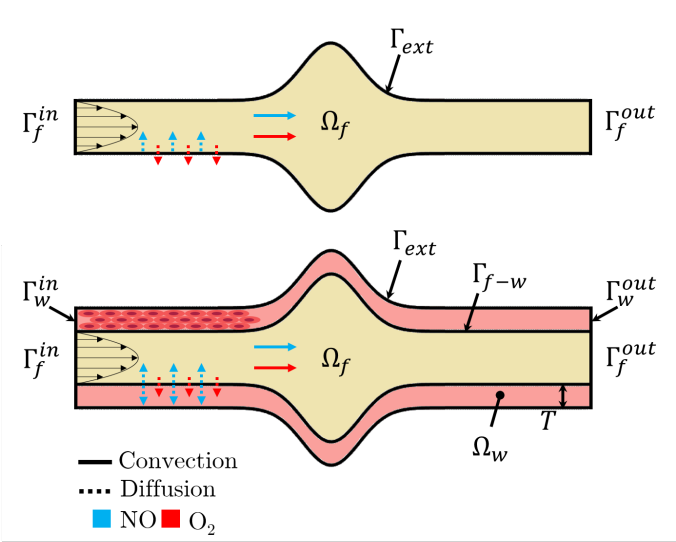

Figure 5.2: Visualization of the computational domain with the boundaries for lumen-only (top) and lumen-wall (bottom) simulations with wall thickness T and the main processes of mass transfer for oxygen (O_2) and nitric oxide (NO); the domain includes a lumen (Ω_f) and wall (Ω_w) zones and boundaries: lumen inlet (Γ_f^{in}), wall inlet (Γ_w^{in}), lumen outlet (Γ_f^{out}), wall outlet (Γ_w^{out}), outside wall (Γ_{ext}), and lumen-wall interface (Γ_{f-w}); and highlighted major mechanisms of NO and O_2 mass transfer within the different domains.

5

Boundary Conditions and Modelling of Aortic Wall

Fig. 5.2 visualizes the different domains (lumen (Ω_f) and wall (Ω_w) zones) and boundaries (lumen inlet (Γ_f^{in}), wall inlet (Γ_w^{in}), lumen outlet (Γ_f^{out}), wall outlet (Γ_w^{out}), outside wall (Γ_{ext}), and lumen-wall interface (Γ_{f-w})) for lumen-only (a) and lumen-wall (b) simulations. In addition, Fig. 5.2 also visualizes the dominant means of O_2 and NO mass transport (either convection or diffusion) within the different zones of the computational domain.

We treated the wall as a homogeneous porous medium with modeled superficial velocity as

$$S_i = -\left(\frac{\mu}{\alpha_w}\mathrm{v_i} + \mathrm{C_{2w}}\frac{1}{2}\rho|\mathbf{v}|\mathrm{v_i}\right) \tag{5.12}$$

where S_i is the source term for the $\mathrm{i^{th}}$ (x, y, or z) momentum equation, α_w is the aortic wall permeability, and C_{2w} is the inertial resistance.

Flow boundary conditions: The inlet boundary condition (Γ_f^{in}) was specified as a plug velocity profile using the time-dependent velocity information at the inlet extracted from the reconstructed 4D-flow MRI. The data points for the average velocity at the inlet (n_{HC} = 34, n_P = 32) were interpolated in time using linear interpolation, Fig. 5.1 (c) for HC and (d) for P.

The outlet boundaries (Γ_f^{out}) were treated for both cases with the assumption of zero-diffusive flux (for all the flow variables) and a mass balance correction. Specifically for the

HC and P, each outlet was assigned a fraction of the flow (w_m), which was defined as

$$w_m = \frac{Q_m}{Q_i} \cdot \frac{1}{\sum_{m=1}^{M} w_m} \tag{5.13}$$

where Q_m is the flow at the respective outlets and M is the total number of outlets (M_{HC} = 3, M_P = 4). The fluid-wall interface (Γ_{f-w}), endothelium, was treated as a simplified one-dimensional representation of a thin membrane, with specified pressure drop Δp:

$$\Delta p = -\left(\frac{\mu}{\alpha_{f-w}} \mathbf{v} + \mathrm{C_{2f-w}} \frac{1}{2} \rho \mathbf{v}^2 \right) \Delta m \tag{5.14}$$

where α_{f-w} represents the permeability of endothelium, C_{2f-w} is the pressure jump coefficient, and Δm is the endothelial thickness. The values of the biological parameters for physical properties of the different layers of the aortic wall are listed in Tab. 5.2 together with the scaled-averaged properties of the homogeneous (single-layer) walls.

5

Table 5.2: Physiological parameters of the aortic wall and the weighted averages for the homogeneous wall.

	ϵ [-]	α_w [m^2]	T_w [mm]
Endothelium	5.00e-04	3.20e-21	2.00e-03
Intima	0.983	2.20e-16	0.40
Media	0.258	2.00e-18	1.20
Adventitia	0.85	3.00e-19	0.60
Homogeneous wall	0.551	4.12e-17	2.20
Ref.	[26–29]	[26]	[25, 26]

The external wall for lumen-only simulations or vasa vasorum for lumen-wall simulations (Γ_{ext}) was assumed to be identical, with a no-slip condition assumption. Finally, Γ_w^{in} and Γ_w^{out} were assumed to have zero normal velocity.

O_2 and NO mass transfer boundary conditions: The boundary conditions for O_2 and NO at the boundaries shown in Fig. 5.2 were as follows:

(a) Γ_f^{in}: p_{O2}=90 mmHg; p_{NO}=0 mmHg

(b) Γ_f^{out}: dp_{O2}/dt=0; dp_{NO}/dt=0

(c) Γ_{ext}: p_{O2}=45 mmHg; dp_{NO}/dt=0

(d) Γ_{f-w}: dp_{O2}/dt=0; for NO see Eq. 5.10

(e) Γ_w^{in} and Γ_w^{out}: zero normal gradient for O_2 and NO

Physical Properties

The shear thinning property of blood was accounted for by applying the Carreau-Yasuda model:

$$\mu(\dot{\gamma}) = \mu_\infty + (\mu_0 - \mu_\infty)\left[1 + (\lambda\dot{\gamma})^\alpha\right]^{\frac{n-1}{\alpha}} \tag{5.15}$$

where μ_∞ the viscosity at infinite shear, μ_0 the viscosity at zero shear, λ the relaxation time, $\dot{\gamma}$ the shear rate, α a shape parameter, and n the power-law index. We adopted the exact values for these parameters from Gijsen et al. [30]. The density of the complete mixture was defined using the volume-weighted mixing law:

$$\overline{\rho} = \frac{1}{\sum_i \frac{Y_i}{\rho_i}} \tag{5.16}$$

where Y_i and ρ_i are the mass fraction and density of species i, respectively. The density for the respective species was defined as: ρ_{blood} = 1060 kg/m^3, ρ_{O_2} = 1.29 kg/m^3, and ρ_{NO} = 1.34 kg/m^3. Since $Y_{blood} >> \left(Y_{O_2} + Y_{NO}\right)$ the effective density was close to ρ_{blood} with average fluid density $\overline{\rho}$ = 1057.76 kg/m^3. The values for all other biological parameters can be found in Tab. 5.3.

Table 5.3: Biological parameters used in this study.

Parameter	Value	Unit	Ref.
α	2.50e-5	ml O_2/ ml blood/mmHg	[15]
α_T	2.40e-5	ml O_2/ ml blood/mmHg	[15]
$\mathscr{D}_f^{NO}$	3.30e-9	m^2/s	[21]
$\mathscr{D}_w^{NO}$	8.48e-10	m^2/s	[21]
$\mathscr{D}_w^{O_2}$	0.90e-9	m^2/s	[15]
$\mathscr{D}_f^{O_2}$	1.20e-9	m^2/s	[15]
$\mathscr{D}_c$	1.50e-11	m^2/s	[15]
$[Hb]$	0.20	ml O_2/ ml blood	[15]
$\overline{p_{O_2}}$	75.0	mmHg	[31]
n	2.70	-	[15]
k_{ery}	23.0	s^{-1}	[21]
k_w	0.01	s^{-1}	[21]
k_{O_2}	7.56e-6	nM^{-1}s^{-1}	[21]
r_{ref}	150	μMs^{-1}	[21]
τ_{ref}	2.40	Pa	[21]
$r_w^{O_2}$	2.10e-5	ml O_2/ml tissue/s	[15]

Mesh and Numerical Setup

For both of the studied cases concerning lumen-only simulations, we have created a polyhedral mesh with refinement consisting of ten layers close to the wall (Γ_{ext}). The mesh dependency was performed for one of the cases (HC) at the peak-systolic conditions, and the mesh dependency study can be found in Appendix A. The final meshes consisted of approximately 2.3 mil. cells for HC and 2.2 mil. cells for P.

The mesh consisted of polyhedral elements for the lumen-wall simulations, with refinement close to Γ_{f-w} and Γ_{ext}. The dependency of the solution on the mesh was tested with varying numbers of refinement layers close to the fluid-wall interface, Appendix A. The final meshes for lumen-wall simulations consisted of 6.2 mil. cells for HC and 6.5 mil. cells for P.

Post-processing and Data Analysis

MRI-based WSS was estimated using CAAS MR Solutions v5.2, similarly as described in our previous publication [14]. To analyze the hemodynamics and mass transfer of species, we have calculated several (time-averaged) quantities. From the hemodynamical properties, first, the time-averaged wall shear stress (TAWSS) was calculated using the following:

$$\mathrm{TAWSS} = \frac{1}{\mathrm{T}} \int_0^{\mathrm{T}} \left| \overrightarrow{\tau_w} \right| \mathrm{dt} \tag{5.17}$$

where T is the cycle length. The oscillatory shear index (OSI) was calculated as follows:

$$\mathrm{OSI} = \frac{1}{2} \left(\frac{\left| \int_0^{\mathrm{T}} \overrightarrow{\tau_w} \, \mathrm{dt} \right|}{\int_0^{\mathrm{T}} \left| \overrightarrow{\tau_w} \right| \mathrm{dt}} \right) \tag{5.18}$$

Finally, the endothelial cell activation potential (ECAP) was calculated as:

$$\mathrm{ECAP} = \frac{\mathrm{OSI}}{\mathrm{TAWSS}} \tag{5.19}$$

To study the mass transfer of O_2 and NO close to the wall, we have calculated the Sherwood number for species i ($\mathrm{Sh_i}$) as

$$\mathrm{Sh_i} = \frac{-\left(\frac{\partial c_\mathrm{i}}{\partial n}\right)_\mathrm{w}}{c_\mathrm{ib} - c_\mathrm{iw}} \tag{5.20}$$

where c_i is the local concentration of species i, c_{ib} is the bulk concentration of the species, and c_{iw} is the concentration at the wall. The time-averaged $\mathrm{Sh_i}$ can be written as

$$TASh_i = \frac{1}{T} \int_0^T Sh_i \, dt \tag{5.21}$$

To estimate the hypoxic area for lumen-only simulations, the species' consumption rate within the wall must be determined. For this, the rate of species consumption can be estimated using non-dimensional Damköhler number (Da), defined as:

$$\mathrm{Da} = \frac{\dot{Q}_{\mathrm{O_2 b}} \mathrm{T_w a}}{\mathrm{K} \mathscr{D}_{\mathrm{O_2}} p_{\mathrm{O_2 b}}} \tag{5.22}$$

where $\dot{Q}_{O_2 b}$ is the oxygen consumption rate of arterial tissue, T_w is the arterial wall thickness, a is the mean arterial diameter, K is Henry's constant, $\mathscr{D}_{O_2}$ is the oxygen diffusion coefficient and $p_{O_2 b}$ is the bulk partial pressure of oxygen. The region that suffers from hypoxia due to mass transfer limitations is characterized by the O_2 transport being lower than its consumption by the wall, or $\mathrm{Sh_{O_2}} < \mathrm{Da}$.

Finally, we have defined a few specific parts of the aorta used for further analysis, as shown in Fig. 5.1. The specific regions are: ascending aorta (AscAo), aortic arch (Arch), and descending aorta (DescAo) (for both subjects). In addition, aortic root (AoR) was defined for analysis of HC and thoracic aortic aorta (TAA) for P.

5.3 Results

5.3.1 Validation of Hemodynamics in Lumen

Fig. 5.3 shows the comparison of MRI normalized WSS (WSS/WSS_{ave}) to the CFD simulated results. WSS was normalized using the respective average values of WSS for MRI and CFD. The data are visualized at peak systole for both HC (Fig. 5.3a) and P (Fig. 5.3b).

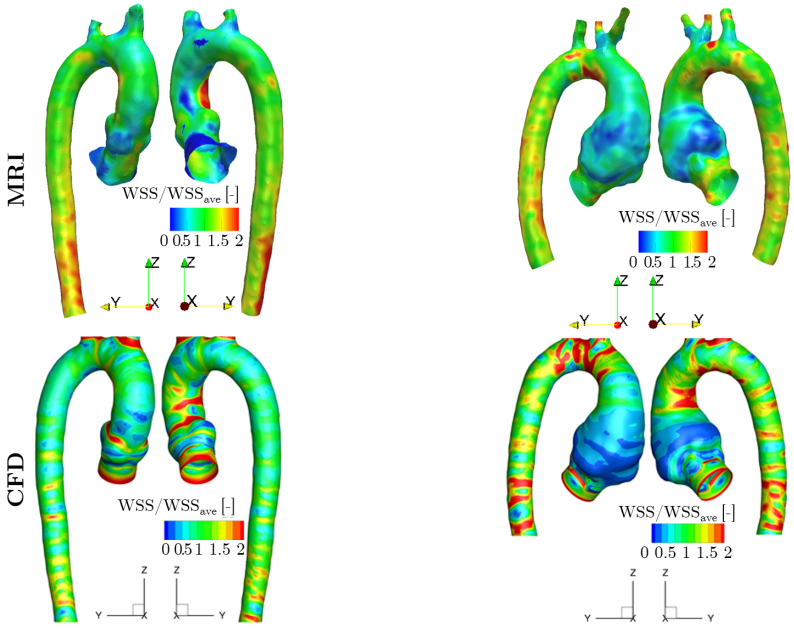

(a) Healthy Control (b) Patient

Figure 5.3: Comparison between MRI (top) and CFD (bottom) at peak systole for the healthy control (HC - (a)) and patient (P - (b)) in terms of normalized wall shear stress (WSS/WSS_{ave} [-]) where WSS was normalized by the respective spatially average values (WSS_{ave}) for MRI and CFD.

The maximal and average values and standard deviation (σ) of WSS for each of the cases and methods can be seen in Tab.5.4

Table 5.4: The maximal, mean, and standard deviation (σ) of wall shear stress (WSS) for healthy control and patient based on MRI and CFD.

	WSS_{max} [Pa]	WSS_{mean} [Pa]	σ [Pa]
Healthy Control			
MRI	4.36	1.35	0.62
CFD	65.16	3.31	2.78
Patient			
MRI	3.29	1.15	0.51
CFD	69.57	6.32	5.39

5.3.2 Time-Averaged Hemodynamics in Lumen

The time-averaged quantities that quantify the hemodynamics close to the aortic wall are shown in Fig. 5.4 for both HC and P. We have visualized the time-averaged wall shear stress (TAWSS [Pa]), Oscillatory Shear Index (OSI [-]), and the Endothelial Cell Activation Potential (ECAP [Pa^{-1}]). For both HC and P, the color bar limits are set to the same values to allow an adequate comparison.

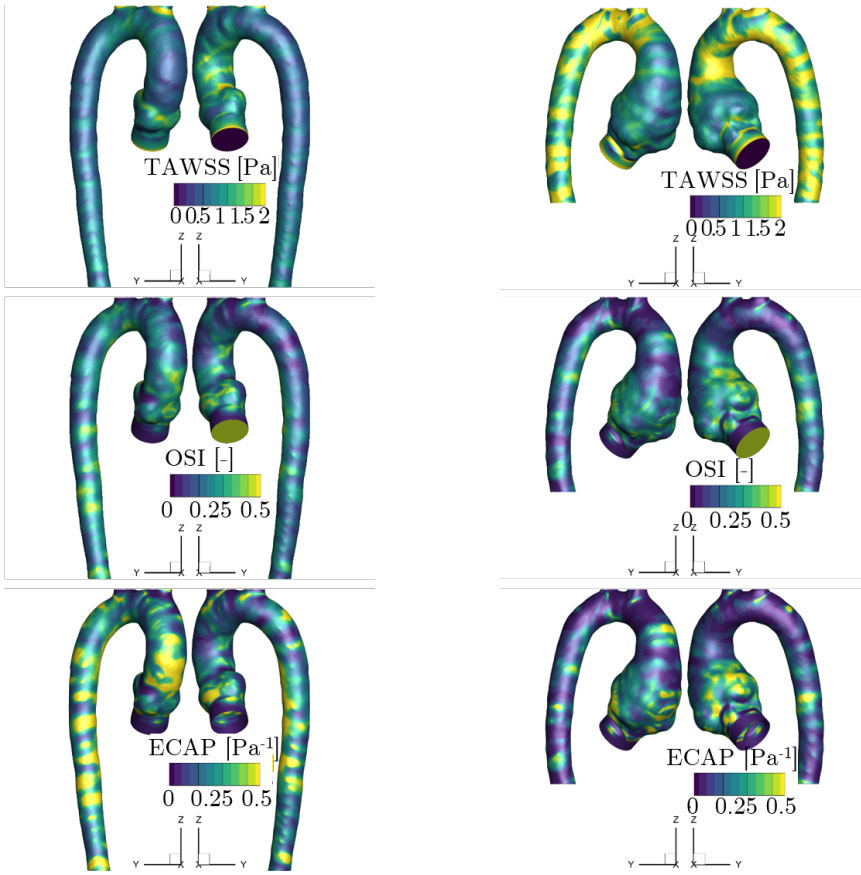

(a) Healthy Control (b) Patient

Figure 5.4: Time-averaged wall shear stress (TAWSS [Pa]), Oscillatory Shear Index (OSI [-]), and Endothelial Cell Activation Potential (ECAP [Pa^{-1}]) for healthy control (a) and patient (b) in the lumen-only approximation of aorta.

5.3.3 Mass Transfer of O_2 and NO in Lumen

To study the effects of O_2 and NO mass transfer in the lumen, we have calculated and visualized the time-average Sherwood number (TASh [-]) for the different species in Fig. 5.5. For O_2, $TASh_{O_2}$ is shown for two different modes of transport are shown - passive (top) and active (bottom). The data range for the passive $TASh_{O_2}$ is half of active $TASh_{O_2}$.

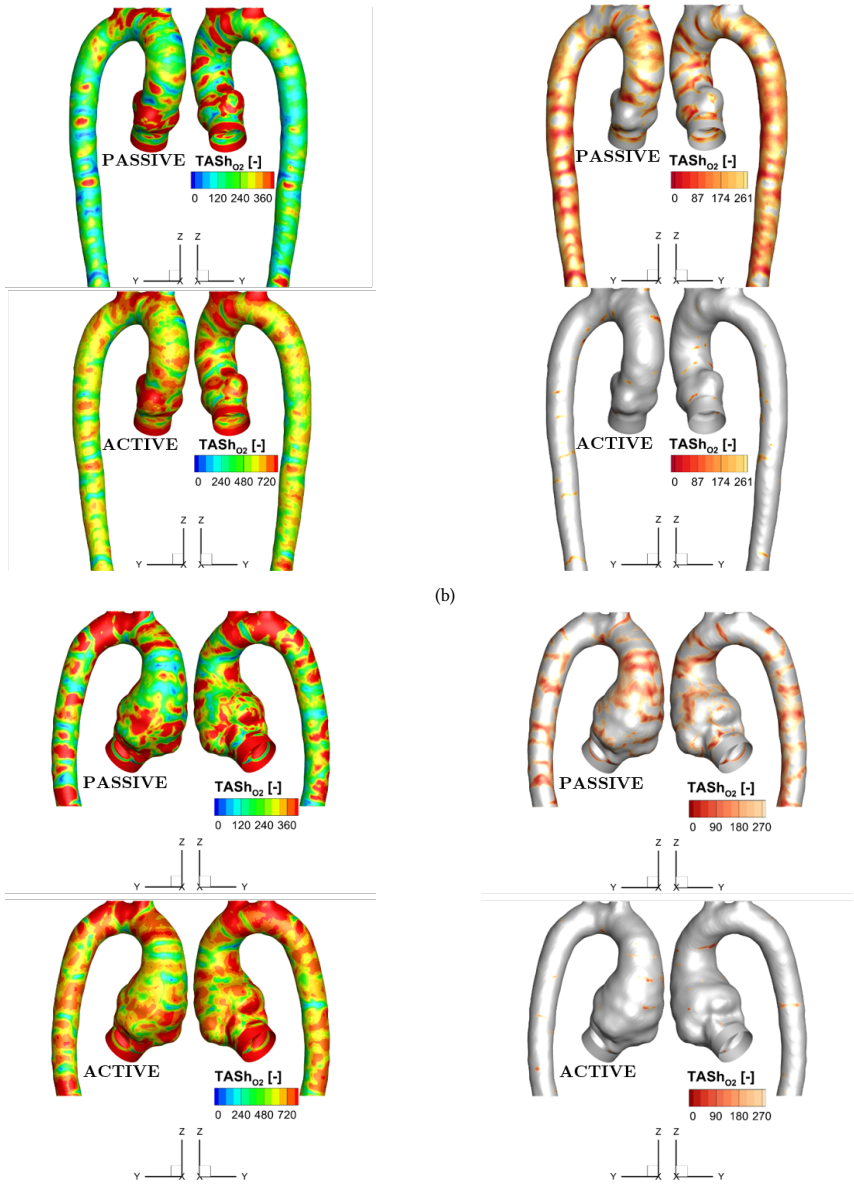

Figure 5.5: Time-averaged Sherwood number for (from top to bottom) oxygen ($TASh_{O_2}$ [-]) for passive oxygen transport (top) and active oxygen transport (bottom) and Time-averaged Sherwood number for nitric oxide transport ($TASh_{NO}$ [-]) for healthy control (a) and patient (c) and the estimation of hypoxic areas based on Sherwood number lower then Damköhler number (Da<Sh) visualized using $TaSh_{O_2}$ [-] for healthy control (b) with Da_{HC} = 290 and patient (d) with Da_P = 304 in the lumen-only approximation of aorta.

Fig. 5.5 (b) and (d) also show the estimated hypoxic regions for passive and active O_2 mass transport. The locations of hypoxia occur if the O_2 mass transfer towards the wall (Sh) is lower than its consumption by the wall (Da), i.e., if TASh < Da applies. We have estimated Da (as defined in Eq. 5.22), separately for HC and P based on the average diameter of the aorta (healthy portion only for P). The estimated values were: Da_{HC} = 290 for HC and Da_P = 304 for P. Additionally, we have calculated the relative percentage area affected by hypoxia (A_{hyp}), defined as the hypoxic area per the total area, in the ascending aorta (AscAo), aortic arch (Arch) and descending aorta (DescAo). A_{hyp} for both studied subjects is shown in Tab. 5.5 (for passive and active O_2 transport).

Finally, Fig. 5.6b shows the time-averaged Sh for NO ($TASh_{NO}$ [-]) for both studied cases.

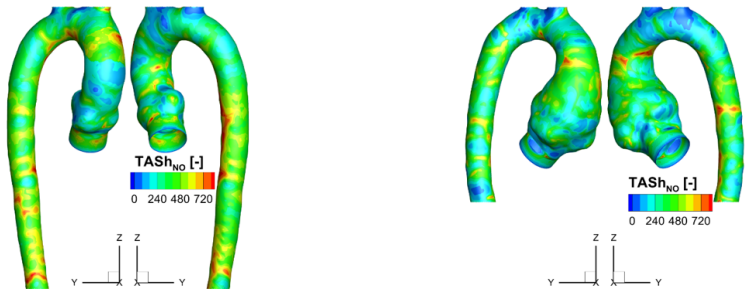

(a) (b)

Figure 5.6: Time-averaged Sherwood number for nitric oxide transport ($TASh_{NO}$ [-]) for healthy control (a) and patient (b) in the lumen-only approximation of aorta.

Next, we have visualized the circumferential average of various hemodynamic quantities (TAWSS, OSI, and ECAP) together with TASh for NO and O_2 (passive and active) alongside the normalized centerline length (l/l_{max}) for both studied subjects, Fig. 5.7. The centerline length was normalized by its maximum (l_{max}), and the different sections of the aorta are highlighted (ascending aorta - AscAo, aortic arch - Arch, descending aorta - DescAo, and for P only: aneurysm - TAA). For HC, to achieve an adequate comparison, only the data within the range of centerline length for P were taken into account since the simulated domain was longer. The average values in the regions of interest (Aor, AscAo, Arch, DescAo, and TAA for P) of all the studied quantities for HC and P are shown in Tab. 5.5.

Until now, we have primarily focused on the absolute behavior of the cardiac cycle by analyzing the time-averaged quantities. While this approach allows for understanding the complete mass transfer and blood flow behavior, it may cause the concealment of specific details due to the averaging. Therefore, we have extracted data at peak systole alongside two lines (inseam and outseam) for both studied subjects, as shown in Fig. 5.8. We have visualized WSS with Sh for NO and active O_2 mass transport. The length of the inseam and outseam (l) were non-denationalized using the respective maximal values. Finally, the boundaries for the specific regions of interest are highlighted.

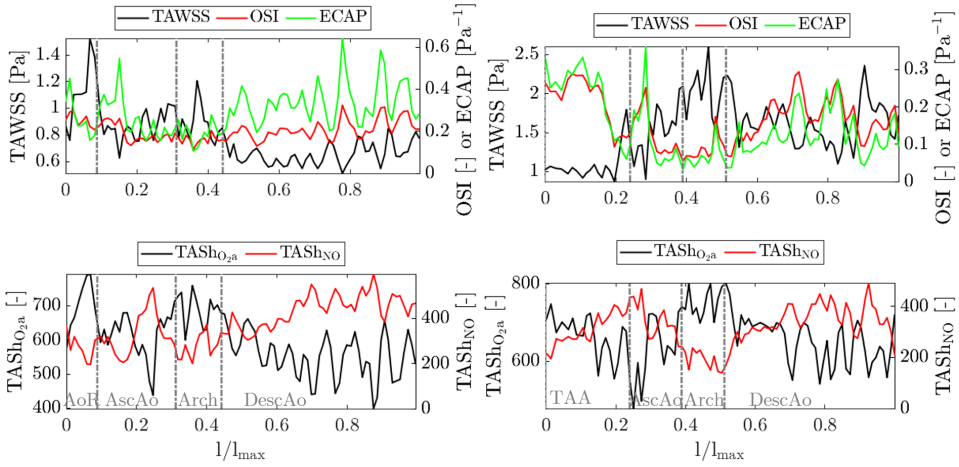

(a) Healthy Control (b) Patient

Figure 5.7: Circumferential average alongside the normalized centerline length (l/l_{max}) for: time-averaged wall shear stress (TAWSS [Pa]), oscillatory shear index (OSI [-]), endothelial cell activation potential (ECAP [Pa^{-1}], Time-averaged Sherwood number for active oxygen (TASh$_{O_2a}$ [-]), and Time-averaged Sherwood number for nitric oxide (TASh$_{NO}$ [-]); for healthy control (a) and patient (b) in the lumen-only approximation of aorta; we divided the domain to highlight the ascending aorta (AscAo), aortic arch (Arch), descending aorta (DescAo), and aneurysm (TAA - for the patient only).

Table 5.5: Average values of hemodynamic mass transfer properties for healthy control (HC) and patient (P) within specific sections of aorta (ascending aorta - AscAo, aortic arch - Arch, descending aorta - DescAo, for H only aortic root - AoR, and for P only aneurysm - TAA); the evaluated variables are: relative percentage hypoxic area for passive (A_{hypP}) and active (A_{hypP}) transport, time-averaged wall shear stress (TAWSS), oscillatory shear index (OSI), endothelial cell activity potential (ECAP), time-averaged Sherwood number for passive oxygen transport (TASh$_{O2P}$), active oxygen transport (TASh$_{O2A}$), and nitric oxide transport (TASh$_{NO}$).

		Healthy Control				Patient			
		AoR	**AscAo**	**Arch**	**DescAo**	**TAA**	**AscAo**	**Arch**	**DescAo**
Hemodynamics									
TAWSS	[Pa]	0.12	0.88	0.90	0.65	1.06	1.49	2.06	1.63
OSI	[-]	0.03	0.20	0.16	0.21	0.23	0.13	0.09	0.17
ECAP	[Pa^{-1}]	0.03	0.26	0.18	0.34	0.25	0.29	0.06	0.13
Mass Transfer									
TASh$_{O2P}$	[-]	29	242	316	179	322	260	416	298
TASh$_{O2A}$	[-]	71	611	686	559	671	623	745	660
TASh$_{NO}$	[-]	37	332	280	432	301	351	199	338
Hypoxic Area									
A_{hypP}	[%]	25	63	45	85	38	58	19	47
A_{hypA}	[%]	2.0	3.8	3.3	5.4	1.3	3.5	0.8	1.6

5.3.4 Mass Transfer of O_2 and NO in Aortic Wall

Fig. 5.9 shows the normalized concentration of O_2 ($c^{O_2}/c^{O_2}_{max}$ [-]) and NO (c^{NO}/c^{NO}_{max} [-]) visualized at different locations of interest (A - root, B - ascending aorta, C - after arch) alongside with the velocity field with normalized velocity magnitude ($v/\overline{v_{in}}$ [-]) for peak

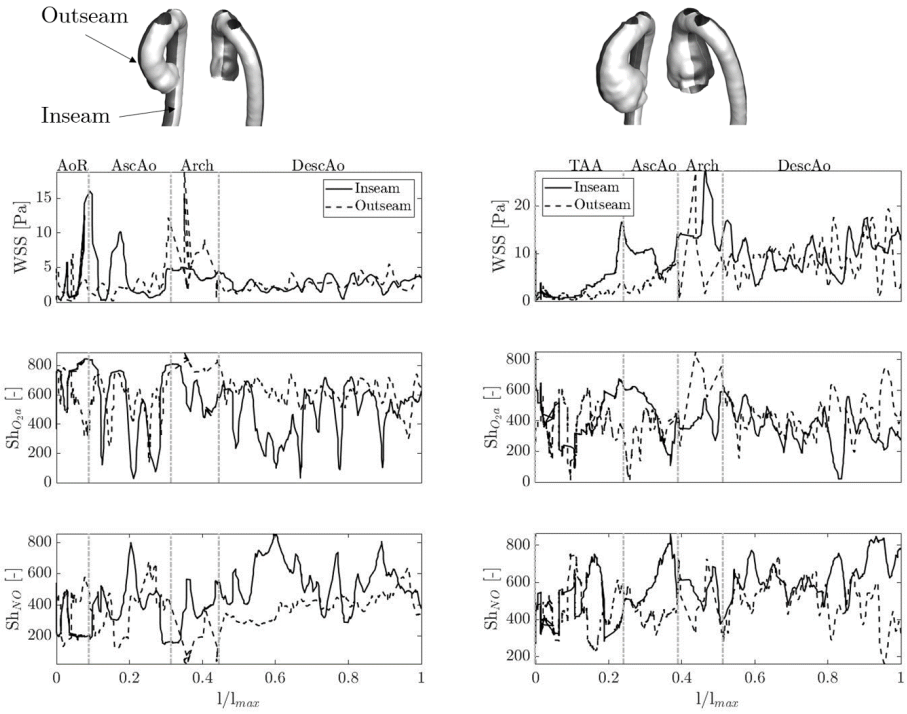

(a) Healthy Control

(b) Patient

Figure 5.8: Wall shear stress (WSS [Pa]), Sherwood number for active oxygen (Sh_{O_2a} [-]), and Sherwood number for nitric oxide (Sh_{NO} [-]) alongside the normalized centerline length (l/l_{max}) extracted alongside the inseam and outseam for: healthy control (a) and patient (b) in the lumen-only approximation of aorta; the domain is divided to highlight the ascending aorta (AscAo), aortic arch (Arch), descending aorta (DescAo), and aneurysm (TAA - for the patient only).

systole. The concentration of both species was normalized using the inlet (maximal) $c_{max}^{O_2}$ for O_2 and global maximum c_{max}^{NO} for NO. The velocity magnitude was normalized using the average velocity at the inlet $\overline{v_{in}}$. Additionally, the data are visualized alongside the lines extracted from (A1 and C1) in Fig. 5.10. We visualized the data alongside a normalized diameter of the particular slice (d/d_{max}), with d_{max} being the maximal lumen diameter of the slice.

5.4 Discussion

In this study, we have conducted simulations of blood flow and combined mass transfer of O_2 and NO in a subject-specific aorta and its wall, focusing on two cases: a healthy control (HC) and a patient (P) with a root aneurysm. The simulations were based on 4D-flow MRI measurements, from which geometry and boundary flow conditions were extracted. To examine flow dynamics in the wall, we have developed a simplified, single-layer model of the aortic wall, featuring a constant thickness and physical properties based on the average

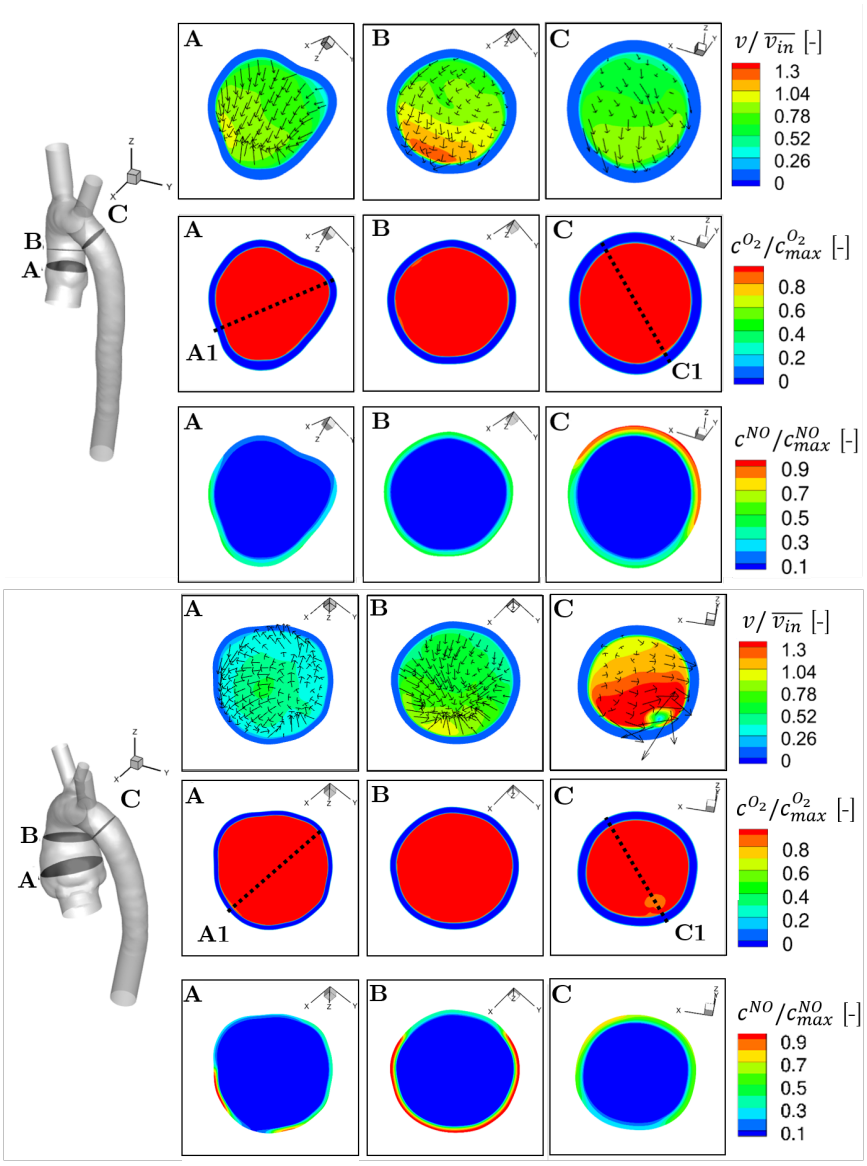

Figure 5.9: Normalized concentration of O_2 ($c^{O_2}/c^{O_2}_{max}$ [-]) and NO (c^{NO}/c^{NO}_{max}) [-]) and normalized velocity magnitude ($v/\overline{v_{in}}$ [-]) for healthy control (top) and patient (bottom) visualized at several locations of interest.

of intima, media, and adventitia.

Since the information for the blood flow was derived from a single 4D-flow MRI measurement, we used this data to validate our simulated flow field within the lumen. Comparing normalized values of WSS for both cases at peak systole, the simulated blood flow shows similar behavior to the measured one. We note that while there are some

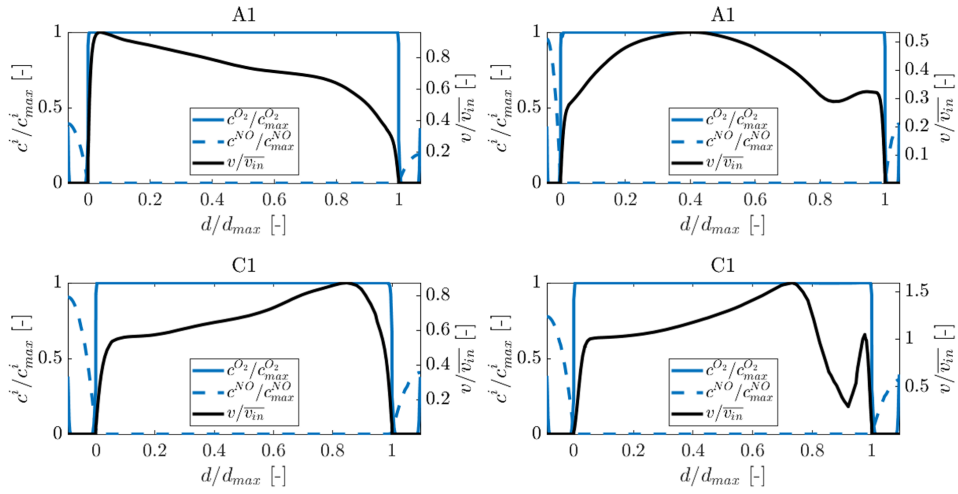

(a) Healthy Control (b) Patient

Figure 5.10: Normalized concentration of O_2 and NO (c^i/c^i_{max} [-]) and normalized velocity magnitude ($v/\overline{v_{in}}$ [-]) for healthy control (top) and patient (bottom) visualized alongside extracted line with normalized distance for the particular location (d/d_{max}), where d_max is the maximal lumen diameter.

differences between the two methods, as reported in our previous studies [13, 14, 32], the data from both methods agree well in capturing the global behavior of WSS including areas of local maximal and minimal values. We conclude that the blood flow data obtained from simulations adequately represent reality, as demonstrated in our earlier research [13, 14].

Besides WSS within the aorta, several previous studies have focused on time-averaged hemodynamical quantities to establish potential biomarkers for the progression of TAA. In this study, we have explored potential biomarkers for the progression of TAA by examining the effects of time-averaged hemodynamical quantities such as TAWSS, OSI, and ECAP, as shown in Figure 5.4, in both HC and P cases. When comparing the healthy and aneurysmal cases, the section suffering from TAA indicates few striking characteristics. For instance, TAWSS shows a global minimum in the area of TAA, similar to previously reported behavior in TAA and AAA [33, 34]. Moreover, TAA also suffers from higher OSI than the healthy aorta, and the ECAP is significantly higher in the location of TAA compared to the rest of the aorta. These three characteristics indicate a potentially higher risk for additional growth or rupture due to impaired endothelial cell activity. Endothelial cells respond to non-physiological values of WSS and change in the direction of WSS during the cardiac cycle in various ways [35, 36], which, among others, affects the production of different species (like NO). However, since we have only simulated two subjects, we cannot conclude whether TAWSS, OSI, and ECAP are reliable predictors of aneurysms. Instead, we suggest that these hemodynamical indicators should be further investigated in a large population study with multiple HC and patients with TAA, as we observed apparent differences between HC and P in these variables. Moreover, to determine if these biomarkers are associated with aneurysm growth, longitudinal data are necessary to be included in the analysis.

We also highlight the region of the AscAo immediately following the TAA. In this

region, the artery experiences a sudden increase in TAWSS (in the transition between TAA and the *'healthy'* part), as can be observed in Fig. 5.7. This behavior is also evident in the instantaneous WSS at peak systole, as depicted in Fig. 5.8. Additionally, a sudden increase in OSI and ECAP occurs further downstream of the TAA, as shown in Fig. 5.7. In contrast, such behavior is not evident in the AscAo of HC. These findings suggest that a further aberrant blood flow occurs downstream of TAA, potentially leading to additional growth, the genesis of the secondary aneurysm, or even the onset of aortic dissection (AD). Consistent with this observation, Peng et al. have demonstrated a strong correlation between the hemodynamics close to the tear in AD and aberrant blood flow, as well as high OSI [37]. Furthermore, TAA is considered a risk factor for AD [1].

In addition to hemodynamics, we also simulated the mass transfer of O_2 and NO in the lumen and aortic wall. Within the lumen, both species show non-uniform distribution. Moreover, we found an inverse correlation between the two species, as regions with lower O_2 exhibited higher NO concentration and vice-versa, as depicted in Fig. 5.7 for the time-averaged quantities and in Fig. 5.8 for instantaneous mass transfer at peak systole. We can also observe similar behavior regarding concentration boundary layer thickness within the lumen. For both cases, the boundary layer is very thin, with a sudden decrease in concentration for both species. The observed relationship can be explained by the relative thickness of the concentration boundary layer compared to the momentum boundary layer, expressed in Schmidt number (Sc). For both species, Sc is very high, with values of Sc^{NO} ~ 1000 for NO and $Sc_p^{O_2}$ ~ 3000 and $Sc_a^{O_2}$ ~ 30000 for passive and active O_2 respectively. Thus, NO is almost instantly consumed within the lumen, and the O_2 concentration gradient at the wall is very steep, with minimal influence from lumen-side mass transfer limitations. Similar observations were previously reported for idealized arteries by Plata et al. for NO [19] and Moore and Ethier for O_2 [15], as well as for mass transfer in aorta [21].

In regard to O_2 mass transfer, this phenomenon is also manifested in the estimation of hypoxic regions within the aorta. The hypoxic area can be estimated by comparing the mass transfer towards the wall (Sh) with the estimated consumption of the wall (Da). In our study, the hypoxic region occurred if Sh was lower than Da = 290 for HC and Da = 304 for P. Notably, the estimated hypoxic area for passive O_2 is much greater than for the active O_2. For the latter mentioned, just one to four percent of the total aortic area suffers from estimated hypoxia. In addition, we can observe subtle differences between HC and P. The hypoxic area is lower in P, particularly in DescAo, which could also be attributed to the estimated value of Da. Moreover, Da was estimated to be lower in HC. This discrepancy in Da was influenced by the calculated average diameter (a) of the artery, which was higher for P, even though we excluded the majority of TAA from the calculations. To address this limitation, an adaptive calculation of Da should be employed, with variable a as a function of centerline distance. However, when considering only estimated hypoxia in P, no significant differences between the healthy tissue and TAA are apparent.

Nevertheless, the impact of hemodynamics on O_2 concentration persists. In the case of P, a distinct recirculation zone is evident just after the arch (slice C in Fig. 5.9). This recirculation zone causes a slight reduction in O_2 concentration. Similar hemodynamics-induced variations in concentration were previously observed in the stenotic region of the carotid artery [18]. Thus, monitoring areas with aberrant blood flow within the aorta is crucial, as prolonged hypoxia can trigger extracellular matrix remodeling and degradation

[38] and play an essential factor in aneurysm pathogenesis [39].

The distribution of NO closely follows the TAWSS distribution in the aorta since WSS triggers NO production. Consequently, NO is unevenly distributed in the lumen and the aortic wall, as can be observed in our simulations as well as previously reported NO distribution in the aortic wall [21] and in coronary arteries [23]. Notably, the distribution of NO within the aortic wall differs significantly between P and HC, particularly near the root, as shown in Fig. 5.9 and 5.10, due to the presence of TAA. Here, the gradient in NO concentration is very high between the inner and outer curves of the aorta, with additional disruptions in the proximity of the inner curve. These variations could indicate dysfunction of the arterial wall due to uneven stimulation of smooth muscle cells within TAA, which may contribute to further growth.

We identified several limitations in our study. Firstly, we restricted our analysis to only two subjects, precluding us from drawing a statistically significant conclusion regarding the effects of limitations in O_2 and NO transport on aortic aneurysm development. To enable us to draw definitive conclusions, it is imperative that we expand our sample size to include a more substantial pool of healthy controls and patients, taking into account diverse locations of aortic aneurysms. Nonetheless, our study was primarily aimed at establishing a framework for modeling species transport and proposing a set of hemodynamic and biochemical biomarkers that could be evaluated in more significant population studies. Secondly, while numerous studies presented approaches for a multi-layer representation of (simple) arterial wall [40, 41], we assumed a homogeneous single-layer aortic wall approximation. In reality, the aortic wall is composed of three layers (intima, media, and adventitia), each exhibiting unique physiological behavior. Therefore, our model lacks the capacity to determine the nature of mass transfer in each of the layers. However, we established the properties of the wall using scaled averages based on the respective properties of intima, media, and adventitia, thereby creating a model of the wall with overall average properties identical to a three-layer wall model. Thus, while we cannot provide insights into the specific behavior of each layer, we can reasonably capture the understanding of joined dynamics, especially for identifying hypoxia. Thirdly, we assumed a plug velocity profile at the inlet instead of a realistic one. However, our prior research has shown that if the root of the aorta is segmented correctly (as in our studied domains), the differences between the plug velocity profile and actual velocity profile are minimal [42]. Finally, the most significant limitation of our study is the absence of validation of O_2 and NO concentration within the aortic wall and lumen with direct measurements. The lack of validation originates from the current limitations of available methods for (in)direct non-invasive examination of these species in human arteries [9–12]. While an indirect comparison of our results can be made with invasive experiments that report on the concentration of O_2 using the hot cathode method on animal models [43, 44], a direct comparison is not presently possible.

5.5 Summary and Conclusions

This study aimed to simulate the mass transfer of O_2 and NO in the aorta of healthy control (HC) and patient (P) with root thoracic aortic aneurysm (TAA). To achieve this, a complex model was developed for the mass transfer of both species, incorporating hemoglobin-based transfer of O_2 in the domain, production of NO based on the local variation of WSS, and

mass transfer (via diffusion) and consumption of both species in the arterial wall. The arterial wall was constructed with a single-layer assumption with homogeneous physical properties based on the average behavior of intima, media, and adventitia. Both simulations (HC and P) were based on 4D-flow MRI, with geometry and boundary conditions at the inlet and outlet directly based on the measurements. The simulated velocity field and WSS were validated against measured data, demonstrating good agreement.

The study revealed significant differences in hemodynamics between P and HC in and around the root, where P developed TAA. In these regions, WSS was markedly lower, while OSI and ECAP were elevated for P, whereas HC showed a more uniform distribution of these parameters. The distribution of O_2 and NO varied spatially in both the lumen and aortic wall, with apparent differences between healthy tissue and TAA in NO concentrations. In contrast, the concentration of O_2 was not influenced by the presence of TAA. However, the study demonstrated how aberrant blood flow could lead to hypoxia, indicating that O_2 should be monitored as a potential precursor for TAA pathogenesis.

In conclusion, the findings suggest that the studied quantities could be used as hemodynamical and biochemical predictors for TAA pathogenesis. However, due to the limited number of cases investigated, no statistically significant conclusions can be drawn. The authors propose that these hemodynamical and biochemical indicators be investigated in extensive population studies with multiple HC and patients with TAA, including longitudinal data. Such research could enhance the understanding of the aortic lumen and wall processes and ultimately improve the diagnosis and treatment of TAA.

Appendix A: Mesh Dependency

Our mesh dependency analysis focused on two aspects:

1. Lumen-only - dependency of the simulated results on the varying size of volume mesh for lumen-only geometry

2. Lumen-wall - dependency of the simulated results on the varying number of extruded layers close to the lumen-wall interface for simulations with wall included

In this section, we will elaborate on these mesh dependency studies.

Lumen-only

To perform the mesh dependency study, we have created three meshes: coarse (≈ 1 mil. polyhedral elements), medium (≈ 2 mil. polyhedral elements), and fine (≈ 4 mil polyhedral elements). After performing simulations, we compared WSS, as shown in Fig. 5.11 at the surface (with detail on ascending aorta), and its local variation alongside an extracted line, as shown in Fig. 5.12. We can see that the three meshes agree well upon qualitative analysis, with only a small variation. We have also analyzed the Grid Convergence Index (GCI) to quantify these findings, as presented in Tab. 5.6.

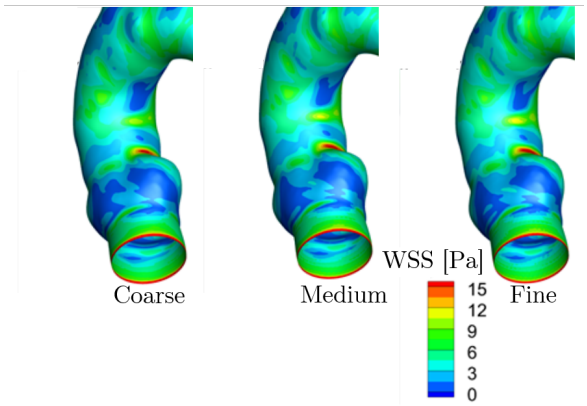

Figure 5.11: Wall shear stress (WSS [Pa]) for the healthy control with lumen-only approximation, using a coarse, medium, and fine mesh.

Table 5.6: Grid convergence index (GCI) estimation for the healthy control; f_1 is wall shear stress for the fine mesh, f_2 is for the medium mesh, and f_3 is for the coarse mesh; r is the remeshing factor, p is the order of convergence, $f_{h=0}$ is the Richardson solution, $GCI_{1,2}$ is the GCI for fine and medium mesh, and $GCI_{2,3}$ is the GCI for medium and coarse mesh.

	f_3	f_2	f_1	r	p	$f_{h=0}$	$GCI_{1,2}$ [%]	$GCI_{2,3}$ [%]	Asymptotic?
Lumen-only	4.51	4.76	4.85	2.00	1.42	4.90	1.43	3.90	1.019
Lumen-wall	4.40	3.92	3.88	2.25	3.29	3.88	0.08	1.144	0.992

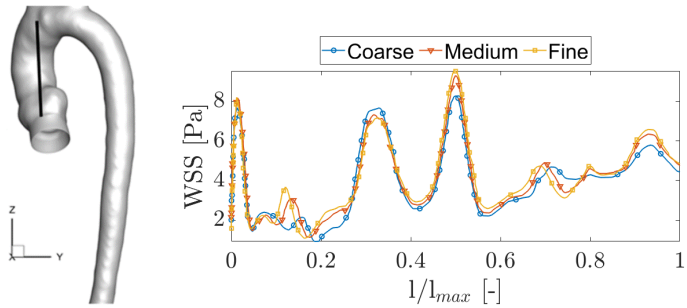

(a) (b)

Figure 5.12: Extracted local Wall shear stress (WSS [Pa]) alongside the line visualized in a) with normalized length l/l_{max} [-] where l_{max} is the total distance of the line, for the healthy control with lumen-only approximation, using a coarse, medium, and fine mesh.

Lumen-wall

We have adopted a different approach to the mesh sensitivity analysis for the case when the wall is included in the simulations. Here, we created three meshes with volume settings based on the medium mesh from the lumen-only analysis. The differences between the meshes were the number of extruded layers (the wall side) in the proximity of the lumen-wall interface, with two, five, and ten layers for the coarse, medium, and fine mesh, respectively. We performed blood flow simulations to test the meshes and calculated WSS on the lumen-wall interface. Subsequently (for visualization and analysis purposes), WSS was interpolated on the vasa vasorum, where we have performed the mesh sensitivity analysis, as shown in Fig. 5.13 for the surface with detail on the ascending aorta and in Fig. 5.14 for the local variation in WSS alongside an extracted line. As for the previous case, we have also calculated GCI, reported in Tab. 5.6

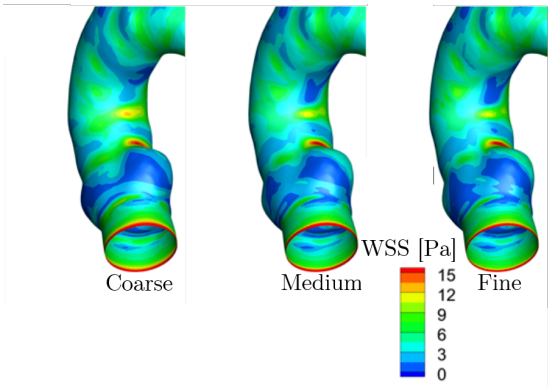

Figure 5.13: Wall shear stress (WSS [Pa]) for the healthy control with lumen-wall approximation, using coarse, medium, and fine mesh.

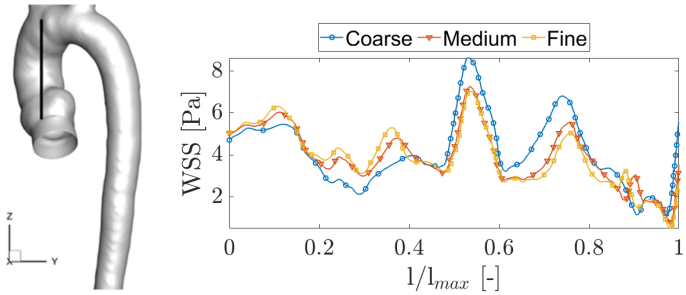

(a) (b)

Figure 5.14: Extracted local Wall shear stress (WSS [Pa]) alongside the line visualized in a) with normalized length l/l_{max} [-] where l_{max} is the total distance of the line, for the healthy control with lumen-wall approximation, using a coarse, medium, and fine mesh.

References

[1] *2014 ESC Guidelines on the diagnosis and treatment of aortic diseases,* European Heart Journal **35**, 2873 (2014).

[2] P. Visser, G. J. M. Akkersdijk, and J. D. Blankensteijn, *In-hospital operative mortality of ruptured abdominal aortic aneurysm: A population-based analysis of 5593 patients in the netherlands over a 10-year period,* European Journal of Vascular and Endovascular Surgery **30**, 359 (2005).

[3] M. Billaud, J. C. Hill, T. D. Richards, T. G. Gleason, and J. A. Phillippi, *Medial hypoxia and adventitial vasa vasorum remodeling in human ascending aortic aneurysm,* Frontiers in Cardiovascular Medicine **5** (2018), 10.3389/fcvm.2018.00124.

[4] H. Tanaka, N. Zaima, T. Sasaki, T. Hayasaka, N. Goto-Inoue, K. Onoue, K. Ikegami, Y. Morita, N. Yamamoto, Y. Mano, M. Sano, T. Saito, K. Sato, H. Konno, M. Setou, and N. Unno, *Adventitial vasa vasorum arteriosclerosis in abdominal aortic aneurysm,* PloS one **8**, e57398 (2013), 23460850[pmid].

[5] M. Sano, N. Unno, T. Sasaki, S. Baba, R. Sugisawa, H. Tanaka, K. Inuzuka, N. Yamamoto, K. Sato, and H. Konno, *Topologic distributions of vasa vasorum and lymphatic vasa vasorum in the aortic adventitia – implications for the prevalence of aortic diseases,* Atherosclerosis **247**, 127 (2016).

[6] H. WOLINSKY and S. GLAGOV, *Nature of species differences in the medial distribution of aortic vasa vasorum in mammals,* Circulation Research **20**, 409 (1967).

[7] J. Oller, N. Méndez-Barbero, E. J. Ruiz, S. Villahoz, M. Renard, L. I. Canelas, A. M. Briones, R. Alberca, N. Lozano-Vidal, M. A. Hurlé, D. Milewicz, A. Evangelista, M. Salaices, J. F. Nistal, L. J. Jiménez-Borreguero, J. De Backer, M. R. Campanero, and J. M. Redondo, *Nitric oxide mediates aortic disease in mice deficient in the metalloprotease adamts1 and in a mouse model of marfan syndrome,* Nature Medicine **23**, 200 (2017).

[8] A. de la Fuente-Alonso, M. Toral, A. Alfayate, M. J. Ruiz-Rodríguez, E. Bonzón-Kulichenko, G. Teixido-Tura, S. Martínez-Martínez, M. J. Méndez-Olivares, D. López-Maderuelo, I. González-Valdés, E. Garcia-Izquierdo, S. Mingo, C. E. Martín, L. Muiño-Mosquera, J. De Backer, J. F. Nistal, A. Forteza, A. Evangelista, J. Vázquez, M. R. Campanero, and J. M. Redondo, *Aortic disease in marfan syndrome is caused by overactivation of sgc-prkg signaling by no,* Nature Communications **12**, 2628 (2021).

[9] D. P. Guensch, M. C. Michel, S. P. Huettenmoser, B. Jung, P. Gulac, A. Segiser, S. L. Longnus, and K. Fischer, *The blood oxygen level dependent (bold) effect of in-vitro myoglobin and hemoglobin,* Scientific Reports **11**, 11464 (2021).

[10] J. Ruiz-Cabello, B. Barnett, P. Bottomley, and J. Bulte, *Fluorine (19f) mrs and MRI in biomedicine,* NMR in biomedicine **24**, 114 (2011).

[11] A. H. Schmieder, S. D. Caruthers, J. Keupp, S. A. Wickline, and G. M. Lanza, *Recent advances in 19fluorine magnetic resonance imaging with perfluorocarbon emulsions,* Engineering **1**, 475 (2015).

[12] S. Chaudhary, N. Akter, A. Rajeev, M. Hwang, and S. Sirsi, *Hemoglobin microbubbles for in vivo blood oxygen level dependent imaging: Boldly moving beyond MRI,* The Journal of the Acoustical Society of America **150**, A27 (2021), https://doi.org/10.1121/10.0007507 .

[13] R. Perinajová, J. F. Juffermans, J. J. Westenberg, R. L. van der Palen, P. J. van den Boogaard, H. J. Lamb, and S. Kenjereš, *Geometrically induced wall shear stress variability in CFD-MRI coupled simulations of blood flow in the thoracic aortas,* Computers in Biology and Medicine **133**, 104385 (2021).

[14] R. Perinajová, J. F. Juffermans, J. L. Mercado, J.-P. Aben, L. Ledoux, J. J. M. Westenberg, H. J. Lamb, and S. Kenjereš, *Assessment of turbulent blood flow and wall shear stress in aortic coarctation using image-based simulations,* BioMedical Engineering OnLine **20**, 84 (2021).

[15] J. Moore and C. R. Ethier, *Oxygen mass transfer calculations in large arteries,* Journal of Biomechanical Engineering **119**, 469 (1997).

[16] C. Cheng, R. van Haperen, M. de Waard, L. C. A. van Damme, D. Tempel, L. Hanemaaijer, G. W. A. van Cappellen, J. Bos, C. J. Slager, D. J. Duncker, A. F. W. van der Steen, R. de Crom, and R. Krams, *Shear stress affects the intracellular distribution of eNOS: direct demonstration by a novel in vivo technique,* Blood **106**, 3691 (2005).

[17] C. Cheng, D. Tempel, A. Oostlander, F. Helderman, F. Gijsen, J. Wentzel, R. van Haperen, D. B. Haitsma, P. W. Serruys, A. F. van der Steen, R. de Crom, and R. Krams, *Rapamycin modulates the eNOS vs. shear stress relationship,* Cardiovascular Research **78**, 123 (2007).

[18] S. Tada and J. M. Tarbell, *Oxygen mass transport in a compliant carotid bifurcation model,* Annals of Biomedical Engineering **34**, 1389 (2006).

[19] A. M. Plata, S. J. Sherwin, and R. Krams, *Endothelial nitric oxide production and transport in flow chambers: The importance of convection,* Annals of Biomedical Engineering **38**, 2805 (2010).

[20] X. Chen, D. G. Buerk, K. A. Barbee, P. Kirby, and D. Jaron, *3D network model of no transport in tissue,* Medical & Biological Engineering & Computing **49**, 633 (2011).

[21] X. Liu, Z. Wang, P. Zhao, Z. Fan, A. Sun, F. Zhan, Y. Fan, and X. Deng, *Nitric oxide transport in normal human thoracic aorta: Effects of hemodynamics and nitric oxide scavengers,* PLOS ONE **9**, 1 (2014).

[22] X. Li, X. Liu, P. Zhang, C. Feng, A. Sun, H. Kang, X. Deng, and Y. Fan, *Numerical simulation of haemodynamics and low-density lipoprotein transport in the rabbit aorta and their correlation with atherosclerotic plaque thickness,* Journal of The Royal Society Interface **14**, 20170140 (2017).

[23] S. Qian, T. Ma, N. Zhang, X. Liu, P. Zhao, X. Li, D. Chen, L. Hu, L. Chang, L. Xu, X. Deng, and Y. Fan, *Spatiotemporal transfer of nitric oxide in patient-specific atherosclerotic carotid artery bifurcations with MRI and computational fluid dynamics modeling,* Computers in Biology and Medicine **125**, 104015 (2020).

[24] B. W. Allen, J. S. Stamler, and C. A. Piantadosi, *Hemoglobin, nitric oxide and molecular mechanisms of hypoxic vasodilation,* Trends in Molecular Medicine **15**, 452 (2009).

[25] M. Bukač and M. Alber, *Multi-component model of intramural hematoma,* Journal of Biomechanics **50**, 42 (2017).

[26] L. Ai and K. Vafai, *A coupling model for macromolecule transport in a stenosed arterial wall,* International Journal of Heat and Mass Transfer **49**, 1568 (2006).

[27] S. Chung and K. Vafain, *Effect of the fluid–structure interactions on low-density lipoprotein transportwithin a multi-layered arterial wall,* Journal of Biomechanics **45**, 371 (2012).

[28] G. Pontrelli and F. de Monte, *A multi-layer porous wall model for coronary drug-eluting stents,* International Journal of Heat and Mass Transfer **53**, 3629 (2010).

[29] G. Pontrelli, A. Di Mascio, and F. de Monte, *Local mass non-equilibrium dynamics in multi-layered porous media: application to the drug-eluting stent,* International Journal of Heat and Mass Transfer **66**, 844 (2013).

[30] F. Gijsen, F. van de Vosse, and J. Janssen, *The influence of the non-newtonian properties of blood on the flow in large arteries: steady flow in a carotid bifurcation model,* Journal of Biomechanics **32**, 601 (1999).

[31] E. Ortiz-Prado, J. Dunn, J. Vasconez, D. Castillo, and G. Viscor, *Partial pressure of oxygen in the human body: a general review.* American journal of blood research **9**, 1 (2019).

[32] R. Perinajová, P. van Ooij, and S. Kenjereš, *On the identification of hypoxic regions in subject-specific cerebral vasculature by combined cfd/mri,* Royal Society Open Science **10**, 220645 (2023).

[33] M. Y. Salmasi, S. Pirola, S. Sasidharan, S. M. Fisichella, A. Redaelli, O. A. Jarral, D. P. O'Regan, A. Y. Oo, J. E. Moore, X. Y. Xu, and T. Athanasiou, *High wall shear stress can predict wall degradation in ascending aortic aneurysms: An integrated biomechanics study,* Frontiers in Bioengineering and Biotechnology **9** (2021), 10.3389/fbioe.2021.750656.

[34] A. J. Boyd, D. C. Kuhn, R. J. Lozowy, and G. P. Kulbisky, *Low wall shear stress predominates at sites of abdominal aortic aneurysm rupture,* Journal of Vascular Surgery **63**, 1613 (2016).

[35] Y.-S. J. Li, J. H. Haga, and S. Chien, *Molecular basis of the effects of shear stress on vascular endothelial cells,* Journal of Biomechanics **38**, 1949 (2005).

[36] D. A. Chistiakov, A. N. Orekhov, and Y. V. Bobryshev, *Effects of shear stress on endothelial cells: go with the flow,* Acta Physiologica **219**, 382 (2017), https://onlinelibrary-wiley-com.tudelft.idm.oclc.org/doi/pdf/10.1111/apha.12725 .

[37] L. Peng, Y. Qiu, Z. Yang, D. Yuan, C. Dai, D. Li, Y. Jiang, and T. Zheng, *Patient-specific computational hemodynamic analysis for interrupted aortic arch in an adult: Implications for aortic dissection initiation,* Scientific Reports **9**, 8600 (2019).

[38] E. P. Manning, A. B. Ramachandra, J. C. Schupp, C. Cavinato, M. S. B. Raredon, T. Bärnthaler, C. Cosme, I. Singh, G. Tellides, N. Kaminski, and J. D. Humphrey, *Mechanisms of hypoxia-induced pulmonary arterial stiffening in mice revealed by a functional genetics assay of structural, functional, and transcriptomic data,* Frontiers in Physiology **12** (2021), 10.3389/fphys.2021.726253.

[39] O. J. Erdozain, S. Pegrum, V. R. Winrow, M. Horrocks, and C. R. Stevens, *Hypoxia in abdominal aortic aneurysm supports a role for hif-1α and ets-1 as drivers of matrix metalloproteinase upregulation in human aortic smooth muscle cells,* Journal of Vascular Research **48**, 163 (2011).

[40] S. Kenjereš and A. de Loor, *Modelling and simulation of low-density lipoprotein transport through multi-layered wall of an anatomically realistic carotid artery bifurcation,* Journal of The Royal Society Interface **11**, 20130941 (2014).

[41] S. Kenjereš, J. van der Krieke, and C. Li, *Endothelium resolving simulations of wall shear-stress dependent mass transfer of ldl in diseased coronary arteries,* Computers in Biology and Medicine **114**, 103453 (2019).

[42] R. Perinajova, T. vna de Ven, E. Roelse, F. Xu, J. Juffermans, J. Westenberg, H. J. Lamb, and S. Kenjereš, *A comprehensive MRI-based computational model of blood flow in compliant aorta using radial basis function interpolation,* SSRN Electronic Journal (2022), 10.2139/ssrn.4029428.

[43] D. G. Buerk and T. K. Goldstick, *Arterial wall oxygen consumption rate varies spatially,* American Journal of Physiology-Heart and Circulatory Physiology **243**, H948 (1982), pMID: 7149047, https://doi.org/10.1152/ajpheart.1982.243.6.H948 .

[44] S. M. Santilli, R. B. Stevens, J. G. Anderson, W. D. Payne, and M. D. Caldwell, *Transarterial wall oxygen gradients at the dog carotid bifurcation,* American Journal of Physiology-Heart and Circulatory Physiology **268**, H155 (1995), pMID: 7840259, https://doi.org/10.1152/ajpheart.1995.268.1.H155 .

6

Modelling of O_2 in Circle of Willis

Long-time exposure to lack of oxygen (hypoxia) in some regions of the cerebrovascular system is believed to be one of the causes of cerebral neurological diseases. In the present study, we show how a combination of Magnetic Resonance Imaging (MRI) and Computational Fluid Dynamics (CFD) can provide a non-invasive alternative for studying blood flow and transport of oxygen within the cerebral vasculature. We perform computer simulations of oxygen mass transfer in the subject-specific geometry of the Circle of Willis. The computational domain and boundary conditions are based on 4D flow MRI measurements. We consider two different oxygen mass transfer models: passive (where oxygen is treated as a dilute chemical species in plasma) and active (where oxygen bonds to hemoglobin) models. We show that neglecting hemoglobin transport results in a significant underestimation of the arterial wall-mass transfer of oxygen. We identified the hypoxic regions along the arterial walls by introducing the critical thresholds that are obtained by comparison of the estimated range of Damköhler number ($Da \subset \langle 9; 57 \rangle$) with the local Sherwood number. Finally, we recommend additional validations of the combined MRI/CFD approach proposed here for larger groups of subject- or patient-specific brain vasculature systems.

This chapter has been published as: R. Perinajová, P. van Ooij, S. Kenjereš, *On the identification of hypoxic regions in subject-specific cerebral vasculature by combined CFD/MRI*, Royal Society Open Science 10 (2023).

6.1 Introduction

Hypoxia occurs when an organ or tissue suffers from a lack of oxygen, eventually leading to cellular necrosis [1]. Several studies have hypothesized that this lack of oxygen can trigger mechanisms responsible for various types of pathological conditions/diseases such as dementia [2, 3], atherosclerosis [4], or aneurysm generation and progression, as shown for the thoracic aortic aneurysm [5]. Circulation hypoxia occurs when the red blood cells carry the oxygen but do not deliver it to the tissue, [6]. Morphometric changes in the blood vessels can cause this phenomenon, as previously demonstrated in [7, 8] for stenotic arteries. Due to stenosis, small recirculation zones are generated that are characterized by insufficient oxygen transfer to the arterial wall, causing local hypoxia. Therefore, identifying these regions can provide more insights into the initial screening and potential improvements in treatment for the pathologies mentioned above. The oxygen concentration needs to be accurately measured to predict the degree of hypoxia in blood vessels. Unfortunately, the present generation of measuring methods of the local oxygen concentration cannot provide the required spatial resolution or are intrusive and, as such, not applicable to clinical settings. Furthermore, *in vivo* tests on animal models also demonstrated high inter-subject sensitivity and obtained results cannot be easily generalized, as shown in [2, 3]. Consequently, a new method, which will provide detailed insights into oxygen mass transfer in blood vessels, needs to be introduced. Here, we propose a method that integrates specific data from 4D-flow MRI (precisely the geometry and flow boundary conditions) with advanced computational fluid dynamics (CFD) that includes mass transfer modeling in cerebrovascular systems. Performing such simulations will be able to provide a detailed mapping of the local blood flow patterns and corresponding mass transfer limitations far beyond current measurement capabilities.

In recent years, a continuous increase in computational capabilities enabled detailed numerical simulation studies of the blood flow in the complex patient-specific geometries of the cardiovascular system. To obtain subject-specific results, we can utilize the 4D-flow MRI measurements to provide both computational domain and boundary conditions for CFD simulations, [9–19]. In addition to the flow, we must define mass transfer modeling. For example, for many diseases, it is essential to understand local variations in the concentration of different species, e.g., oxygen or low-density lipoprotein (LDL) (for the onset of atherosclerosis), [20–22]. Few modeling approaches for oxygen mass transfer were performed either in simplified models of arteries, as in [7, 8, 23–30], or in the subject-specific computational geometries obtained from CT or MRI imaging techniques, as shown in [31–33]. In numerous previous computational studies of oxygen mass transfer in blood vessels, researchers focus on two approaches: (i) oxygen transport as a free species in plasma, [7, 23, 26, 29, 30, 33, 34], (ii) oxygen transport by hemoglobin, [27, 28, 31, 32, 35, 36]. It was suggested that the inclusion of hemoglobin-mediated oxygen transport was essential to obtain a proper representation of oxygen mass transfer in blood vessels, [27].

In the present study, we propose an integral approach, which combines the transport of oxygen through free diffusion in the plasma with transport by hemoglobin in the subject-specific brain vascular system. We base the numerical simulations on the geometry and blood flow rates of the detailed cerebrovascular network of blood vessels obtained from 7T 4D-flow MRI scans. Utilizing 4D-flow MRI enables a direct comparison between the calculated (CFD) and observed (MRI) blood flow patterns, which are essential prerequisites

for accurate predictions of oxygen transport. Based on these simulations, we propose a novel method for the identification of the regions within the cerebrovascular system wherein the hypoxia can take place.

6.2 Methods

6.2.1 Clinical data set - MRI

The volunteer (male, 25 years old) underwent a 4D flow MRI examination on a 7T MRI scanner (Achieva, Philips Healthcare, Cleveland, USA) that was retrospectively gated with a peripheral pulse unit. Non-interpolated spatial resolution was $0.47 \times 0.47 \times 0.50$ mm^3. Echo time was 3.1 ms, repetition time was 6.8 ms, and the flip angle was 20°. Velocity encoding was 150 in the x, y, and z directions. We reconstructed twelve cardiac phases, resulting in a temporal resolution of 75 ms at an average heart rate of 54 beats/minute. The adopted protocol accelerates the scan with a SENSE factor of 3 in the right-left direction. Additionally, we corrected phase images for the concomitant field and eddy-current-related phase offsets. The lumen of the Circle of Willis was semi-automatically segmented using commercial software (Mimics, Materialise, Leuven, Belgium). Finally, we calculated the wall shear stress (WSS) as previously described [37].

6.2.2 Computational fluid dynamics and mass transfer

Governing equations

he conservation of mass was solved using the continuity equation under the assumption that the whole blood behaves as an incompressible fluid (ρ = constant):

$$\nabla \cdot \mathbf{u} = 0 \tag{6.1}$$

where $\mathbf{u}$ is the velocity vector, and the Navier-Stokes equations were used for solving the conservation of momentum:

$$\rho \frac{\partial \mathbf{u}}{\partial t} + \rho (\mathbf{u} \cdot \nabla) \mathbf{u} = -\nabla p + \nabla \cdot (\mu \nabla \mathbf{u}) \tag{6.2}$$

where p is the pressure and μ is the dynamic viscosity of the blood.

Oxygen transport by plasma, also known as passive oxygen transport, can be described by the dilute approximation. We use the convection-diffusion equation to describe the transport of species 'i', which can be written as:

$$\frac{\partial c^{(i)}}{\partial t} + \nabla \cdot \left(\mathbf{u} c^{(i)} \right) = \nabla \cdot \left(\mathscr{D} \nabla c^{(i)} \right) + R^{(i)} \tag{6.3}$$

where the last term $R^{(i)}$ is the source/sink, omitted for passive oxygen transport. In the case of active oxygen transport (transport of oxygen bound to hemoglobin) the source/sink term describes the reaction process of binding/releasing oxygen to/from hemoglobin. There are four available locations for oxygen molecules to bind to a hemoglobin molecule and the binding process is enhanced by already bound oxygen molecules [38]. The reactions

occurring are:

$$\begin{aligned} \mathrm{Hb} + \mathrm{O_2} &\xrightarrow{\mathrm{K_1}} \mathrm{HbO_2} \\ \mathrm{HbO_2} + \mathrm{O_2} &\xrightarrow{\mathrm{K_2}} \mathrm{Hb(O_2)_2} \\ \mathrm{Hb(O_2)_2} + \mathrm{O_2} &\xrightarrow{\mathrm{K_3}} \mathrm{Hb(O_2)_3} \\ \mathrm{Hb(O_2)_3} + \mathrm{O_2} &\xrightarrow{\mathrm{K_4}} \mathrm{Hb(O_2)_4} \end{aligned} \tag{6.4}$$

with K_1, K_2, K_3 and K_4 being the reaction constants. With this approach, a total of six species need to be specified and solved in Eq.(6.3). This would make the calculations computationally too extensive. Instead, the oxygen-hemoglobin dissociation curve was chosen to model the binding process. The oxygen-hemoglobin dissociation curve has a sigmoidal shape and relates the saturation of hemoglobin (S) to the partial pressure of oxygen (PO_2). This process can be described by Hill's equation [39]:

$$\mathrm{S} = \frac{{\mathrm{PO_2}}^n}{{\mathrm{PO_2}}^n + {\mathrm{P_{50}}}^n} \tag{6.5}$$

with coefficients n (Hill's coefficient) and P_{50} (partial pressure of oxygen for saturation of 50%) equal to $n = 2.7, \mathrm{P_{50}} = 26.6$ mmHg, respectively [8].

Several models can be used to describe the dependency between the partial pressure of oxygen and saturation of hemoglobin. Hill's equation is the preferred calculation approach because of its relative simplicity. Previously, Collins et al. demonstrated that Hill's equation predicts the actual clinical state accurately [40]. Using the oxygen-hemoglobin dissociation curve to describe active transport results in two convection-diffusion equations, which correspond to the two different species - oxygen and hemoglobin - as follows:

$$\alpha \left(\frac{\partial \mathrm{PO_2}}{\partial t} + \nabla \cdot (\mathbf{u}\mathrm{PO_2}) \right) = \alpha \nabla \cdot (\mathscr{D}_b \nabla \mathrm{PO_2}) + r \tag{6.6}$$

where α is the solubility coefficient of oxygen, $\mathscr{D}_b$ is the oxygen diffusion coefficient in blood, and r is the oxygen release rate by the heme group. The transport equation for saturated hemoglobin can be written as

$$[\mathrm{Hb}] \left(\frac{\partial \mathrm{S}}{\partial t} + \nabla \cdot (\mathbf{u}\mathrm{S}) \right) = [\mathrm{Hb}] \nabla \cdot (\mathscr{D}_c \nabla \mathrm{S}) - r \tag{6.7}$$

where [Hb] is the oxygen-carrying capacity of hemoglobin in blood and $\mathscr{D}_c$ is the oxyhemoglobin diffusion coefficient in blood. When combining these two equations, the reaction terms are eliminated, and an equation for the transport of oxygen then is:

$$\left(1 + \frac{[\mathrm{Hb}]}{\alpha} \frac{d\mathrm{S}}{d\mathrm{PO_2}} \right) \left(\frac{\partial \mathrm{PO_2}}{\partial t} + \mathbf{u} \cdot \nabla \mathrm{PO_2} \right) = \nabla \cdot \left[\mathscr{D}_b \left(1 + \frac{[\mathrm{Hb}]}{\alpha} \frac{\mathscr{D}_c}{\mathscr{D}_b} \frac{dS}{d\mathrm{PO_2}} \right) \nabla \mathrm{PO_2} \right] \tag{6.8}$$

where on the left-hand side of the equation, coefficients in the bracket can be interpreted as a non-constant oxygen carrying capacity, and the coefficient can be understood as a non-constant diffusivity on the right side. The resulting equation is nonlinear as both new

coefficients are dependent on the term $\frac{dS}{dPO_2}$, [8]. We can further reduce computational time by linearizing nonlinear terms in Eq.(6.8). After performing a first-order Taylor series expansion of Eq.(6.5) one can obtain

$$\frac{d\overline{S}}{d\overline{PO_2}} = \frac{n\overline{S}}{\overline{PO_2}}\left(1-\overline{S}\right) \tag{6.9}$$

where $\overline{PO_2}$ is a reference value of the partial pressure of oxygen (for the highest minimization of the error, a value of 75 mmHg is used) and $\overline{S}$ is a saturation level of oxygen evaluated at $\overline{PO_2}$. This equation can be used to linearize both sides of Eq.(6.8), yielding ([8]):

$$\begin{aligned}\left(1+\frac{[Hb]}{\alpha}\frac{n\overline{S}}{\overline{PO_2}}\left(1-\overline{S}\right)\right)\left(\frac{\partial PO_2}{\partial t}+\mathbf{u}\cdot\nabla PO_2\right) = \\ \nabla\cdot\left[\mathscr{D}_b\left(1+\frac{[Hb]}{\alpha}\frac{\mathscr{D}_c}{\mathscr{D}_b}\frac{n\overline{S}}{\overline{PO_2}}\left(1-\overline{S}\right)\right)\nabla PO_2\right]\end{aligned} \tag{6.10}$$

where the coefficient on the right-hand side is the non-constant diffusivity of oxygen and the coefficient on the left-hand side as the non-constant carrying capacity of oxygen, respectively.

Finally, the non-dimensional mass transfer is evaluated through the Sherwood number, which defines the ratio between the total mass transport and purely diffusive mass transport, and which we calculate as:

$$Sh_w = \frac{-d_0\left(\frac{\partial c^{(i)}}{\partial n}\right)_w}{c_b^{(i)}-c_w^{(i)}} \tag{6.11}$$

where d_0 is the diameter of the studied artery, at its entry, subscripts b and w correspond to the bulk and wall, respectively.

Computational domain and numerical mesh

In this study, we performed simulations on the geometry of the Circle of Willis. Fig.6.1(a) shows the studied domain after pre-processing and meshing. The arterial system consists of three inlets: Basilar Artery - BA, Left and Right Internal Carotid Artery - L(R)ACA, six outlets: Left and Right Middle Cerebral Artery - L(R)MCA, Left and Right Posterior Cerebral Artery - L(R)PCA, Left and Right Superior Cerebellar Artery - L(R)SCA and two connecting arteries: ACoM and PCoM. For the geometry manipulation (which includes: smoothing, opening ends, and adding extensions), we used open-source software, Vascular Modeling Toolkit (VMTK) [41].

We have opted for a polyhedral mesh to perform our simulations with boundary layer refinement. In total, mesh contained ten boundary layers, with the first element width of $\sim 5\cdot10^{-3}D_0$ and the total width of $\sim 7\cdot10^{-2}D_0$ (in BA), where D_0 is the diameter of the inlet of BA. The final polyhedral grid used for the simulations is shown in Fig.6.1(a) with the details of the boundary layer refinement. This mesh was proven adequate for the simulations, as shown in the mesh-dependency analysis in the Supplementary Material. We have created a finer and a coarser mesh to perform the mesh sensitivity study. The coarse mesh

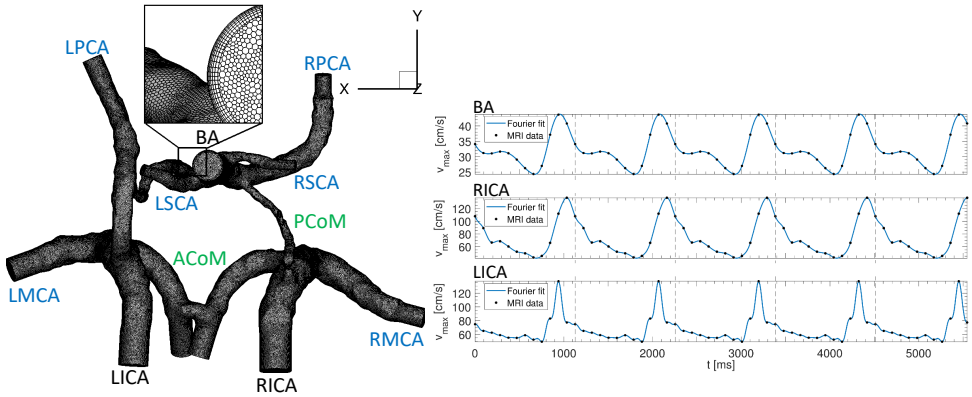

a) b)

Figure 6.1: (a) The pre-processed geometry with added outflow extensions and the created polyhedral mesh. The black labels correspond to the inlet arteries, the blue to the outlet arteries and green to the connecting arteries. (b) The average velocity over time at the inlets (BA-Basilar Artery, RICA-Right Internal Carotid Artery, LICA-Left Internal Carotid Artery).

consisted of approximately 1.3 million polyhedral elements (initially 5 million tetrahedral elements). In contrast, the medium mesh consisted of roughly 2.3 million polyhedral elements (initially 12 million tetrahedral elements), and finally, the finer mesh included approximately 5 million polyhedral elements (initially 40 million tetrahedral elements). In our previous work, in which we addressed the transport of the momentum and magnetic drug carriers in the brain vascular system, a similar numerical mesh resolution proved sufficient to obtain grid-independent solutions, [42]. We have performed a mesh sensitivity analysis that can be found in Supplementary Material, confirming that the results obtained on the medium mesh are grid-independent. Appendix D includes the grid convergence index (GCI) study and a comparison of the locally extracted WSS profiles.

Boundary conditions

We assumed a rigid wall, with the no-slip condition for the flow, and the oxygen concentration was considered zero. Three inlets are present in the subject-specific geometry of the Circle of Willis - Basilar Artery (BA), Left Internal Carotid Artery (LICA) and Right Internal Carotid Artery (RICA). The 4D-MRI measurement technique measured the velocities for each artery mentioned for one cycle (1034 ms) every 94 ms by the four-dimensional MRI measurement technique. Subsequently, we fitted an appropriate curve for the obtained velocity data points. Fourier series predicts that each curve, which shows some periodicity, can be decomposed into a sum of sine and cosine functions. MRI data with fitted curves are shown in Fig.6.1(b). The numbers obtained for harmonics used to describe the inlets of the arteries are: BA (n = 5), RICA (n = 8) and LICA (n = 12). The n-values were chosen, so the statistical term R^2 (squared residuals) was equal to 1.00.

The time-dependent curves were implemented as an inlet boundary condition, and

a parabolic velocity profile was constructed. We specified the outlet mass flow rates by Murray's law based on the conservation of mass at the branching points of arteries [43, 44]. It can be written as

$$\frac{q_0}{q_{D_i}} = \left(\frac{R_0}{R_{D_i}}\right)^{1/3} \tag{6.12}$$

where q_0 stands for the volumetric flow through a mother artery of radius R_0 and q_{D_i} is the volumetric flow through one of the branches with radius R_{D_i}. The resulting ratios of the total mass flow rate are as follows: LACA - 12%, LMCA - 25%, LPCA - 9%, LSCA - 5%, RACA - 11%, RMCA - 29%, RPCA - 7%, and RSCA - 2%.

Materials and physical setup

The physical properties of the fluid (blood) are specified as follows: density equal to 1060 kg/m^3, hematocrit level of 45% and non-Newtonian viscosity behavior defined by the Carreau-Yasuda model [45]:

$$\mu_{eff}(\gamma) = \mu_\infty + (\mu_0 - \mu_\infty)(1 + (\lambda\gamma)^a)^{\frac{n-1}{a}} \tag{6.13}$$

where μ_0 is viscosity at zero shear rate, μ_∞ is viscosity at infinite shear rate, λ is a relaxation time, n and a are the power indices. The estimated parameters are based on fitting measured viscosity of blood for the hematocrit level of 45% [46]: μ_0 = 213.1 mPa·s, μ_∞ = 3.14 mPa·s, λ = 50.2 s, n = 0.331 and a = 0.8588.

For the passive transport of oxygen, we used a characteristic value of the Schmidt number of Sc = 2917. The oxygen-carrying capacity [Hb] is specified as 0.2 ml O_2/ml blood, with the following properties: the oxygen solubility $\alpha = 2.5 \times 10^{-5}$ ml O_2/ml plasma/mmHg, the oxygen diffusion coefficient in blood $\mathscr{D}_b = 1.5 \times 10^{-9}$ m^2/s and the oxyhemoglobin diffusion coefficient in blood $\mathscr{D}_c = 1.5 \times 10^{-11}$ m^2/s [8].

Numerical Setup

In this study, the second-order upwind discretization scheme for convective terms in transport equations was applied, which ensures higher stability and accuracy of the results, [47]. The solution methods used in this study for all the models mentioned here are listed below.

- Solver - pressure based
- Pressure-Velocity Coupling - SIMPLE
- Spatial discretization
  - Gradient - Least Squares Cell-Based
  - Pressure - Second-Order
  - Momentum - Second-Order Upwind
  - Species - Second-Order Upwind
- Time discretization - Second-Order Implicit
- Residuals (continuity, velocity components, and O_2) - 10^{-5}

6.2.3 Post-processing and Data Analysis

In total, five cycles of simulations were performed (as shown in Fig. 6.1b), and only the last cycle was used for further analysis. To analyze the blood flow and oxygen mass transfer, we have calculated several additional parameters. First, the wall shear stress (τ_w) was calculated as

$$\tau_w = \mu \cdot \dot{\gamma_w} \tag{6.14}$$

where μ is the dynamic viscosity of the blood and $\dot{\gamma_w}$ is the shear rate at the wall. For comparison purposes between CFD and MRI, we have normalized τ_w using the respective maximal values of wall shear stress as:

$$\left(\tau_w^i\right)^* = \left(\tau_w^i\right) / \left(\tau_w^i\right)_{max} \tag{6.15}$$

where i denotes MRI or CFD. Additionally, we have calculated the time-averaged quantities for τ_w and Sh as:

$$\text{TAWSS} = \frac{1}{T}\int_0^T \left|\vec{\tau_w}\right| dt \tag{6.16}$$

$$\text{TASh} = \frac{1}{T}\int_0^T |\text{Sh}_w| \, dt \tag{6.17}$$

where T is the period of a cardiac cycle, $\left|\vec{\tau_w}\right|$ is the absolute value of shear stress vector at the wall, and $|\text{Sh}_w|$ is the Sherwood number. To identify the level of oxygen consumption in the wall, we have calculated the Damköhler number (Da), which is defined as

$$Da = \frac{\dot{Q} T d}{K \mathscr{D} P_b} \tag{6.18}$$

where $\dot{Q}$ is oxygen consumption rate of arterial tissue, T is the arterial wall thickness, d is the mean arterial diameter, K is Henry's constant, $\mathscr{D}$ is the oxygen diffusion coefficient and P_b is the bulk pressure of oxygen, [38]. We have adopted the following values of the transport coefficients, $\frac{\dot{Q}}{K\mathscr{D}} = 1.96 \cdot 10^5$ mmHg/cm^2 and $P_b = 90$ mmHg, in accordance with [48] and [25].

Finally, if any variables (ϕ) were compared, we have calculated the relative difference ($\Delta\phi$) as:

$$\Delta\phi = \frac{\phi_{\text{MRI}} - \phi_{\text{CFD}}}{0.5 \cdot (\phi_{\text{MRI}} + \phi_{\text{CFD}})} \cdot 100 \;\text{ in }\; [\%] \tag{6.19}$$

where ϕ_{MRI} and ϕ_{CFD} are the values of the compared variable for MRI and CFD, respectively. To be able to make more objective comparisons, the CFD results were mapped to the MRI mask by applying the following steps:

- CFD results were interpolated onto a grid with an equal cell size of 0.001 mm - to eliminate the high cell density close to the wall
- For the voxel-to-voxel comparison, the CFD mask was registered on the MRI mask

Afterward, the percentage difference was calculated as shown in Eq.6.19.

6.3 Results

6.3.1 Blood flow validation in CoW

A comparative assessment of blood flow at the systole, obtained from CFD and MRI, is shown in Fig.6.2(a). We plotted stream traces and contours of the velocity magnitude for both cases. The details of the flow in the LICA bifurcation are shown in the highlighted regions. Fig.6.2(b) shows the net volumetric flow for each of the outlets as acquired by MRI (black) and calculated by CFD (grey). Additionally, we have calculated the relative percentage difference in the outflows between the two methods, Fig.6.2(b). To statistically evaluate the agreement between the calculated and measured velocity magnitude of the blood flow in the subject-specific CoW, Fig.6.2(c) shows the voxel-to-voxel correlation of the data sets. In this plot, we have selected ten horizontal slices (along the z–direction) and performed extrapolation of the CFD data to the corresponding MRI mask. The Pearson product-moment correlation coefficient was 0.79, which implies a good correlation between CFD and MRI.

We provide a more detailed comparison between the CFD and MRI results by zooming into a characteristic horizontal cross-section shown in Fig.6.3. This cross-section shows parts of the RICA and LICA along with a small fraction of the PCoMs. The contours of the velocity magnitude are superimposed with in-plane velocity vectors. Comparing the overall agreement between the CFD (-left) and MRI (-right) shows that both methods capture the most salient flow features. A zoomed-in selection (LICA) is shown in Fig.6.3 for CFD (c) and MRI (d) together with a voxel-to-voxel relative percentage difference between the two methods (e). To calculate this, we have interpolated the CFD data on the MRI grid and calculated a voxel-to-voxel difference between the two data sets, Fig.6.2.

6.3.2 Wall Shear Stress validation in CoW

The non-dimensional WSS for MRI and CFD at the peak systole, for two characteristic views (the front view-top and the back view-bottom), are shown in Fig.6.4. Note that the values were made dimensionless for each case separately with the respective mean values. To perform comparisons between MRI and CFD more quantitatively, values of the overall maximal and averaged values of WSS for three distinct time instants of the pulsating cycle were selected ($t = k \cdot \omega$ beginning of diastole, $t = 0.6k \cdot \omega$ end of diastole, $0.9k \cdot \omega$) peak systole) and results are shown in Table 6.1.

Table 6.1: Global maximal and mean values of the wall shear stress (WSS) for MRI and CFD results, for 3 characteristic times of a k-th cardiac cycle (k·ω), where 0.6k·ω represents the diastole and 0.9k·ω the systole, k = 0, 1, 2, ...

	Maximal WSS			Average WSS		
Time [ms]	**MRI**	**CFD**	**Difference [%]**	**MRI**	**CFD**	**Difference [%]**
k·ω	18.66	84.63	127.74	2.89	4.61	45.87
0.6k·ω	21.72	23.24	6.76	1.81	2.04	11.95
0.9k·ω	17.82	87.62	132.40	3.97	7.42	60.58

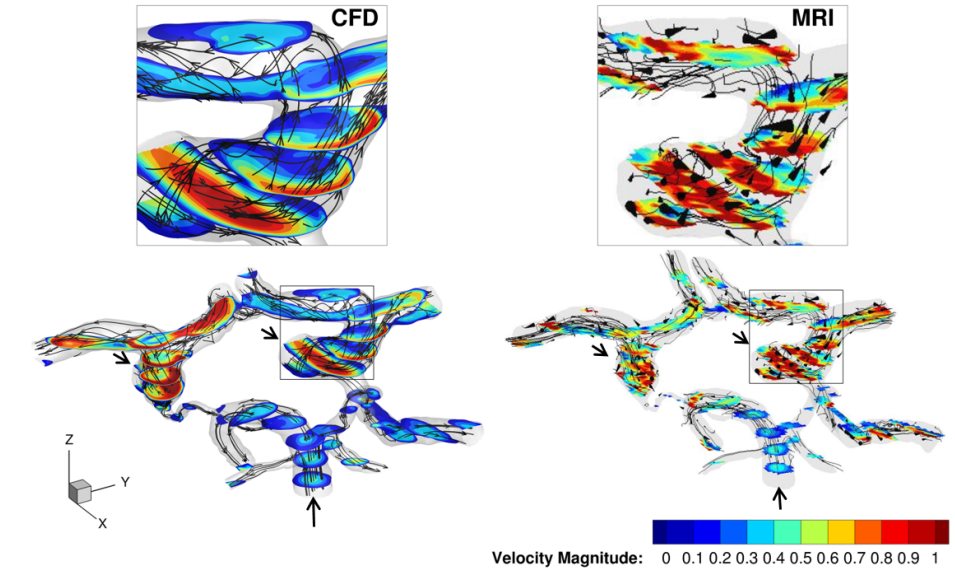

(a)

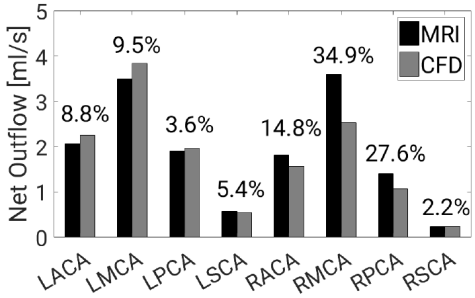

(b)

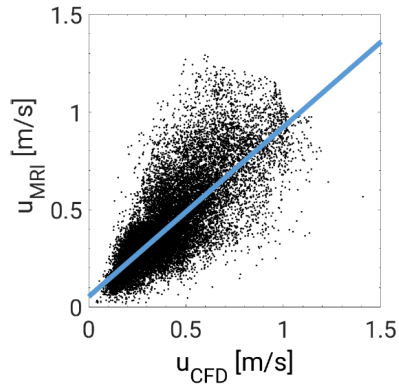

(c)

Figure 6.2: Contours of velocity magnitude at the peak systole as obtained from CFD (left) and MRI (right) details of one of the bifurcations (a), comparison of flow rate in ml/s at all of the outlet faces of the Circle of Willis for CFD and MRI with the estimated relative difference between the MRI and CFD of the outlet net flow rate (b) and the correlation plot of velocity magnitude between CFD and MRI for ten randomly chosen Z-slices (out of 40 total), where the calculated R coefficient is equal to 0.79 (c).

6.3.3 Mass transport of oxygen in CoW

To find a possible correlation between the momentum (flow) and mass (oxygen) transfer over the entire cardiac cycle, the time-averaged wall shear stress (TAWSS) and time-averaged Sherwood number (TASh) are calculated for both the passive and active oxygen transfer. They are visualized in Fig.6.5, for both investigated modes of oxygen transport (passive - O_2 and active - HEM).

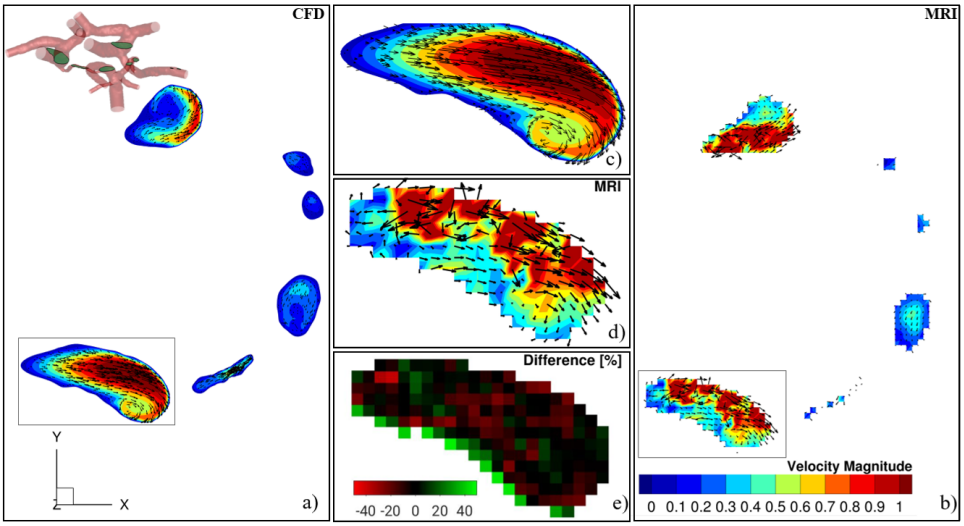

Figure 6.3: Velocity magnitude with in-plane velocity vectors for a characteristic horizontal cross-section of the Circle of Willis: the results of CFD (a) and MRI (b) with the details of one of the arteries are shown for both CFD (c) and MRI (d) and the percentage difference between MRI and CFD (e).

To perform a more detailed comparison between the passive and active mass transfer of oxygen, the difference between the two models is calculated for each control volume and shown in Fig.6.6 (for two perspective views - from the front (-left) and from the back (-right)). Note that this difference was calculated similarly to Eq.6.19.

6.3.4 Identification of Hypoxic Regions

A possible way to identify hypoxia is to compare oxygen consumption within the wall with the mass transport from the luminal side. The consumption of oxygen within the wall can be characterized by the non-dimensional Damköhler number (Da) as defined in Eq.6.18. The estimated values of Da for different regions in CoW are listed in Table 6.2 together with the averaged diameter of the corresponding arteries (d_{ave}) and the respective estimated wall thickness (T).

In theory, hypoxia occurs if the mass transport towards the wall (defined by Sherwood number - Sh) is lower than the consumption of oxygen in the wall (defined by Damköhler number - Da) - hence, if the condition Sh<Da applies. In Fig.6.7 we highlight the regions of CoW where Sh<Da. The color range is adjusted according to the estimated values of Da, Tab.6.2. We show the hypoxic regions for the passive oxygen transport (O_2) in a) and for the active oxygen transport (HEM) in b). Additionally, Fig.6.7(c) show the percentage of the total surface area of CoW potentially affected by hypoxia for both modes of transport (passive and active) and passive×2. Finally, we show the reduction (in %) of hypoxic area

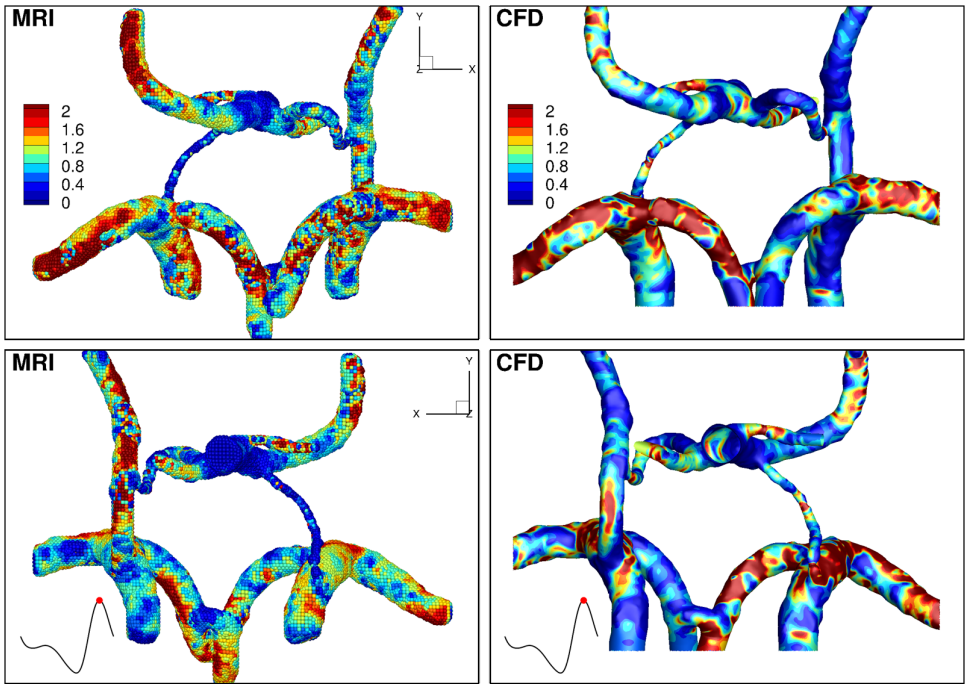

Figure 6.4: Normalized wall shear stress (WSS/WSS_{mean}) at the peak systole as obtained from MRI (left) and CFD (right) from two perspectives (top/bottom); WSS was normalized for both cases separately by the corresponding mean value.

Table 6.2: Average diameter (d_{ave}), estimated wall thickness (T), and calculated values of the Damköhler number (Da) for all major arteries of CoW (ICA - Internal Carotid Artery, BA - basilar artery, ACA - Anterior Choroidal Artery, MCA - Middle Cerebral Artery, PCA - Posterior Cerebral Artery, PcoM - Posterior Communicating Artery, AcoM - Anterior Communicating Artery, SCA - Superior Cerebellar Artery). Note that the arterial wall thickness estimates were based on the study of [49].

Artery	d_{ave} [mm]	T [mm]	Da [-]
ICA	4.00	0.66	57
BA	4.00	0.61	53
ACA	2.50	0.45	25
MCA	3.50	0.58	44
PCA	3.00	0.51	33
PcoM	1.00	0.39	9
AcoM	1.00	0.39	17
SCA	2.00	0.44	19

concerning the passive transport for passive×2 and active oxygen transport, Fig.6.7(d).

6.4 Discussion

In this work, we have investigated the blood flow and oxygen mass transfer in the Circle of Willis, an integral part of the cerebrovascular system. The simulations were based on

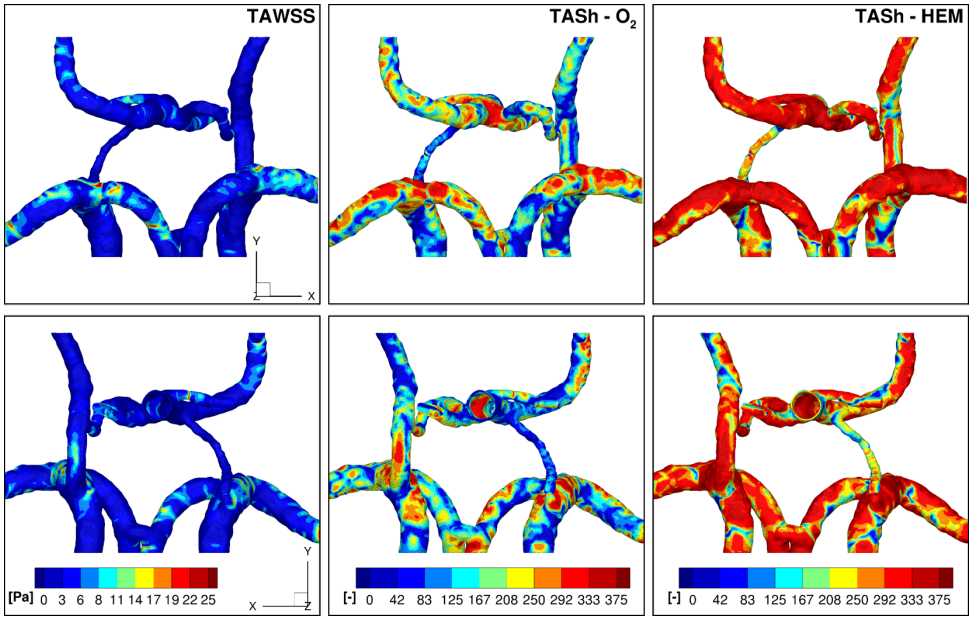

Figure 6.5: Time-averaged wall shear stress (TAWSS) (-left), time-averaged Sherwood number for passive transport (TASh-O_2) (-middle) and active transport (TASh-HEM) (-right).

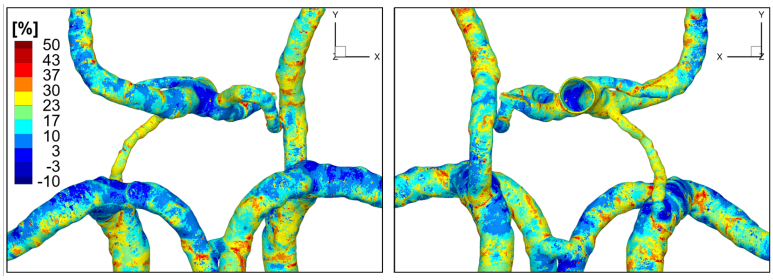

Figure 6.6: Relative percentage difference in the Sherwood number between the passive and active model from the front (left) and back (right).

4D-flow MRI. We have used these measurements to define the computational domain and the inlet boundary conditions. We have also validated the simulated blood flow with the 4D-flow MRI measurements. For oxygen mass transfer, we have used and compared two different models of oxygen transport - passive transport (free diffusion in plasma) and active transport (combined diffusion in plasma and bound to hemoglobin). Finally, we proposed a method to identify the hypoxic regions, based on the ratio between oxygen mass transfer towards the wall and the estimated consumption by the wall.

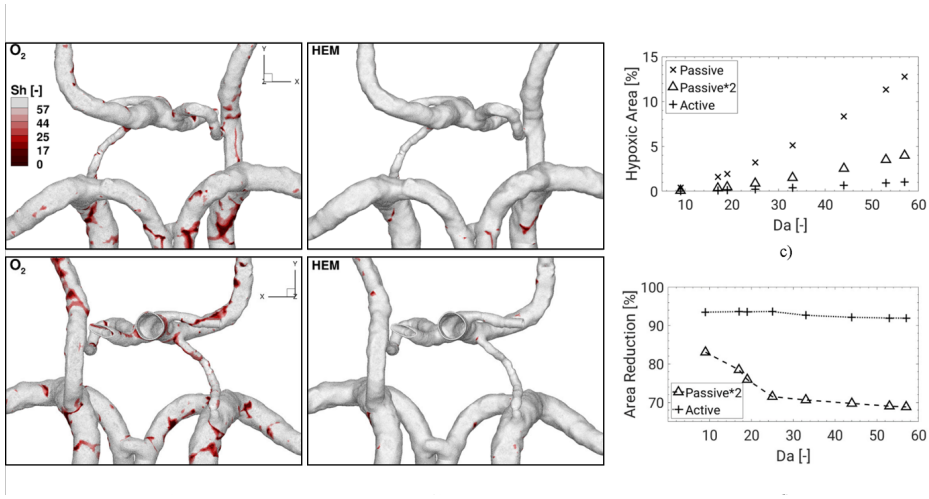

Figure 6.7: Comparison of the hypoxic regions area for both oxygen mass transport models - as dissolved species (O_2) -(a) and as bonded to hemoglobin (HEM) - (b) for the boundary condition at the wall of 0 mmHg. The hypoxic regions (when Sh<Da) are shown in red, and the percentage of the arterial the surface area with hypoxic behavior based on the passive, two times passive, and active oxygen transport models (c) and the hypoxic area reduction in comparison to the passive model for the range of the Damköhler number (d).

6.4.1 Agreement in Flow Field

To validate the simulated results, we have compared the calculated flow field to the 4D-flow MRI measurements, Fig.6.3 and Fig.6.2. The velocity distribution within the CoW obtained from CFD is in qualitatively reasonable agreement with MRI results. At the same time, we can observe some significant deviations in certain parts of the CoW. For example, the inlet region of the ICAs from CFD shows that the flow field is fully developed. However, MRI measurements do not display this behavior. The difference between the two results from the CFD simulation has a parabolic velocity profile as the inlet condition. In reality, the velocity profile is often not fully developed, and it can change during the cardiac cycle. Consequently, the assumption of a fully developed parabolic velocity profile used at the inlet can produce differences compared to the MRI. On the other hand, the real velocity profiles based on the characteristic pulsating Womersley solution (with values of the Womersley number estimated here as $\alpha = D\sqrt{\omega/\nu}$ to be between 1 and 3, [50], [51]) are similar to parabolic solutions. Deviations from these estimates are mainly present for the ICAs, which can partially explain the above-discussed differences between MRI and CFD in the proximity of the inlet.

To provide even more detailed comparisons between MRI and CFD, we extract a single location, as indicated in the middle panel in Fig.6.3. We can see reasonable agreement between CFD and MRI, for this location, with a maximal absolute difference of 40%. However, we have to highlight that the maximal deviation is (as expected) obtained in the near-wall region because of the limited spatial resolution of MRI and boundary-layer resolving numerical mesh used in CFD. We illustrate an additional comparison between MRI and CFD in Fig.6.2b, which shows the characteristic outlet flow rates (with eight outlets in total).

Again, we can see overall good agreement between CFD and MRI for the majority of outlets, except for the RMCA and RPCA where CFD calculation predicts 35% and 28% lower flow rates, respectively.

6.4.2 Agreement in Wall Shear Stress

A very high resolution close to the aortic wall is necessary to capture WSS adequately. Previous studies show that MRI cannot capture the velocity gradient adequately, and the absolute values of WSS are often underestimated by MRI [52, 53]. We see similar observations also in our data. For peak systole ($t = 0.9k \cdot \omega$), the difference between the maximal WSS of MRI and CFD is very large. In contrast, at the diastole ($t = 0.6k \cdot \omega$), the agreement is much better with less than a 10% difference. These trends are similar also for the averaged WSS, although with significantly more minor deviations. We again saw the most significant deviation at the peak systole with a difference of 60%. Both maximal and averaged values of WSS obtained from MRI show consistently lower values than CFD.

While MRI generally underestimates the absolute values of WSS, the local distributions of high/low WSS can still be adequately estimated by this technique [19]. Therefore, to compare the WSS distribution between CFD and MRI, we have normalized both data sets by their respective average values. The normalization allows for a qualitative comparison between the two methods [19]. As shown in Fig.6.4, the local WSS distribution in the different arteries of CoW is similar for MRI and CFD. However, the agreement between measured (from MRI) and numerically calculated (from CFD) WSS is significantly less satisfactory than the velocity magnitude. Generally, the decreased agreement can be expected since estimating the WSS requires a very accurate calculation of the velocity gradients in the proximity of the arterial wall. Here we postulate that one of the primary reasons for this difference is due to the different spatial resolutions of MRI and CFD. In contrast to a uniform spatial resolution of MRI, the CFD spatial resolution is significantly refined in the arterial wall's proximity to correctly resolve hydrodynamic (momentum) boundary layers. This refinement will lead to more accurate calculations of the velocity gradients and, consequently, to more precise WSS.

6.4.3 On the modeling of the oxygen mass transfer

We can observe that at many locations with high values of TAWSS, the TASh distributions also reach their local maximum. The contour plots of the TASh number for passive (O_2) and active (HEM-hemoglobin) oxygen transport exhibit qualitatively similar behavior, with the latter showing at first-sight significantly higher values in almost the entire CoW. That is the consequence of an increase in the effective diffusivity of the oxygen for the active model.

The difference in Sh between passive and active oxygen mass transfer indicates the significance of active oxygen mass transfer, i.e., the importance of the hemoglobin coupling in oxygen mass transport modeling. This difference shows a solid local dependency, with values between +50% and -10%, and with the highest distinction in regions characterized by a low Sherwood number. Based on this distribution, we can also conclude that there is no simple pre-factor scaling of the passive oxygen mass transfer that would be able to match the active mass transfer of oxygen locally.

6.4.4 Identification of hypoxia

The low values of Sherwood numbers are associated with regions of a low wall-mass transfer of oxygen, which potentially can lead to hypoxia. To identify hypoxic regions at the arterial wall, we will use the criterion that the local rate of oxygen consumption is higher than the local Sherwood number, [32, 54]. The non-dimensional rate of oxygen consumption can be expressed as Damköhler number (Da), which is defined in Eq.6.18.

In the present study, the calculated averaged mean diameters of the major arteries and their estimated wall thickness are given in Tab.6.2. Note that the estimate of the arterial wall thickness was based on the study of Harteveld et al. [49]. Based on our simulations, the potential hypoxic regions are significantly reduced in the case of active oxygen transport. The comparison between the percentage of the arterial wall surface affected by hypoxia for passive and active mass transfer of oxygen r different values of Da is shown in Fig.6.7c. Some studies in the literature suggest that the simplified calculation of the oxygen mass transfer based on the passive model, can be sufficient when the final results of the non-dimensional wall mass transfer were multiplied by a factor of two, which provided a good agreement with the results of the active model, [25]. This study motivated us also to include results of the passive model multiplied by a factor two in Fig.6.7c. The percentage of the hypoxic area increases with Da, and that maximum area of 13%, 4%, and 1% for the passive, passive scaled twice, and active oxygen models, respectively. Additionally, we calculated the hypoxic area reduction as predicted by the active and twice passive models compared with the passive oxygen transfer model, and summarized results are given in Fig.6.7d. Values of around 70% were obtained for the majority of big arteries for the twice passive oxygen transfer model, whereas values of approximately 90% were obtained for the active oxygen transfer model. We can conclude that a simple pre-scaling by a factor of two cannot provide a close agreement with the active oxygen transport model. This also additionally confirms the need to apply a more advanced active model of oxygen transport to identify possible hypoxic regions within the subject- or patient-specific cerebral vascular system.

Finally, we need to comment on the validity of the identified hypoxic regions. While we could locate a considerable percentage of the total surface area to be hypoxic, the data might have been affected by the uncertainty brought to the simulations due to the relatively low resolution of 4D-flow MRI. Similarly to WSS variability due to segmentation in the aorta [53], we also expect variability in the Sh number. Thus, the analysis of hypoxic regions should be validated on a larger cohort, including intra- and inter-observer analysis. However, the proposed method for identifying hypoxia in the cerebrovascular system shows potential for use in further studies.

6.4.5 Limitations

We made several assumptions in this study; therefore, we must mention the pertinent limitations of the models. Regarding blood flow simulations, we initially attempted to match the CFD outflows at the outlet faces to be as close as possible to the measured MRI values. Unfortunately, due to limited MRI resolution, the measured velocity field does not comply with the overall divergence-free condition in CFD (i.e., conservation of mass was not satisfied), which resulted in a compromising approach where we utilized Murray's law to calculate the flow rates at the outlets. Additionally, we have assumed a rigid wall. In

reality, compliance of arteries allows the wall to move during the cardiac cycle. However, for the case of Circle of Willis, the arterial wall movement is very limited [55]. Hence, this assumption should not affect the calculated flow field and the derived variables.

Regarding oxygen transport, we made the following simplifications. Firstly, flux through the wall was assumed to be the same for the whole CoW - in reality, the flux differs as it is highly dependent on the thickness of the arterial wall and its physical properties, which vary spatially [48]. Moreover, in all of the simulations, a wall-free model was assumed. Therefore no wall mass transfer resistance was present, and we only studied the fluid mass transfer resistance. Secondly, the calculation of Damköhler number was based on the properties from literature and not patient-specific ones. Therefore, it is necessary to gain this information from MRI together with the geometry and flow for exact estimates. Thirdly, we have been able only to validate the velocity field, not the oxygen distribution. To directly validate the presented results, the mass transfer of oxygen through the wall has to be measured by a non-intrusive technique. However, the resolution of state-of-the-art non-intrusive imaging techniques is very limiting, and the changes in oxygen concentration in the lumen and the arterial wall is beyond their capabilities [56–59].

Finally, we have included only a single subject (a healthy volunteer, 25 years old) in this study. More subjects should be assessed to draw statistically significant conclusions, including healthy volunteers and patients with different pathologies and diseases. Nevertheless, the goal of our study was to present a framework for identifying hypoxia using subject-specific simulations.

6.5 Summary and conclusions

In the present study, we addressed the application of the combined MRI/CFD approach to provide detailed insights into the blood flow and corresponding transport of oxygen in the subject-specific brain vascular system. We considered two models of oxygen mass transfer: passive transfer, where the oxygen was treated simply as a dissolved chemical species in plasma, and active transfer, in which we included hemoglobin-bound oxygen in the model.

In the investigation, a subject-specific geometry of a part of the brain vascular system (Circle of Willis) is analyzed by a combined MRI/CFD approach. We specified the flow conditions to closely mimic the MRI measurements at the characteristic inlets and outlets. A detailed comparison of the blood flow field revealed a good agreement between 4D flow MRI and CFD results. On the other hand, the comparison between CFD and MRI was less satisfactory in predicting the local distributions of the wall shear stress. The primary reason for this discrepancy was the low spatial resolution of MRI in the proximity of the arterial wall. Finally, after obtaining the blood velocity fields, we activated the oxygen transport to determine the local concentration of oxygen along the arterial walls. We showed that significant differences between the passive and active models of oxygen transport were obtained, not only in the magnitude of the non-dimensional arterial wall mass transfer, but also in their local distributions. This finding also confirmed the importance of using a more advanced model of oxygen transport in the subject-specific geometries of the brain vascular system. Finally, by comparing the local non-dimensional oxygen mass transfer at the arterial wall (Sherwood number) and corresponding non-dimensional rate of oxygen consumption (Damköhler number), we were able to identify the potential hypoxic regions within the cerebral vasculature. The Damköhler number was estimated to be in a range

$Da \subset \langle 9;57 \rangle$ for the case studied. Due to geometrical changes in the Circle of Willis, we identified several locations with the Sherwood number lower than the Damköhler number. This suggests the fluid phase limits oxygen transport to the wall. This information can be helpful in follow-up patient studies dealing with early diagnosis or progression of dementia.

Appendix A: Hemodynamics in the simplified geometry

A simplified arterial geometry was designed to match the test case proposed by [8]. This geometry is characterized by a rigid-walled axisymmetric cosine-function-shaped stenosis (defined as: $r(z)/R = 1 - \delta/D[1 + cos(2\pi z/z_0)]$, where $r(z)$ is the radius of artery at the streamwise position z in the stenosed region (from $-2D$ to $2D$)) with maximum lumenal area reduction of 88.9% and an extension of two artery diameters on either side of the stenosis center (i.e. $\delta = D/6, z_0 = 4D$). A fully developed Hagen-Poiseuille profile is imposed at the inlet with the characteristic Reynolds number of $Re_D = 50$. The total length of the simulated geometry was $L = 20D$. The constant pressure boundary condition was specified at the outlet. A hybrid mesh was applied to obtain grid-independent solutions consisting of the hexagonal elements in the proximity of the arterial wall and tetrahedra in the central part of the lumen. Special attention was devoted to also adequately resolving the concentration boundary layers (due to high values of Schmidt number $Sc = 2917$). The coarse and fine mesh had approximately 3.5 and 7 million control volumes and with the characteristic thickness of the first row of control volumes in the proximity of the arterial wall of $\Delta r_1 = 0.03D$ and $0.02D$, respectively. The magnitude of Wall Shear Stress (WSS) ($\tau_w = \mu \left(\partial u_{||}/\partial r_n\right)_{wall}$) extracted along the wall is compared with the results of [8], Fig. 6.8. Note that the locally calculated WSS was normalized by the Hagen-Poiseuille value of WSS for a straight cylinder.

As shown in Fig.6.8, the WSS profile follows the one predicted by the Hagen-Poiseuille expression upstream of the stenosed region. At the center of the stenosed region, due to the increase of the streamwise velocity, the WSS increases up to a value approximately 40 times greater than the value in the non-stenosed area. Afterward, the importance of WSS starts to decrease as the diameter of the stenosed region increases. Finally, the minimum of the WSS is located approximately at the 1D distance from the end of the stenosed region and reaches values below the values predicted by the Hagen-Poiseuille solution. Further downstream, the WSS slowly approaches the value of the undisturbed flow. It can be concluded that WSS behavior predicted from the present study agrees well with the results of [8].

Appendix B: Oxygen mass transport in the simplified geometry

The mass transfer boundary conditions for the case of the simplified stenosed artery were chosen as follows. Both the inlet and outlet partial pressure of oxygen were set to be 90 mmHg, which is a reasonable assumption based on [8]. For the arterial wall, the partial pressure of oxygen was kept at a constant value of 0 mmHg for all simulations presented here. While this assumption is somewhat arbitrary, it is still a reasonable first approximation to test the limits of the blood-side transport equation. By imposing this boundary value of the partial pressure at the wall, the most extreme variation in the slope of oxyhemoglobin saturation function can be studied, [8].

The constant pressure boundary condition and zero-gradient concentration of oxygen were specified at the outlet. The calculated Sherwood number for the passive and active

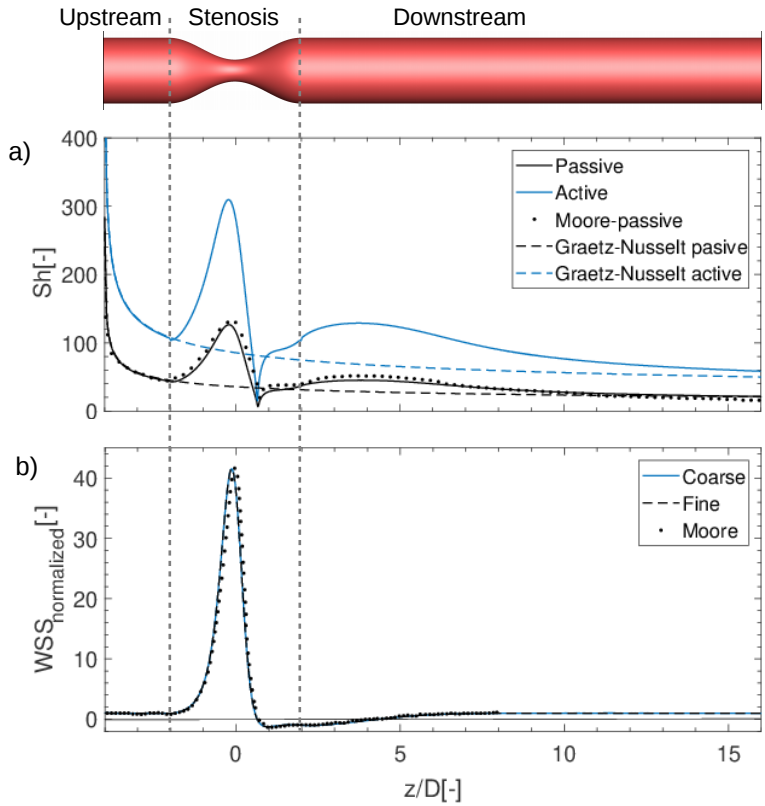

Figure 6.8: (a) Profile of the Sherwood number for passive and active oxygen extracted along the top-line of the simplified artery with comparison to results from the literature [8] and theoretical Graetz-Nusselt solution for a straight cylinder, and (b) wall shear stress normalized with the theoretical value for a straight cylinder for two different grids (coarse and fine) and results from the literature [8].

oxygen transport are shown in Fig.6.8(a), whereas the grid dependency on the local wall mass transfer is shown in Fig.6.8(b). It can be seen that the present passive oxygen study agrees well with the data of [8]. The Sherwood number profile follows the theoretical Graetz-Nusselt solution upstream from the stenosed region. After entering the stenosed region, the Sherwood number profile exhibits a steep increase up to a value of around $Sh = 125$ in the proximity of the stenosis throat. In the second part of the stenosed region, the Sherwood number decreases with a minimum located at approximately 0.75D with a value close to zero, where the thickest mass transport boundary layer can be found. Farther downstream of the stenosed region, the extracted Sherwood number approaches the Graetz-Nusselt solution again, as the momentum boundary layer thins. The result obtained with the active oxygen transport shows qualitatively similar behavior to the passive solution, but with significantly higher Sherwood number values. The characteristic local maximal and minimal values are more than twice higher for active oxygen transport.

Appendix C: The Hill equation

The oxygen-hemoglobin dissociation curve is shown in Fig.6.9(a) as described by the Hill equation. The curve has its characteristic sigmoidal shape. Comparing the calculated data for different partial pressure of oxygen to the measurements demonstrated that Hill's equation accurately predicts the actual clinical state, as shown in Fig.6.9(b).

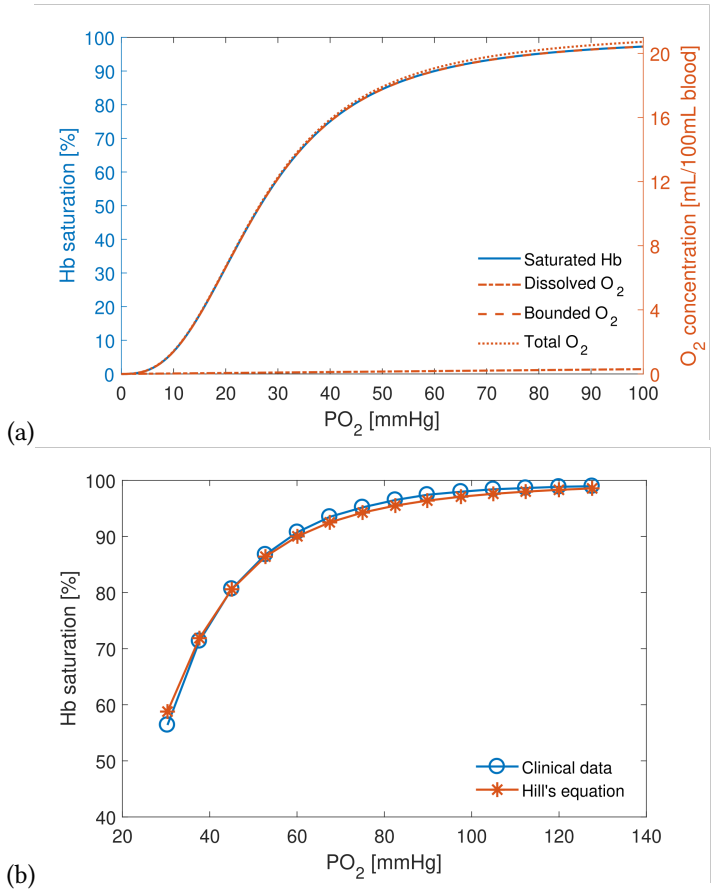

Figure 6.9: (a) Oxygen-Hemoglobin dissociation curve as described by Hill's equation with oxygen concentration both in plasma and bound by hemoglobin; (b) Comparison of Hill's equation with the clinical data [40] (bottom).

Appendix D: Mesh sensitivity analysis: brain vasculature (CoW)

Figure 6.10 shows the contours of WSS for three different meshes (top to bottom: coarse, medium, and fine) and extracted values of WSS alongside the visualized curve. The contours show WSS is very similar for all of the meshes. Similar findings can also be seen for the

extracted values, where the curves overlap. Also, the average values for all three meshes are close to each other.

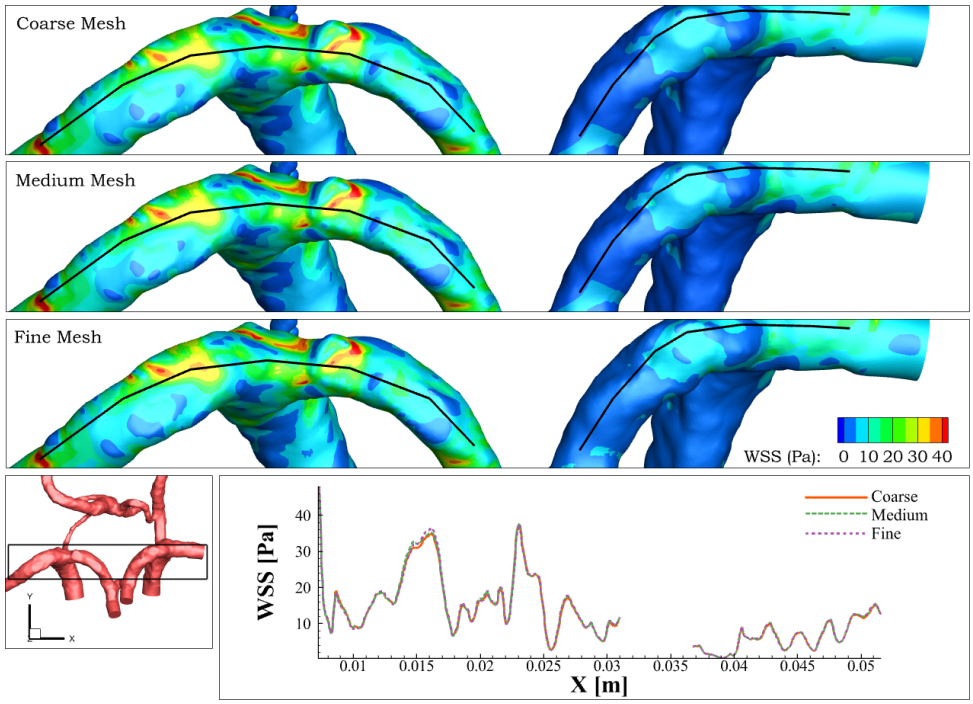

Figure 6.10: Wall shear stress with a marked extraction line for the coarse mesh, medium mesh, and fine mesh. The extracted wall shear stress alongside the lines with a global wall shear stress average for the coarse and fine mesh (-bottom).

Additionally, we have performed the grid dependency study based on Grid Convergence Index (GCI). The results, based on average WSS alongside the extracted line, are shown in Tab. 6.3 As shown, the grid is convergent, and an asymptotic range has been achieved. Based on both of the analyses, we have continued with the medium mesh for all of the simulations.

Table 6.3: Grid convergence index (GCI) estimation for the volunteer; WSS_1 is wall shear stress for the fine mesh, WSS_2 is for the medium mesh, and WSS_3 is for the coarse mesh; r is the remeshing factor, p is the order of convergence, $f_{h=0}$ is the Richardson solution, $GCI_{1,2}$ is the GCI for fine and medium mesh, and $GCI_{2,3}$ is the GCI for medium and coarse mesh.

	WSS_1 [Pa]	WSS_2 [Pa]	WSS_3 [Pa]	r	p	$f_{h=0}$	$GCI_{1,2}$ [%]	$GCI_{2,3}$ [%]	Asymptotic?
Whole Domain	5.66	5.65	5.62	1.99	2.46	5.66	0.03	0.14	1.001
Extracted Line	11.24	11.21	11.09	1.99	1.88	11.25	0.14	0.51	1.003

References

[1] C. R. Lenihan and C. T. Taylor, *The impact of hypoxia on cell death pathways,* Biochemical Society Transactions **41**, 657 (2013), http://www.biochemsoctrans.org/content/41/2/657.full.pdf .

[2] M. Dallas, H. E. Boycott, L. Atkinson, A. Miller, J. P. Boyle, H. A. Pearson, and C. Peers, *Hypoxia suppresses glutamate transport in astrocytes,* Journal of Neuroscience **27**, 3946 (2007).

[3] H. E. Boycott, M. Dallas, J. P. Boyle, H. A. Pearson, and C. Peers, *Hypoxia suppresses astrocyte glutamate transport independently of amyloid formation,* Biochemical and Biophysical Research Communications **364**, 100 (2007).

[4] E. Marsch, J. C. Sluimer, and M. J. Daemen, *Hypoxia in atherosclerosis and inflammation,* Current Opinion in Lipidology **24** (2013).

[5] M. Billaud, J. C. Hill, T. D. Richards, T. G. Gleason, and J. A. Phillippi, *Medial hypoxia and adventitial vasa vasorum remodeling in human ascending aortic aneurysm,* Frontiers in Cardiovascular Medicine **5** (2018), 10.3389/fcvm.2018.00124.

[6] R. Pittman, *Regulation of Tissue Oxygenation, Second Edition*, Colloquium Series on Integrated Systems Physiology: From Molecule to Function (Biota Publishing, 2016).

[7] M. Kaazempur-Mofrad, S. Wada, J. Myers, and C. Ethier, *Mass transport and fluid flow in stenotic arteries: Axisymmetric and asymmetric models,* International Journal of Heat and Mass Transfer **48**, 4510 (2005).

[8] J. Moore and C. R. Ethier, *Oxygen mass transfer calculations in large arteries,* Journal of Biomechanical Engineering **119**, 469 (1997).

[9] M. Markl, W. Wallis, and A. Harloff, *Reproducibility of flow and Wall Shear Stress analysis using flow-sensitive four-dimensional MRI,* Journal of Magnetic Resonance Imaging **33**, 988 (2011).

[10] J. R. Cebral, C. M. Putman, M. T. Alley, T. Hope, R. Bammer, and F. Calamante, *Hemodynamics in normal cerebral arteries: qualitative comparison of 4D phase-contrast magnetic resonance and image-based Computational Fluid Dynamics,* Journal of Engineering Mathematics **64**, 367 (2009).

[11] S. Meier, A. Hennemuth, O. Friman, J. Bock, M. Markl, and T. Preusser, *Non-invasive 4D blood flow and pressure quantification in central blood vessels via PC-MRI,* in *Computing in Cardiology, 2010* (IEEE, 2010) pp. 903–906.

[12] P. Ooij, J. J. Schneiders, H. A. Marquering, C. B. Majoie, E. V. Bavel, and A. J. Nederveen, *3D cine phase-contrast MRI at 3T in intracranial aneurysm compared with patient-specific computational fluid dynamics,* American Journal of Neuroradiology **34**, 1785 (2013).

[13] V. C. Rispoli, J. F. Nielsen, K. S. Nayak, and J. L. Carvalho, *Computational Fluid Dynamics simulations of blood flow regularized by 3D phase contrast MRI,* BioMedical Engineering OnLine **14**, 110 (2015).

[14] H. Gharahi, B. A. Zambrano, D. C. Zhu, J. K. DeMarco, and S. Baek, *Computational Fluid Dynamic simulation of human carotid artery bifurcation based on anatomy and volumetric blood flow rate measured with Magnetic Resonance Imaging,* International Journal of Advances in Engineering Sciences and Applied Mathematics **8**, 46 (2016).

[15] D. I. Hollnagel, P. E. Summers, D. Poulikakos, and S. S. Kollias, *Comparative velocity investigations in cerebral arteries and aneurysms: 3D phase-contrast MR angiography, laser Doppler velocimetry and Computational Fluid Dynamics,* NMR in Biomedicine **22**, 795 (2009).

[16] H. Isoda, Y. Ohkura, T. Kosugi, M. Hirano, M. T. Alley, R. Bammer, N. J. Pelc, H. Namba, and H. Sakahara, *Comparison of hemodynamics of intracranial aneurysms between MR fluid dynamics using 3D cine phase-contrast MRI and MR-based Computational Fluid Dynamics,* Neuroradiology **52**, 913 (2010).

[17] P. van Ooij, A. Guédon, C. Poelma, J. Schneiders, M. Rutten, H. Marquering, C. Majoie, E. VanBavel, and A. Nederveen, *Complex flow patterns in a real-size intracranial aneurysm phantom: phase contrast MRI compared with particle image velocimetry and Computational Fluid Dynamics,* NMR in Biomedicine **25**, 14 (2012).

[18] P. Berg, D. Stucht, G. Janiga, O. Beuing, O. Speck, and D. Thévenin, *Cerebral blood flow in a healthy Circle of Willis and two intracranial aneurysms: Computational Fluid Dynamics versus four-dimensional phase-contrast Magnetic Resonance Imaging,* Journal of Biomechanical Engineering **136**, 041003 (2014).

[19] R. Perinajová, J. F. Juffermans, J. J. Westenberg, R. L. van der Palen, P. J. van den Boogaard, H. J. Lamb, and S. Kenjereš, *Geometrically induced wall shear stress variability in CFD-MRI coupled simulations of blood flow in the thoracic aortas,* Computers in Biology and Medicine **133**, 104385 (2021).

[20] C. Ethier, *Computational modeling of mass transfer and links to atherosclerosis,* Annals of Biomedical Engineering **30**, 461 (2002).

[21] S. Kenjeres and A. de Loor, *Modeling and simulation of low-density-lipoprotein (ldl) transport through multi-layered wall of an anatomically realistic carotid artery bifurcation,* Journal of the Royal Society Interface **11**, 1 (2014).

[22] S. Kenjereš, *On recent progress in modelling and simulations of multi-scale transfer of mass, momentum and particles in bio-medical applications,* Flow, Turbulence and Combustion **96**, 837 (2016).

[23] M. Caputo, C. Chiastra, C. Cianciolo, E. Cutrì, G. Dubini, J. Gunn, B. Keller, F. Migliavacca, and P. Zunino, *Simulation of oxygen transfer in stented arteries and correlation with in-stent restenosis,* International Journal for Numerical Methods in Biomedical Engineering **29**, 1373 (2013).

[24] M. Khakpour and K. Vafai, *Critical assessment of arterial transport models,* International Journal of Heat and Mass Transfer **51**, 807 (2008).

[25] G. Coppola and C. Caro, *Oxygen mass transfer in a model three-dimensional artery,* Journal of The Royal Society Interface **5**, 1067 (2008).

[26] T. Zheng, J. Wen, W. Jiang, X. Deng, and Y. Fan, *Numerical investigation of oxygen mass transfer in a helical-type artery bypass graft,* Computer Methods in Biomechanics and Biomedical Engineering **17**, 549 (2014), pMID: 22794110.

[27] E. Murphy, A. S Dunne, D. Martin, and F. J Boyle, *Oxygen mass transport in stented coronary arteries,* Annals of Biomedical Engineering **44** (2016), 10.1007/s10439-015-1501-6.

[28] P. Causin, G. Guidoboni, F. Malgaroli, R. Sacco, and A. Harris, *Blood flow mechanics and oxygen transport and delivery in the retinal microcirculation: multiscale mathematical modeling and numerical simulation,* Biomechanics and Modelling in Mechanobiology **15** (2015), 10.1007/s10237-015-0708-7.

[29] F. Iori, L. Grechy, R. W. Corbett, W. Gedroyc, N. Duncan, C. G. Caro, and P. E. Vincent, *The effect of in-plane arterial curvature on blood flow and oxygen transport in arterio-venous fistulae,* Physics of Fluids **27**, 031903 (2015).

[30] S. Tada, *Numerical study of oxygen transport in a carotid bifurcation,* Physics in Medicine and Biology **55**, 3993 (2010).

[31] J. Chen, E. Gutmark, G. Mylavarapu, P. F. Backeljauw, and I. Gutmark-Little, *Numerical investigation of mass transport through patient-specific deformed aortae,* Journal of Biomechanics **47**, 544 (2014).

[32] F. Yan, W.-T. Jiang, R.-Q. Dong, Q.-Y. Wang, Y.-B. Fan, and M. Zhang, *Blood flow and oxygen transport in descending branch of lateral femoral circumflex arteries after transfemoral amputation: A numerical study,* Journal of Medical and Biological Engineering **37**, 63 (2017).

[33] N. Sun, J. H. Leung, N. B. Wood, A. D. Hughes, S. A. Thom, N. J. Cheshire, and X. Y. Xu, *Computational analysis of oxygen transport in a patient-specific model of abdominal aortic aneurysm with intraluminal thrombus,* The British Journal of Radiology **82**, S18 (2009), pMID: 20348531.

[34] C. Ji, Y. He, and F. Liang, *A modeling study of blood flow and oxygen transport in the Circle of Willis,* Lixue Xuebao/Chinese Journal of Theoretical and Applied Mechanics **3**, 1114 (2010).

[35] D. Liu, N. Wood, N. Witt, A. Hughes, S. A Thom, and X. Xu, *Computational analysis of oxygen transport in the retinal arterial network,* Current Eye Research **34**, 945 (2009).

[36] X. Liu, Y. Fan, and X. Deng, *Effect of spiral flow on the transport of oxygen in the aorta: A numerical study,* Annals of Biomedical Engineering **38**, 917 (2010).

[37] L. Václavů, Z. A. V. Baldew, S. Gevers, H. J. M. M. Mutsaerts, K. Fijnvandraat, M. H. Cnossen, C. B. Majoie, J. C. Wood, E. VanBavel, B. J. Biemond, P. Ooij, and A. J. Nederveen, *Intracranial 4D flow magnetic resonance imaging reveals altered haemodynamics in sickle cell disease,* British Journal of Haematology **180**, 432.

[38] R. Fournier, *Basic Transport Phenomena In Biomedical Engineering*, Chemical Engineering Series (Taylor & Francis, 1998).

[39] A. Hill, *Proceedings of the physiological society: The possible effects of the aggregation of the molecules of haemoglobin on its dissociation curves,* The Journal of Physiology **40**, i (1910).

[40] J.-A. Collins, A. Rudenski, J. Gibson, L. Howard, and R. O'Driscoll, *Relating oxygen partial pressure, saturation and content: the haemoglobin–oxygen dissociation curve,* Breathe **11**, 194 (2015).

[41] *Vascular modelling toolkit: http://www.vmtk.org/,* .

[42] S. Kenjereš and B. W. Righolt, *Simulations of magnetic capturing of drug carriers in the brain vascular system,* International Journal of Heat and Fluid Flow **35**, 68 (2012).

[43] C. D. Murray, *The physiological principle of minimum work i. the vascular system and the cost of blood volume,* PNAS **12**, 207 (1926).

[44] D. Stephenson, A. Patronis, D. M. Holland, and D. A. Lockerby, *Generalizing murray's law: An optimization principle for fluidic networks of arbitrary shape and scale,* Journal of Applied Physics **118**, 174302 (2015).

[45] P. Carreau, *Rheological equations from molecular network theories,* Journal of Rheology **16**, 99 (1972).

[46] S. Chien, *Shear dependence of effective cell volume as a determinant of blood viscosity,* Science **168**, 977 (1970).

[47] M. Khan, K. Valen-Sendstad, and D. Steinman, *Narrowing the expertise gap for predicting intracranial aneurysm hemodynamics: Impact of solver numerics versus mesh and time-step resolution,* American Journal of Neuroradiology **36**, 1310 (2015), http://www.ajnr.org/content/36/7/1310.full.pdf .

[48] D. G. Buerk and T. K. Goldstick, *Arterial wall oxygen consumption rate varies spatially,* American Journal of Physiology - Heart and Circulatory Physiology **243**, H948 (1982), http://ajpheart.physiology.org/content/243/6/H948.full.pdf .

[49] A. A. Harteveld, N. P. Denswil, W. V. Hecke, H. J. Kuijf, A. Vink, W. G. Spliet, M. J. Daemen, P. R. Luijten, J. J. Zwanenburg, J. Hendrikse, and A. G. van der Kolk, *Data on vessel wall thickness measurements of intracranial arteries derived from human Circle of Willis specimens,* Data in Brief **19**, 6 (2018).

[50] J. R. Womersley, *Method for the calculation of velocity, rate of flow and viscous drag in arteries when the pressure gradient is known,* The Journal of Physiology **127**, 553 (1955).

[51] C. G. Caro, T. J. Pedley, R. C. Schroter, and W. A. Seed, *The Mechanics of the Circulation* (Oxford University Press, 1978) p. 527.

[52] M. Cibis, W. V. Potters, F. J. Gijsen, H. Marquering, P. van Ooij, E. vanBavel, J. J. Wentzel, and A. J. Nederveen, *The effect of spatial and temporal resolution of cine phase contrast MRI on wall shear stress and oscillatory shear index assessment,* PLOS ONE **11**, 1 (2016).

[53] R. Perinajová, J. F. Juffermans, J. J. Westenberg, R. L. van der Palen, P. J. van den Boogaard, H. J. Lamb, and S. Kenjereš, *Geometrically induced wall shear stress variability in CFD-MRI coupled simulations of blood flow in the thoracic aortas,* Computers in Biology and Medicine **133**, 104385 (2021).

[54] Y. Qiu and J. M. Tarbell, *Numerical simulation of oxygen mass transfer in a compliant curved tube model of a coronary artery,* Annals of Biomedical Engineering **28**, 26 (2000).

[55] P. Studinger, Z. Lénárd, Z. Kováts, L. Kocsis, and M. Kollai, *Static and dynamic changes in carotid artery diameter in humans during and after strenuous exercise,* The Journal of Physiology **550**, 575 (2003), https://physoc.onlinelibrary.wiley.com/doi/pdf/10.1113/jphysiol.2003.040147 .

[56] D. P. Guensch, M. C. Michel, S. P. Huettenmoser, B. Jung, P. Gulac, A. Segiser, S. L. Longnus, and K. Fischer, *The blood oxygen level dependent (bold) effect of in-vitro myoglobin and hemoglobin,* Scientific Reports **11**, 11464 (2021).

[57] J. Ruiz-Cabello, B. Barnett, P. Bottomley, and J. Bulte, *Fluorine (19f) mrs and MRI in biomedicine,* NMR in biomedicine **24**, 114 (2011).

[58] A. H. Schmieder, S. D. Caruthers, J. Keupp, S. A. Wickline, and G. M. Lanza, *Recent advances in 19fluorine magnetic resonance imaging with perfluorocarbon emulsions,* Engineering **1**, 475 (2015).

[59] S. Chaudhary, N. Akter, A. Rajeev, M. Hwang, and S. Sirsi, *Hemoglobin microbubbles for in vivo blood oxygen level dependent imaging: Boldly moving beyond MRI,* The Journal of the Acoustical Society of America **150**, A27 (2021), https://doi.org/10.1121/10.0007507 .

7

Conclusions and Outlook

7.1 Conclusions

Progress in diagnosing and treating cardiovascular pathologies is driven by the level of understanding of their pathogenesis. One such pathology is an aneurysm, which can occur in various major arteries. Aneurysms often remain asymptomatic until their rupture, which leads to sudden death in 70% of the cases. For many years, blood flow hemodynamics were thought to be the main driver behind the aneurysm development and progression. However, a detailed analysis of the flow in aneurysms is not feasible due to the limitations of current clinically used imaging methods, especially their spatiotemporal resolution. In this thesis, we have tried to overcome this problem and unravel the processes behind the genesis, progression, and diagnosis of aneurysms using a numerical approach. An important aspect when using a numerical approach is properly defining each studied case's subject-specific nature. To do this, we have created custom 4D-flow magnetic resonance imaging (MRI) based computational fluid dynamics (CFD) models.

To create a subject-specific model, we have to focus on the level of accuracy (e.g., how many specific details we include in the model) versus the level of computational efficiency. The latter is essential for the clinical availability of simulation-driven diagnostics. The arteries and blood flow are complex biological systems with many variations from subject to subject. Hence, modeling each detail of the arterial system or all of the mechanisms occurring during blood transport would not be feasible. Due to this, the focus of this thesis was to define subject-specific models with a variable amount of assumptions and evaluate their accuracy of how well they represent the blood flow, especially in the aorta.

Before looking at blood flow modeling, we first needed to understand ***what is the level of uncertainty brought to the simulations by the input data?*** We addressed this in Chapter 2, where we looked into variability in simulations due to small geometrical changes in arteries caused by the segmentation of 4D-flow MRI. The deviations in geometry were caused by the manual segmentation procedure of 4D-flow MRI data sets. Here we compared simulated hemodynamics (with a focus on wall shear stress - WSS) within the aorta of ten volunteers, with four segmentation for each volunteer: geometry based on the scan (1) and re-scan after 30 minutes (2), geometry based on repeated segmentation of a scan by the same person (inter-observer) (3) and by a different person (intra-observer)

(4). Based on our analysis, we have found that the highest deviation of the calculated WSS was for segmentations based on intra-observer. Hence, in studies that include multiple subjects, it should be preferable to use geometries based on segmentation by a single person. Doing this the error in the simulated flow will be reduced. We have also evaluated three different methods of analysis: (1) *'0-dimensional'* where the cases were compared based on average values within a certain part of the aorta, (2) *'1-dimensional'* comparison of circumferentially averaged values alongside the complete aorta, and (3) *'2-dimensional'* comparison of absolute values on flattened surfaces. We have found that the analysis method strongly influenced the perceived agreement between the different segmentations. The Spearman correlation coefficient decreases with the increasing order of the analysis method. While this behavior elucidates some discrepancies between different studies presented in the literature, it does not mean that any analysis methods are superior. Each of the methods focuses on different aspects: the collective behavior of the whole segment (1), the behavior of the particular circumference (2), or the complex behavior of each voxel (3). Therefore, the choice of the analysis method should be based on the study's goal. This choice is crucial for extensive population studies, where different healthy controls and patients are compared. Hence, to answer the initial question, the level of uncertainty in simulations caused by the input data (specific geometry) varies with the level of detail we want to assess.

An essential aspect of modeling blood flow in the aorta is to define an appropriate model to capture its turbulent nature. While many discussions were raised about whether turbulence can occur in CVS, the peak Reynolds number in the aorta can approach $Re \sim 10\,000$, especially for specific aortic pathologies, e.g., the coarctation of the aorta (CoA). CoA is a significant reduction in aortic diameter (stenosis) that causes sudden acceleration of blood velocity and an increase in aortic pressure. Hence, the blood flow can show turbulent behavior. However, ***what is the most efficient yet accurate model to account for the instantaneous and localized turbulence of the blood flow?*** We investigated this problem in Chapter 3, assessing several different Reynolds averaged Navier-Stokes (RANS) models within CoA. To eliminate any possible misinterpretation due to geometrical variation (as presented in Chapter 2), we first performed a thorough analysis of turbulent blood flow in an idealized representation of CoA. This analysis was done using 4D-flow MRI and CFD with different RANS models (standard $k-\epsilon$, $k-\omega$ Shear Stress Transport - SST, and Reynolds Stress Model - RSM). Our analysis shows that the $k-\epsilon$ model is inadequate for turbulent blood flow simulations in the aorta. This model under-predicts the velocity behavior in and after the bend (aortic arch). In this region, we can identify the creation of counter-rotating vortices due to the adverse pressure in the flow. Unfortunately, the $k-\epsilon$ model cannot correctly capture this behavior and compensates for it with the over-prediction of turbulent kinetic energy. The SST model closely captured the blood flow behavior in the curved artery. However, compared to 4D-flow MRI, we could still identify several differences. On the other hand, the simulated velocity field using RSM closely resembled the measured blood flow in the phantom. Based on these observations, we have performed simulations of turbulent blood flow in patient-specific CoA using RSM. These simulations showed that even in such a complex geometry, RSM-based CFD could efficiently and accurately capture the flow in the proximity of stenosis, similar to the 4D-flow MRI. Because of this, we recommend using RSM to model turbulent blood flow in

the aorta with high accuracy and efficiency.

Another critical aspect in modeling blood flow in the aorta is the treatment of its wall. The aortic wall moves during the cardiac cycle due to the (1) motion of the heart and (2) the contraction of smooth muscle cells within the aortic wall. While, until now, we have assumed the aortic wall to be static, as many other studies do due to the complexity, this can potentially impact the simulated blood flow. In Chapter 4, we have tried to answer another important question in modeling blood flow in moving arteries: ***How can the patient-specific nature of aortic wall movement be defined?*** To do this, we have developed and proposed a novel method based on Radial Basis Function (RBF) interpolation of key-frame segmentations (extracted from 4D-flow MRI). By doing this, we could ensure that our model is highly subject-specific since we did not make any assumptions about the mechanical properties of the aortic wall. Our initial results showed that the RBF-based prescribed motion matched the *'real'* aortic motion (based on 4D-flow MRI) well, with most movement recorded close to the root and ascending part. These regions also showed the highest variation in hemodynamical parameters that are often considered potential biomarkers: time-averaged wall shear stress (TAWSS) and oscillatory shear index (OSI). We have observed a relationship between the degree of motion and the variability in TAWSS and OSI. Hence, to properly model aortic blood flow, the motion of its wall should always be considered in the computational model. To do so, we recommend using image-based modeling since it is computationally efficient and robust, does not require many (usually unknown) mechanical parameters, and is genuinely subject-specific by nature.

Until now, we have only focused on hemodynamics as the sole factor that may affect the aortic aneurysm pathogenesis. However, the pathways triggered by hemodynamical changes might be one of many possible causes of aneurysm formation. An important aspect of unraveling the aneurysm pathogenesis is understanding different species' abnormal behavior. Potential biochemical markers could be nitric oxide (NO) and oxygen (O_2). Hence, to find an answer to ***What is the role of hemodynamics and biochemical parameters in the AA formation and rupture?***, we have performed a thorough investigation in Chapter 5. Here, we investigated the effects of mass transfer resistance in the lumen and wall of oxygen and nitric oxide and evaluated their potential (accompanied by hemodynamics) to be predictive biomarkers. We have performed simulations on healthy control and a patient with a thoracic aortic aneurysm (TAA). We considered the blood flow and mass transfer in the lumen and the arterial wall. We could identify several essential differences between a healthy aorta and TAA based on our analysis. First, the impaired hemodynamics in TAA could be identified by low TAWSS, high OSI, and high endothelial cell activation potential (ECAP). Additionally, high OSI and ECAP were also present in a location downstream of the TAA, which could potentially lead to additional growth or even aortic dissection. Concerning the effect of TAA on NO and O_2 distribution, NO showed a significantly uneven distribution within the aortic wall in TAA compared to the healthy tissue. This deviation could lead to an impaired function of the aortic wall since NO is an essential regulator of arterial hemostasis. On the other hand, the concentration of O_2 was not significantly affected by the presence of TAA. However, we could still identify several locations suffering from hypoxia, especially in the descending aorta, distal to the arch, where the recirculation zone created an area with increased luminal mass transfer resistance of O_2. Prolonged hypoxia could lead to extracellular matrix remodeling and potential offset

of arterial pathologies, such as an aneurysm. Hence, the hemodynamical biomarkers for aneurysm development should be accompanied by biochemical factors, such as NO and O_2.

Finally, in Chapter 6, we have addressed the last question: ***How can the models be applied for use in other parts of the cardiovascular system?*** Here, we have specifically focused on the Circle of Willis (CoW) an essential part of the cerebrovascular system. We have studied the transfer of species in this section of CVS, with a specific focus on O_2. Understanding of lumen-side mass transfer limitations of O_2 in CoW is vital since the lack of O_2 (hypoxia) here can lead to a variety of pathologies - e.g., dementia, atherosclerosis, and aneurysm. Due to the essential nature of CoW, these pathologies can cause high morbidity and mortality. In our analysis, we have considered two different modes of O_2 transport - *'passive'*, where O_2 is transported as free species in plasma and *'active'*, where O_2 is transported as bounded to hemoglobin. We have found significant differences between these two modes of transport and highlighted the importance of incorporating the more physiologically based model (*'active'*) to study O_2 mass transfer in arteries. After that, we uncovered that even healthy CoW might suffer from circulation hypoxia. To identify hypoxia, we have defined a threshold limit. The limiting factor for hypoxia is when the O_2 mass transfer towards the wall from the luminal side is lower than the consumption of O_2 by the wall, expressed in terms of non-dimensional numbers as Sherwood number is lower than Damköhler number ($Sh < Da$). We have found that approximately 1% of the surface suffered from hypoxia based on the *'active'* model and 14% based on the *'passive'* model. This study shows the importance of physiologically based modeling and the consideration of hypoxia as a pre-factor for arterial pathologies. Finally, to clarify the original problem, in this Chapter, we have shown that the proposed procedures and models for modeling blood flow in the aorta can be easily adjusted and applied to other parts of CVS. Hence, this unravels many possibilities for studying and diagnosing other vascular diseases.

7.2 Future Work

With this thesis, we have addressed several important aspects of modeling the blood flow in the human cardiovascular system. However, due to the complex nature of the blood flow and behavior of the vessels, we can still identify several aspects that need to be addressed. We can summarize these in two main categories:

1. modeling aspects - definition of the domain, modeling of turbulence and growth, and automation
2. scalability (parametric and population studies)

Below, we will propose research possibilities for all these challenges.

Data Sources for Aortic Morphology

As shown in Chapter 2, CFD simulations are sensitive to the small geometrical changes in segmentation, especially if WSS is examined. Hence, this opens the opportunity for an essential improvement in subject-specific modeling. While other imaging techniques (such as computed tomography - CT) can produce high spatial resolution anatomy images, they often lack acquisitions at different steps in the cycle (important for movement modeling). Additionally, they cannot directly produce velocity information, an essential input for

subject-specific modeling of blood flow. Therefore, here we will look only into techniques and potential improvements that can provide the necessary information.

In this thesis, we have used 4D-flow data sets as an initial input to our CFD model. This method accurately acquires data needed for the flow boundary conditions. However, due to the manual nature of the segmentation process, the input geometries cause uncertainty for CFD. To overcome this, Berhane et al. recently proposed a fully automated approach for the segmentation of 4D-flow data based on deep learning and convolutional neural networks [1]. This method shows great potential, as the segmentation process was rapid and consistent, with comparable accuracy to manual segmentations.

In addition, high spatiotemporal resolution of CFD data, in combination with imaging data (e.g., 4D-flow MRI), can be used to train machine learning reduce-order models (ROM) [2]. We can use the trained ROMs to reduce the level of uncertainty in CFD data coming from the slight geometrical variation due to segmentation and pre-processing. While this method is still more theoretical, it shows a high potential to overcome the segmentation variability problem.

Finally, segmenting multiple data sets through the cardiac cycle is time-consuming due to many necessary manual adjustments. To overcome this, we propose to apply the radial-basis function (RBF) interpolation, presented in Chapter 4, to the segmentation process. In doing this, only a few key-frames would need to be segmented and consecutively interpolated to obtain the morphology of the aorta for the whole cycle.

Modelling and Validation of Turbulence in Blood Flow

While the research community still needs to be unified on whether turbulence occurs in healthy arteries, modeling and analyzing turbulent blood flow is often explored in diverse aortic pathologies. In these, a disturbed flow occurs naturally, and hence, various approaches to model turbulence can be tested. In Chapter 3, we have shown that the RSM turbulence model can potentially study disturbed blood flow in the aorta. However, many studies still call for *'validation'* of the results, for example, by using direct numerical simulations (DNS), since the imaging data usually do not account for turbulence. Nevertheless, is modeling turbulent blood flow using DNS with the assumption of homogeneous fluid even valid?

As we have discussed, blood consists of numerous cells suspended in plasma. Hence, it cannot be considered a homogeneous fluid. Instead, we have to look at it as a dense suspension; therefore, the turbulence models should be chosen with this condition in mind. Antiga et al. hypothesize that the size of the smallest eddies is not the Kolmogorov microscale, but rather, they are in order of magnitude similar to the size of red blood cells [3]. In this situation, the energy does not dissipate due to the viscosity but rather due to cell-cell interaction. Hence, a more accurate analysis would be to consider DNS with resolved RBCs size, e.g., as shown by Zheng et al. [4] for a spherical particle flow, with modifications to use shapes of RBCs. However, this approach is highly computationally expensive, so its applicability is limited. Therefore, the main objective should be to utilize it in the validation of other turbulence models (e.g., RANS, DES, or LES) for precise modeling of blood flow in the aorta.

Modelling of Growth and Rupture

In this thesis, we have presented a model for the prescribed movement of the aortic wall (Chapter 5), which allows us to understand blood flow within a single cardiac cycle. However, the progress of the aortic pathologies is slow and cannot be captured by this technique. Thus, we must employ a different approach to model the progress of aortic pathologies. Implementing a Fluid-Structure-Growth (FSG) framework is possible, in which the two-way coupled fluid-structure interaction is enhanced with the remodeling of extracellular matrix (ECM) that causes a simulated growth. Here, we will discuss several opportunities for implementing the FSG framework to simulate the growth of an aortic aneurysm.

Several studies have proposed approaches to model the growth of the aortic aneurysm. They started with the Finite Element Modelling (FEM) approach by Baek et al. [5], who presented a mathematical model for enlarging intracranial aneurysms. In this model, the aneurysm was represented via thin-wall assumption (single wall layer) with axisymmetrical properties and no influence of the fluid on the growth (just solid modeled). They reported that the (in-) stability of the growth process strongly correlates with collagen remodeling and alignment. The growth and failure of a simplified spherical AAA utilizing FEM were also reported by Volokh et al. [6]. Their study presents a thin-wall isotropic model, where they consider the coupling between the growth, the stiffening of the material, and the decreasing of its strength. This model incorporates the microstructural changes (the elastin degradation or collagen remodeling) by influencing the macroscopic parameters (stiffness, strength, and others) without directly modeling these processes. Additionally, this approach does not account for the fluid-side influence on the progression of AA.

To account for the influence of blood flow, the first coupled fluid-growth-structure model for a patient-specific AAA was proposed by Grytsan et al. [7]. This study presents a model of a thick-walled aorta as a non-linear tube with two layers (intima-media and adventitia) composed of elastin. They model elastin degradation. However, only a simplified model is used to describe the degradation of ECM, assuming a direct correlation with WSS changes. The proposed model can successfully capture the growth of an aneurysm; however, it allows it to grow in one direction with the assumption of left-right symmetry. The unidirectional model was a severe simplification compared to the actual cases [8]. Also, they considered Newtonian assumption for blood viscosity and additional simplification for the fluid modeling (steady-state and rigid wall). Therefore, the model does not account for the compliance of the aorta during the cardiac cycle. The model proposed by Grytsan et al. [7] was used to study the rupture risk potential of four patient-specific AAAs [9]. The primary outcomes are that the examination at a single time point in the aneurysm's lifetime is insufficient. This deficit is due to growth-related significant changes in the hemodynamical parameters like WSS and pressure, which are often connected to its rupture [10–13].

Finally, the growth model for all the presented studies lacked validation by medical imaging techniques, providing excellent potential for improvement. The possibility to overcome this was shown by Joly et al. [14], who studied the flow in the patient-specific AAA for three different time points over eight years. However, they did not include the growth model in their simulations. Instead, they only compared the hemodynamics in three different instances. Hence, it would be favorable to implement the FSG framework

to simulate the growth of an aneurysm in a data set containing patient and healthy cases with periodic follow-ups.

Automation for Clinical Application

The primary factor in the applicability of computational methods (based on the Eulerian approach) within the medical field is process automation's ability (and feasibility). When considering CFD in human arteries, the major hurdle is the creation of the computational mesh. The mesh is necessary for discretizing the computational domain in smaller parts, where the governing equations are solved (in this thesis - we have used the finite-volume method - FVM). Due to this, the results of numerical studies are highly dependent on the quality of the computational mesh [15]. Hence, this particular stage requires serious attention, especially for specific pathologies, such as aortic dissection, for which the discretization process is very complicated. Because of this, the meshing step often cannot be automatized, requires an input of a skilled professional, and often takes much time. Additionally, the complications with meshes become even more pronounced if the flow is studied in a domain with a moving boundary (as presented in Chapter 4). Movement of the boundary causes additional deformation of the mesh and decreases its quality, which can lead to a need for re-meshing the domain and increased simulation time.

A possibility to overcome this problem is to implement a mesh-less, Lagrangian-based method, such as Smoothed Particle Hydrodynamics (SPH) [16, 17]. Instead of numerically solving the governing equations in a discretized domain using a finite number of volumes, SPH represents the flow based on particles (points with a given mass and known velocity at each point in time) [18]. The collective motion of these particles approximates the motion of liquids and gasses. SPH has shown to be a feasible alternative for modeling complex flow (such as blood flow), mainly due to the simplicity of introducing multi-phase flow [19] and non-Newtonian properties of fluid [20], as well as its excellent behavior for simulating moving domain [21].

Biomedical application of SPH was previously shown in a model of stenosed artery [22], and left ventricle with dynamic movement [23]. While Qin et al. show high deviations between SPH and conventional CFD due to the low particle density that was utilized [22], the latter mentioned highlights the potential of SPH for simulating flows with dynamic motion of boundary [23]. Due to this, we have performed a preliminary feasibility study of SPH application in simulating blood flow in the subject-specific aorta. In Fig. 7.1, we show velocity magnitude in the ascending aorta and arch for a healthy volunteer using SPH and CFD. As can be seen, both methods produce very similar velocity fields, showing the potential for clinical application.

Nevertheless, we have discovered several limitations that still need to be addressed. First and foremost, the method was initially developed for boundary-free flows. Unfortunately, this leads to a re-occurring problem with flows in the closed domain. Next, partially associated with the previous point, the no-slip boundary condition is not enforced at the wall. Finally, the boundary layer has to be refined for calculating WSS due to the steep velocity gradients in this region. While the mesh refinement in these regions is relatively simple, the size and number of particles cannot be easily increased in the wall's proximity. However, these points can be overcome by introducing a large enough number of particles.

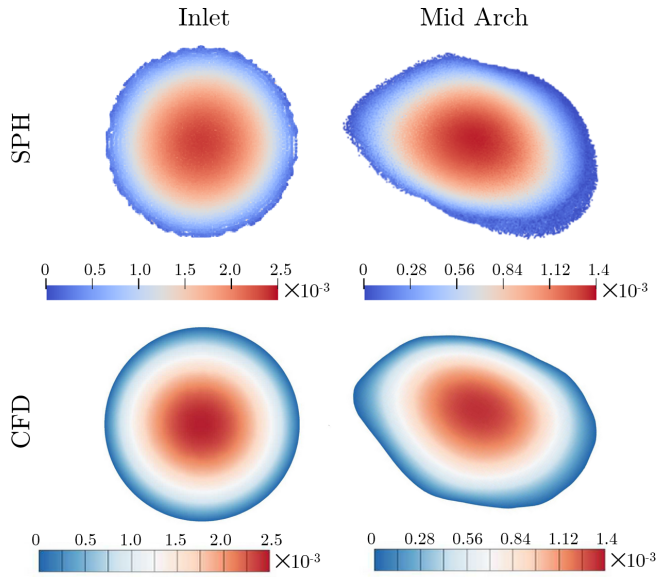

Figure 7.1: Velocity magnitude [m/s] for two different locations in the aorta (inlet - left and mid arch - right) as obtained using smoothed particle hydrodynamics (SPH - top) and computational fluid dynamics (CFD - bottom) for blood flow with Re = 50, the scale changes per location, based on MSc thesis of D. Krauklys [24].

7

Population Study

Finally, in this thesis, we have primarily focused only on simulating a small number of cases since the goal of our study was to create and test diverse modeling approaches. Hence, we could not analyze the influence of hemodynamics in a wide variety of cases. To do this, an in-depth population study has to be performed that would include enough healthy volunteers and patients with different aortic pathologies (e.g., aneurysm, dissection, and coarctation) to find a statistically significant relationship between hemodynamics and pathogenesis. Specifically for aneurysms, it would be preferable if such a population study also includes follow-up of patients at a different stage of this pathology - e.g., when diagnosed and at regular intervals during its growth. Since full 3D hemodynamical data are only sometimes available during these interventions, patient-specific modeling of blood flow shows great potential to be utilized in population studies.

An essential outcome of a population study would be the definition of biomarkers for aneurysm development and growth. Based on our blood flow analysis and species mass transfer, we recommend which variables have the highest potential to be predictive biomarkers for aneurysm formation and growth. Hemodynamical-based parameters are time-averaged wall shear stress, oscillatory shear index, and pressure distribution. Finally, we also highlight to study of the distribution of certain species that might affect the aortic wall function (i.e., O_2 and NO).

7.3 Outlook

CFD analysis is often utilized in various engineering fields, for example, to test the performance or to examine different actors in the proposed design. The potential of applying the same methodology also to analyze the flow in the human body, create a detailed plan for patient-specific intervention, or study the drug delivery to tissue is very high. While the computational methods do not suffice the clinical needs regarding the speed-to-accuracy ratio, the continuous computing power improvements could allow for patient-specific CFD models' implementation directly into clinical practice. This implementation can lead to highly personalized medicine, with treatment options directly adjusted to the patient. In this thesis, we showed the impact of patient-specific CFD models, coupled with imaging data, and their ability to capture hemodynamics accurately in the aorta. However, several actors still play an essential role in the widespread adoption of *'computational medicine'*. In the authors' opinion, perhaps the most critical factor is the confidence of patients and doctors in this technology. As with any other advancement, multiple elements may affect the view on the predictive modeling of diseases, such as poor understanding or fear of sensitive data exploitation. However, the advantages patient-specific modeling could bring to personalized medicine might eventually bring CFD methods to clinical practice.

'Nothing in life is to be feared; it is only to be understood. Now is the time to understand more, so that we may fear less.' **Marie Curie**

References

[1] H. Berhane, M. Scott, M. Elbaz, K. Jarvis, P. McCarthy, J. Carr, C. Malaisrie, R. Avery, A. J. Barker, J. D. Robinson, C. K. Rigsby, and M. Markl, *Fully automated 3D aortic segmentation of 4D flow MRI for hemodynamic analysis using deep learning,* Magnetic Resonance in Medicine **84**, 2204 (2020).

[2] A. Arzani and S. T. M. Dawson, *Data-driven cardiovascular flow modelling: examples and opportunities,* Journal of The Royal Society Interface **18**, 20200802 (2021).

[3] L. Antiga and D. A. Steinman, *Rethinking turbulence in blood,* Biorheology **46**, 77 (2009), 2.

[4] E. Zheng, M. Rudman, S. Kuang, and A. Chryss, *Turbulent coarse-particle non-newtonian suspension flow in a pipe,* International Journal of Multiphase Flow **142**, 103698 (2021).

[5] S. Baek, K. R. Rajagopal, and J. D. Humphrey, *A theoretical model of enlarging intracranial fusiform aneurysms,* Journal of Biomechanical Engineering **128**, 142 (2005).

[6] K. Volokh and D. Vorp, *A model of growth and rupture of abdominal aortic aneurysm,* Journal of Biomechanics **41**, 1015 (2008).

[7] A. Grytsan, P. N. Watton, and G. A. Holzapfel, *A thick-walled fluid-solid-growth model of abdominal aortic aneurysm evolution: Application to a patient-specific geometry,* Journal of Biomechanical Engineering **137**, 031008 (2015).

[8] J. van Prehn, J. A. van Herwaarden, K. L. Vincken, H. J. Verhagen, F. L. Moll, and L. W. Bartels, *Asymmetric aortic expansion of the aneurysm neck: Analysis and visualization of shape changes with electrocardiogram-gated magnetic resonance imaging,* Journal of Vascular Surgery **49**, 1395 (2009).

[9] R. R. F. Stevens, A. Grytsan, J. Biasetti, J. Roy, M. Lindquist Liljeqvist, and T. C. Gasser, *Biomechanical changes during abdominal aortic aneurysm growth,* PLOS ONE **12**, 1 (2017).

[10] M. F. Fillinger, M. Raghavan, S. P. Marra, J. L. Cronenwett, and F. E. Kennedy, *In vivo analysis of mechanical wall stress and abdominal aortic aneurysm rupture risk,* Journal of Vascular Surgery **36**, 589 (2002).

[11] M. F. Fillinger, S. P. Marra, M. Raghavan, and F. E. Kennedy, *Prediction of rupture risk in abdominal aortic aneurysm during observation: Wall stress versus diameter,* Journal of Vascular Surgery **37**, 724 (2003).

[12] A. Venkatasubramaniam, M. Fagan, T. Mehta, K. Mylankal, B. Ray, G. Kuhan, I. Chetter, and P. McCollum, *A comparative study of aortic wall stress using finite element analysis for ruptured and non-ruptured abdominal aortic aneurysms,* European Journal of Vascular and Endovascular Surgery **28**, 168 (2004).

[13] J. P. Vande Geest, D. H. J. Wang, S. R. Wisniewski, M. S. Makaroun, and D. A. Vorp, *Towards a noninvasive method for determination of patient-specific wall strength distribution in abdominal aortic aneurysms,* Annals of Biomedical Engineering **34**, 1098 (2006).

[14] F. Joly, G. Soulez, D. Garcia, S. Lessard, and C. Kauffmann, *Flow stagnation volume and abdominal aortic aneurysm growth: Insights from patient-specific computational flow dynamics of lagrangian-coherent structures,* Computers in Biology and Medicine **92**, 98 (2018).

[15] M. Khan, K. Valen-Sendstad, and D. Steinman, *Narrowing the expertise gap for predicting intracranial aneurysm hemodynamics: Impact of solver numerics versus mesh and time-step resolution,* American Journal of Neuroradiology **36**, 1310 (2015), http://www.ajnr.org/content/36/7/1310.full.pdf .

[16] R. A. Gingold and J. J. Monaghan, *Smoothed particle hydrodynamics: theory and application to non-spherical stars,* Monthly Notices of the Royal Astronomical Society **181**, 375 (1977).

[17] J. Monaghan, *An introduction to sph,* Computer Physics Communications **48**, 89 (1988).

[18] T. Ye, D. Pan, C. Huang, and M. Liu, *Smoothed particle hydrodynamics (sph) for complex fluid flows: Recent developments in methodology and applications,* Physics of Fluids **31**, 011301 (2019).

[19] F. R. Ming, P. N. Sun, and A. M. Zhang, *Numerical investigation of rising bubbles bursting at a free surface through a multiphase sph model,* Meccanica **52**, 2665 (2017).

[20] N. S. Martys, W. L. George, B.-W. Chun, and D. Lootens, *A smoothed particle hydrodynamics-based fluid model with a spatially dependent viscosity: application to flow of a suspension with a non-newtonian fluid matrix,* Rheologica Acta **49**, 1059 (2010).

[21] A.-m. Zhang, P.-n. Sun, F.-r. Ming, and A. Colagrossi, *Smoothed particle hydrodynamics and its applications in fluid-structure interactions,* Journal of Hydrodynamics **29**, 187 (2017).

[22] Y. Qin, J. Wu, Q. Hu, D. N. Ghista, and K. K. Wong, *Computational evaluation of smoothed particle hydrodynamics for implementing blood flow modelling through CT reconstructed arteries,* Journal of X-Ray Science and Technology **25**, 213 (2017), 2.

[23] W. Mao, A. Caballero, R. McKay, C. Primiano, and W. Sun, *Fully-coupled fluid-structure interaction simulation of the aortic and mitral valves in a realistic 3D left ventricle model,* PLOS ONE **12**, 1 (2017).

[24] D. Krauklys, *Preliminary study of the application of SPH for modelling aortic aneurysms.*, Master's thesis, Delft University of Technology (2019).

Acknowledgments

First and foremost, I would like to thank my promotors **Saša** and **Hildo**. Thank you both for the opportunity you have given me to work on this interesting topic. **Saša** I enjoyed our weekly discussions; thank you for always pushing me. I admire your constant research enthusiasm, especially while working with students. It was a pleasure to co-supervise many bachelor and master students with you. I enjoyed all the conferences we have attended together; thank you for showing me a bit around Belgrade. **Hildo** it was nice to experience the medical side of the research thanks to you. Thank you for all your feedback and fruitful discussions.

During my PhD trajectory, I worked between two groups: the Cardiovascular Imaging group in Leiden and the Transport Phenomena (TP) group in Delft. I have many thanks to the people in both.

Starting in Leiden, **Jos**, you were an invaluable link for me between the medical and technical world. I appreciate all your feedback on the research and articles. Thank you for teaching me a lot about the 4D-flow MRI and for the opportunity to experience it from the patient's perspective. **Joe**, my Leiden counterpart, thank you for all the help with the initial data for my simulations; without your input, none of the work presented in this thesis would be possible. Thank you as well for explaining me more about 4D-flow MRI; it was nice to understand well how the data are acquired. I thoroughly enjoyed all of our chats when I was in Leiden. **Hans**, thanks for all the challenging questions and chats during lunch. **Mitch**, while you were not directly in Leiden, we have mostly met there. It was nice to work with you. **Paul** it was always nice to chat with you - I hope your left ventricle model will move with ease.

Now coming to Delft, my (pre-covid) office mates made each working day more exciting. **Annekatrien**, I thoroughly relished all of our discussions which often took more than a few minutes. Your help with all the office problems was essential. I enjoyed all the cakes you have made, and I appreciate you taking me into account while baking them. Your persistence is truly inspiring. **Manas**, your bubbly personality matched your research focus so well. Thank you for all the long discussions during the coffee breaks and borrels, on topics other than work. **Stefi**, my office/housemate for a while. It was always nice to hang out with you. Thanks for keeping an eye on the house while I was on holiday. **Lorenz**, always kicking each other's feet, the barrier had to come. **Sid** coffee breaks, VrijMiBo, FOM, and CTP tutoring would be much less enjoyable without you; we still need to finish the CTP 'Hall of fame'! **Elin**, I thoroughly enjoyed all of our midnight talks and early morning swims during conferences; thank you for all your help with cluster and Linux. **Artem**, my fellow Slavic tovarich, see you again in the corridors of Veldhoven. **Manu**, I knew why we were always out of hagelslag. **Xiaolin**, your enthusiasm and smile always cheered me up, especially when you were haunted by the triplets. **Maulik**, **Matheus**, **Kosta**, **Peng**, **Kevin**, **Snehal**, **Fei**, **Jorrit**, **Nathalie**, **Rose**, **Christiaan**, **Evert**, **David**, **Valeria**, **Luis**,

and everybody else from TP I might have forgotten to mention, it was always nice to chat with you during our coffee breaks, TP seminars, lunch, or just outside the coffee machine.

Much of my research would not be possible without all the bachelor's and master's students that crossed my PhD trajectory. **Merel**, my almost first, and **Bob**, my truly first, MEP students, helped me a lot with learning how to supervise and asking tough questions. In the next *'batch'* were **Jonhattan** and **Adriana**, who were invaluable in helping me process a large amount of data, co-supervise LOR students, and filling in for TA during CTP. I enjoyed our dinners and all the laughs and talks. **Dominykas**, you fought such a challenging topic bravely; thank you for always asking hard questions. **Henrieke** helped me understand how to translate knowledge among different disciplines. I am still impressed by how quickly you were able to perform CFD without any technical background. **Elise** and **Joel**, you came in during the complicated transition towards working from home; you both did a great job in your thesis and kept me sane during our long weekly online sessions with a lot of other chit-chats. **Thijn**, I admire your structured way of working; our talks were always full of insightful ideas. Lastly, **Conchita**, you still managed to defend before my contract ended, even through all the obstacles! Thank you for all the good discussions and contributions towards the last study. I also enjoyed working on interesting topics with BEP students, **Jack** and **Lorena**; while you both had little-to-no experience with CFD before, you have impressed me with how fast you were able to master it and produced very nice results. Other than directly co-supervising, many students came across the *'Bio-group'*; I enjoyed all the discussions with you **Jonathan**, **Duco**, **Rene**, **Rosemary**, **Michelle**, **Pieter**, **Isa**, and all the rest.

I thank all my friends and family (either the real or my 'adoptive') who were always there for me. Specifically, to **Kači**, who started the Prague and Delft journey with me and persisted in going to De Lelie, cafes, and long walks-and-talks. Dankjewel **Annemieke** en **Marino** dat jullie altijd voor ons klaar staan. **Mima**, tvoje krásne fotky prírody mi vždy zdvihli náladu keď bolo moc roviny. **Mami**, vďaka za všetko!

Finally, a huge thank you goes to **Kris**, for always being there for me. I cannot express how much I appreciate you re-rereading the articles and thesis. I truly would not be able to do this without your love and support.

Romana
World, November 2022

Curriculum Vitæ

Romana Perinajová

3. 2. 1994	Born in Martin, Slovakia
2000-2004	Sklabiňa Primary School Sklabiňa, Slovakia
2004-2006	Mudroňova Primary School Martn, Slovakia
2006-2012	Viliam Pauliny-Tóth Gymnasium Martin, Slovakia
2012-2015	Bachelor in Nano and Microtechnologies in Chemical Engineering University of Chemistry and Technology Prague Prague, Czech Republic
2015-2017	Master of Science in Chemical Engineering Delft University of Technology Delft, The Netherlands
2018-2022	Ph.D. candidate Delft University of Technology Delft, The Netherlands
Thesis:	Modelling of Blood Flow in Arteries
Promotor(s):	Prof. dr. Saša Kenjereš, Dipl.-Ing. and Prof. dr. Hildo J. Lamb, MD (LUMC)
2022-	Physics Design Engineer ASML Eindhoven, The Netherlands

List of Publications

6. **R. Perinajová**, T. van den Ven, E. J. Roelse, J. F. Juffermans, F. Xu, J. J. Westenberg, H. J. Lamb, S. Kenjereš, *A Comprehensive MRI-Based Computational Model of Blood Flow in Compliant Aorta Using Radial Basis Function Interpolation.* (submitted to BioMedical Engineering OnLine)

5. **R. Perinajová**, J. F. Juffermans, C. Borrás Álvarez-Cuevas, J. J. Westenberg, H. J. Lamb, S. Kenjereš, *Influence of aortic aneurysm on the local distribution of NO and O_2 using image-based computational fluid dynamics*, Computers in Biology and Medicine 160 (2023).

4. **R. Perinajová**, P. van Ooij, S. Kenjereš, *On the identification of hypoxic regions in subject-specific cerebral vasculature by combined CFD/MRI*, Royal Society Open Science 10 (2023).

3. X. Wu, S. Gürzing, C. Schinkel, M. Toussaint, **R. Perinajová**, P. van Ooij, S. Kenjereš, *Hemodynamic Study of a Patient-specific Intracranial Aneurysm: Comparative Assessment of Tomographic PIV, Stereoscopic PIV, in vivo MRI and Computational Fluid Dynamics*, Cardiovasc Eng Tech 1869-4098, (2021).

2. **R. Perinajová**, J. F. Juffermans, J. Lorenzo Mercado, J. P. Aben, L. Ledoux, J. J. Westenberg, H. J. Lamb, S. Kenjereš, *Assessment of Turbulent Blood Flow and Wall Shear Stress in Aortic Coarctation Using Image-based Simulations*, BioMed Eng OnLine 20 (2021).

1. **R. Perinajová**, J. F. Juffermans, J. J. Westenberg, R. L. van der Palen, P. J. van den Boogaard, H. J. Lamb, S. Kenjereš, *Geometrically induced wall shear stress variability in CFD-MRI coupled simulations of blood flow in the thoracic aortas*, Computers in Biology and Medicine 133 (2021).